Effect of Aging and High Temperature on High Strain Rate Mechanical Properties of SAC305 and Its Application to Shock and Vibration Environment

by

Di Zhang

A dissertation submitted to the Graduate Faculty of
Auburn University
in partial fulfillment of the
requirements for the Degree of
Doctor of Philosophy

Auburn, Alabama
August 4th, 2018

Keywords: High Temperature, High Strain Rate, Long-term Aging, SAC305, Shock, Vibration

Approved by

Pradeep Lall, Chair, John and Anne MacFarlane Professor of Mechanical Engineering
Jeffery Suhling, Quina Distinguished Professor of Mechanical Engineering
Michael Zabala, Assistant Professor of Mechanical Engineering
Robert Dean, McWane Endowed Professor of Electrical and Computer Engineering

Abstract

Electronic products may experience large and transient deformation under thermal-mechanical load simultaneously during normal usage. Second-level interconnect is one of the weakest link in electronic products. Solder joints have high susceptibility to failure in fine pitch electronics. In recent years, industry has migrated to lead-free solder alloy compositions, because it is environmental friendly. The Tin-Silver-Cooper (SAC) based solder alloys have been widely used to replace the standard 63Sn-37Pb eutectic solder. But the literature on high strain rate mechanical properties of lead-free solder is limited. Moreover, the mechanical properties of lead-free solder can be highly affected by aging duration and operating temperature. However, previous research on this subject is scarce. In this research, effect of aging and operating temperature on high strain rate mechanical properties of SAC305 has been studied. The experiment has been carried out at totally 7 aging duration (Pristine, 60, 120, 180, 240, 300, 360 days). At each aging condition, SAC305 is tested at high strain rates of 10, 35, 50, 75 /s. At each strain rate condition, 8 different testing temperatures (25, 50, 75, 100, 125, 150, 175, 200 °C) have been used as operating temperature to perform high strain rate testing. High speed data acquisition system (was set up by Lall, et.al [1][2][3]) has been built up for measurement. A load cell was used to capture stress history. DIC method with high speed camera has been used to calculate strain data. At each aging condition, a set of Anand constants is computed. At last, predictive model was compared with experimental results.

Electronic products such as smart phone, tablet, personal computer have been populated in recent years, those devices may accidentally fall on the ground during operation. Therefore, understanding the reliability performance of those devices during impact is very necessary. Previously, JEDEC has published a drop test standard JESD22-B111 [4]. This

standard has standardized the test procedures and test conditions. Since board level drop test is a key qualification test for portable electronic devices, lots of researchers have been interested in both experiment and simulation. Since solder joint is one of the weakest link in electronic products, it is important to quantify the stress and strain amplitude of solder joint during drop and shock. However, there is lacking of method to measure the stress and strain of solder joint experimentally, because the size of solder ball is way small. Simulation is a way to approximate the stress and strain values of interconnects during deformation. In the literature, the Anand model have been widely used in thermal cycling simulation to characterize the mechanical properties of solder alloys. But it is barely used in drop and shock simulation. In this study, Input-G method with implicit solver was used to simulate the drop test. The Anand model was used to describe the constitutive behavior of lead free solder and compared with linear material. 3-D DIC was used to measure the dynamic full field response of PCB during drop test at different G-level. Further, experimental data was used to compare with simulation results at drop condition of 1500G and 0.5ms. Hysteresis loop and plastic work density were also extracted to evaluate damage to solder joint per impact.

In automotive applications, electronic system can get exposed to high temperature and vibration during their life cycles. Simultaneously high temperature and vibration can cause failure in electronic system. The reliability of electronic products can be improved through understanding of solder joint interconnects in the electronic system. Presently, the literature on mechanical behavior of lead-free alloys under simultaneous harsh environment of high-temperature vibration is sparse. Most of the prior research in this area of reliability of solder joints are focused on thermal cycling which includes low cycle fatigue failure modes. Relatively few researchers have studied the reliability in the simultaneous environment of thermal cycling and vibration. Previously, finite element method has been widely used to quantify deformation of solder joint during high temperature vibration. In this study, it mainly focuses on effect of high temperature vibration on reliability of electronic packages.

JEDEC dimension boards with 12 packages mounted are tested at its first natural frequency with different G-level and operating temperature. Digital image correlation method is used to measurement displacement and strain of the PCB during deformation. Finite element method is also used to simulate vibration event with Input-G method combining with Anand model. In order to increase the computational efficiency, a nonlinear sub-modeling technique is carried out to running simulation. Displacement and strain results were also extracted from simulation and verified with experimental results. Hysteresis loop and plastic work density have also been calculated from simulation. Weibull analysis was used to analyze characteristic life of electronic packages subjected high temperature vibration. Effect of temperature and vibration G-level on fatigue life of CABGA288 have been discussed. Based on the characteristic life, plastic work density and characteristic life of solder joint, life prediction models were carried out to predict the useful life of packages on board. Failure analysis was performed to find the failure mode.

Acknowledgments

I would like to express my special appreciation and thanks to my advisor Dr. Pradeep Lall, many thanks for your mentoring to my research and allowing me to grow as a research scientist. Your advice on both research as well as on my career have been priceless. I would also like to thank my committee members, professor Jeffrey Suhling, professor Michael Zabala, professor Robert Dean for serving as my committee members. Special thanks go to professor Bart Prorok for serving as my doctoral dissertation university reader.

I also thank my mother-in-law, father-in-law, my mother, and father for all of the sacrifices that they have made on my behalf. I would also like to thank all of my friends and colleagues who supported me in my research. At the end I would like express thanks for my beloved wife Dr. Simin Zou who supports me all the time. Words cannot express how grateful I am to her.

Table of Contents

List of Figures

List of Tables

Chapter 1

Introduction

1.1 Overview of Electronic Packaging

In recent decades, electronic products have been used more frequently than ever. For example, cell phones have changed our life a lot, which were used only for calling. Now we used it for watching video, playing games, even computing etc. With increasing functionality of electronic devices, the size of those devices are also shrink much than their original size. With such a big reliance on electronic products, there will be a lot concern related to the design, manufacturing, cost and reliability. Electronic packaging is an art based on science of placing and interconnecting different levels of electronic systems [5]. There are lots of functions of electronic packaging. Main of them are signal distribution, power distribution, heat dissipation and protection of components and interconnection. Figure 1.1 ([5]) shows the assembly hierarchy of electronic packing. In the first level, a silicon based integrated circuit chip is put on the top of carrier. There are also interconnects between chip and carrier. Some of them are connected by wire bond or tiny solder bump. This assembly between chip and carrier is called first level interconnect. The connection between multiple chip carriers and Printed Circuit Board (PCB) is called second level interconnect. For the third level package, several PCBs are put into mother board.

In this dissertation, the reliability of the secondary level interconnects is a key area of concern. There are basically two types of secondary level interconnect, one is using surface mount technology, the other is mounting the package on PCB as a through hole component. With increasing function densities of electronic products, more and more devices are using surface mount technology instead of the early through hole technology. But comparing with the traditional through hole technology, surface mount devices (SMDs) have some drawbacks.

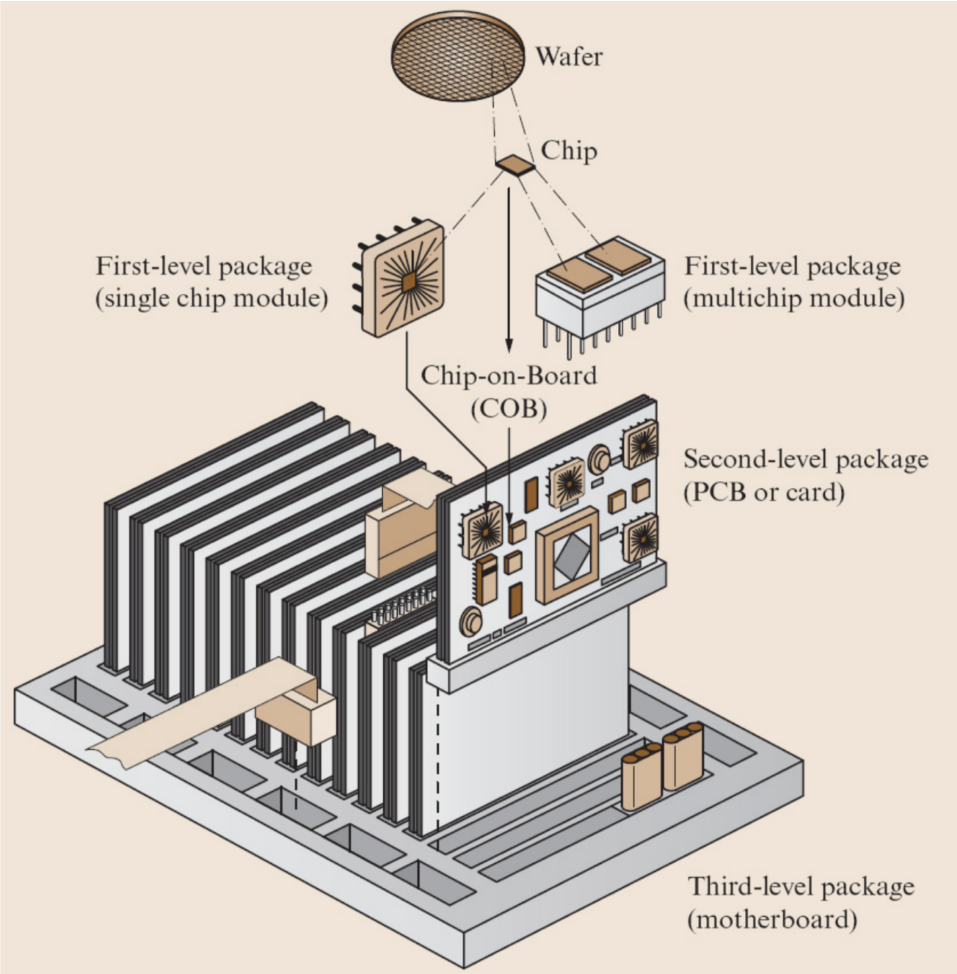

Figure 1.1: Assembly hierarchy of electronic packaging [5]

Although SMDs provide us more functionality, the reliability performance is worse than the old way, such as thermal, drop and shock performance.

1.2 Reliability Issues of Second Level Interconnects

Soldering is one of the main method to attach electronic components to PCB. Reflow oven is usually used as the equipment to perform the soldering process. During reflowing, inter-metallic layer is formed between solder ball and copper pad. This layer is brittle and the thickness of layer is increasing with time increasing. And grain structure also changes a lot with increasing time of usage. Reliability issues can cause failure of those electronic devices after long-term of usage. During reflowing, void can be formed inside of solder joint due to outgassing. In normal operation, stress concentration may happen to the void of solder joint, which cause the failure of the secondary interconnects.

1.3 Typical Soldering Material

With the development of electronic packaging industry in recent years, solder materials are also evolved as well. During the past, Tin Lead solder (63Sn-37Pb) has been widely used by industry. Because its relative low melting point which is around 183 °C. This composition of alloys provides great reliability and excellent ductility at the same time. But industries are trying to find replacement for tin-lead solder that is harmful for not only environment but also human health. Therefore, researchers put their effort to find the perfect alloy composition to replace tin-lead to produce the same or better performance.

1.3.1 Sn-Ag-Cu (SAC)

SAC solder is one of the most widely used solder material in industry. By using these three element composition, one of the main benefit is their relative low melting temperature comparing with 96.5Sn-3.5Ag binary eutectic alloy. At the same time, SAC solders

also show excellent mechanical reliability and durability when comparing with other alloy composition. In current application, there are varieties of SAC alloys with different weight compositions. Those different chemical compositions are proposed by lots of users and companies and are desired to be used in various application at different environment. The compositions include: SAC105 (98.5Sn-1.0Ag-0.5Cu), SAC205 (97.5Sn-2.0Ag-0.5Cu), SAC305 (96.5Sn-3.0Ag-0.5Cu), and SAC405 (95.5Sn-4.0Ag-0.5Cu), are named SACN05 series; SAC387 (95.5Sn-3.8Ag-0.7Cu), SAC396 (95.5Sn-3.9Ag-0.6Cu), and SAC357 (95.2Sn-3.5Ag-0.7Cu), is known as near eutectic SAC choices; SAC3810 (95.2Sn- 3.8Ag-1.0Cu), SAC3595 (95.55Sn-3.5Ag-0.95Cu), SAC0307 (9Sn-0.3Ag-0.7Cu), and SAC107 (98.3Sn-1.0Ag-0.7Cu), are developed for special needs such as high temperature application, drop and shock optimization, etc. Since SAC solder alloy are using to replace the original Sn-Pb solders, It is very important to understand the melting temperature of those SAC series. Figure1.2 shows the Sn-Ag-Cu ternary phase diagram Most of the solder materials which are available in markets are found within the eutectic region. For this region, the melting temperature are around 217 °C.

1.3.2 Sn-Cu

Unlike the SAC alloys, Sn-Cu removes the silver, which cause the melting temperature is slightly higher than SAC compositions. For example, one of the typical composition is 99.2Sn-0.7Cu has a melting temperature around 227 °C. In this case, this binary composition can be used as high temperature application. But one of the drawback of this alloy is its relatively poor reliability performance comparing with SAC composition.

1.3.3 Sn-Bi

By combining Bi with Sn together, a relative low melting temperature was achieved which is around 139 °C. Therefore, it is better to be used in low temperature application. The eutectic Sn-Bi has a composition of 42Sn-58Bi. But, everything has two sides. For Bi

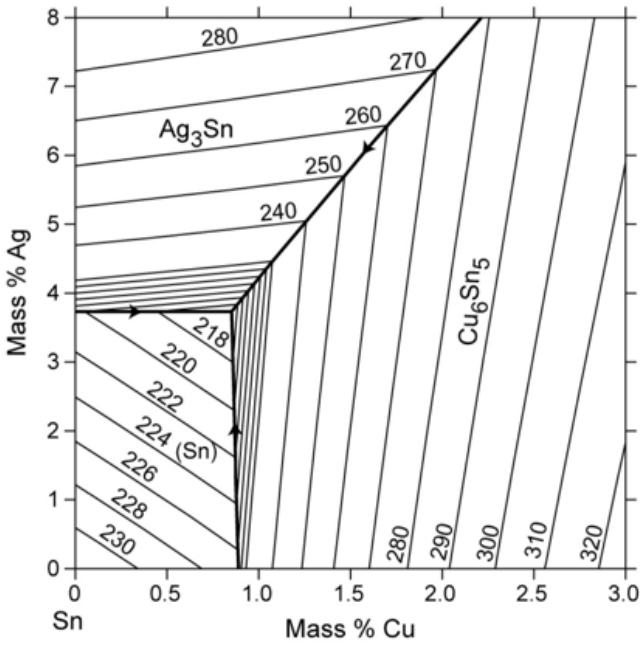

Figure 1.2: Sn-Ag-Cu ternary phase diagram

doped solder alloy, the crack is easily happened at the intermetallic layer which is between solder joint and copper trace.

1.3.4 Sn-Ag-Cu+X

As we discussed above, SAC solders has been widely used by industry and researchers. But experts are continuing to find the perfect solution. Some researchers come with the idea by doping some other elements to get better physical performance. The proposed dopants include: Bi, Ni, Co, Ge, Zn, Fe, etc. Lots of researchers have studied the effect of alloy composition on reliability performance of secondary interconnect which are subjected to thermal cycling, drop, shock and vibration. SAC+X can alter the mechanical properties and improve reliability performance, however it is very time consuming to figure out what are the dopants and the weight of dopants to increase physical performance.

1.4 Uniaxial Tensile Testing

Since the secondary interconnects provide support to packages, it is very important to understand the mechanical properties of solder alloy to improve the reliability performance of the whole electronic system. Most of failures are occurred at interconnections, which may be caused by drop, shock, vibration and thermal cycling during normal operations. Uniaxial tensile testing is one of the most frequently methods to obtain he mechanical properties of materials. Before the test, specimens are needed to be prepared. Casting is one of the ways to prepare uniform samples. By doing casting, the size of specimens is under controlled. With less variation in sample size, the repeatability of testing results is better. In the test, samples should be fixed at both end on the fixture. The grip should be strong enough to hold the sample without sliding from fixtures. Otherwise, the measurement can not be accurate. During testing, the tensile load should to be recorded in order to compute stresses by dividing the cross-section area. Meanwhile, displacement data are also saved to convert to strain value by dividing the original gauge length. By analyzing the stress-strain relationship, the constitutive relationship can be achieved. Mechanical properties of materials may be affected operational temperature and deformation rate. For this kind of materials, we called it viscous material. SAC alloys are considered as visco-plastic material. In this study, SAC305 will be tested at different operating temperate and different high strain rate conditions within different aging periods.

1.4.1 General Instrument

INSTRON, as shown in Figure 1.3, is one of general instrument using for tensile test, creep test, compression test and three-point bending test. INSTRON is machine built with strain gauges, load cells and servo-control systems. This machine can dynamically monitor the displacement and load that applied to samples. With a servo feedback control system

Figure 1.3: Instron Machine

and a load cell, the machine can control test velocity, displacement and load values etc. Stress-strain curves can be output from the computer after performing test.

1.5 Drop and Shock Testing

Electronic product may be failed when they are subjected to large transient deformation during operation. Usually the failure happened to the second level interconnect when the devices are dropped and shocked. Figure 1.4 shows the deformation of solder joint during impact loading. When board is going down, solder joints are suffered from tension stresses. Vice versa, when the board is going up, solder joints are subjected from compression stresses. Therefore, during changing state from tension to compression, the solder joints are exposed to fatigue stresses, which can cause failure to whole electronic system. One way to evaluate

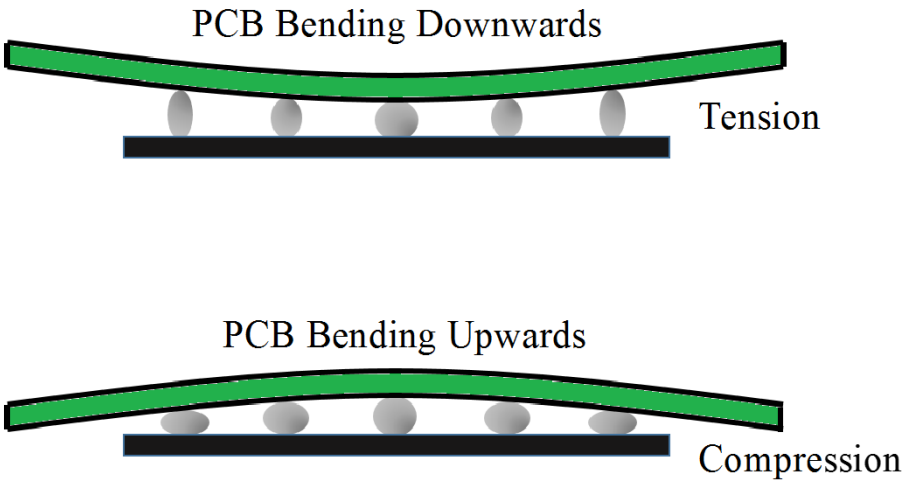

Figure 1.4: PCB bending induced solder joint deformation

the drop and shock reliability of those electronic devices is performing drop testing. Then the drop tower (Figure 2.2 [4]) is brought on the stage to execute testing in lab environment. Sine there are lots of companies and groups who are working on reliability performance of electronic product, a unified standard created by Joint Electron Device Engineering Council (JEDEC) is carried out to guide how to do drop testing. The standard named JESD22-B111 which specified the desired acceleration output during impact event. Figure 1.5 shows the desired impact acceleration output from accelerometer. In this graph, the desired output pulse should be in the shape of half-sine wave. The amplitude shows the testing G-level and the plus width specifies the contact duration. The amplitude and pulse width of output acceleration can be change by lots variables which include: drop height, pulse shaper material and thickness, total mass of testing board etc. In literature, lots of researchers have done testing at various G-level and impact duration to see the performance of electronic product. In this study, a normal testing with G-level is around 1,500g and pulse duration 0.5ms is carried out.

$$A(t) = A_o \sin\left(\frac{\pi t}{t_w}\right)$$

$$\sqrt{2gH} = \frac{2A_o}{C}\frac{t_w}{\pi}$$

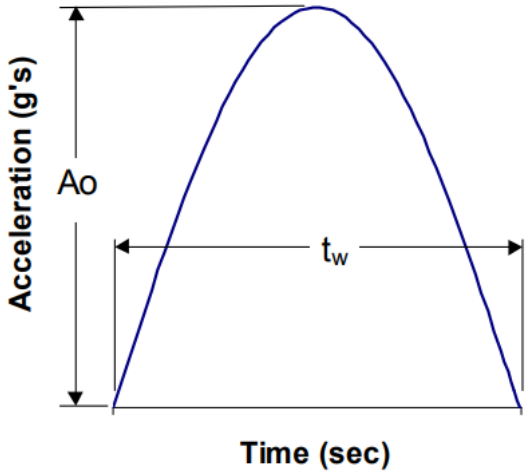

Figure 1.5: Typical shock test half sin pulse graphic and formulas

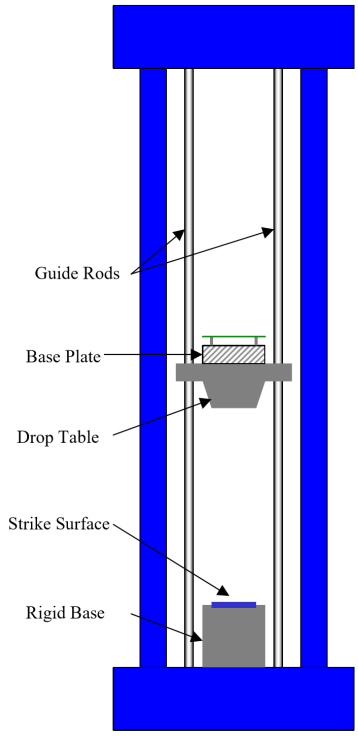

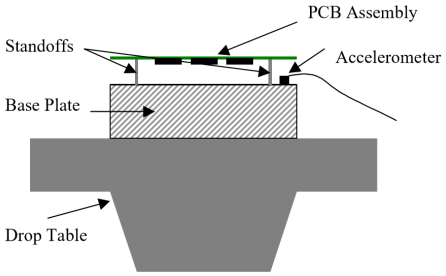

Figure 1.6: Drop tower

1.6 Vibration Testing

In addition to drop and shock, vibration is also one of main reasons to cause failure of secondary level interconnects. Vibration can happen easily to electronic devices in real world, such as electronic sensors for underhood applications, downhole drilling devices, aerospace applications. The Amplitude and frequency of vibration can go randomly high and low. During dynamic vibration, the solder joints are continuing to expose to tension and compression stress frequently. High cycle fatigue causes damage to bulk solder region or intermetallic layers between solder alloy and copper trace. Therefore, it is very important to understand all types of vibration and the response of electronic products to these vibration loads. In automobile application, the electronic control units are usually subjected to high frequency vibration and high temperature simultaneously. Sensors which are used on engine to monitor the status of engine, are usually working above 125 °C and exposed to vibration at the same time. Currently, lots of electronic car are available in the market and some of them are also provide autopilot functionality. During normal operations, electronic failure may cause very serious problems. So, knowing the vibration reliability performance of electronic devices at high temperature is very necessary. In the lab environment, shaker (Figure 1.7) is usually used to simulate the real vibration event, which is controlled by programming profiles. In the programming profiles, we can specify the vibration G-level and frequency or random vibration with power spectrum density (PSD) controlled.

1.7 Finite Element Method

The finite element method (FEM) is a numerical technique for finding approximated solutions to boundary value problems for partial differential equations. It has widely used in engineering world to solve real application problems. With FEM, lots of problems have been solved by approximated solution. Finite element method is more efficient way to solve real application problems than experimentation which is time and cost consuming.

Figure 1.7: Permanent magnet shaker LDS V450

Furthermore, in some scenario, it is impossible to perform some experiments to get desired results. Mathematic approximation method is one of the way to achieve the results. Finite element method can be used to analyze complex structure problems by discretizing the whole system into finite elements. Basically there are 5 steps of FEM

1. Create CAD modeling
2. Generate mesh based on modeling
3. Appling boundary condition and external force
4. Solve PDEs equations
5. Post-processing

The accuracy of finite element method can be improved by introducing higher order elements and increasing the mesh density. But it does not mean the more elements used, the better of simulation will be. With the number of elements increased, the computation time will be increased tremendously, especially for dynamic and nonlinear problems. Modified Newtown method are also introduced to reduce the computational time by not changing the stiffness matrix every iteration. For dynamic problems mass matrix and damping matrix are

also brought to equilibrium equations. In this study, all the simulations involved vibrations and drop testing are nonlinear and dynamic problems.

1.8 Digital Image Correlation (DIC)

In literature, researchers have used digital image correlation to measure the deformation of object in real application. DIC is an optical method to tracking the deformation of object by comparing the reference image with deformed images. Displacement and strain can be computed by computational algorithm. Basically, there are two types of DIC analysis. One is 2D DIC which is used to measure in-plane deformation. The other is 3D DIC which can be used to measure not only in-plane deformation, but also out-plane deformation. However, the required experimental setup is different for these two technique. 3D DIC needs at least two cameras to fulfill analysis, while 2D DIC needs just one. The other difference is calibration technique. 3D DIC is complicated which multiple calibration images are required, however 2D DIC needs just one calibration image. Comparing others deformation measurement techniques such as strain gauge, moir interferometry, DIC is easy to be implemented and no destructive. DIC will also provide full field strain, unlike the strain gauge only shows the strain values at specific point

1.8.1 Software

VIC-2D and VIC-3D are softwares which are commercial available that can be used to perform DIC analysis. In this study, all the DIC analyzing results are computed by these two softwares. VIC-2D is used to perform 2D-DIC analysis, which can only computer the in-plane deformation. VIC-3D is 3-dimensional measurement. It can be used to computed out-of-plane deformation. However, the experimental setup is more complicated than 2D DIC analysis.

1.9 Dissertation Outline

In chapter one, the importance of Pb-free soldering alloys to electronic packaging has been discussed. Furthermore, we introduced the different testing scheme including tensile test, drop test and vibration test. In addition, DIC methods are introduced to measured full field deformation during testing. In the end, FEM is discussed to solve complex dynamic and nonlinear structural problems.

In chapter two, Literature survey starts from mechanical properties of lead-free solder alloys at high strain rate and low strain rate. Aging induced degradation of lead free solder alloys. Furthermore, different constitutive models used to describe SAC solders. Experimental setup up and testing for drop, shock and vibration. Digital Image correlation for dynamic measurement. Finite element method for drop and vibration simulation. Life predication model for solder joint.

In chapter three, this chapter mainly focuses effect of aging and operating temperature on mechanical properties of SAC305 at high strain rates. Starting from sample preparation and experimental setup. After stress and strain curves are achieved, Anand model is introduced to perform nonlinear regression. And then the accuracy of Anand model has been verified by comparing with experimental data.

In chapter four, board level drop testing is executed with 1500G and impact pulse duration 0.5ms. Digital image correlation method is used to measurement full field displacement and strain. Finite element method is also used to simulate this drop event with input G method combining with Anand model. Hysteresis loop and plastic work density have also been calculated by FEM to see the damage accumulated by bending cycle.

In chapter five, this chapter mainly focuses on effect of high temperature and high frequency vibration on reliability performance of electronic packages. JEDEC dimension boards with 12 packages mounted are tested at its first natural frequency with different G-level. Digital image correlation method is used to measurement full field displacement

and strain of the PCB during deformation. Strain gauges are also used to verified the in-plane strain results from DIC measurement. Finite element method is also used to simulate vibration event with Input-G method combining with Anand model. In order to increase the computational efficiency, a nonlinear sub-modeling technique is carried out to running simulation. Displacement and strain results were also extracted from simulation to verify with experimental results. Hysteresis loop and plastic work density have also been calculated by FEM to see the damage accumulated by fatigue cycle. Based on the characteristic life and plastic work density, a life prediction model is carried out to predict the useful life of packages on board.

In chapter six, summary and conclusions of this dissertation are discussed.

Chapter 2

Literature Survey

2.1 Introduction

Electronic products can be exposed to large and transient deformation during normal usage or accidentally drop. Since second level interconnect is one of the weakest link in electronic devices, lots of researchers put a lot effort to explore the solution. Lots of groups and companies put lots of time and energy to search the best composition of solder alloys to replace Tin-Lead solders. However, a larger variance has been found in literature data. This can be caused by lots of reasons. One of the main reason is because of sample preparations differences, different prepared procedures can cause a huge variance in micro-structure. For example, slightly difference in solidifying rate of solder alloy can lead to totally different mechanical properties. Different sample dimensions also cause different mechanical properties. Furthermore, solder alloy is strain rate sensitive material, different testing method and condition will affect the testing results. Drop and shock tests have been used a long time in industry to evaluate the reliability of board level packages.

2.2 Mechanical Properties of Solder Alloys

Previously, eutectic or near eutectic tin-lead based solder joints were widely used in the electronics industry because of their ease of solderability and long term reliability under a variety of commonly used environmental conditions. Recent years, the electronics industry has migrated to lead-free solder alloy compositions to reduce the damage of Pb on the environment. Tin-Silver-Copper (SnAgCu or SAC) alloys are being widely used as replacements for the standard 63Sn-37Pb eutectic solder. Large amount of researchers have studied the

mechanical properties of lead free solder. Motalab [6] [7] has done creep test and tensile test on SAC305 over a variety of operating temperature and aging duration.

2.2.1 Effect of Operating Temperature on Mechanical Properties

Mechanical properties of lead-free solder are highly depended operating temperature. The elastic modulus and ultimate tensile strength change dramatically when it is operating close to its glass transition temperature. Motalab [6] [7] has tested low strain rate mechanical properties of SAC305 from 25 °C to 125 °C. The results show that once increased the operating temperature, the ultimate tensile strength and elastic modulus are both decreased.

2.2.2 Effect of Aging on Mechanical Properties

Since electronic devices may be used for a long time before replacement, knowing the reliability performance of those products after long term aging is very necessary. Lots of researchers have study the effect of aging on mechanical properties of solder alloy. There are basic two types of solder being tested. One is in bulk solder, the other is solder joint in actual component. Most of studies show the significant effect of aging on material properties of solder alloy. Medvedev [8] showed the tensile strength for bulk Sn-Pb solder has reduced by 30 percent after 450 days aging at room temperature. Similarly, this author also showed the tensile strength of Sn-Pb solder joints has a 23 percent of loss at same condition. Lall [9] has done the research on the effect of aging on the high strain rate mechanical properties of SAC105 and SAC305 leadfree alloys, which showed the significant reduction in elastic modulus and tensile strength after long term aging. Ding, et al.[10] investigated the effect of aging on fracture behavior of Sn-Ag solder in pull tests. The tensile strength reduced a large amount by isothermal aging for 120 hours at 180 °C.

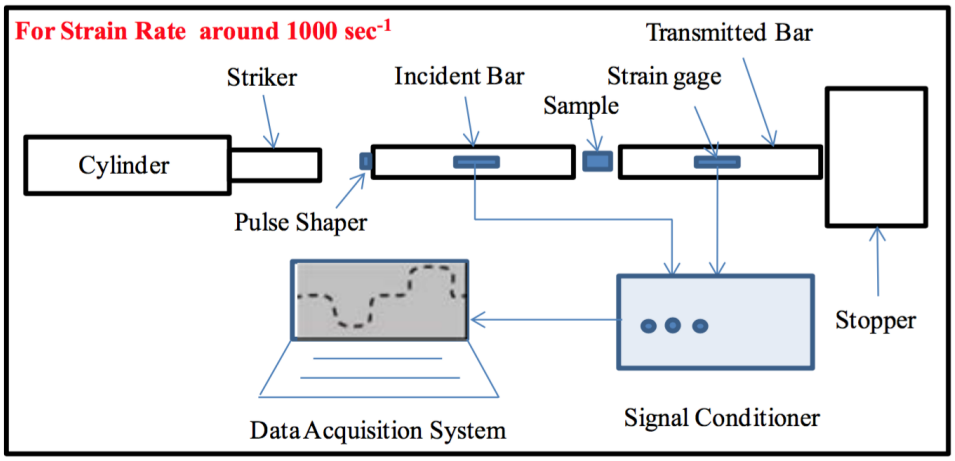

Figure 2.1: Typical Split Hopkinson Pressure Bar for very high strain rate material testing

2.2.3 Effect of Strain Rate on Mechanical Properties

The strain rate range of solder joint during drop and shock is varied from 1 to 100/s. Different deformation rate will effect different response from solder materials. Lall [1] [2] [3] has has investigate the mechanical properties of lead free solder at strain rate range of 1 to 100/s. It showed both the elastic modulus and tensile strength increased with deformation rate increased. Jenq [11] and Siviour [12] both used Split Hopkinson Pressure bar to perform high strain rate testing. Figure 2.1 shows the schematic diagram of Split Hopkinson Pressure bar (http://hdl.handle.net/10415/3799). But the strain rate range for Split Hopkinson Pressure bar is much higher than the typical real environment applications.

2.2.4 Constitutive Model for Solder Material

Solder joints in electronic packaging are usually subjected to complex deformation such as shear and tensile. Therefore accurate constitutive models are necessary to describe the stress and strain relationship. In finite element analysis, an accurate stress-strain relationship can lead to precise simulation results.

2.2.5 Anand Viscoplastic Model

Anand [13] proposed a set of constitutive equation which has been widely used to describe creep and plastic deformation of solder joint by many researchers(Darveaux [14], Basit [15], Motalab [7], Lall [3]). The Anand model is combined of three equations: flow equation 2.1, stress equation 2.2 and evolution equation 2.4. The flow equation 2.1 was selected to accommodate both the power law and the exponential dependence of the strain rate on the stress at constant structure.

$$\dot{\varepsilon}_p = A \cdot \exp\left(-\frac{Q}{R \cdot T}\right) \cdot \left[\sinh\left(\xi \cdot \frac{\sigma}{s}\right)\right]^{\frac{1}{m}} \tag{2.1}$$

The temperature dependence in this function is incorporated via Arrhenius term. While the stress and state dependence are a simple modification of the following hyperbolic sine form first proposed by Garofalo to model steady state creep

In one dimension uniaxial loading case, stress equation can be written by

$$\sigma = c \cdot s \tag{2.2}$$

Where c (c $<$ 1) is a function of strain rate and temperature 2.3, s is the internal variable.

$$c = (\dot{\varepsilon}_p, T) = \left(\frac{1}{\xi}\right) \cdot \sinh^{-1}\left\{\left[\frac{\dot{\varepsilon}_p}{A} \cdot \exp\left(\frac{Q}{R \cdot T}\right)\right]^m\right\} \tag{2.3}$$

The evolution equation 2.4 for the internal variable s is assumed to be function of strain, strain rate and temperature. An explicit form of the evolution equation is expressed as:

$$\dot{s} = \left[h_0 \cdot (|B|)^a \cdot \frac{B}{|B|}\right] \cdot \dot{\varepsilon}_p; (a > 1) \tag{2.4}$$

where,

$$B = 1 - \frac{s}{s^*} \tag{2.5}$$

and

$$s^* = \hat{s} \cdot \left[\frac{\dot{\varepsilon}_p}{A} \cdot \exp\left(\frac{Q}{R \cdot T}\right)\right]^n \tag{2.6}$$

To summarize, the Anand model has nine material constants. These constants can be determined from either stress-strain responses or creep responses characterized over a wide temperature range. The Anand model successfully unifies both rate-dependent creep behavior and rate-independent plastic behavior occurring concurrently, and it has been demonstrated to work well on solder materials. On the other hand, there are still some limitations of the Anand model, such as incapability of predicting the primary and tertiary creep responses, no incorporation with aging effects, etc

2.2.6 Ramberg-Osgood Model

The Ramberg-Osgood equation [16] was created to describe non-linear strain and stress relationship. It is especially useful for strain hardening material with a smooth elastic-plastic transition. Equation 2.7 is the basic strain and stress relationship.

$$\epsilon = \left(\frac{\sigma}{E}\right) + K \cdot \left(\frac{\sigma}{E}\right)^n \tag{2.7}$$

where ϵ is strain, σ is stress, E is young's modulus, K and n are the constants that depend on the material. Lall [17] has derived the high strain rate Ramberg-Osgood for SAC305 and SAC105.

2.3 Drop and Shock

Electronics may often be subjected to drop and shock environment in real life, such as down-hole drilling applications, military missiles. It is necessary to evaluate the survivability of electronic products during drop and shock event. Second level interconnect is one of the weakest link in electronic packaging. During the deformation of PCB, the solder joints are subjected to a huge impact loading which can cause failure in few drops. And after the

contact, the PCB is continuous moving up and down which can also cause fatigue of solder joints. Those factors can lead to the failure of the packages. Therefore, knowing the transient deformation of solder joints during impact load and fatigue load is very necessary to perform better design and optimization.

2.3.1 Experimental Setup

Previously, the drop test has been specified by the JESD22-B111 standard [4]. This standard has been widely used to evaluate the drop and shock reliability of electronic components. The content specified the drop test by controlling the impact acceleration pulse shape and board configuration. One of the common conditions is the impact acceleration with peak at 1500Gs and 0.5 ms duration. Figure 2.2 shows the standard drop tower setup. During the test, the shock pulse shall be measured for each drop to ensure that input pulse remains within the specified tolerance. Adjustments in drop height or replacement of strike surface may be needed if the pulse deviates from the specified.

2.3.2 Simulation Method

Finite element method is always an effective way to simulate event in real environment. In drop and shock application, finite element modeling can be used to estimate the deflection of PCB subjected to different G-level and impact duration. Since the solder joint is very small, there is lacking of method to measure the stress and strain amplitude of this interconnect. Simulation is a great method to estimate the stress and strain of solder interconnect. In literature, there are basic two methods to simulate the drop event. The first one is traditional contact method (Lall [18] [19], [20], [21]). In this method, the model is combined of strike surface and PCB with electronic component mounted on drop base. Figure 2.3 (Lall [21]) shows the finite element model of traditional contact method. Contact elements have to be generated on the contact surface.There is a small gap between the drop base and rigid surface. In order to simulate this event, an initial velocity before the contact is necessary to

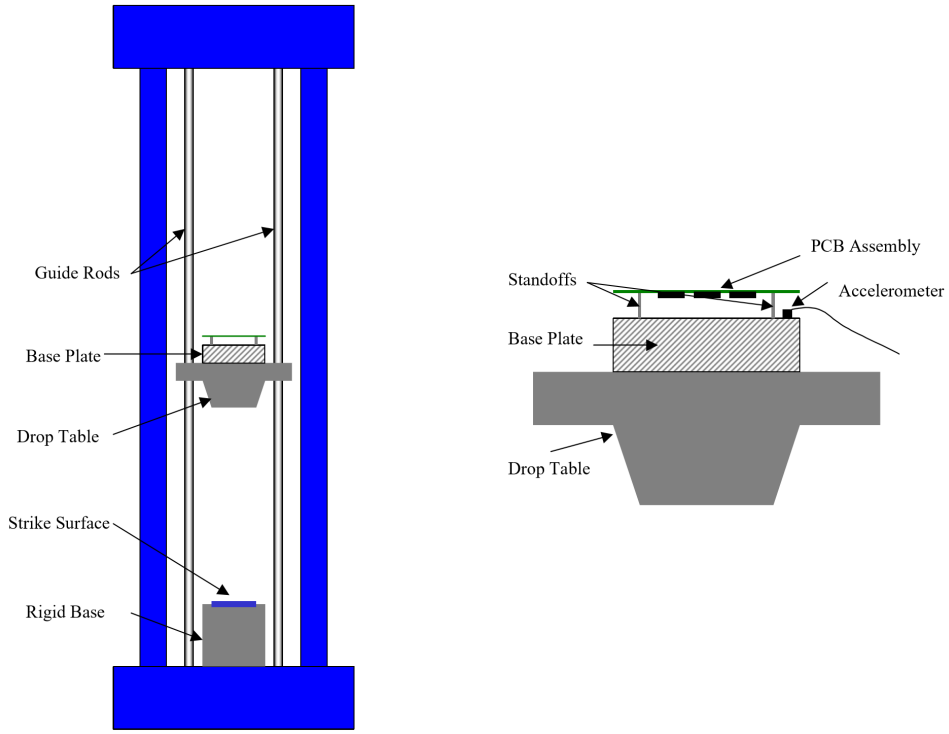

Figure 2.2: Typical drop test apparatus and mounting scheme for PCB assembly

be assigned to the drop base. This velocity can be measured experimentally or calculated theoretically (Lall [21]). Since the contact happened in milliseconds, it has to be running explicitly. The second method is named Input-G method, unlike the previous method, this method is running without contact. Therefore, the computation is less. it can be solved with explicit solver or implicit solver. Syed [22] has developed this methodology and used it in simulation. Luan [23] also used the same methodology to study drop and shock event.

2.4 Vibration

In automotive applications, electronic components are subjected high temperature vibration. According to Johson [24], the maximum operating temperature is up to 140 °C and the vibration G-level is up to 10G RMS. In agriculture applications, the operational environment is even more severer. Since solder joint is one of the weakest link in the electronic packaging system, it is very important to understand how combined temperature and

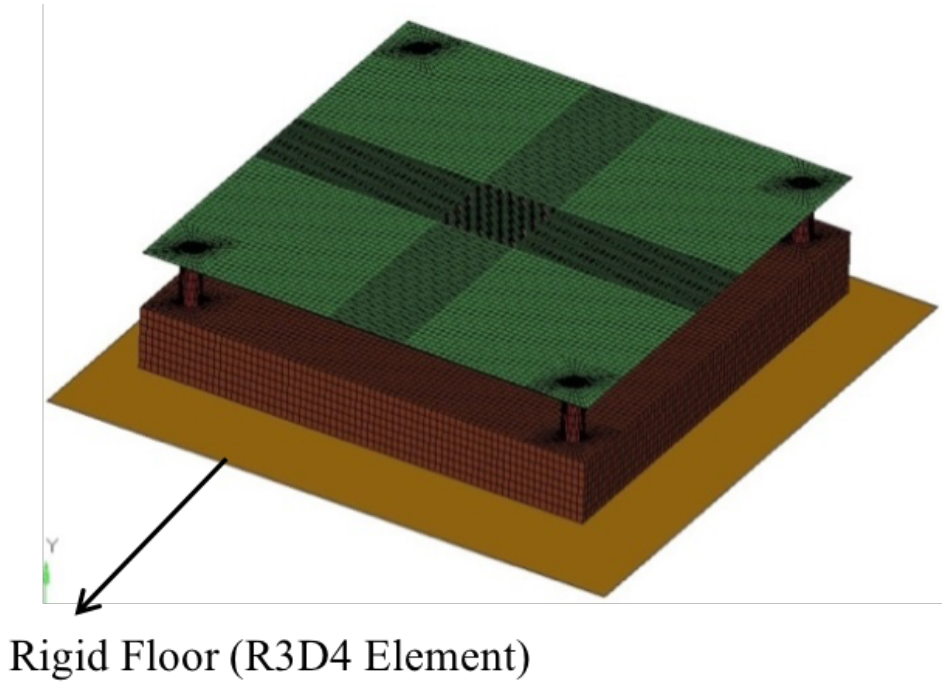

Figure 2.3: Traditional contact finite element model

vibration effect the reliability of solder interconnect. But there is a lack of understanding this combined effect. Most of the researchers are focusing on vibration only (Steinberg [25], Henderson [26], Hu [27], Wong [28]) or thermal cycling only. Very few researchers have studied electronic system in combined thermal and vibration environment (Barker [29], Basaran [30], Qi [31]).

2.5 Fatigue Life Prediction Model

A number of life prediction approaches have been proposed for solder joint fatigue during the past few years. These approaches are based on combined experimental data and simulation results. There are basic three categories : (i) strain-based approach; (ii) stress-based approach; (iii) energy-based approach;

2.5.1 Strain Based

The Coffin-Manson equation has been widely used for fatigue life prediction. A number of researchers have applied it to predict fatigue life of solder alloys subjected to shear strain-dominated deformation (Getkin [32], Shohji [33], Ostergren [34]). Equation 2.8 shows the Coffin-Manson model

$$N_f = a \cdot (\triangle\gamma)^b \tag{2.8}$$

where N_f is the characteristic life, a and b are fatigue constants. $\triangle\gamma$ is the plastic shear strain. This model is usually used to predict the fatigue life of solder joint subjected to thermal cycling.

2.5.2 Stress Based

Stress based method are usually used to solder joint under cyclic loading. Lall [35] used S-N digaram to predict the high cycle fatigue life of solder joint subjected to high temperature vibration. Equation 2.9 shows the basic formula for stress-based method.

$$\sigma_a = \sigma_f \cdot (2 \cdot N_f)^b \tag{2.9}$$

where σ_a is the stress amplitude, σ_f is the fatigue strength coefficient, b is the fatigue strength exponent and N_f is number of cycles to failure.

2.5.3 Energy Based

Strain energy-based methods have been applied to the fatigue of solder joints. The form of energy-based model is very similar to Coffin-Mason equation, both are based on the power law relationship. Unlike Coffin-Mason based on inelastic strain, this model is based on plastic work density. The equation can be written in the following.

$$N_f = a \cdot (\triangle W)^b \tag{2.10}$$

where N_f is the characteristic life, a and b are fatigue constants. $\triangle W$ is the plastic work density accumulated per cycle. Dasgupta [36] has used this energy approach to analyze the fatigue life of solder joint. Darveaux ([14], [37], [38] has further develop this energy method with fracture mechanics and applied to calculate fatigue life of solder joint subjected to thermal cycling. Equation 2.11, 2.12 and 2.13 show the three basic equations for life prediction.

$$N_o = K_1 \cdot (\triangle W)^{K_2} \tag{2.11}$$

where N_o is the number of cycles to crack initiation, K_1 and K_2 are fatigue constants. $\triangle W$ is the plastic work density accumulated per cycle.

$$\frac{dN}{da} = K_3 \cdot (\triangle W)^{K_4} \tag{2.12}$$

where $\frac{dN}{da}$ is the crack propagation rate, K_3 and K_4 are fatigue constants.

$$N_f = N_o + \frac{a}{\frac{dN}{da}} \tag{2.13}$$

where N_f is the characteristic life, a is the copper pad length.

Chapter 3

Effect of Aging and Operating Temperature on High Strain Rate Mechanical Properties of SAC305

3.1 Introduction

Currently, due to the wide popularity of smart devices, the electronic products are required for more high density and multi-functions. With increasing in functionality, the pitch size of electronic packages is becoming smaller and smaller. 3D and 2.5D packages have been widely used in industry in recent years. Therefore the reliability of those powerful electronic products during normal usage is big concern. Failure happened to the device may be caused by lots of reasons. One of dominant failure mechanism is second level interconnect failure. This failure may be caused by lots of possibilities, such as operating at high temperature for long time, dropping by mistake, shocking and vibrating accidentally etc. Lately, because of concerning about environment effect, Tin-lead solder has partially changed to lead-free solder. But very few researchers have studied high strain rates mechanical properties of lead-free solder alloys at high operating temperature. Solders are commonly exposed to those complicated operating conditions. Effect of aging also has strongly influence on mechanical properties of lead-free solder alloys. Motalab, et.al [7] have shown that after long term storage at high temperature, the ultimate tensile strength and elastic modulus show significant decreasing. The reason to cause the great degradation of mechanical properties of lead-free solder is the evolution of micro-structure. Micro-structure is decided by lots of factors including sample solidification rate, isothermal aging period and temperature. Isothermal aging make the micro-structure of lead-free solder evolve with different aging period, which leads to the change of mechanical response of the material. The higher

aging temperature coarsen the physical structure of solder alloy faster, but even in room temperature significant change of grain size can occur after long term of storage.

Previously, Anand, et.al [13] have developed a visco-plastic constitutive model which can be used to describe a time and temperature dependent material. Lots of researchers have applied it to solder material. Darveaux, et.al [14] measured mechanical properties of solder alloy at low strain rate (from 10^{-8} to 10^{-1}). He also applied Anand model to thermal simulation which successfully calculate the plastic work density and plot the hysteresis loop which indicate the damage accumulated per thermal cycle. Basit, et.al [15] have studied effect of aging on Anand constants of SAC305. And also applied to thermal cycling to calculate characteristic life of electronic packages. Motalab, et.al [6] measured both creep and tensile stress-strain curve of SAC305 at low strain rates of 0.001, 0.0001, 0.00001/s to formulate Anand model. This model has been applied to simulation in ANSYS to predict the life of solder joint in thermal cycling environment.

Digital image correlation(DIC) has been used by lots of researchers to measure full field strain and displacement. Lall, et.al [18][20] used high speed to camera to record transient deformation of solder strip in experiment. And he measured full field strain of speckle patterned solder strip by using DIC technique.

In this research, effect of aging and operating temperature on high strain rate mechanical properties of SAC305 has been studied. The experiment has been carried out at totally 7 aging durations (Pristine, 60, 120, 180, 240, 300, 360 days). At each aging condition, SAC305 is tested at high strain rates of 10, 35, 50, 75 /s. At each strain rate condition, 8 different testing temperatures (25, 50, 75, 100, 125, 150, 175, 200 °C) have been used as operating temperature to perform high strain rate testing. High speed data acquisition system (was set up by Lall, et.al [1][2][3]) has been built up for measurement. Load cell was used to capture stress history. DIC method with high speed camera has been used to calculate strain data. At each aging condition, a set of Anand constants is computed. At last, predictive model was compared with experimental.

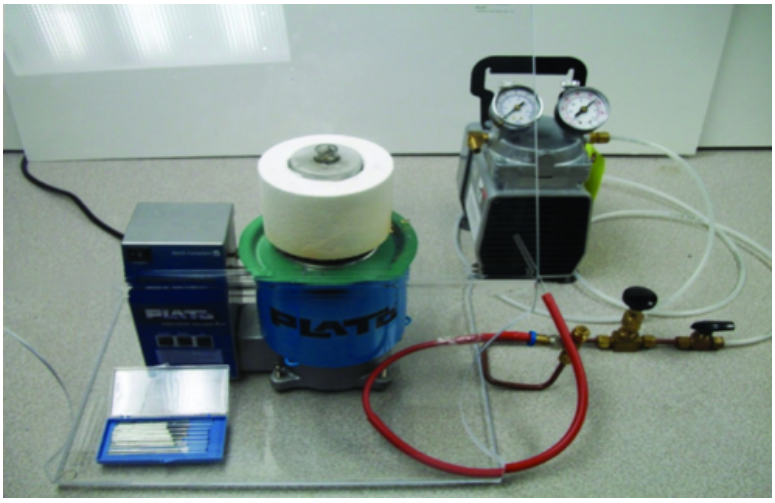

Figure 3.1: Specimen Preparation Setup

3.2 Sample Preparation

In this study, all the rectangular solder strip samples are formed in a glass tube. All the samples are also inspected by x-ray machine in our lab to detect if there is any defect in the tested sample such as void, crack and indentation. The tested samples have a dimension of 60 x 5x 0.5 mm which are decide by the inner dimension of glass tube. Figure 3.1 shows the whole setup of sample preparation system. All the solder alloy was melted first around 220 °C in the melting machine. After the solder turned into liquid, vacuum pump was used to suck the solder out of the melting machine into glass tube. After samples were formed, all of them were quenched into water to cool down, as shown in Figure 3.2. Then, a programmable oven was used to reflow samples. The reflow profile was shown in Figure 3.3. During the reflowing, thermal couples were also used to attach to glass tubes to monitor the temperature inside the reflow oven simultaneously. After reflow processing, all the specimen were inspected by x-ray. All the solder strips under tested should be away from void, indentation or crack etc. Figure 3.4 shows samples under x-ray inspection. Then the samples were either testing or storing in aging chamber. Before testing, the glass tube was gently broken without damaging the solder strip.

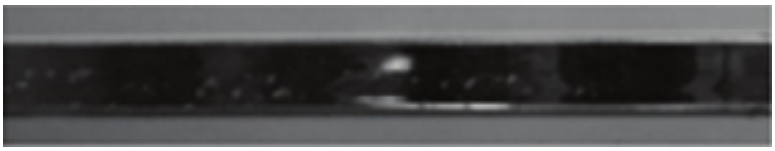

Figure 3.2: Sample Insdie Glass Tube

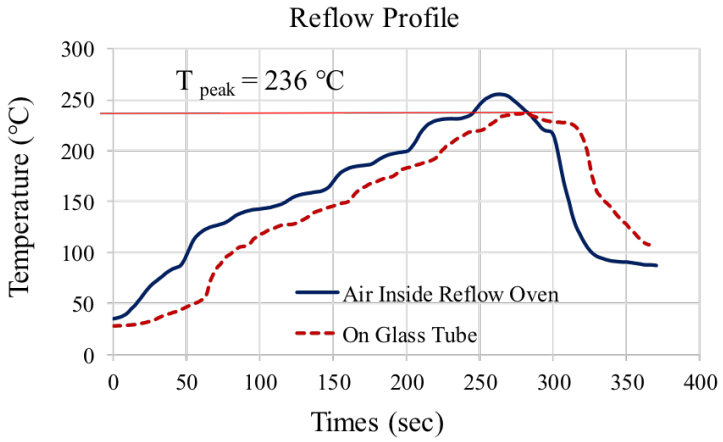

Figure 3.3: Reflow Profile

Figure 3.4: Sample Under X-ray

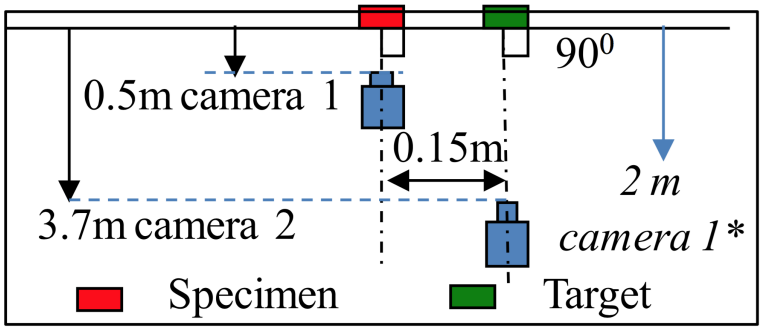

Figure 3.5: Schematic layout of high speed camera

3.3 Experimental Setup

Different weight impact hammer has been used to generate different level of high strain rate tensile testing. To obtain a constant deformation rate, a slip joint is introduced to control the velocity of cross-head. A load cell is used to measure the tensile load during the deformation of sample. Then the output voltages are converted to continuous force data. All the voltages data are save to an oscilloscope with a resolution 5 million samples per second. In addition, the specimen is speckle coated and the deformation of the samples are capture by high speed camera which can be used for strain analysis. The high speed cameras are taking videos with 10000 frame/s. The impact hammer with slip joint which enables this high speed data acquisition system to obtain constant velocity. The load-cell and high speed camera are using to tracking information during deformation. Figure 3.5 shows the schematic layout of two high speed cameras. There are two cameras, one is using to track the full field deformation of samples, the other used to tracking the velocity of frames during experiment. Previously in our group, Lall [9] has discussed the details of whole setup.

3.4 Benchmark Experiment

Previous, Lall [9] has done the benchmark test on AL7075-T6 alloy. Figure 3.6 shows the material and its detail dimension for testing. The benchmark test is carried out at four

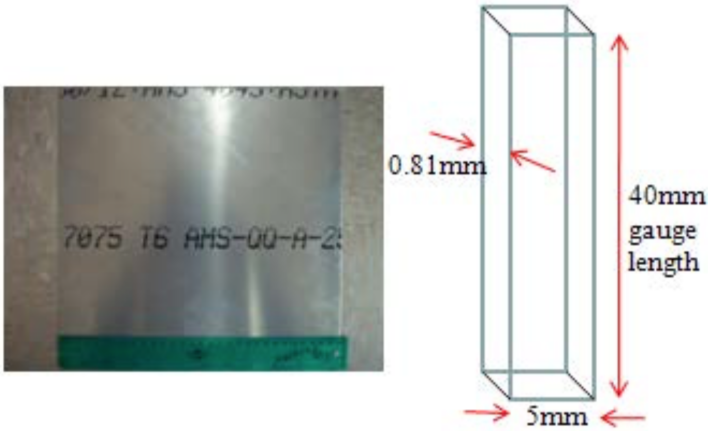

Figure 3.6: Dimension of AL7075-T6 alloy

Table 3.1: Test Matrix

T (C)	Strain Rate (1/s)				Aging (days)
	10	35	50	75	
25	X	X	X	X	Pristine
50	X	X	X	X	60
75	X	X	X	X	120
100	X	X	X	X	180
125	X	X	X	X	240
150	X	X	X	X	300
175	X	X	X	X	360
200	X	X	X	X	

different strain rates of 10, 35, 50 and 75/s. Figure 3.7 shows the testing results. The elastic modulus got from experiment is very close to the actual elastic modulus.

3.5 Test Matrix

In this research, in order to study effect of high temperature and long term aging on high strain rate mechanical properties of SAC 305, tensile testing of SAC305 has been executed at 8 different temperatures (25, 50, 75, 100, 125, 150, 175, 200 °C), 4 different strain rates (10, 35, 50, 75/s) and 7 aging conditions (Pristine, 60, 120, 180, 240, 300, 360 days). Table3.1 shows the details of test matrix.

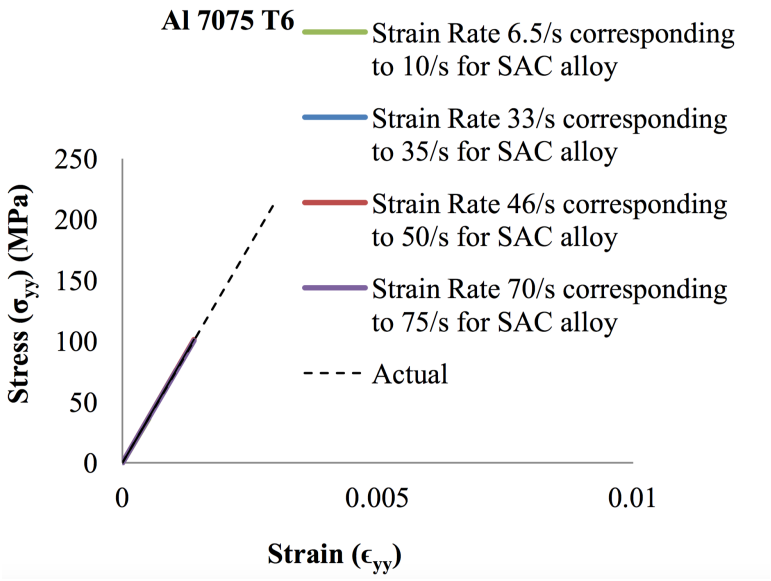

Figure 3.7: Tensile testing results of AL7075-T6 alloy

3.6 Stress-Strain Curves

Uniaxial tensile testing of SAC305 have been executed at 8 different temperatures (25, 50, 75, 100, 125, 150, 175, 200 °C) and 4 different strain rates (10, 35, 50, 75 1/s) shown in table 3.1. The dimensions of the specimen and method to test those samples are the same as described earlier in chapter. For each set of test conditions, multiple samples were tested immediately after reflow process. Those measured data were averaged to obtain the nominal material response at each particular test condition, as shown in Figure 3.8. Figure 3.9 to 3.12 illustrate measured stress and strain data for SAC305 over the 8 temperatures and 4 strain rates.

3.7 Effect of Aging on Mechanical Properties of SAC305

As expected, the ultimate tensile strength and elastic modulus show significant decreasing with aging duration increasing. The reason to cause the great degradation of mechanical properties of lead-free solder is the evolution of micro-structure. Micro-structure is decided

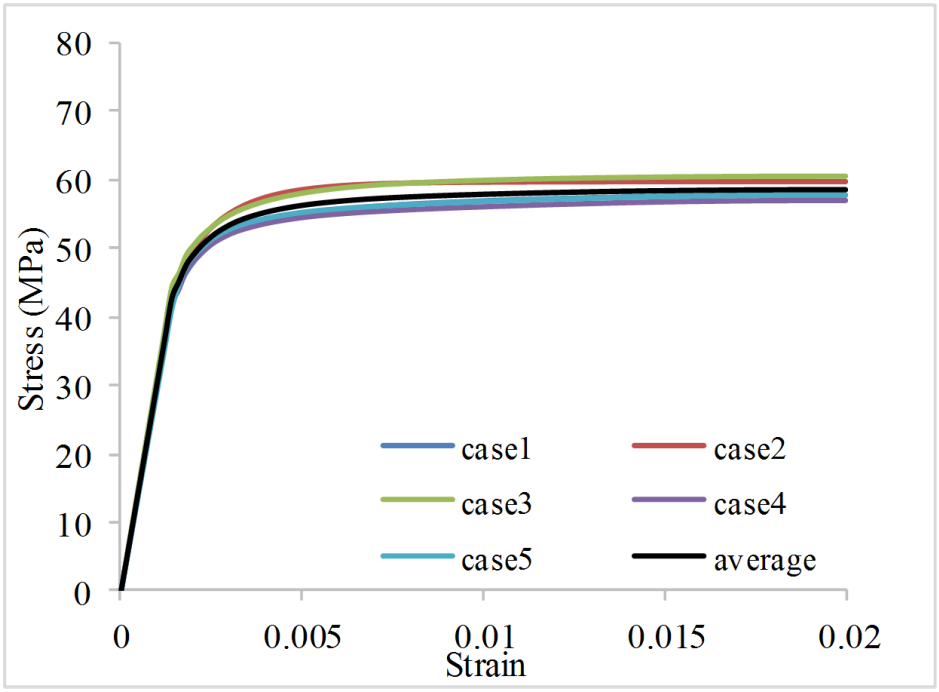

Figure 3.8: Averaging High Strain Rate Data

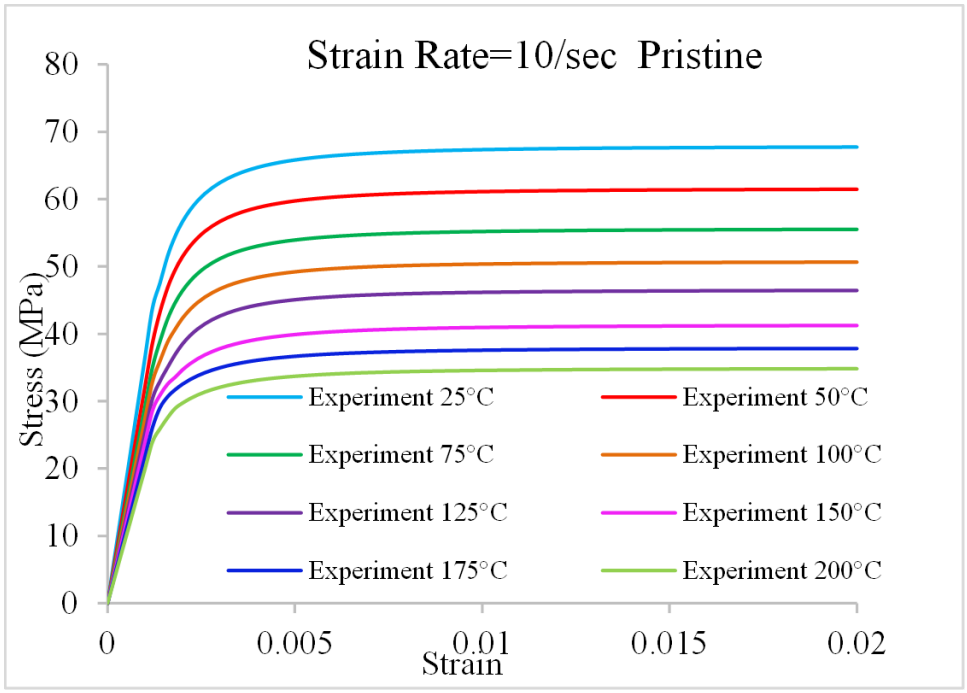

Figure 3.9: Strain Rate = 10/s pristine

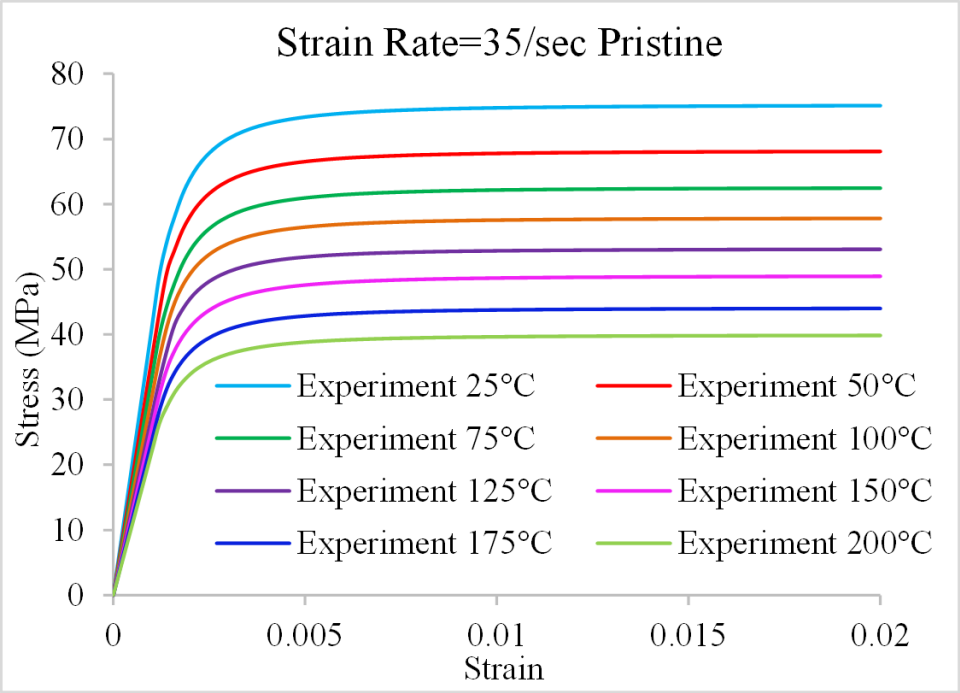

Figure 3.10: Strain Rate = 35/s pristine

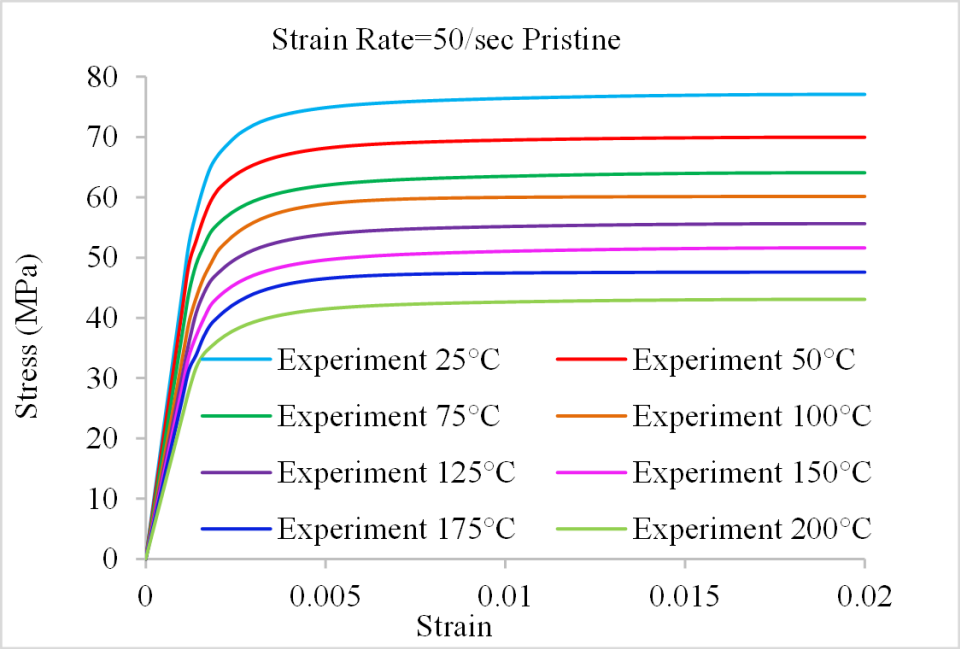

Figure 3.11: Strain Rate = 50/s pristine

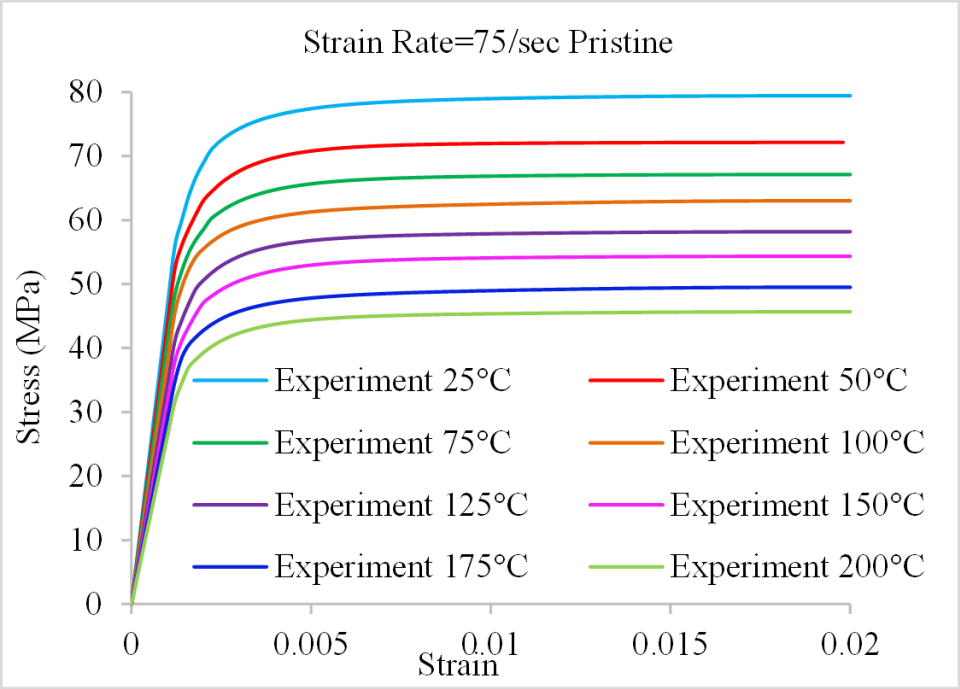

Figure 3.12: Strain Rate = 75/s pristine

by lots of factors including sample solidification rate, isothermal aging period and temperature. Isothermal aging make the micro-structure of lead-free solder evolve with different aging period, which leads to the change of mechanical response of the material. The higher aging temperatures coarsen the physical structure of solder alloy faster, but even in room temperature significant change of grain size can occur after long term of storage. In this research, tensile testing are carried out over a wide range of aging duration of 60, 120, 180, 240, 300 and 360 days. Figure 3.13 to 3.36 show the stress-strain curves of SAC 305 at different aging duration. There are three variables in this tensile testing experiment including aging duration, operating temperature and deformation rate. Each different testing condition can lead difference in experimental results.

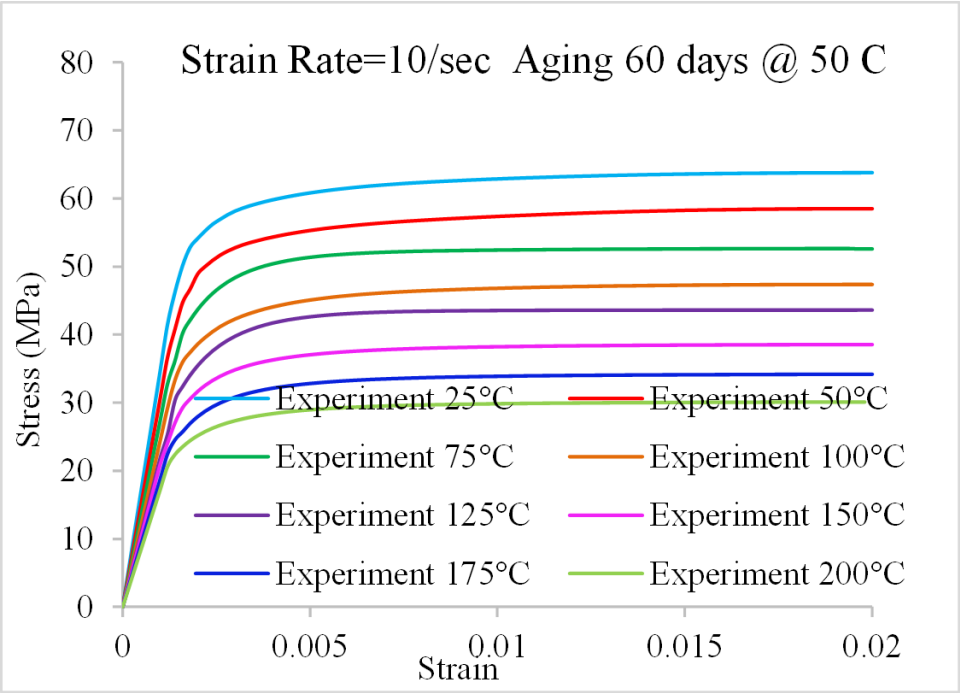

Figure 3.13: Strain rate = 10/s aging 60 days at 50 °C

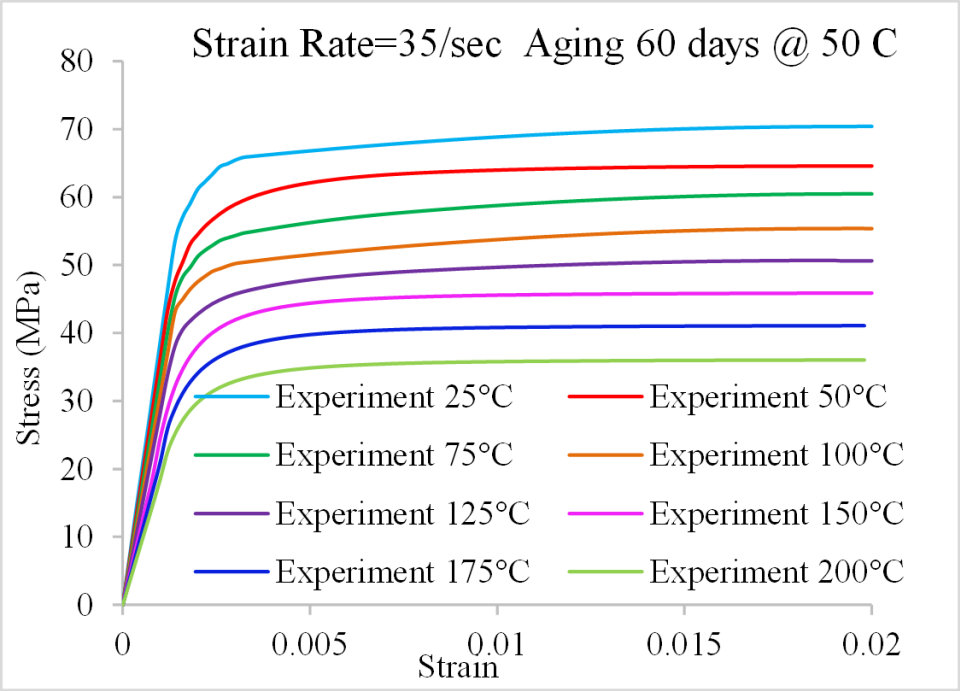

Figure 3.14: Strain rate = 35/s aging 60 days at 50 °C

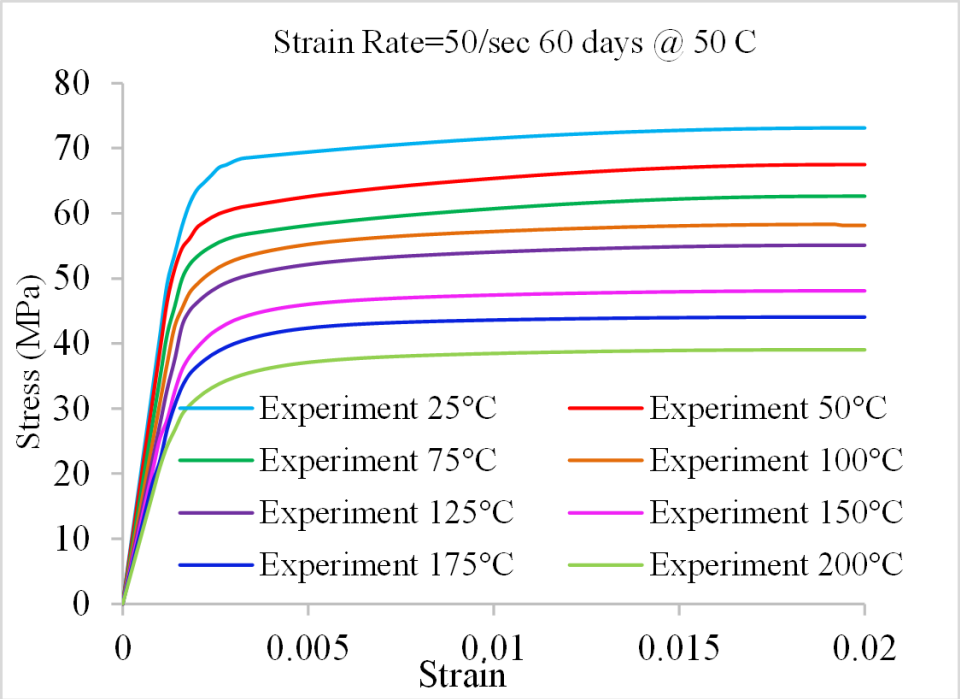

Figure 3.15: Strain rate = 50/s aging 60 days at 50 °C

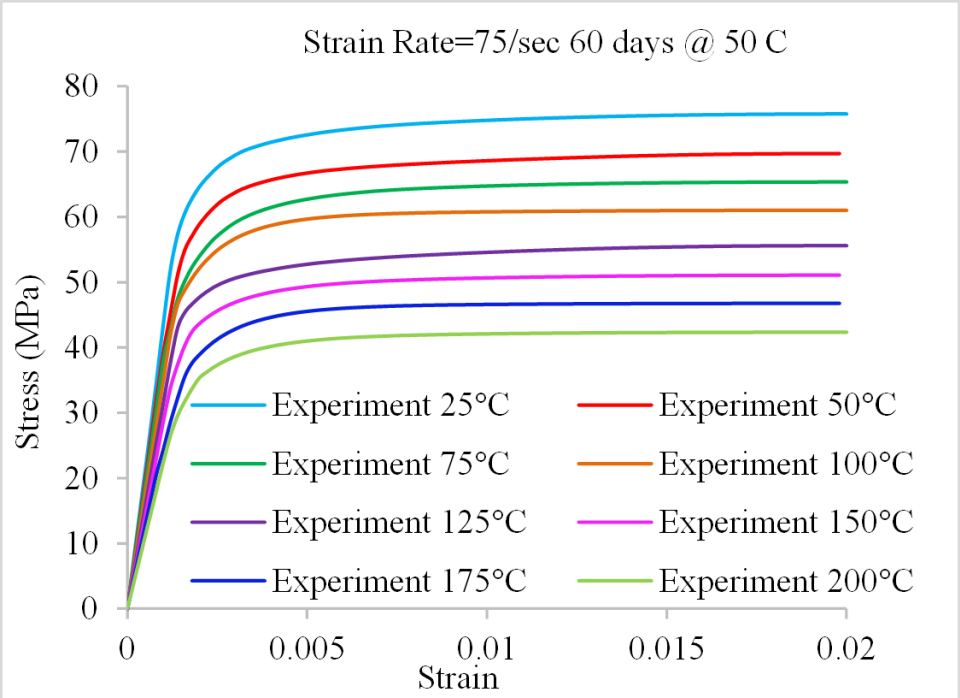

Figure 3.16: Strain rate = 75/s aging 60 days at 50 °C

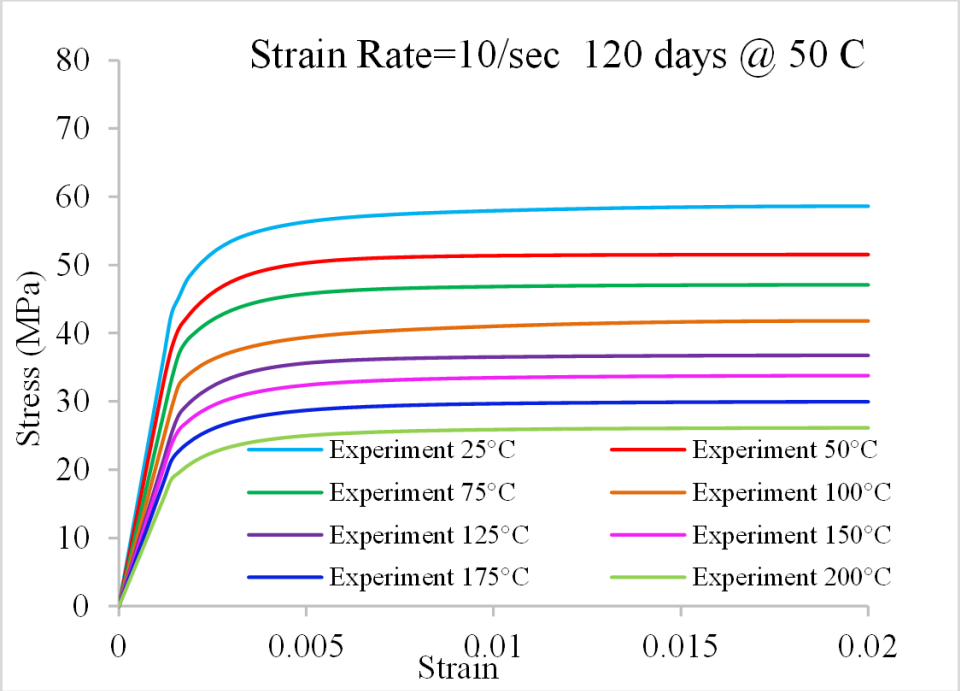

Figure 3.17: Strain rate = 10/s aging 120 days at 50 °C

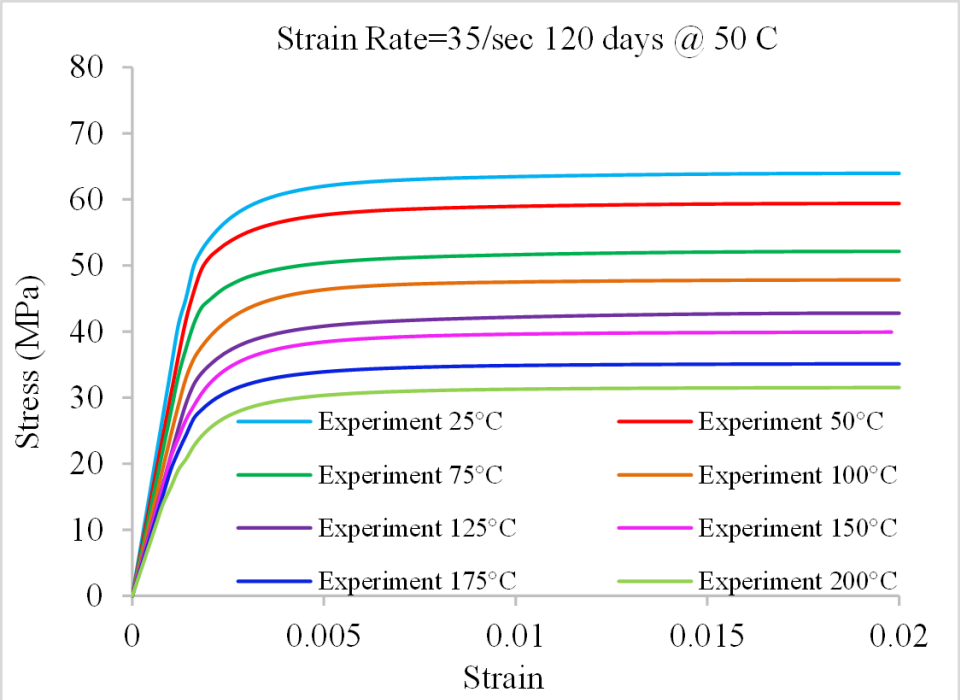

Figure 3.18: Strain rate = 35/s aging 120 days at 50 °C

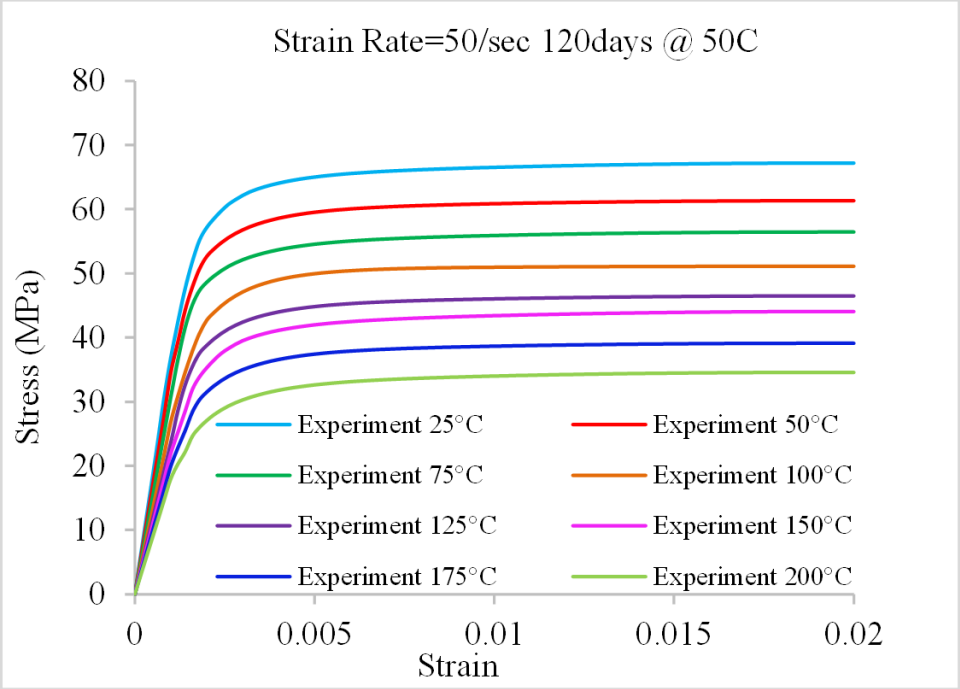

Figure 3.19: Strain rate = 50/s aging 120 days at 50 °C

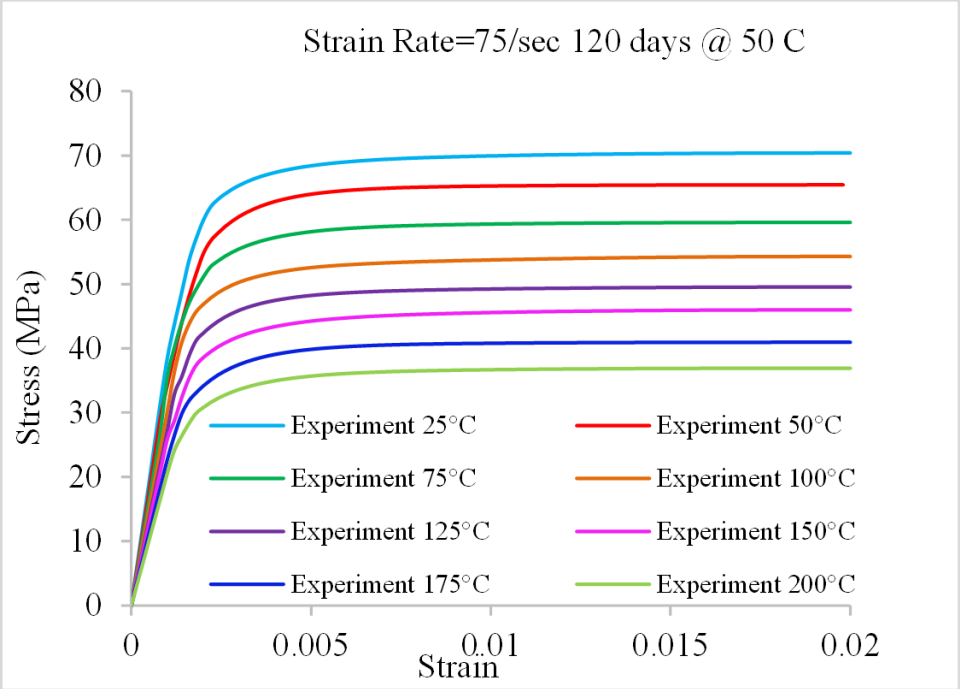

Figure 3.20: Strain rate = 75/s aging 120 days at 50 °C

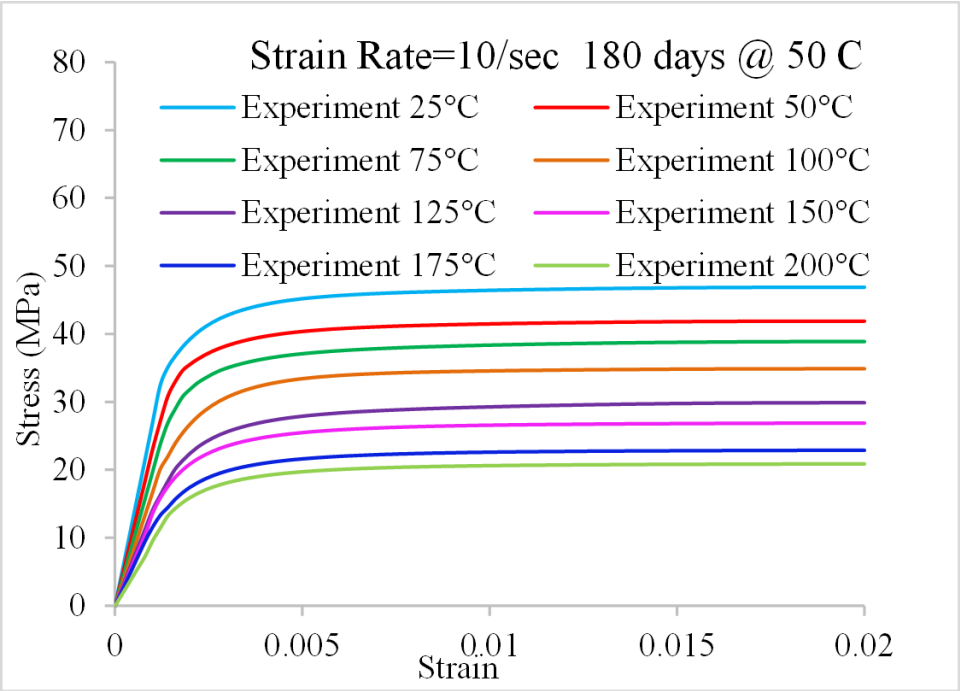

Figure 3.21: Strain rate = 10/s aging 180 days at 50 °C

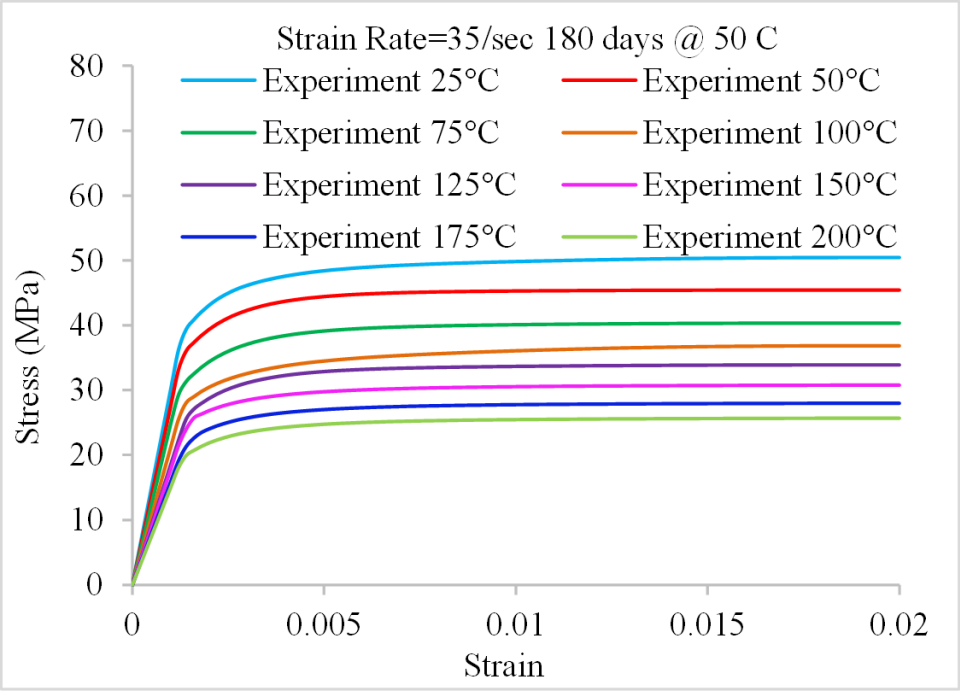

Figure 3.22: Strain rate = 35/s aging 180 days at 50 °C

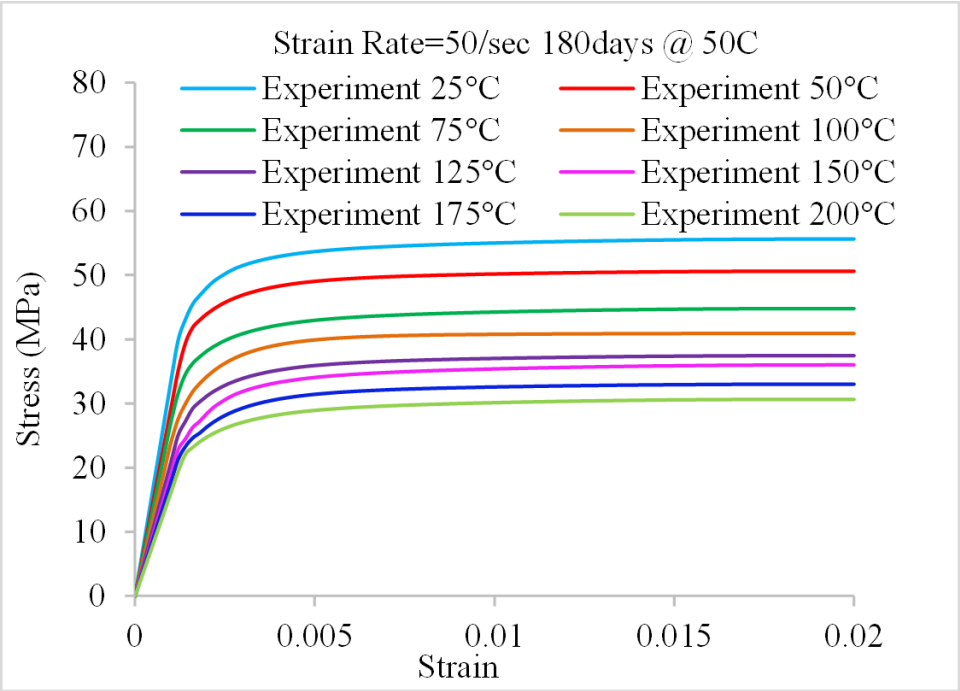

Figure 3.23: Strain rate = 50/s aging 180 days at 50 °C

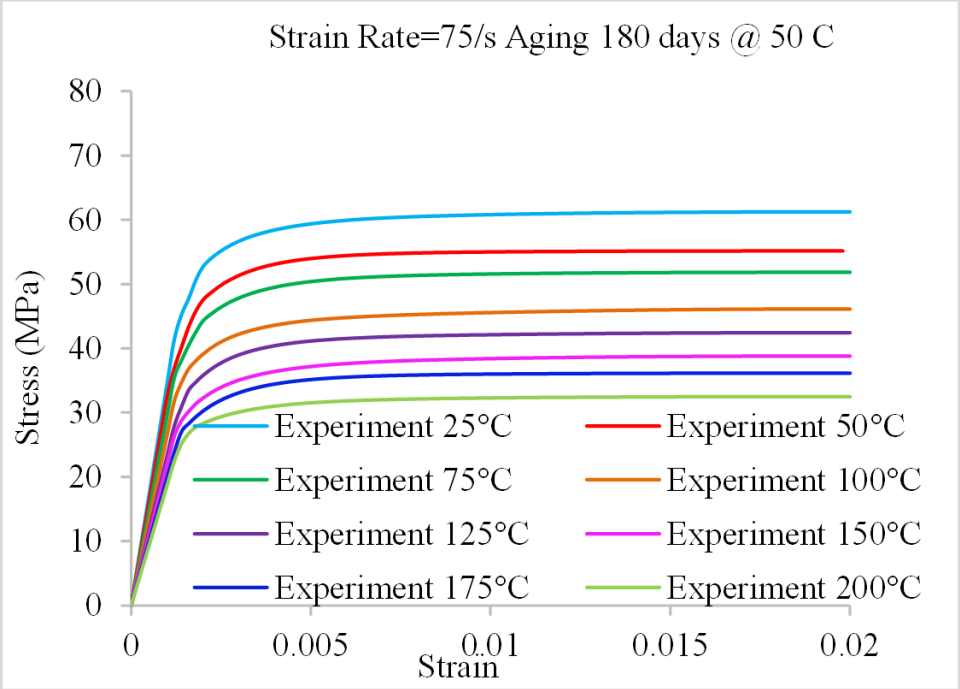

Figure 3.24: Strain rate = 75/s aging 180 days at 50 °C

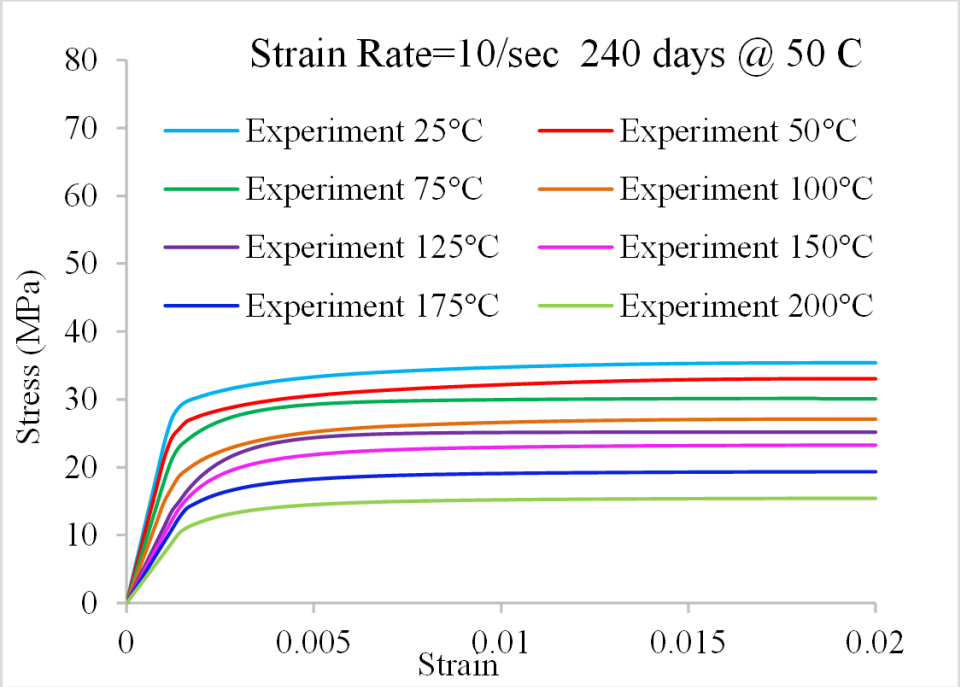

Figure 3.25: Strain rate = 10/s aging 240 days at 50 °C

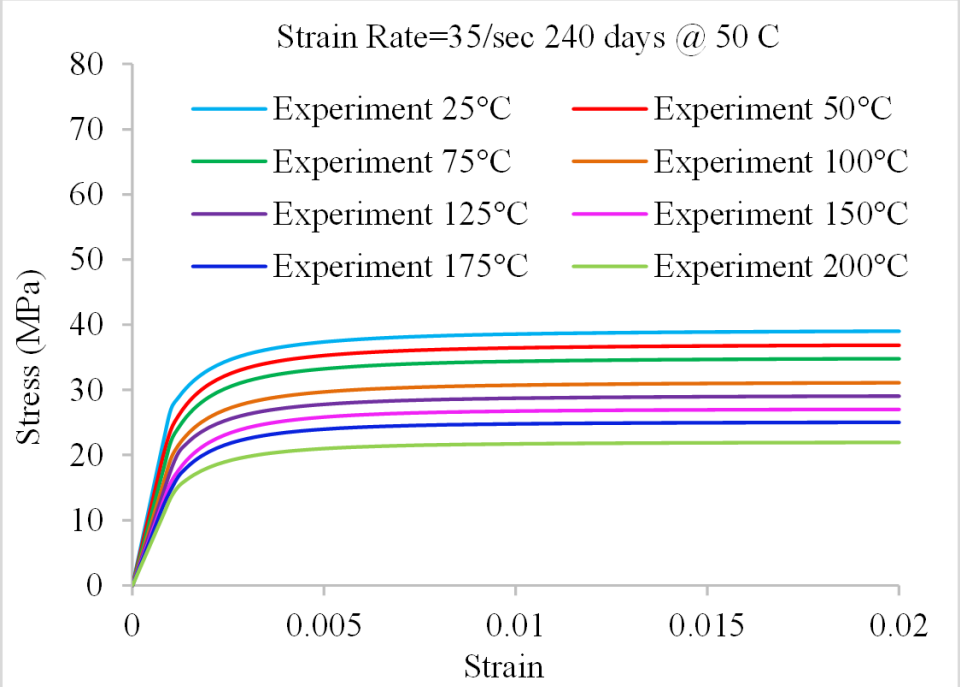

Figure 3.26: Strain rate = 35/s aging 240 days at 50 °C

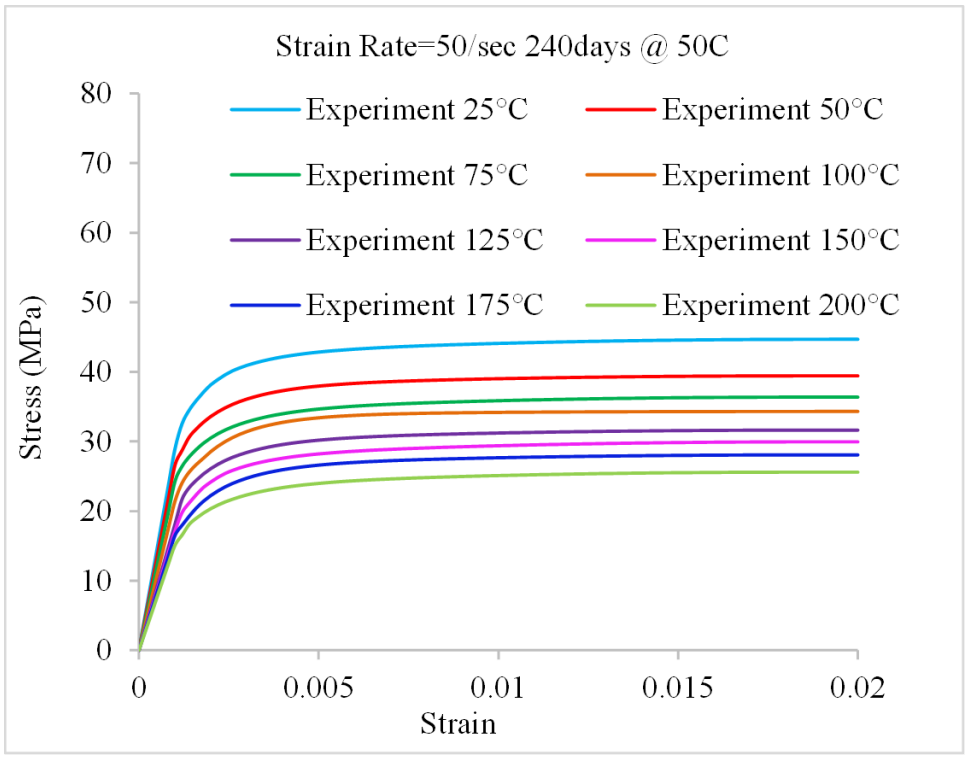

Figure 3.27: Strain rate = 50/s aging 240 days at 50 °C

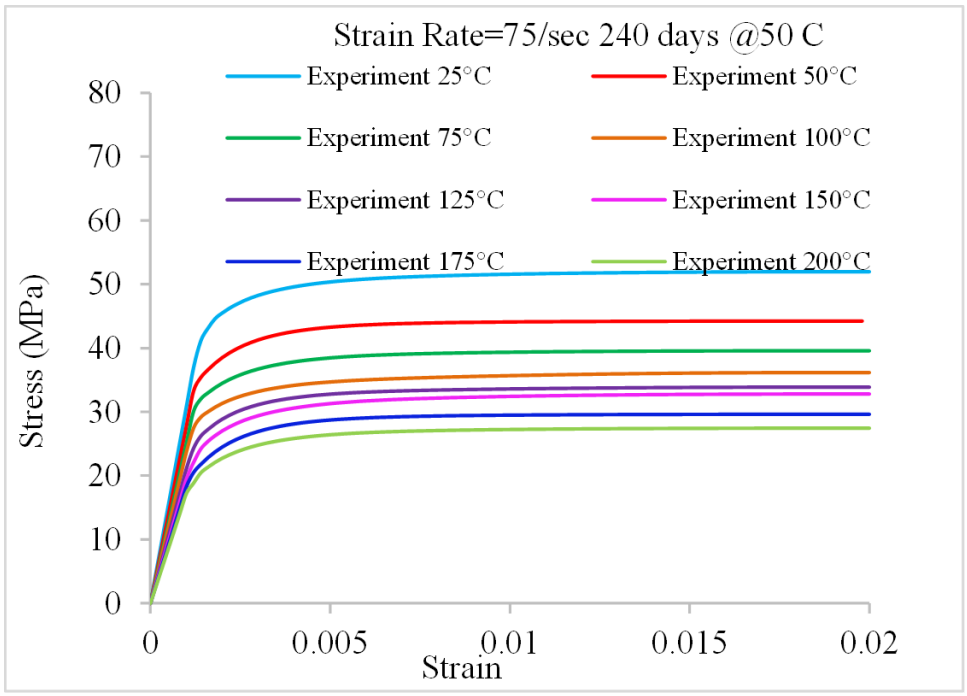

Figure 3.28: Strain rate = 75/s aging 240 days at 50 °C

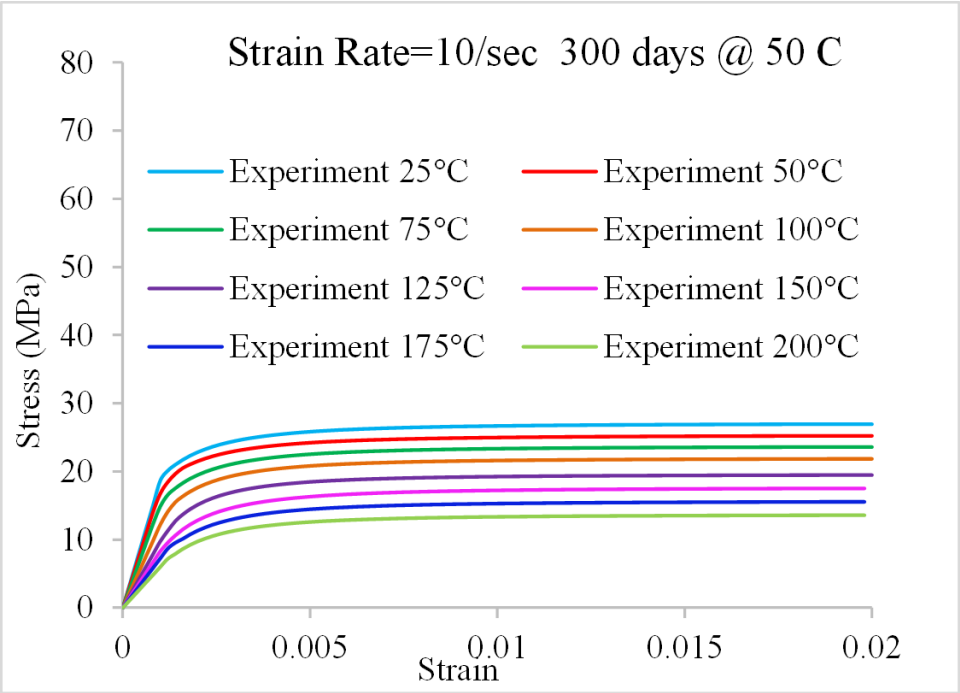

Figure 3.29: Strain rate = 10/s aging 300 days at 50 °C

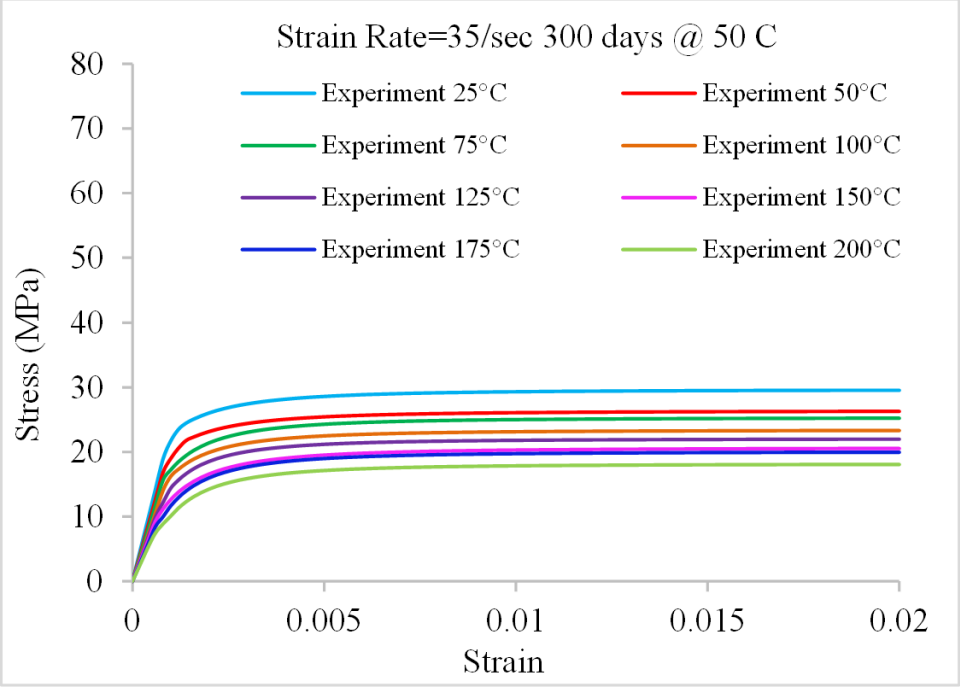

Figure 3.30: Strain rate = 35/s aging 300 days at 50 °C

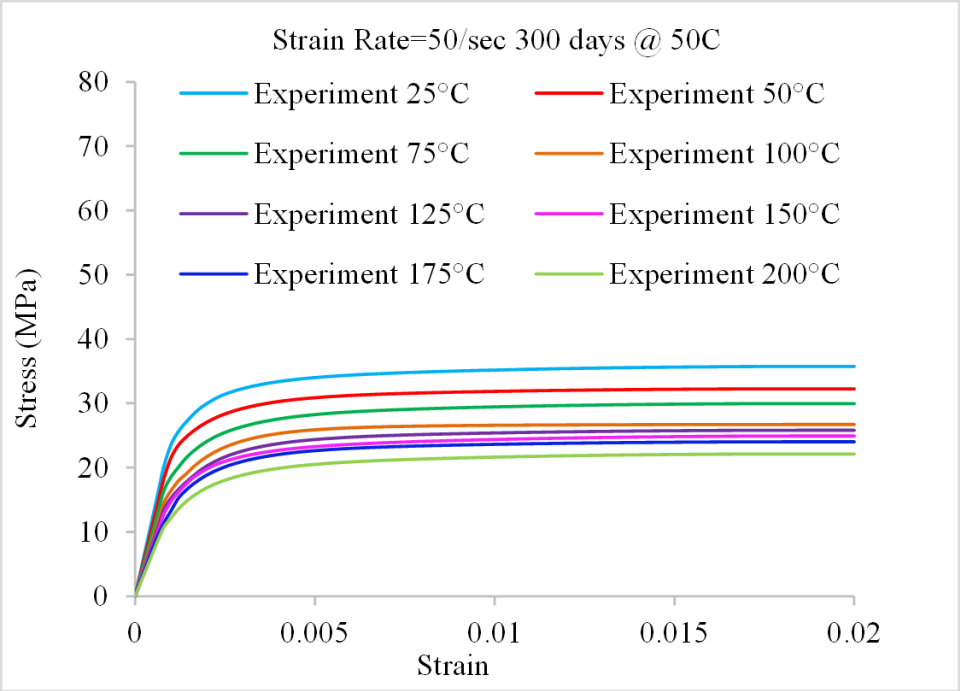

Figure 3.31: Strain rate = 50/s aging 300 days at 50 °C

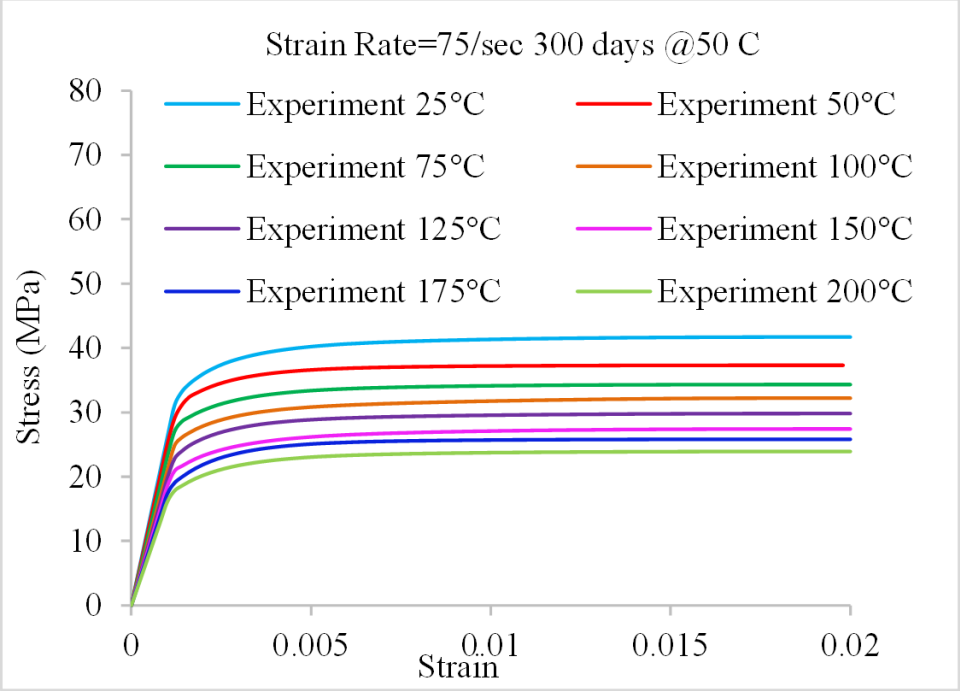

Figure 3.32: Strain rate = 75/s aging 300 days at 50 °C

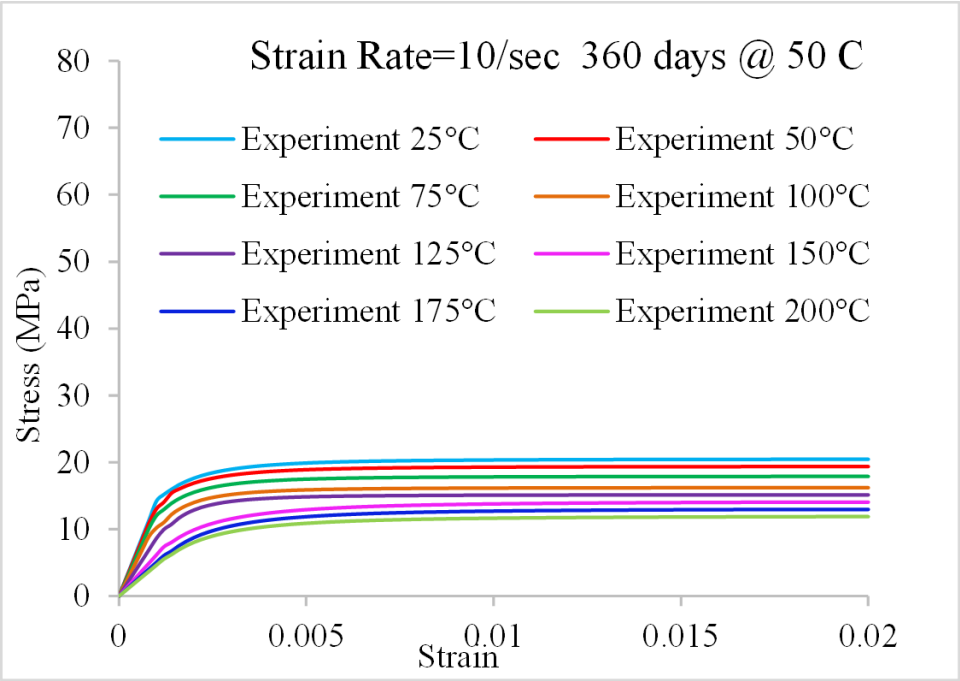

Figure 3.33: Strain rate = 10/s aging 360 days at 50 °C

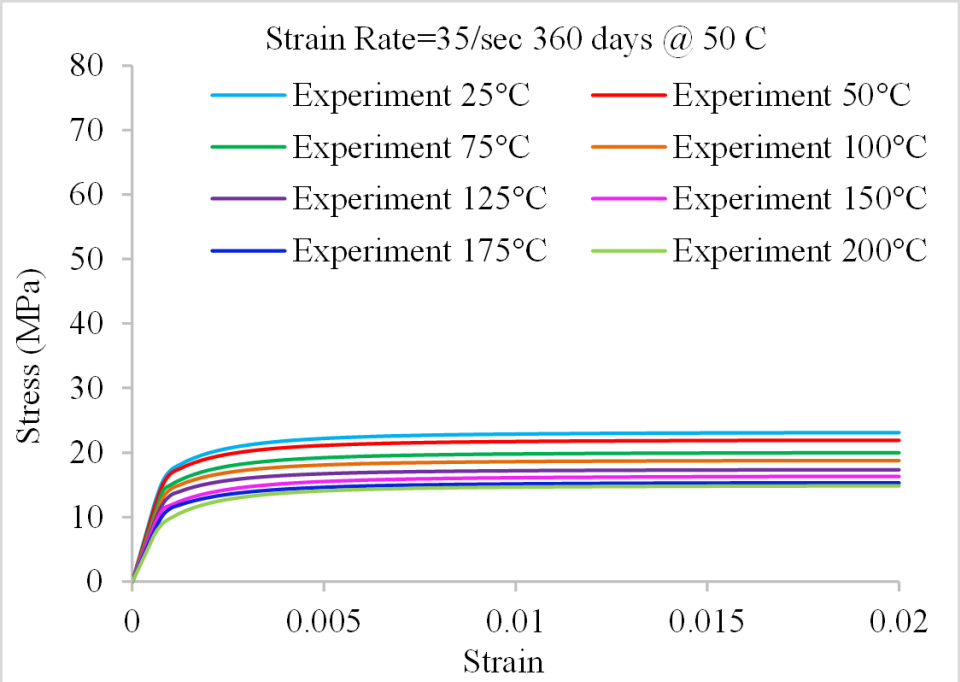

Figure 3.34: Strain rate = 35/s aging 360 days at 50 °C

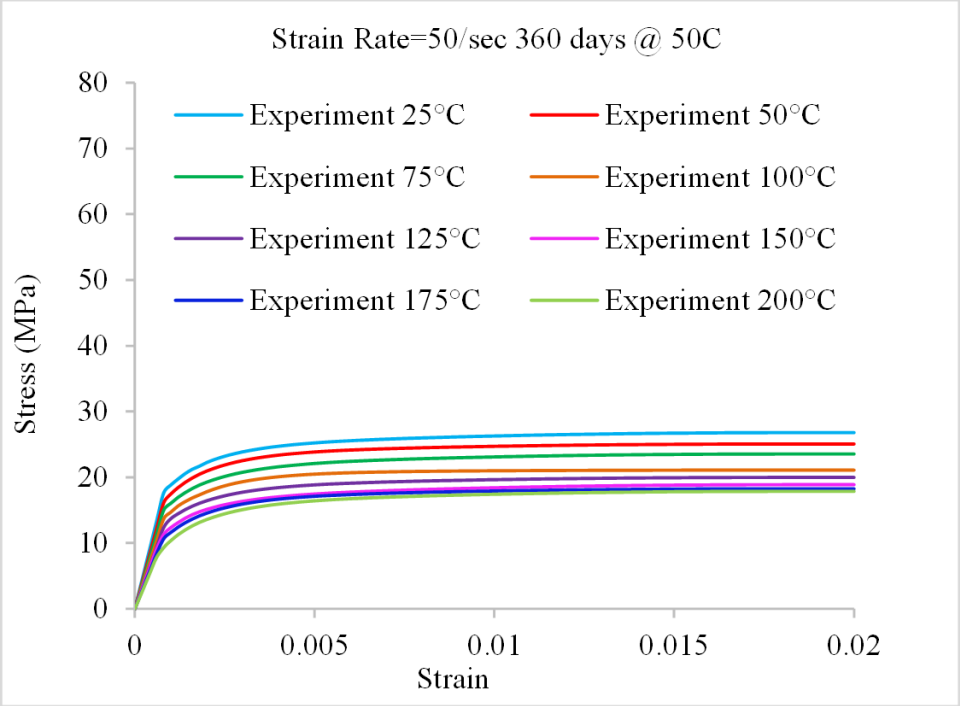

Figure 3.35: Strain rate = 50/s aging 360 days at 50 °C

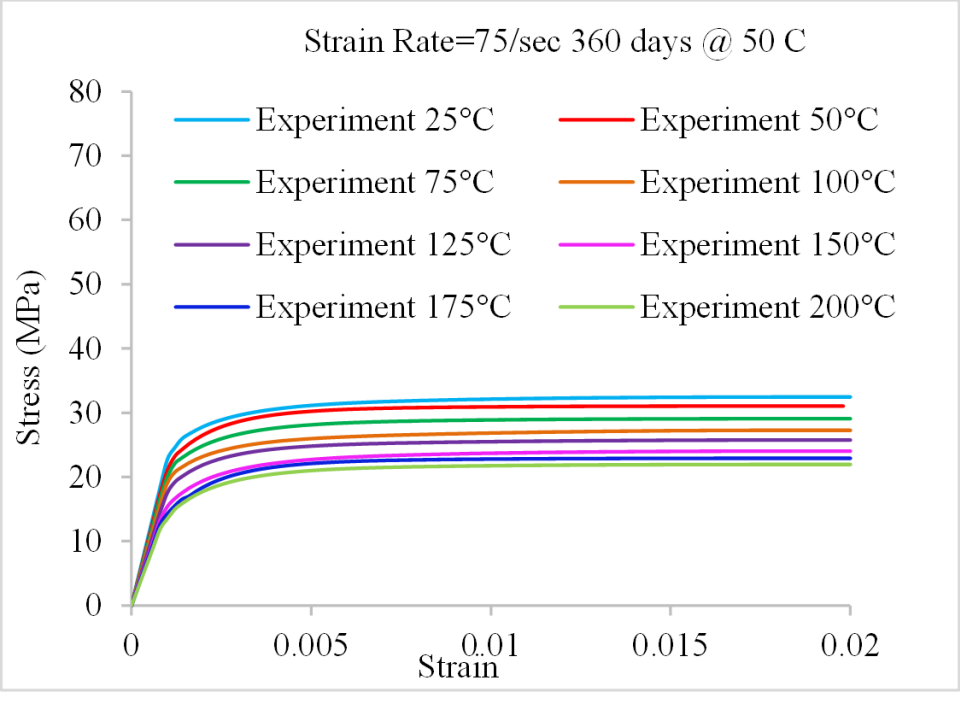

Figure 3.36: Strain rate = 75/s aging 360 days at 50 °C

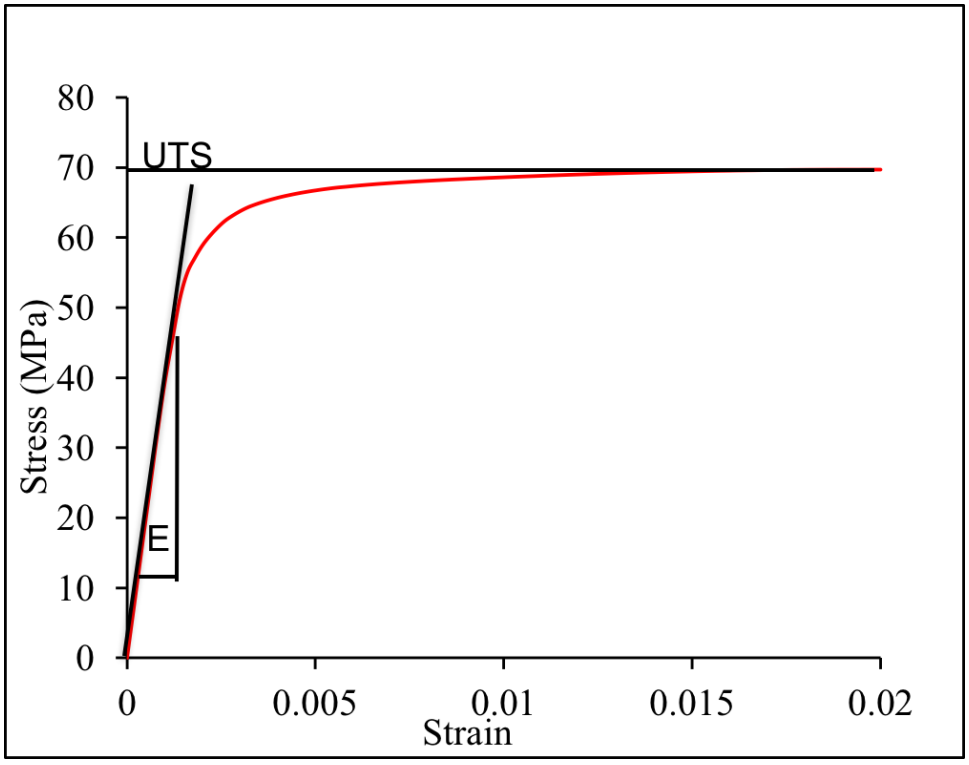

Figure 3.37: Extraction of E and UTS

3.7.1 Effect of Aging on Elastic Modulus

Elastic modulus is ability of material to resist deformation. It changes with microstructure of material after long term aging. In this research, the initial slope of stress-strain curves is considered as Young's modulus.As shown in Figure 3.37. Elastic modulus of SAC 305 at each different aging durations have been extracted from stress-strain curves. Variations of elastic modulus at different aging durations are illustrated from Figure 3.38 to 3.41. For the SAC305 solder alloy, the elastic modulus decreased with increasing aging conditions at all operating environment. And also, the differences of elastic modulus at same operating temperature at each aging duration tend to reduce. For example, at strain rate of 35/s, at operating temperature of 25 °C, the initial difference between pristine and 360 days aging are around 20 GPa. once increasing the testing temperature to 200 °C, the gap is around 10 GPa. The aging effect on Young's modulus decreased with increasing in operating temperature. All the detail values have been listed from Table 3.2 to 3.5.

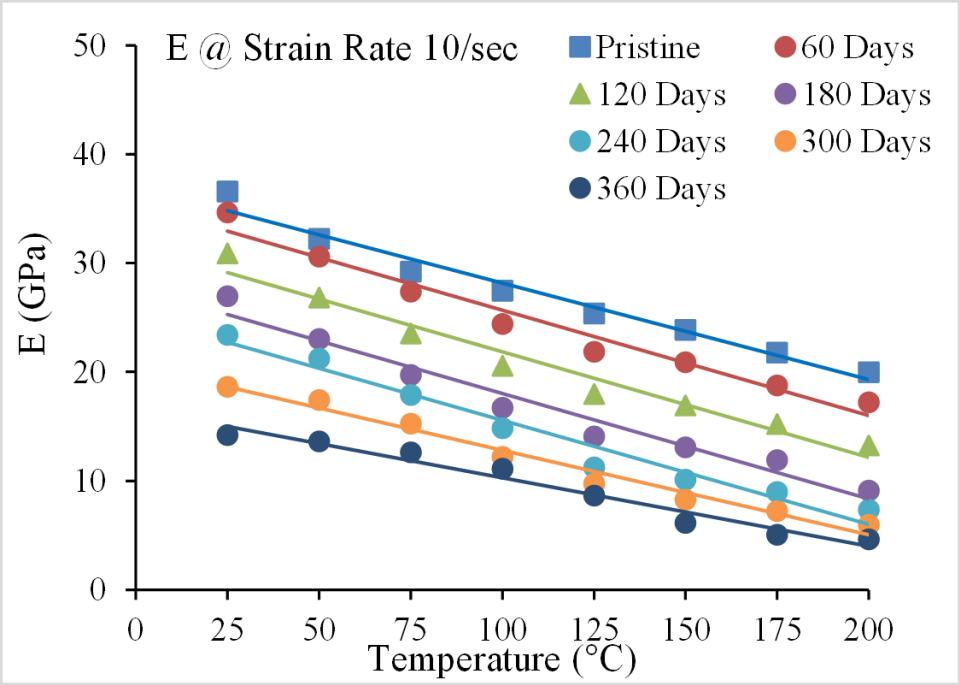

Figure 3.38: Elastic modulus at 10/s

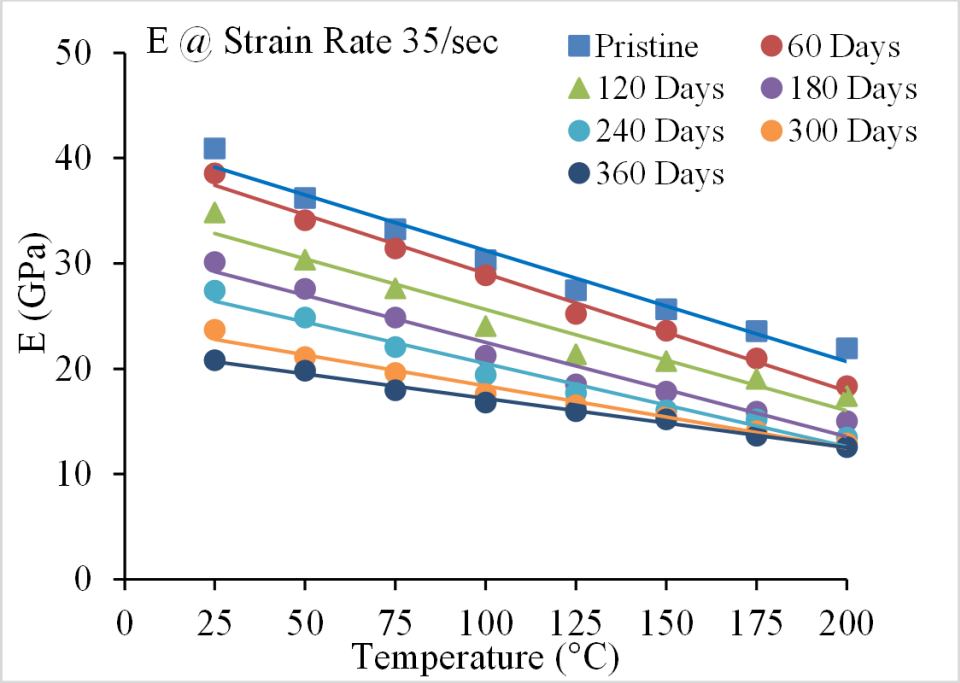

Figure 3.39: Elastic modulus at 35/s

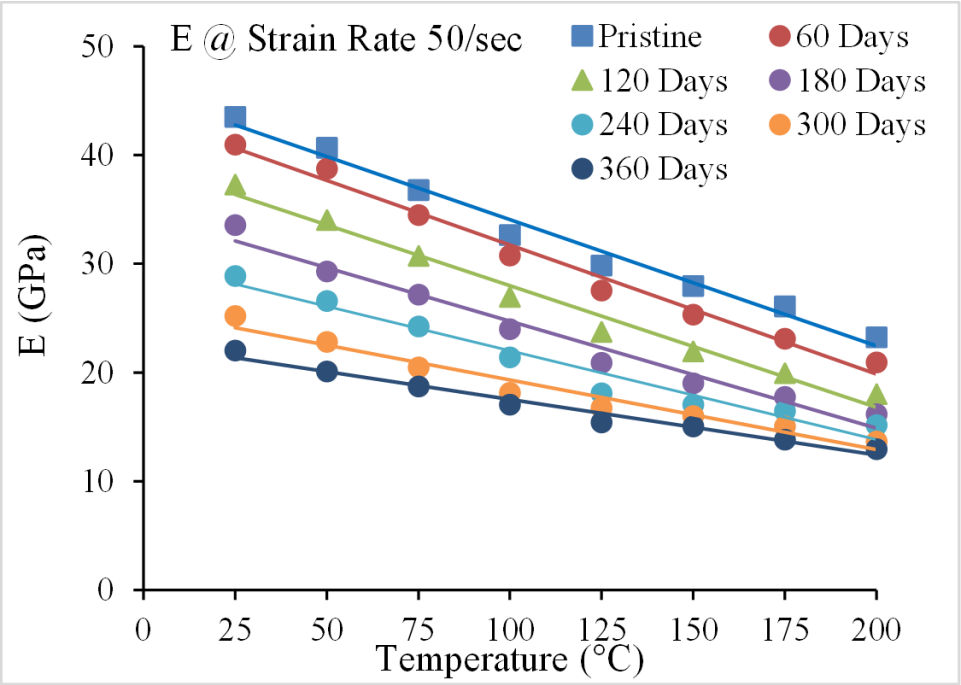

Figure 3.40: Elastic modulus at 50/s

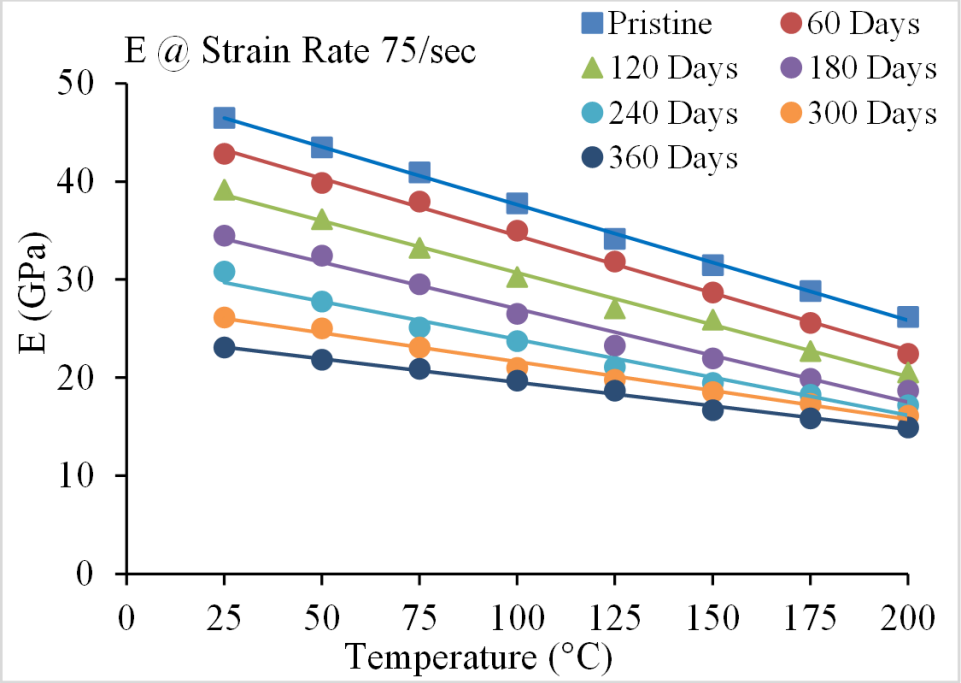

Figure 3.41: Elastic modulus at 75/s

Table 3.2: E at 10/s

Strain Rate=10/s	E (GPa)						
T (C)	Pristine	60 Days	120 Days	180 Days	240 Days	300 Days	360 Days
25	36.57	34.66	30.90	26.95	23.40	18.64	14.19
50	32.24	30.61	26.82	23.02	21.23	17.43	13.64
75	29.23	27.36	23.53	19.71	17.88	15.26	12.63
100	27.45	24.41	20.56	16.70	14.85	12.19	11.13
125	25.36	21.86	17.98	14.10	11.22	9.74	8.64
150	23.87	20.91	16.90	13.10	10.09	8.28	6.14
175	21.78	18.76	15.23	11.90	8.96	7.23	5.05
200	19.99	17.21	13.25	9.09	7.34	5.98	4.62

Table 3.3: E at 35/s

Strain Rate=35/s	E (GPa)						
T (C)	Pristine	60 Days	120 Days	180 Days	240 Days	300 Days	360 Days
25	40.92	38.56	34.85	30.13	27.42	23.70	20.80
50	36.20	34.12	30.36	27.60	24.84	21.08	19.82
75	33.22	31.43	27.64	24.85	22.07	19.58	17.96
100	30.30	28.85	24.04	21.23	19.42	17.61	16.80
125	27.46	25.23	21.38	18.53	17.68	16.53	15.99
150	25.62	23.60	20.71	17.83	16.04	15.46	15.18
175	23.58	20.97	19.05	15.93	15.21	14.09	13.65
200	21.94	18.34	17.38	15.02	13.47	12.91	12.55

Table 3.4: E at 50/s

Strain Rate=50/s	E (GPa)						
T (C)	Pristine	60 Days	120 Days	180 Days	240 Days	300 Days	360 Days
25	43.51	40.97	37.28	33.59	28.90	25.21	22.02
50	40.68	38.74	34.02	29.29	26.57	22.85	20.13
75	36.77	34.50	30.75	27.19	24.24	20.49	18.73
100	32.65	30.77	26.98	23.99	21.39	18.13	17.08
125	29.87	27.56	23.74	20.91	18.09	16.77	15.44
150	27.99	25.35	21.94	19.04	17.08	16.01	15.06
175	26.11	23.14	19.95	17.76	16.47	15.05	13.85
200	23.23	20.93	18.01	16.19	15.17	13.69	12.95

Table 3.5: E at 75/s

Strain Rate=75/s	E (GPa)						
T (C)	Pristine	60 Days	120 Days	180 Days	240 Days	300 Days	360 Days
25	46.48	42.81	39.14	34.47	30.79	26.12	23.05
50	43.46	39.84	36.14	32.44	27.74	25.03	21.83
75	40.92	37.95	33.23	29.51	25.09	23.09	20.91
100	37.77	34.98	30.23	26.48	23.73	20.99	19.70
125	34.12	31.84	27.06	23.28	21.10	19.77	18.65
150	31.47	28.70	25.89	21.94	19.46	18.55	16.66
175	28.82	25.56	22.72	19.87	18.27	17.33	15.84
200	26.17	22.42	20.54	18.67	17.19	16.11	14.92

Table 3.6: UTS at 10/s

Strain Rate=10/s	UTS (MPa)						
T (C)	Pristine	60 Days	120 Days	180 Days	240 Days	300 Days	360 Days
25	67.73	63.80	58.34	46.87	35.40	26.93	20.47
50	61.46	59.32	51.80	41.87	33.04	25.21	19.38
75	55.51	52.59	47.09	38.87	30.08	23.58	17.90
100	50.65	47.11	41.44	34.87	27.10	21.43	16.21
125	46.64	43.33	37.61	29.87	25.18	19.46	15.13
150	41.23	38.54	33.78	26.87	23.26	17.50	14.04
175	37.82	34.18	29.95	22.87	19.34	15.53	12.95
200	34.81	30.10	26.13	20.88	15.42	13.57	11.87

3.7.2 Effect of Aging on UTS

UTS is ultimate strength before sample breaks. For solder material, the UTS values are dependent on the operating environment, deformation rate and storage duration. In this research, the final stress of stress-strain curves were considered as UTS shown in Figure 3.37. All the UTS values of SAC 305 at each different aging durations have been extracted from stress-strain curves. Variations of UTS at different aging durations are illustrated from Figure 3.42 to 3.45. All the values have been listed from Table 3.6 to 3.9. For the SAC305 solder alloy, the UTS values show significantly decreasing with increasing aging conditions at all operating environment. Furthermore, with ascending in testing temperature, the UTS values are dropping almost linearly to its melting point. Same trend as elastic modulus, the aging effect on UTS values decreased with increasing in operating temperature.

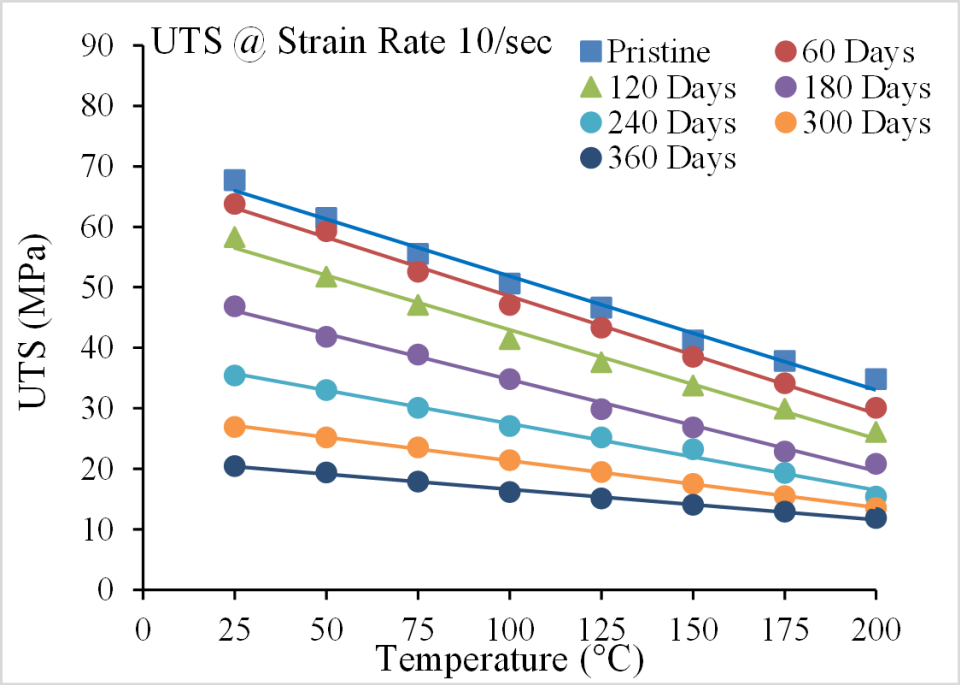

Figure 3.42: UTS at 10/s

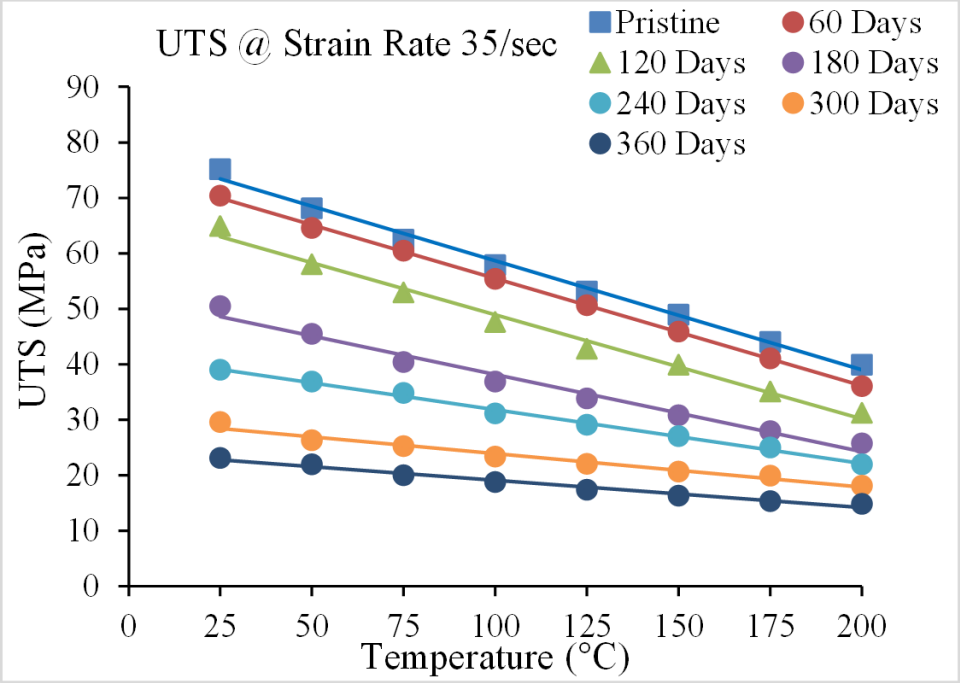

Figure 3.43: UTS at 35/s

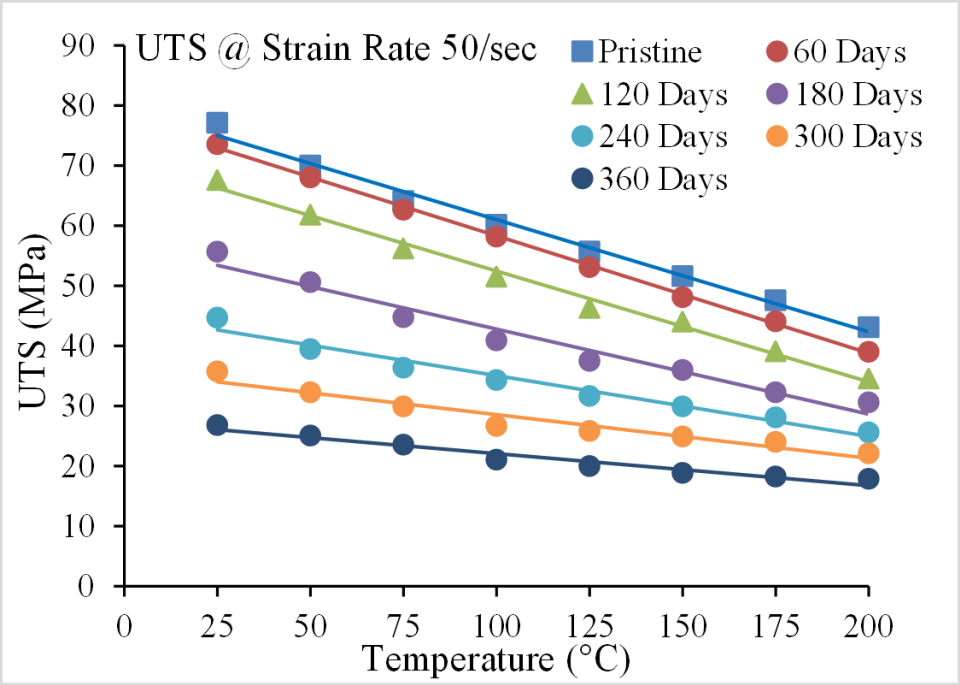

Figure 3.44: UTS at 50/s

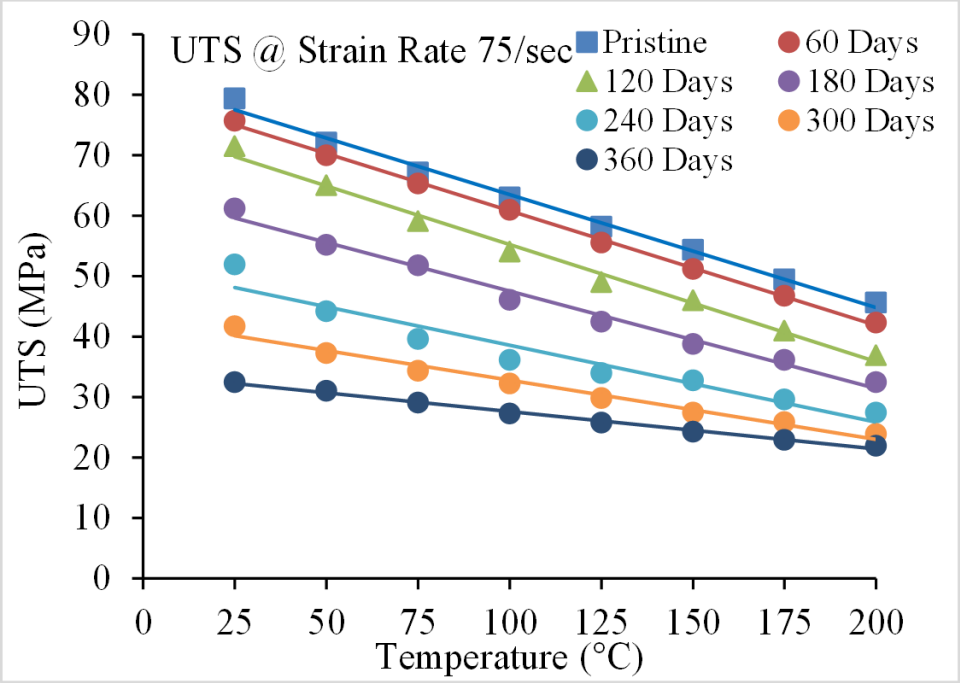

Figure 3.45: UTS at 75/s

Table 3.7: UTS at 35/s

Strain Rate=35/s	UTS (MPa)						
T (C)	Pristine	60 Days	120 Days	180 Days	240 Days	300 Days	360 Days
25	75.12	70.37	64.91	50.45	39.00	29.54	23.08
50	68.09	64.58	58.00	45.43	36.85	26.28	21.90
75	62.46	60.46	52.90	40.34	34.78	25.22	19.96
100	57.81	55.37	47.61	36.84	31.08	23.32	18.76
125	53.07	50.62	42.76	33.80	29.04	21.98	17.32
150	48.93	45.87	39.92	30.76	27.00	20.65	16.29
175	43.99	41.03	35.07	27.92	24.96	19.91	15.26
200	39.85	36.04	31.23	25.68	21.93	18.07	14.82

Table 3.8: UTS at 50/s

Strain Rate=50/s	UTS (MPa)						
T (C)	Pristine	60 Days	120 Days	180 Days	240 Days	300 Days	360 Days
25	77.09	73.53	67.58	55.64	44.69	35.74	26.80
50	69.98	67.99	61.81	50.62	39.44	32.25	25.07
75	64.09	62.63	56.21	44.80	36.38	29.96	23.54
100	60.16	58.15	51.54	40.93	34.32	26.71	21.10
125	55.64	53.12	46.29	37.47	31.64	25.81	19.98
150	51.62	48.09	44.05	36.00	29.96	24.91	18.87
175	47.60	44.07	39.10	32.24	28.08	24.02	18.25
200	43.08	39.04	34.56	30.58	25.60	22.12	17.86

Table 3.9: UTS at 75/s

Strain Rate=75/s	UTS (MPa)						
T (C)	Pristine	60 Days	120 Days	180 Days	240 Days	300 Days	360 Days
25	79.44	75.76	71.50	61.24	51.97	41.71	32.45
50	72.14	70.00	65.08	55.16	44.24	37.32	31.04
75	67.12	65.34	59.09	51.83	39.58	34.33	29.07
100	63.02	61.01	54.06	46.11	36.16	32.22	27.27
125	58.18	55.59	49.02	42.45	33.99	29.82	25.75
150	54.34	51.17	45.98	38.79	32.81	27.42	24.23
175	49.50	46.75	40.94	36.14	29.63	25.82	22.91
200	45.66	42.33	36.90	32.48	27.45	23.92	21.95

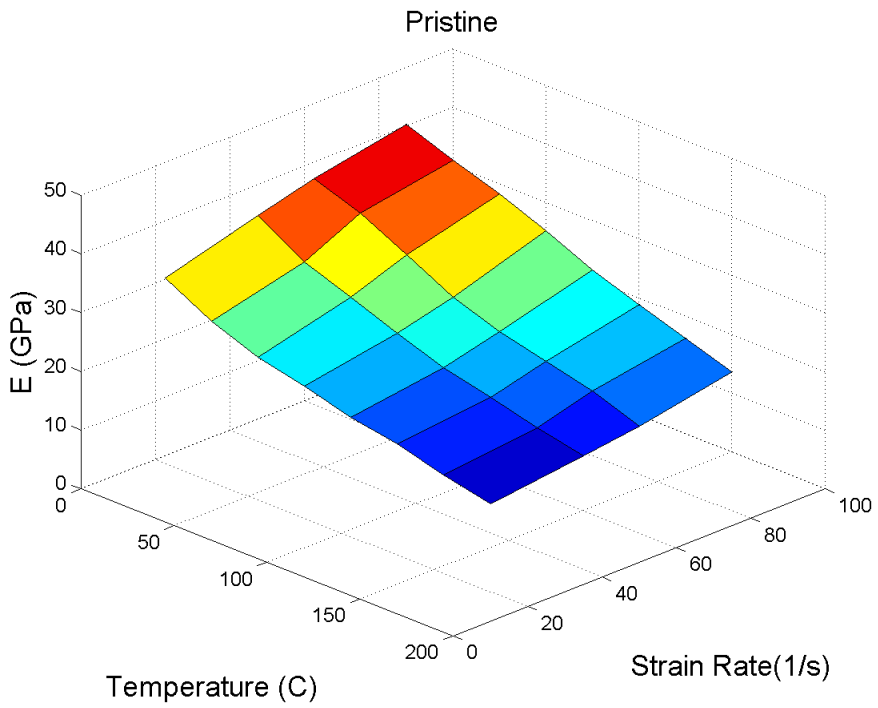

Figure 3.46: E vs. strain rate vs. temperature

3.8 Effect of Strain Rate on Mechanical properties of SAC305

Solder materials such as SnPb and SAC based are sensitive to its deformation rates. Figure 3.46 to Figure 3.52 show the effect of strain rates on elastic modulus. Figure 3.53 to Figure 3.59 show the effect of strain rates on UTS. All of the above graphs show the same trend, the mechanical properties of SAC305 including elastic modulus and UTS are increasing with larger deformation rate.

3.9 Effect of Operating Temperature on Mechanical properties of SAC305

The melting temperature of SAC305 is around 215 C. SAC305 shows degradation even in room temperature. So it is necessary to understand operational temperature on mechanical performance of SAC305. Figure 3.38 to Figure 3.45 already show significant decreasing of mechanical properties of SAC305 with increasing in temperature

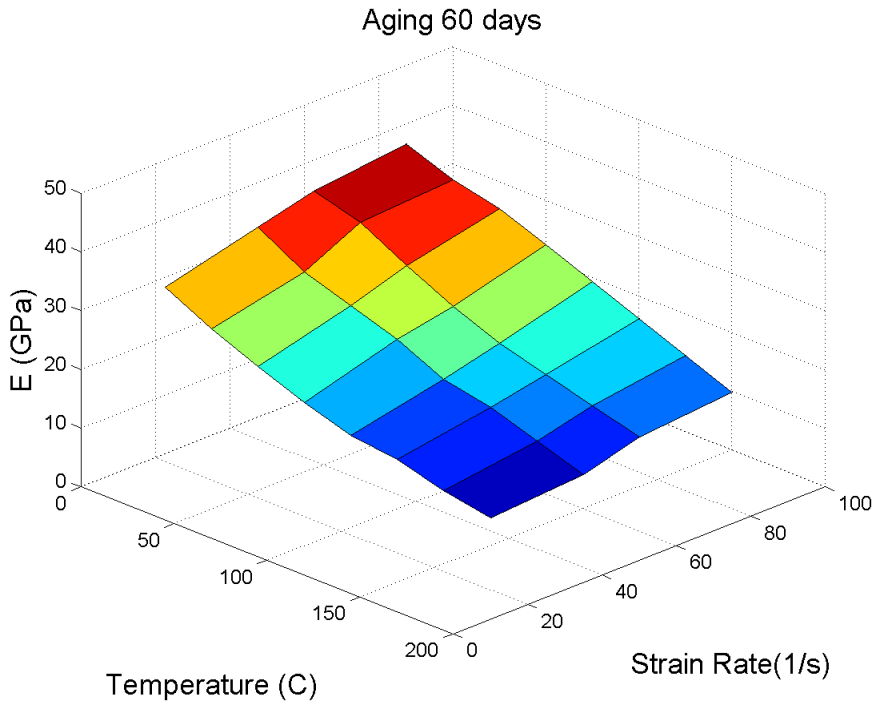

Figure 3.47: E vs. strain rate vs. temperature

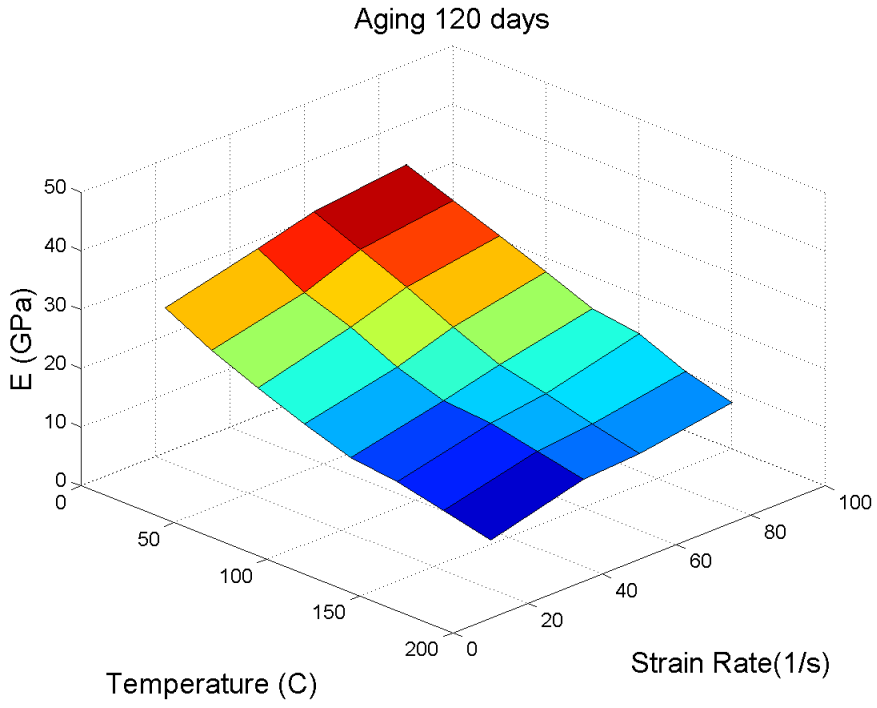

Figure 3.48: E vs. strain rate vs. temperature

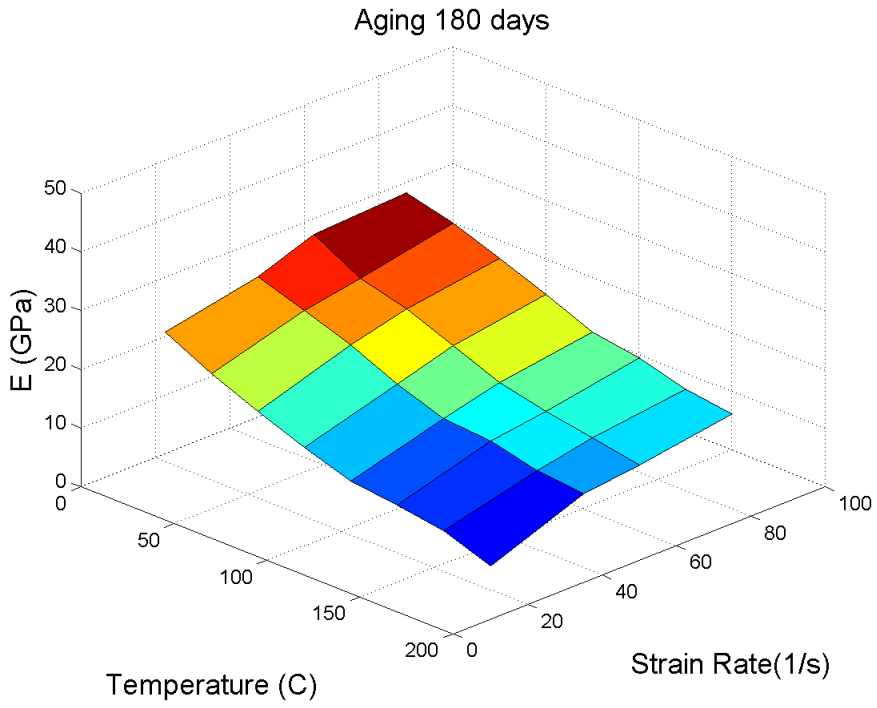

Figure 3.49: E vs. strain rate vs. temperature

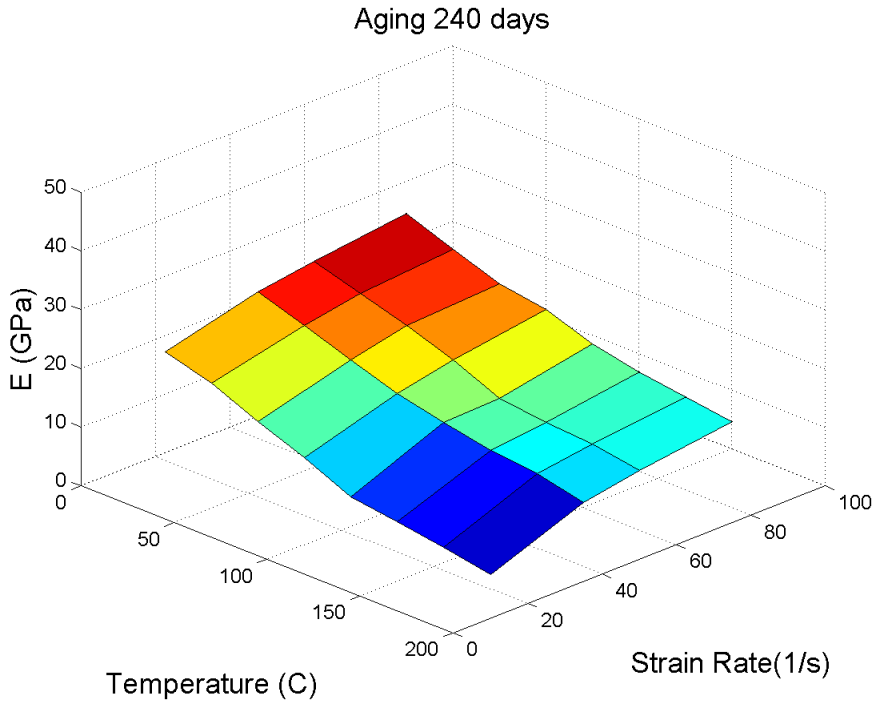

Figure 3.50: E vs. strain rate vs. temperature

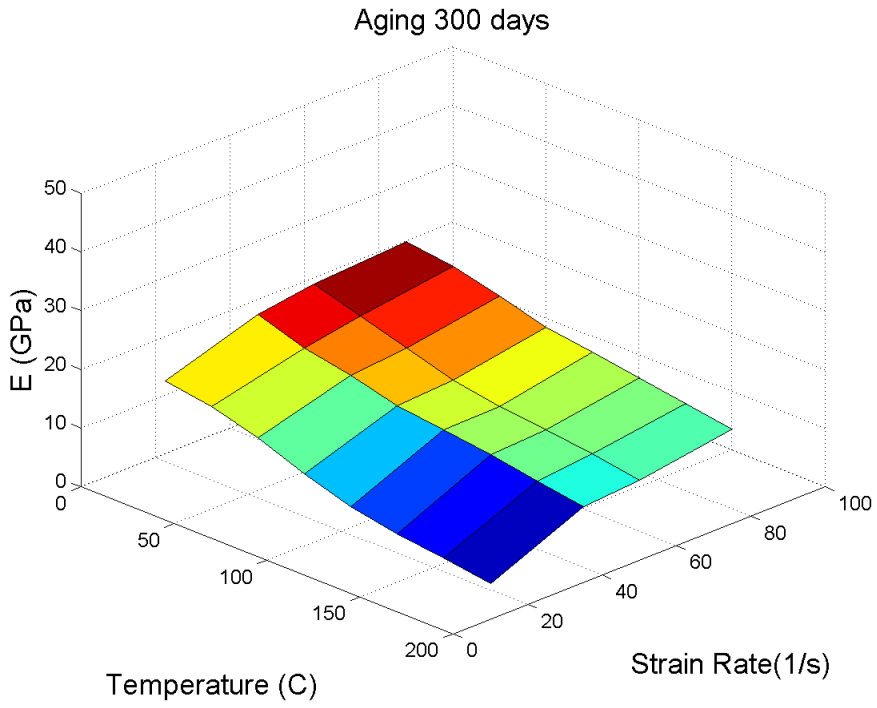

Figure 3.51: E vs. strain rate vs. temperature

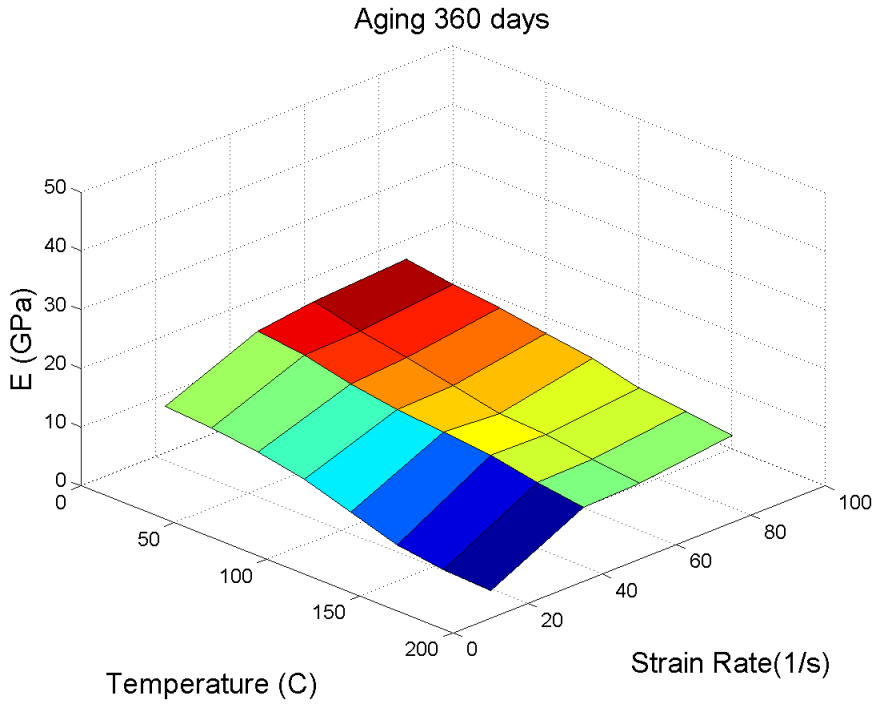

Figure 3.52: E vs. strain rate vs. temperature

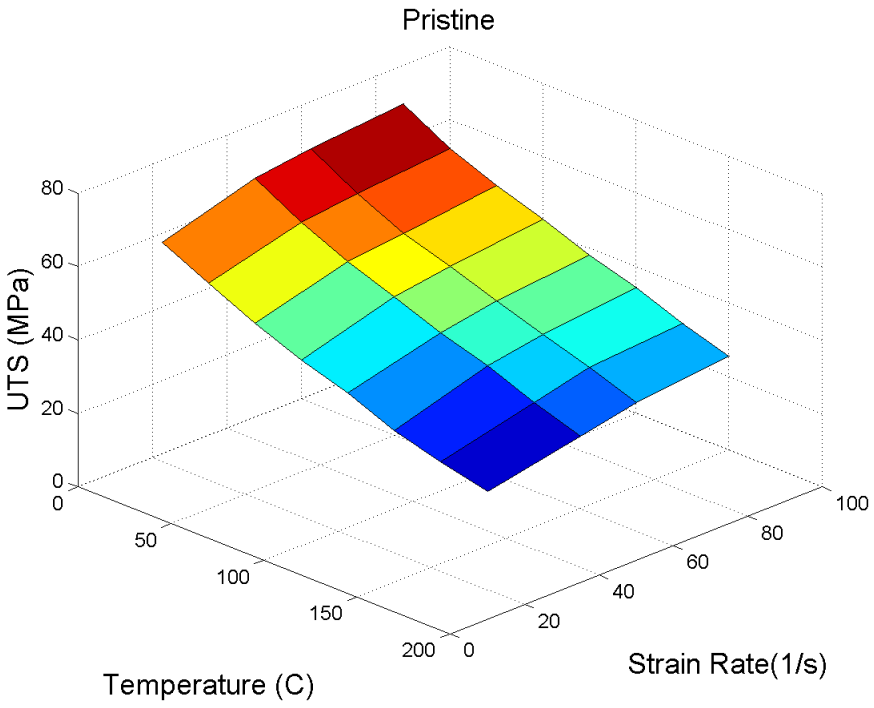

Figure 3.53: UTS vs. strain rate vs. temperature

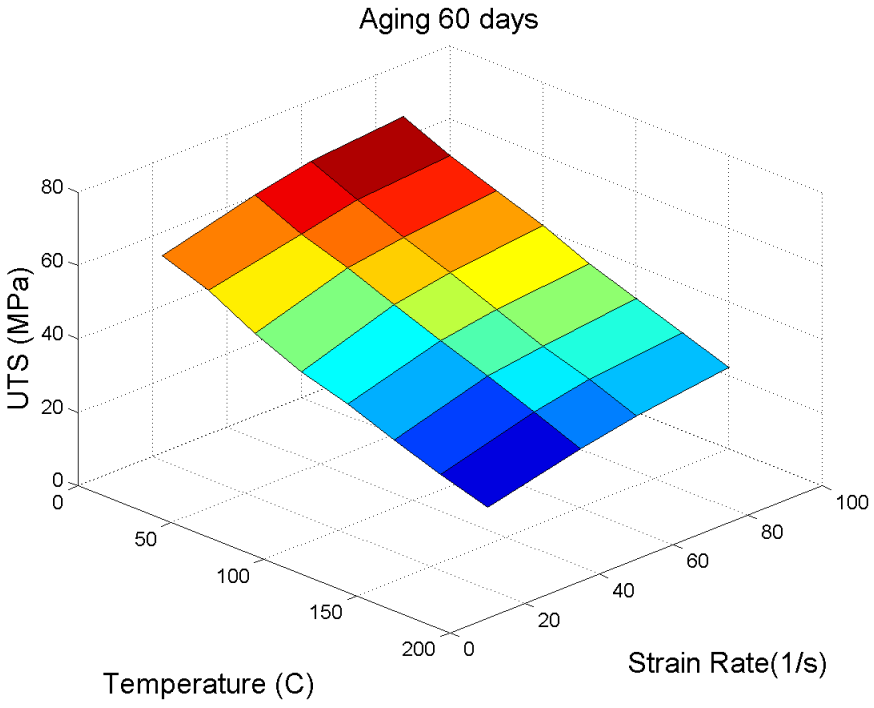

Figure 3.54: UTS vs. strain rate vs. temperature

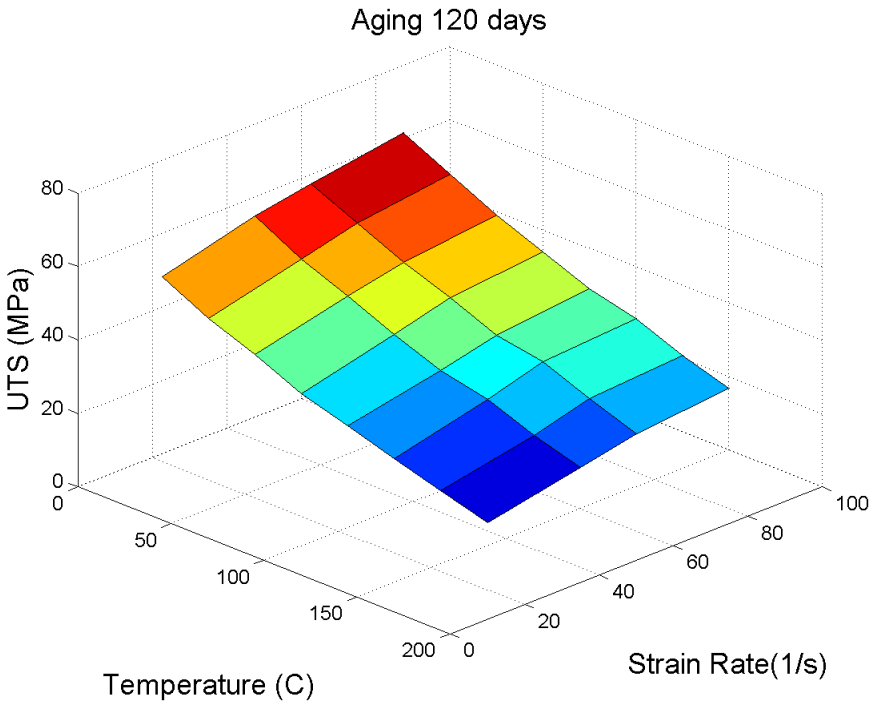

Figure 3.55: UTS vs. strain rate vs. temperature

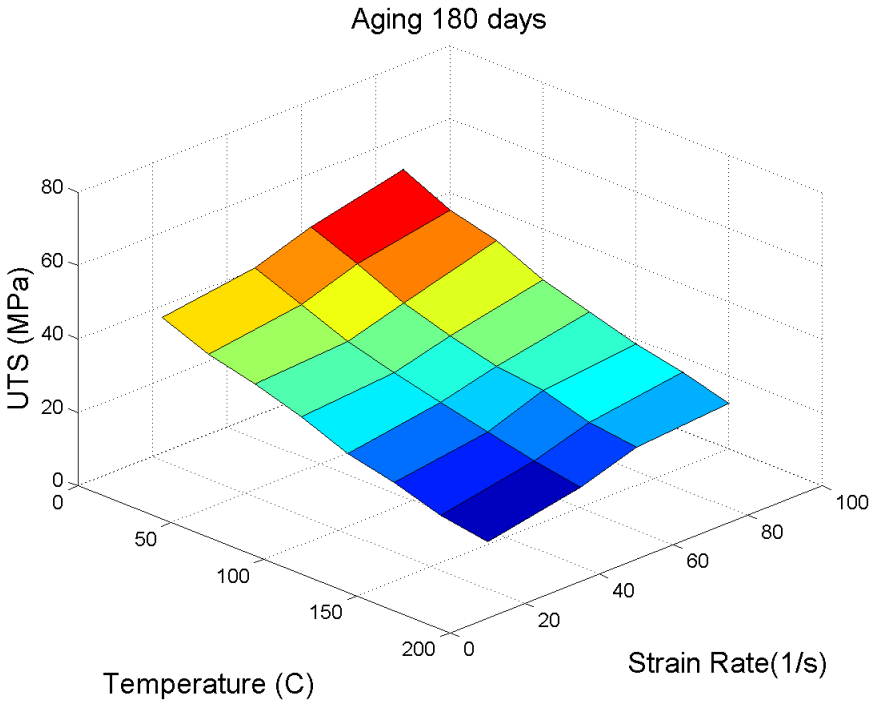

Figure 3.56: UTS vs. strain rate vs. temperature

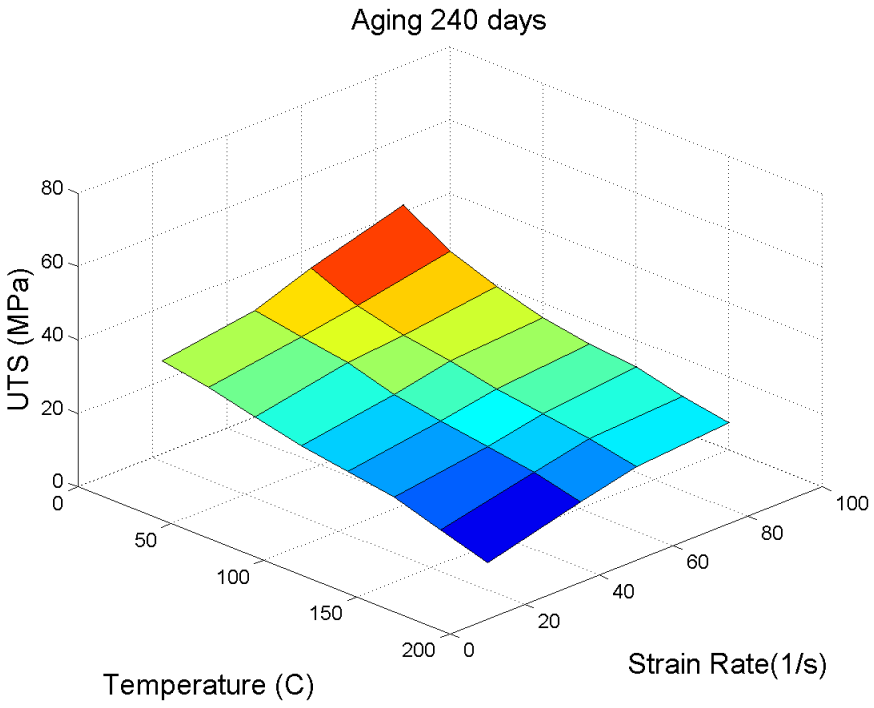

Figure 3.57: UTS vs. strain rate vs. temperature

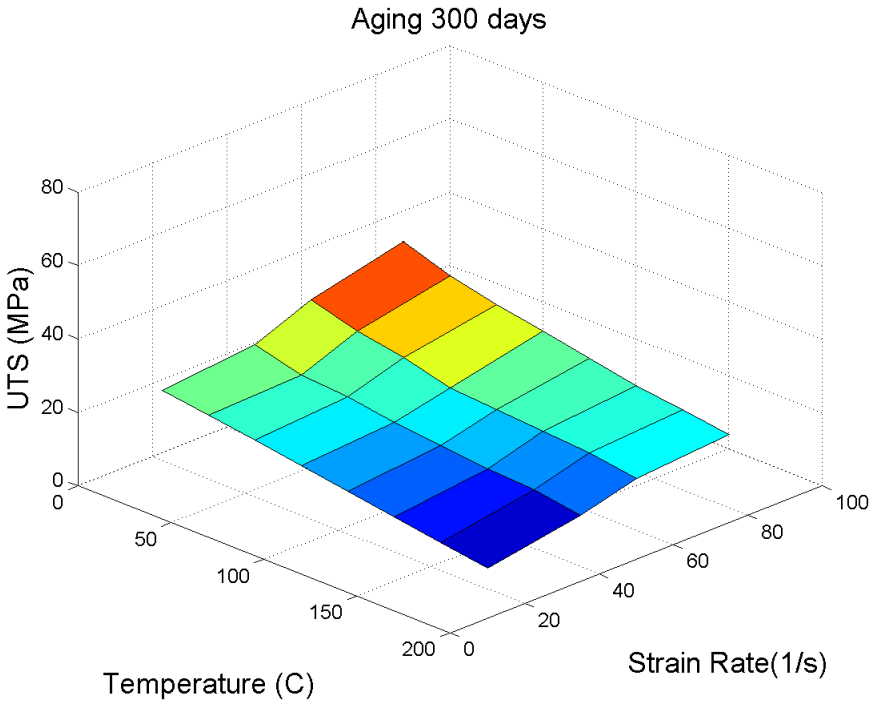

Figure 3.58: UTS vs. strain rate vs. temperature

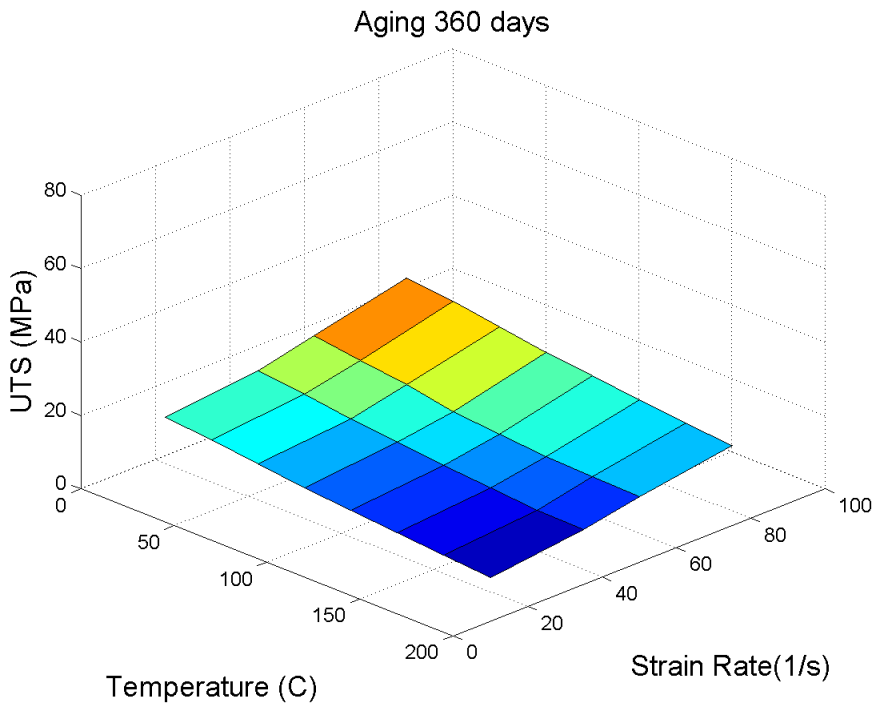

Figure 3.59: U vs. strain rate vs. temperature

3.10 Anand Model

Previously, Anand [13] has developed a constitutive model to describe the material that depend on operating temperature and strain rates. Anand model has unified a stress equation, a flow equation, and an evolution equation to characterize both the creep and rate-dependent plastic performance of the solder alloy. Additionally, for this complicated constitutive equation, no explicit yield condition and no loading or unloading criteria are required. In one dimension uniaxial loading case, stress equation can be written by

$$\sigma = c \cdot s \tag{3.1}$$

Where c (c $<$ 1) is a function of strain rate and temperature, s is the internal valuable.

$$c = (\dot{\varepsilon}_p, T) = \left(\frac{1}{\xi}\right) \cdot \sinh^{-1}\left\{\left[\frac{\dot{\varepsilon}_p}{A} \cdot \exp\left(\frac{Q}{R \cdot T}\right)\right]^m\right\} \tag{3.2}$$

Where $\dot{\varepsilon}_p$ is the inelastic strain rate, is the multiplier of stress, A is the pre-exponential factor, Q is the activation energy, T is the absolute temperature, R is the universal gas constant, and m is the strain rate sensitivity. Substituting Equation 3.1 in Equation 3.2:

$$\sigma = \left(\frac{s}{\xi}\right) \cdot \sinh^{-1}\left\{\left[\frac{\dot{\varepsilon}_p}{A} \cdot \exp\left(\frac{Q}{R \cdot T}\right)\right]^m\right\} \tag{3.3}$$

Based on this equation, solving for which yields the flow equation:

$$\dot{\varepsilon}_p = A \cdot \exp\left(-\frac{Q}{R \cdot T}\right) \cdot \left[\sinh\left(\xi \cdot \frac{\sigma}{s}\right)\right]^{\frac{1}{m}} \tag{3.4}$$

Where s is the internal variable, $\dot{s}$ is assumed to be this form

$$\dot{s} = \left[h_0 \cdot (|B|)^a \cdot \frac{B}{|B|}\right] \cdot \dot{\varepsilon}_p; (a > 1) \tag{3.5}$$

where,

$$B = 1 - \frac{s}{s^*} \tag{3.6}$$

and

$$s^* = \hat{s} \cdot \left[\frac{\dot{\varepsilon}_p}{A} \cdot \exp\left(\frac{Q}{R \cdot T}\right)\right]^n \tag{3.7}$$

Where h_0 is the hardening or softening constant, a $(a > 1)$ is the strain rate sensitivity of hardening or softening process. The quantity s^*represents a saturation value of deformation resistance s, associated with a set of given temperature and strain rate. $\hat{s}$ is a coefficient, and n is the strain rate sensitivity of the saturation value of deformation resistance. For $s < s^*, B > 0$ from Equation 3.6. Then, Equation 3.5 can be simplify as,

$$ds = h_0 \cdot \left(1 - \frac{s}{s^*}\right) d\varepsilon_p \tag{3.8}$$

Integrate on both sides to yield

$$s = s^* - \left\{ \left(s^* - s_0\right)^{1-a} + (a-1) \cdot \left[h_0 \cdot \left(s^*\right)^{-a} \cdot \varepsilon_p \right] \right\}^{\frac{1}{1-a}} \tag{3.9}$$

Where s(0)=s_0 is the initial value of s. Substituting Equation 3.7 in Equation 3.9:

$$s = \hat{s} \cdot \left[\frac{\dot{\varepsilon}_p}{A} \cdot \exp\left(\frac{Q}{R \cdot T} \right) \right]^n -$$

$$\left\{ \left[\hat{s} \cdot \left[\frac{\dot{\varepsilon}_p}{A} \cdot \exp\left(\frac{Q}{R \cdot T} \right) \right]^n - s_0 \right]^{1-a} + (a-1) \cdot \left[h_0 \cdot \left[\hat{s} \cdot \left[\frac{\dot{\varepsilon}_p}{A} \cdot \exp\left(\frac{Q}{R \cdot T} \right) \right]^n \right]^{-a} \cdot \varepsilon_p \right] \right\}^{\frac{1}{1-a}}$$

(3.10)

Substituting Equation 3.10 in Equation 3.3 to get the final version of stress-strain relation:

$$\sigma = \left(\frac{1}{\xi} \right) \cdot \sinh^{-1} \left\{ \left[\frac{\dot{\varepsilon}_p}{A} \cdot \exp\left(\frac{Q}{R \cdot T} \right) \right]^m \right\} \cdot \left\{ \hat{s} \cdot \left[\frac{\dot{\varepsilon}_p}{A} \cdot \exp\left(\frac{Q}{R \cdot T} \right) \right]^n - \right.$$

$$\left\{ \left[\hat{s} \cdot \left[\frac{\dot{\varepsilon}_p}{A} \cdot \exp\left(\frac{Q}{R \cdot T} \right) \right]^n - s_0 \right]^{1-a} + (a-1) \cdot \left[h_0 \cdot \left[\hat{s} \cdot \left[\frac{\dot{\varepsilon}_p}{A} \cdot \exp\left(\frac{Q}{R \cdot T} \right) \right]^n \right]^{-a} \cdot \varepsilon_p \right] \right\}^{\frac{1}{1-a}}$$

(3.11)

From the final expression of stress-strain function, nine material constants of the unified rate dependent Anand model have been included: A, ξ, Q/R, m, h_0, a, s_0 and n. The set of Anand constitutive equations cannot only account for the physical phenomena of strain-rate and temperature sensitivity, but also strain rate history effects, isotropic strain-hardening

and the restoration process of dynamic recovery. The Ultimate Tensile Strength (UTS) can be attained by simply assuming that ε_p goes to infinity.

$$\sigma^* = UTS = \sigma|_{\varepsilon_p \to \infty} = \left[\frac{\dot{\varepsilon}_p}{A} \cdot \exp\left(\frac{Q}{R \cdot T}\right)\right]^n \cdot \left(\frac{\hat{s}}{\xi}\right) \cdot \sinh^{-1}\left\{\left[\frac{\dot{\varepsilon}_p}{A} \cdot \exp\left(\frac{Q}{R \cdot T}\right)\right]^m\right\} \quad (3.12)$$

Substituting this maximum tensile stress back in Equation 3.10 and rewritten as

$$\sigma = \sigma^* - \left\{(\sigma^* - c \cdot s_0)^{1-a} + (a-1) \cdot \left[c \cdot h_0 \cdot (\sigma^*)^{-a}\right] \cdot \varepsilon_p\right\}^{\frac{1}{1-a}} \quad (3.13)$$

3.11 Procedures of Computing Anand Constants

In the Anand model, there are total nine material parameters to characterize the constitutive equations. In order to compute Anand constants, tensile testing were carried out at different high strain rate and high temperature conditions. Stress and strain data were captured by high speed data acquisition system. All the data were fitted by a non-linear least square algorithm. The nine parameters of the Anand model include A, ξ, Q/R, m, h_0, a, s_0 and n. These nine parameters can be obtained by the following procedures.

- Step 1 : Equation 3.12 should be employed to fit saturation stress vs. strain rate and temperature data to determine the value of the parameters A, n, Q/R, m, $\hat{s}/\xi$
- Step 2 : Determination of ξ and $\hat{s}$. The parameter ξ was selected such that the ratio of σ/s is less than unity and then $\hat{s}$ is calculated by the combined term $\hat{s}/\xi$ which has been decided in step.1
- Step 3 : Equation 3.13 has been applied to fit stress vs. plastic strain data at different strain rate and temperatures to determine the values of parameters h_0, a, s_0

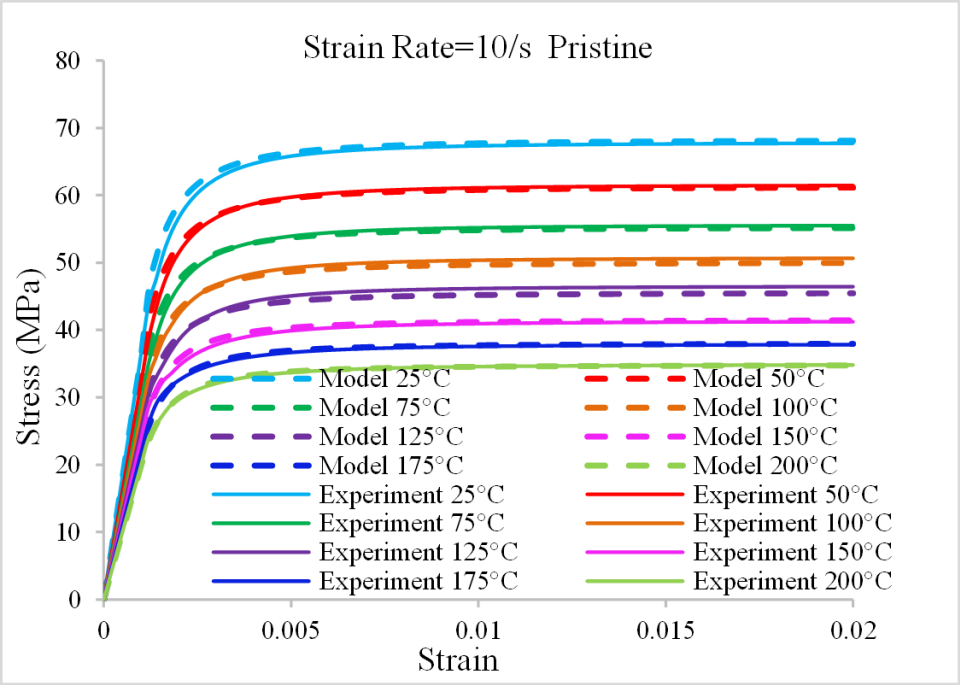

Figure 3.60: Strain rate = 10/s pristine

3.12 Fitting Results

At each aging duration, a set of Anand model was carried out to represent constitutive equation of SAC305. All the Anand constants have been computed with nonlinear least square fitting method that mentioned above. Figure 3.60 to Figure 3.87 demonstrate measured stress−strain data for SAC305 over the 8 temperatures and 4 strain rates with 7 different aging conditions.

3.13 Effect of Aging on Anand Model

All the set of Anand constant at different aging duration have been tabulated into Table 3.10. The trend of those constant can be visualized by plotting each constant vs. aging duration. Figure 3.92 to 3.96 have shown the changing in constants with increasing of aging time. Q/R and ξ are found to be constant with time of aging increasing. Since Q is the activation energy of SAC305 which should be independent of aging. Other than these

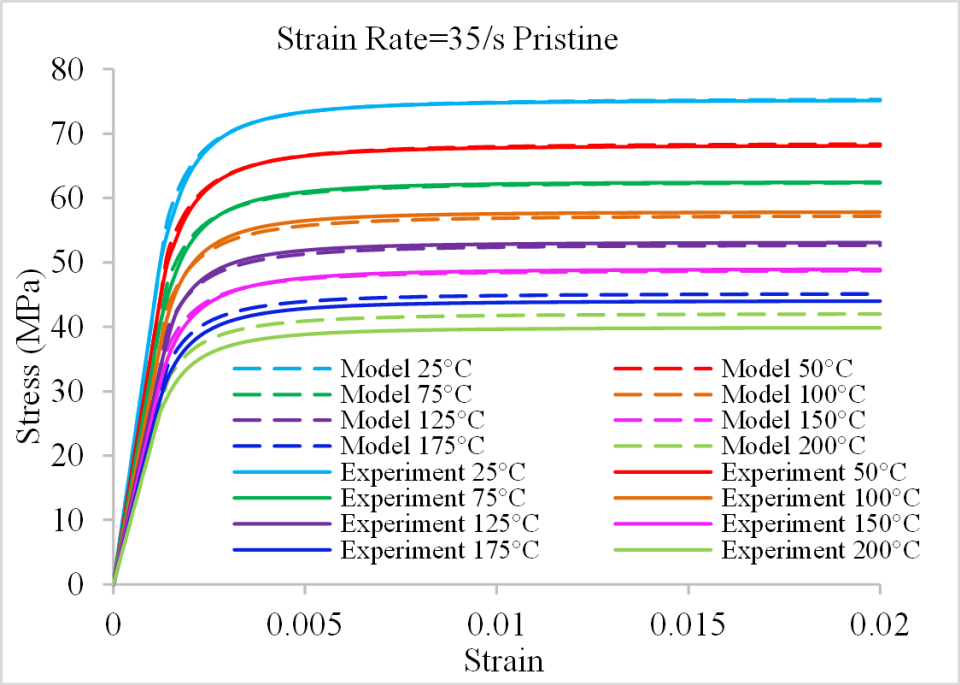

Figure 3.61: Strain rate = 35/s pristine

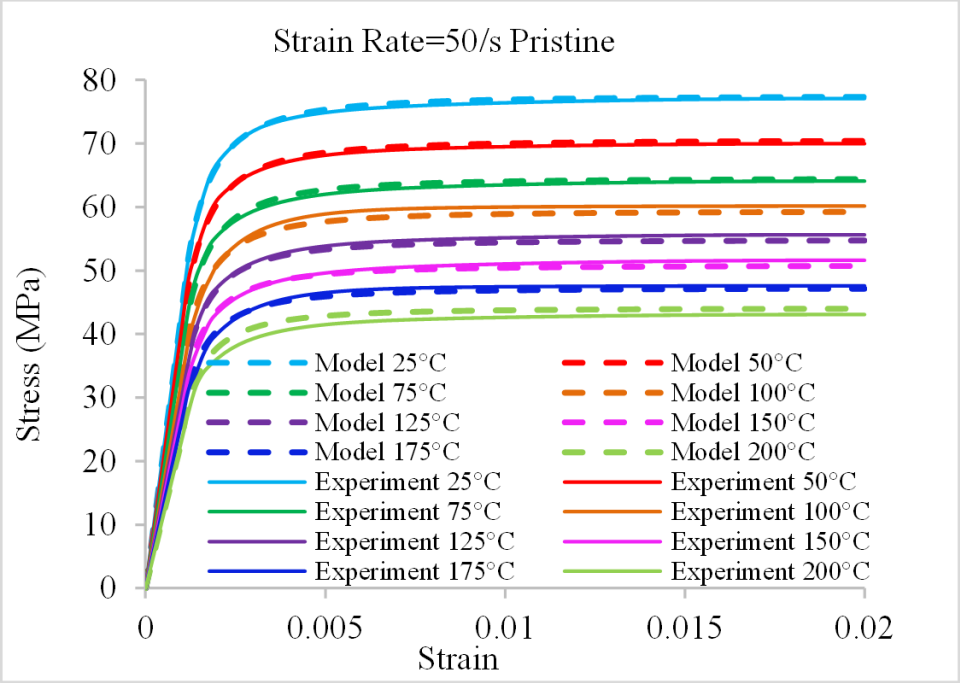

Figure 3.62: Strain rate = 50/s pristine

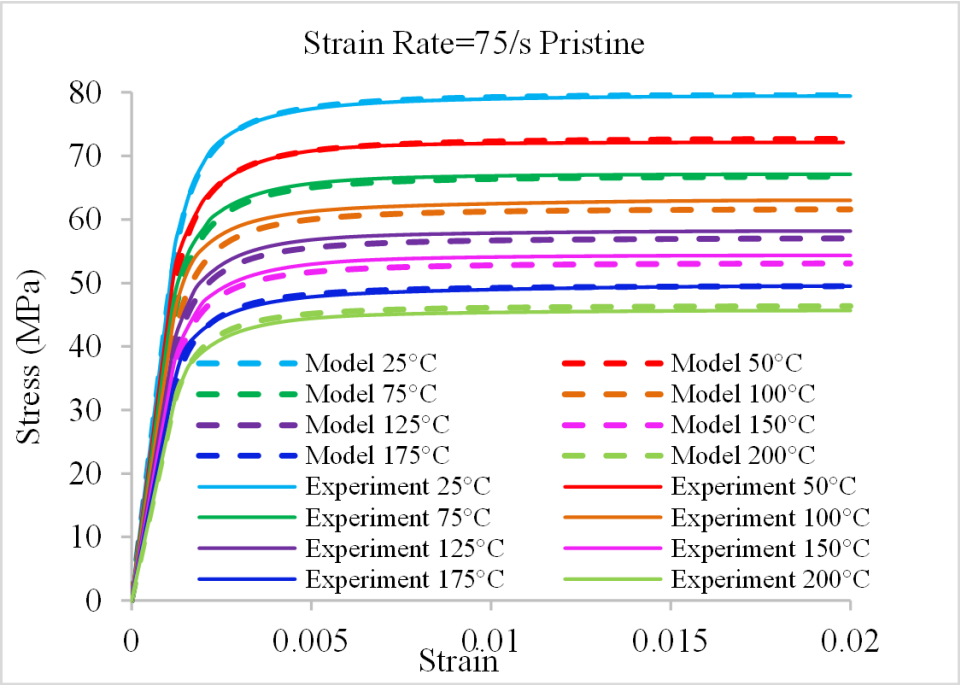

Figure 3.63: Strain rate = 75/s pristine

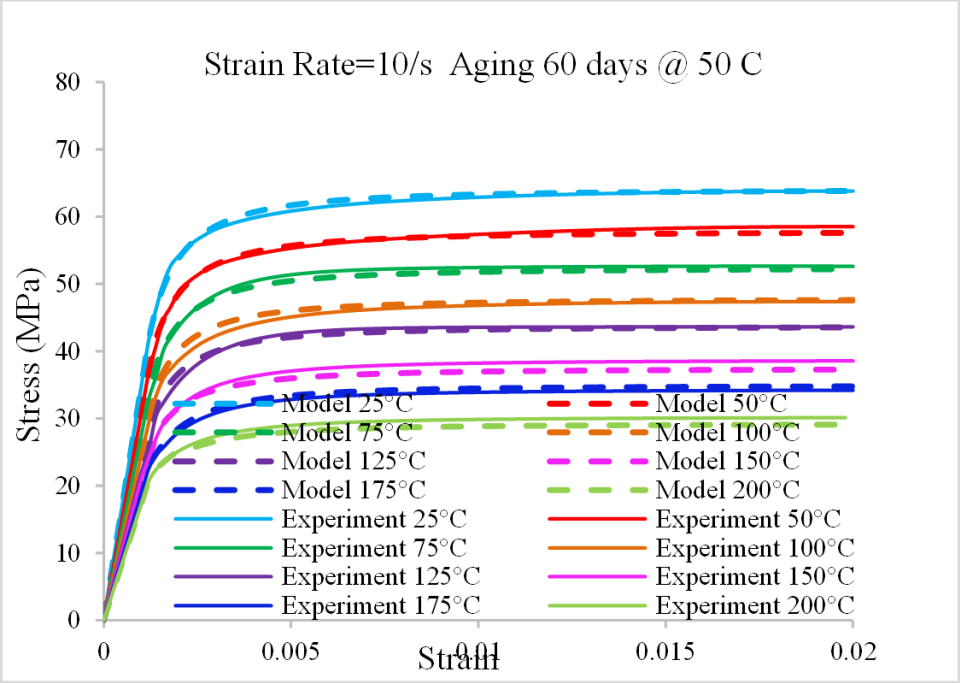

Figure 3.64: Strain rate = 10/s aging 60 days at 50 °C

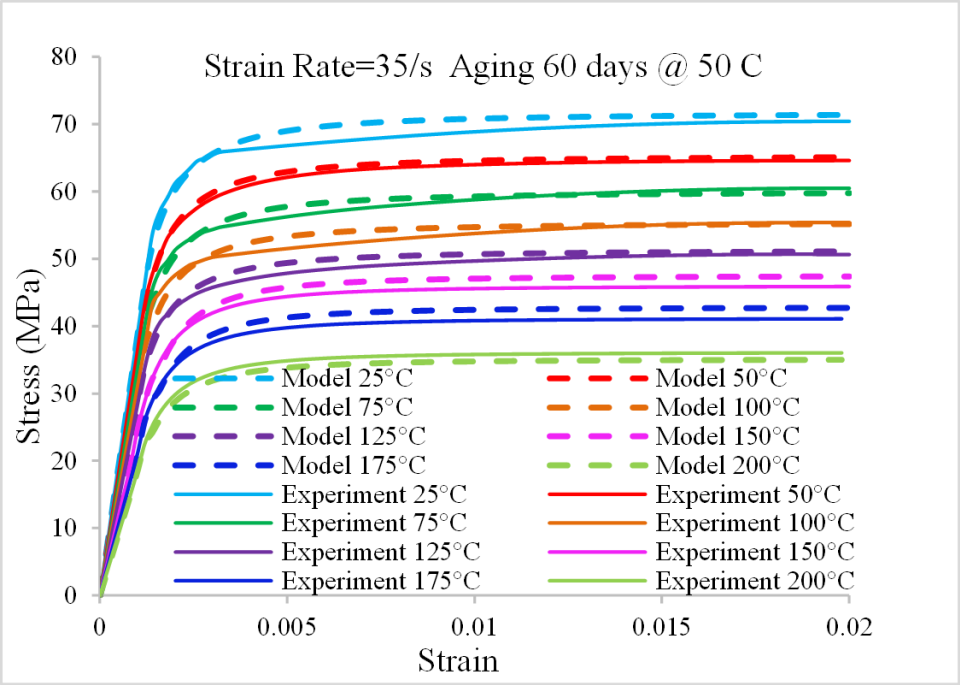

Figure 3.65: Strain rate = 35/s aging 60 days at 50 °C

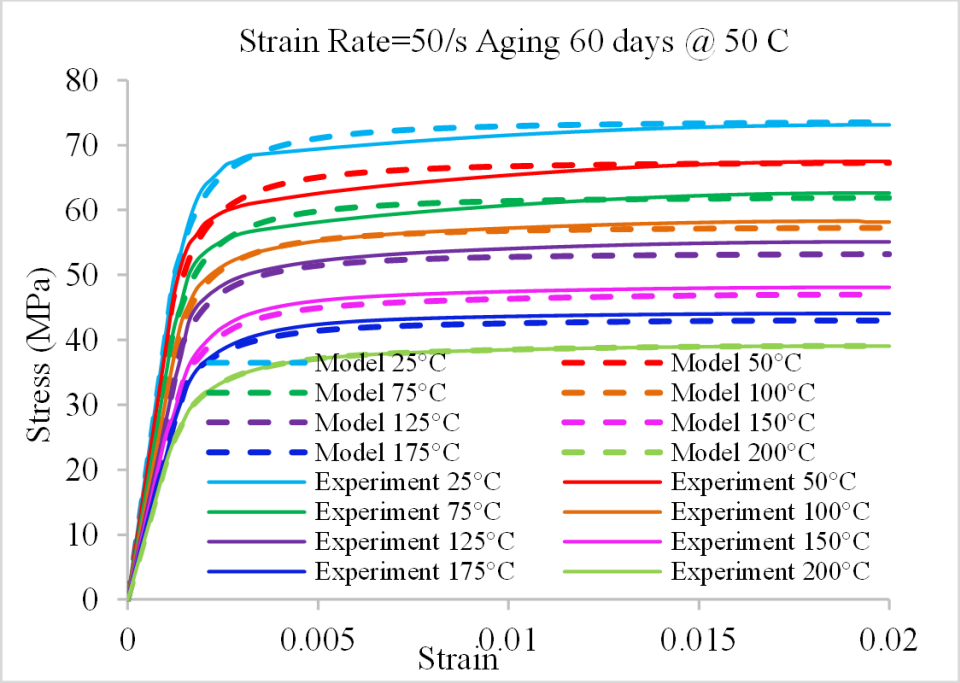

Figure 3.66: Strain rate = 50/s aging 60 days at 50 °C

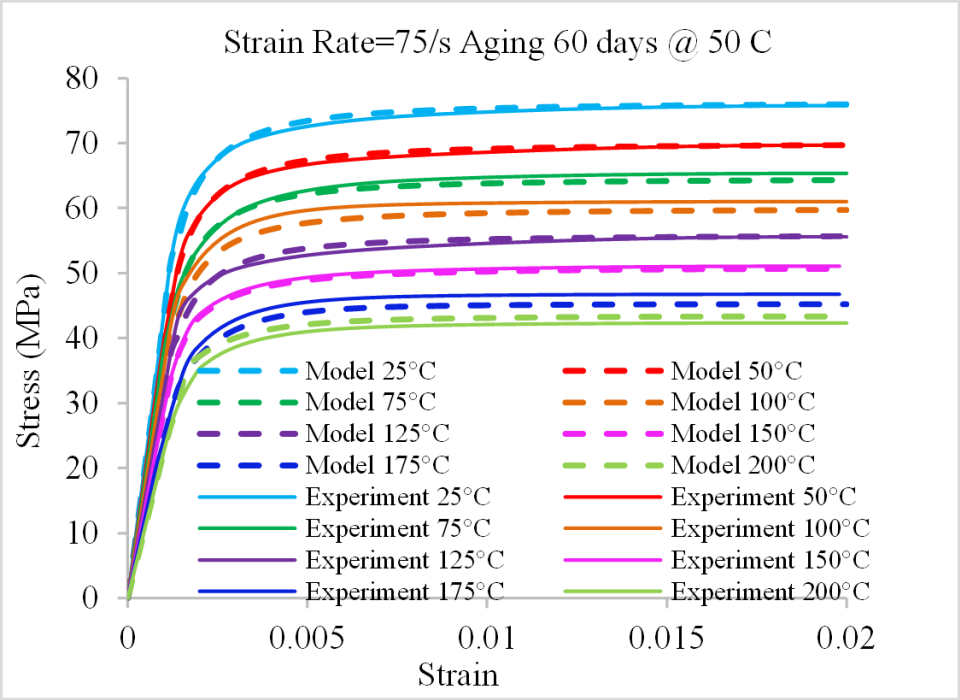

Figure 3.67: Strain rate = 75/s aging 60 days at 50 °C

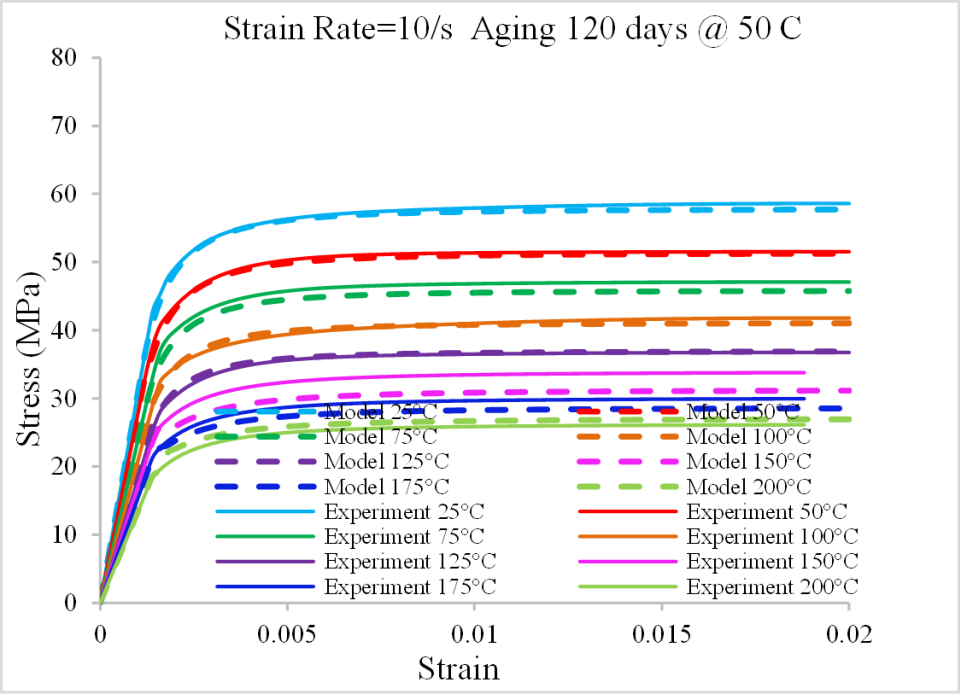

Figure 3.68: Strain rate = 10/s aging 120 days at 50 °C

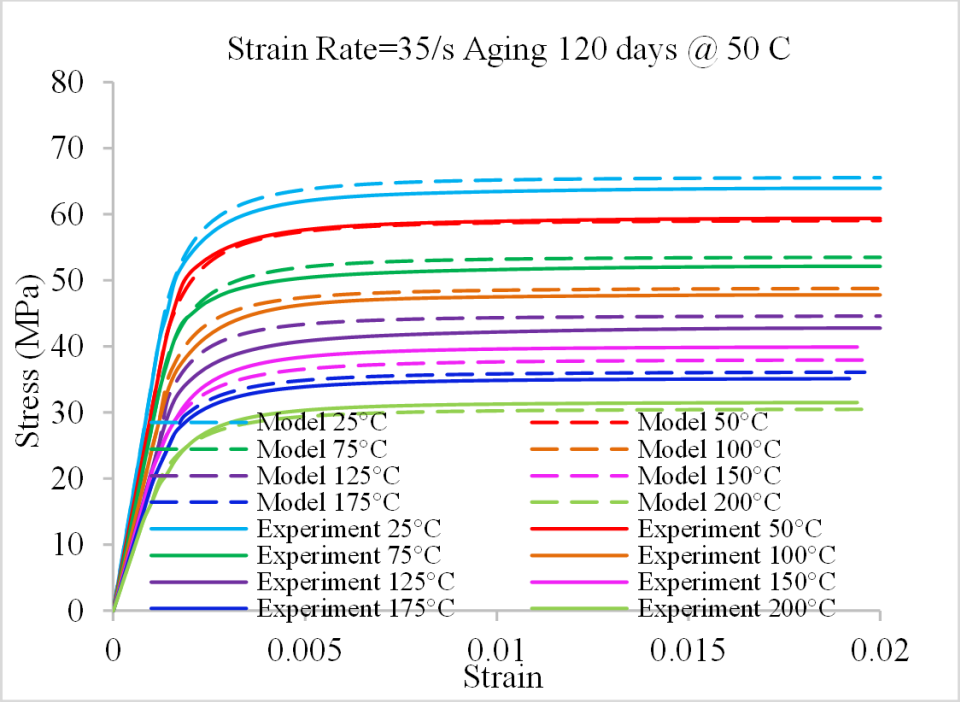

Figure 3.69: Strain rate = 35/s aging 120 days at 50 °C

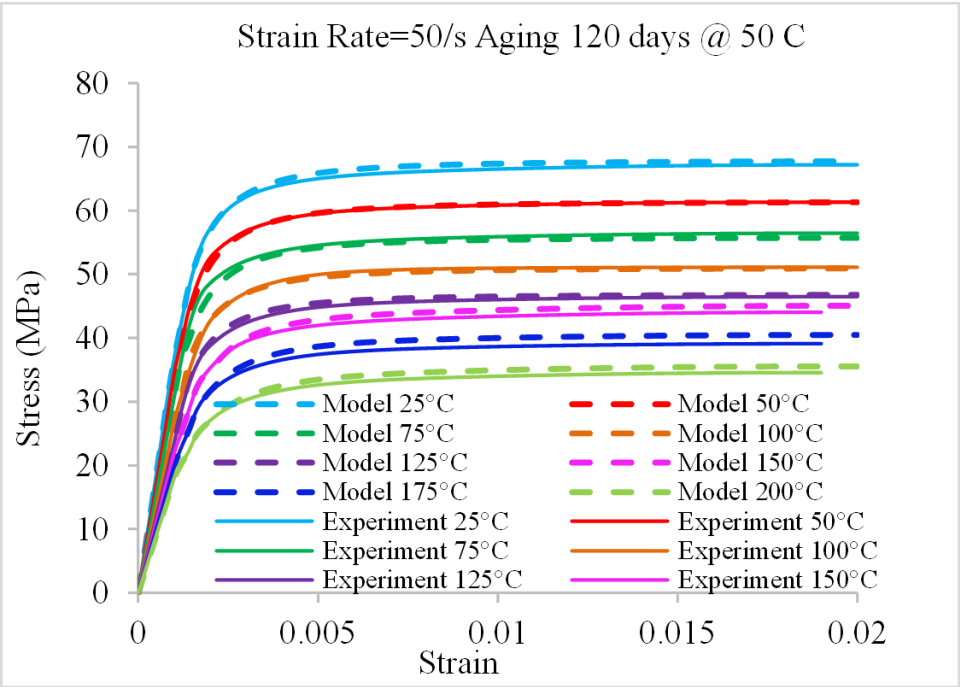

Figure 3.70: Strain rate = 50/s aging 120 days at 50 °C

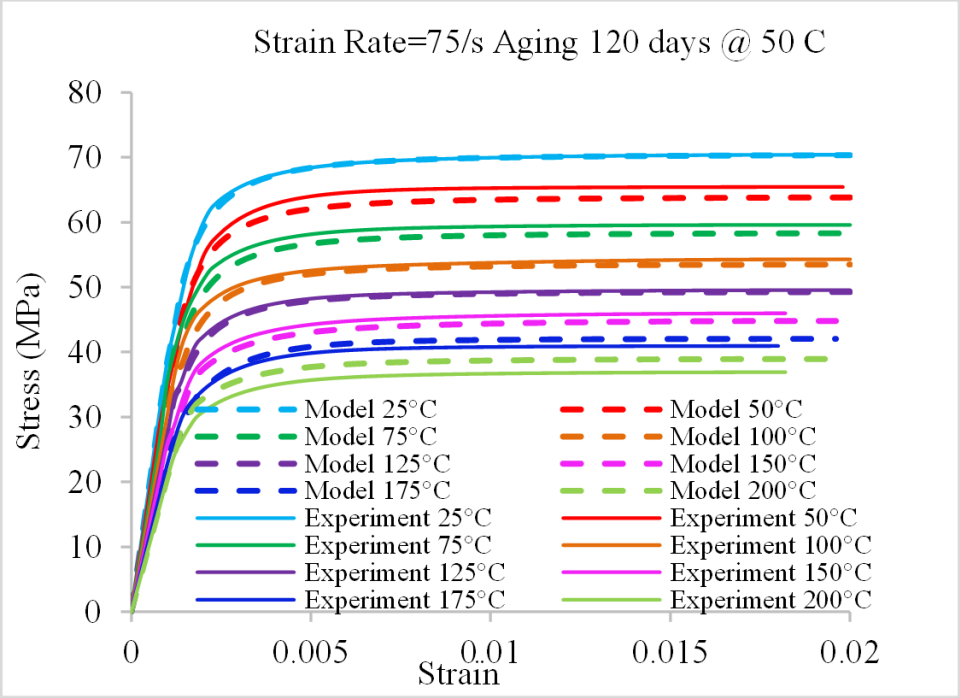

Figure 3.71: Strain rate = 75/s aging 120 days at 50 °C

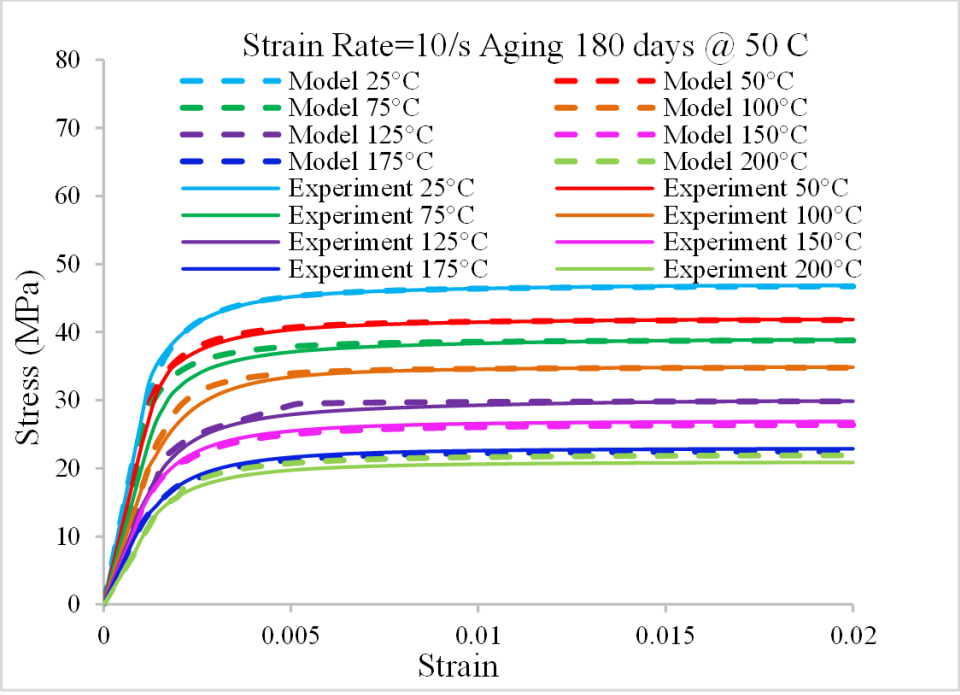

Figure 3.72: Strain rate = 10/s aging 180 days at 50 °C

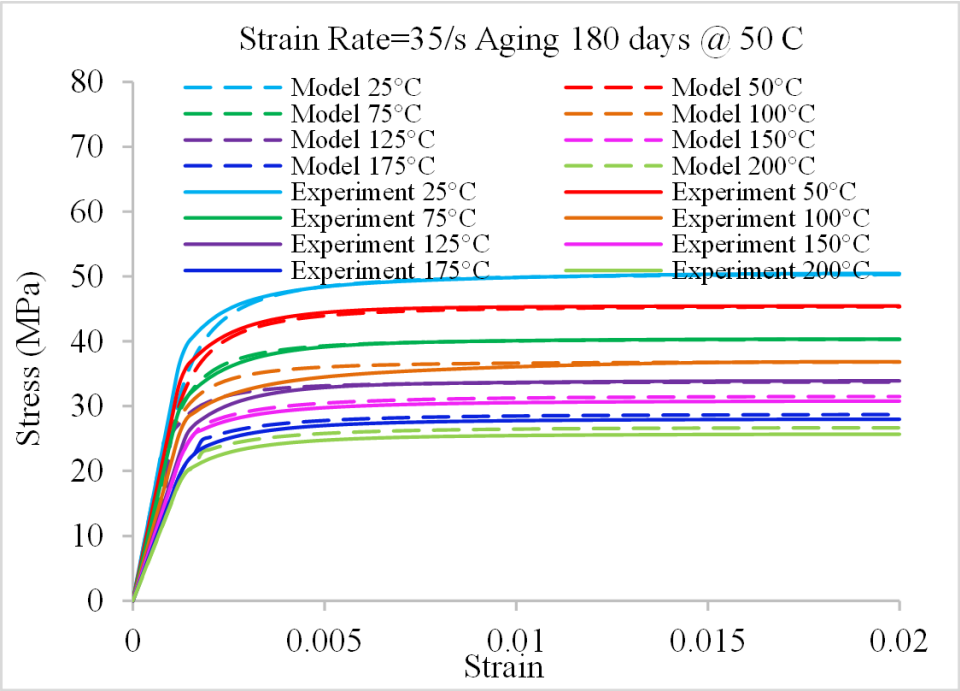

Figure 3.73: Strain rate = 35/s aging 180 days at 50 °C

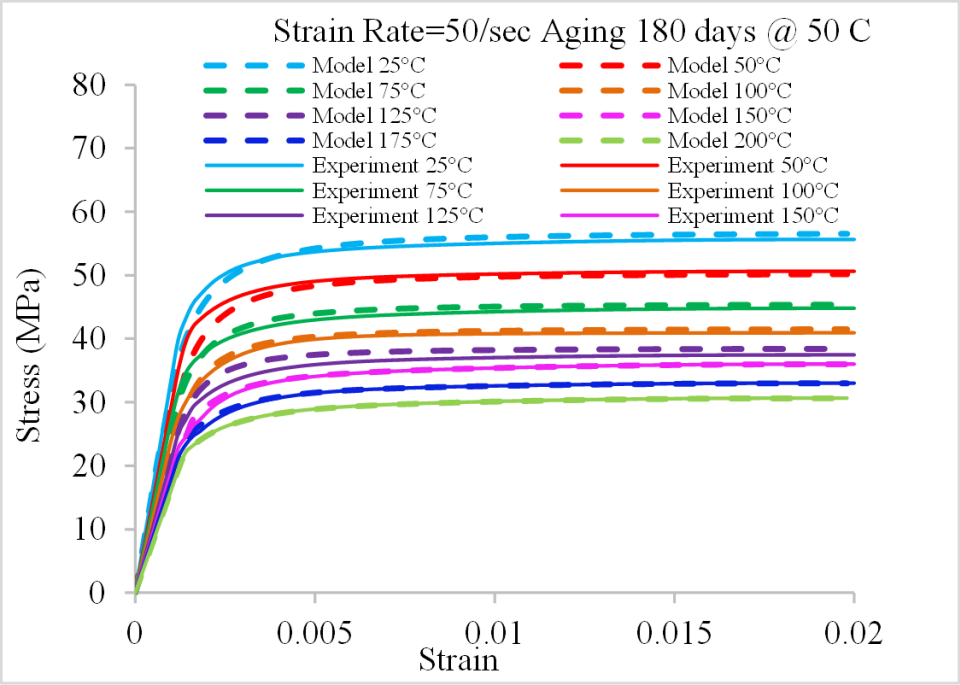

Figure 3.74: Strain rate = 50/s aging 180 days at 50 °C

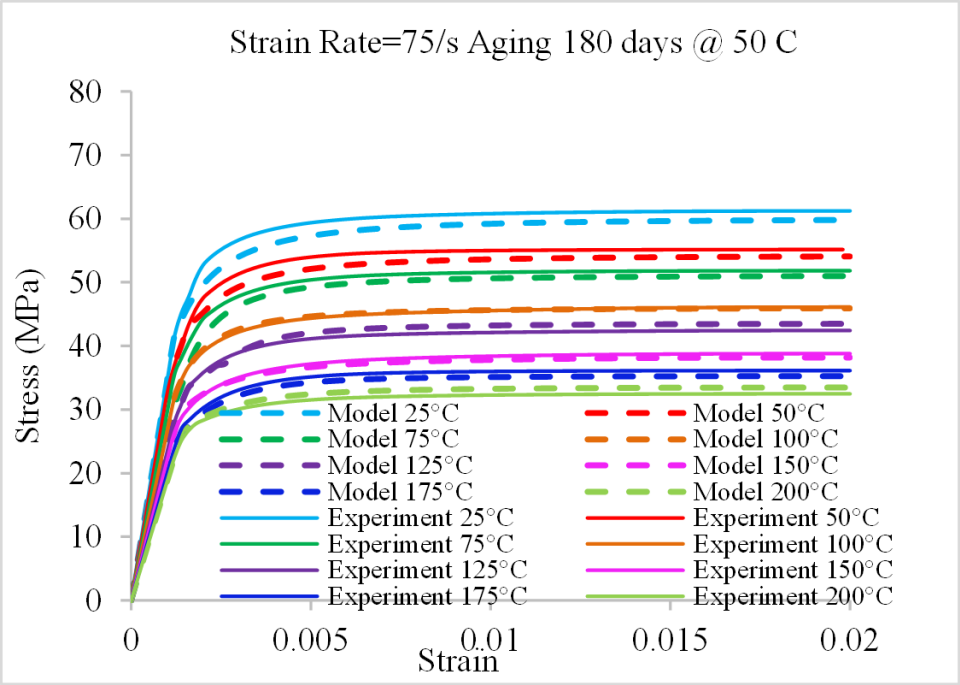

Figure 3.75: Strain rate = 75/s aging 180 days at 50 °C

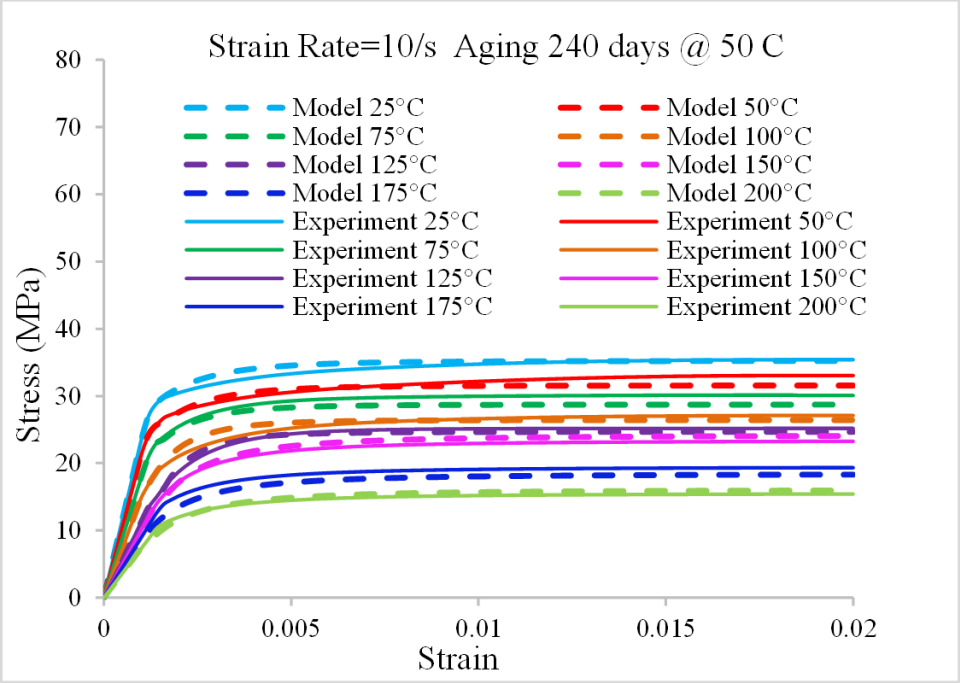

Figure 3.76: Strain rate = 10/s aging 240 days at 50 °C

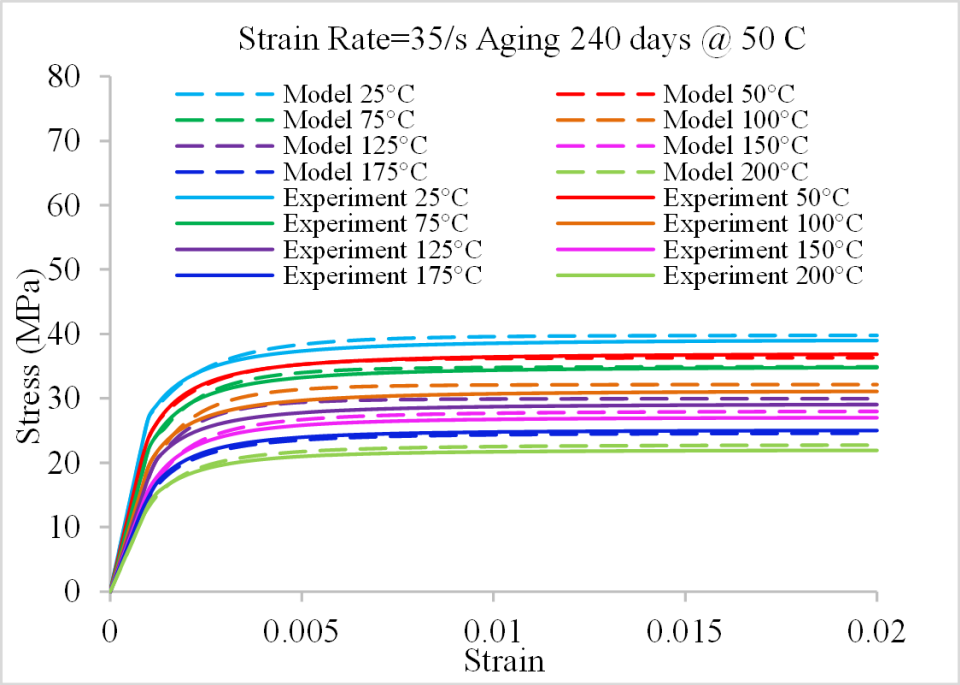

Figure 3.77: Strain rate = 35/s aging 240 days at 50 °C

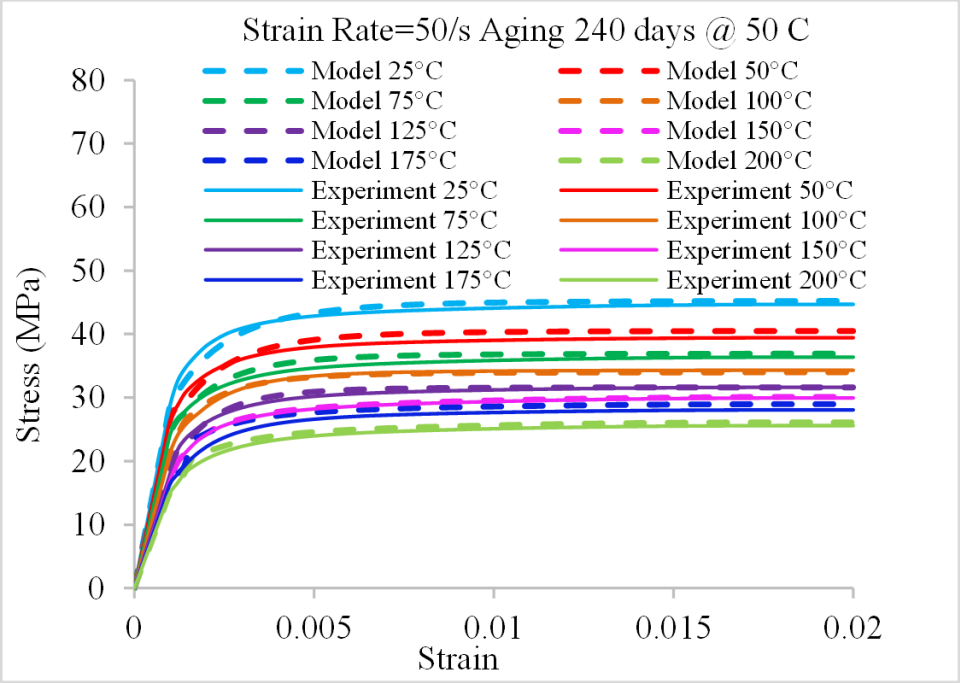

Figure 3.78: Strain rate = 50/s aging 240 days at 50 °C

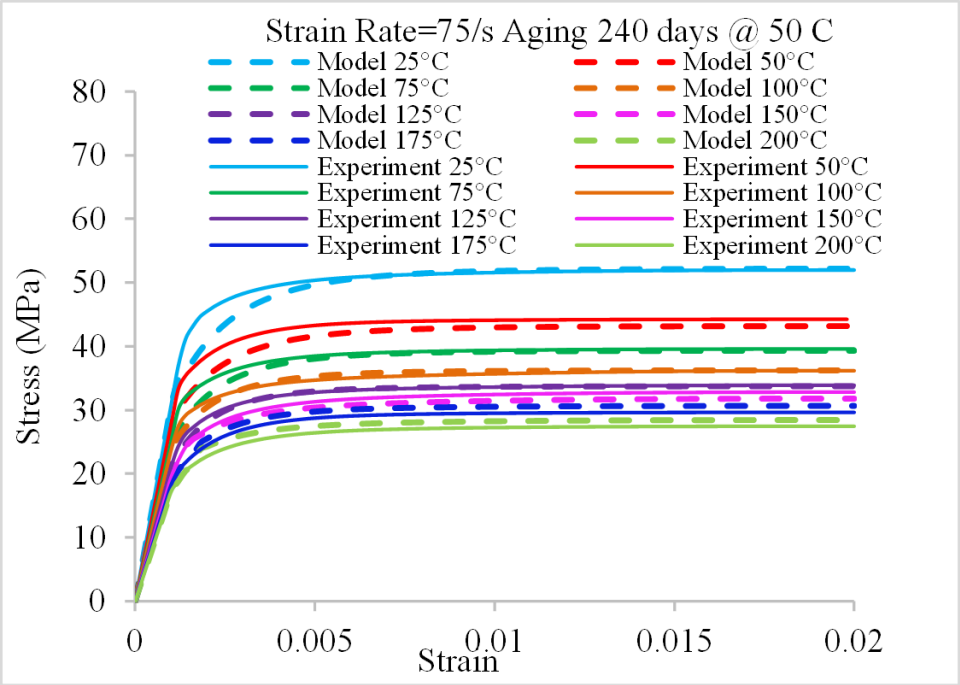

Figure 3.79: Strain rate = 75/s aging 240 days at 50 °C

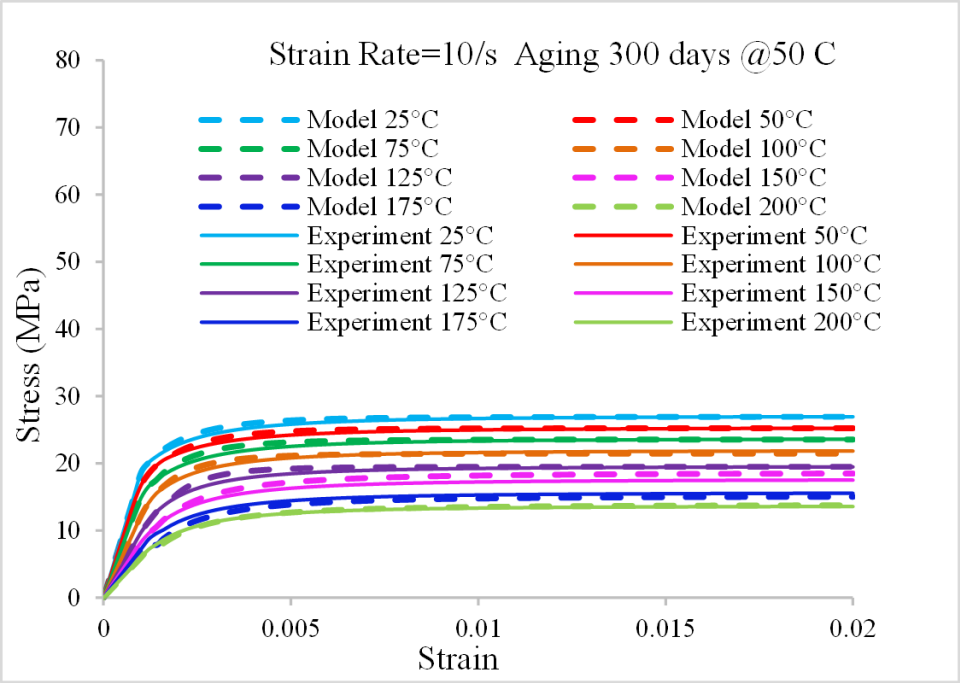

Figure 3.80: Strain rate = 10/s aging 300 days at 50 °C

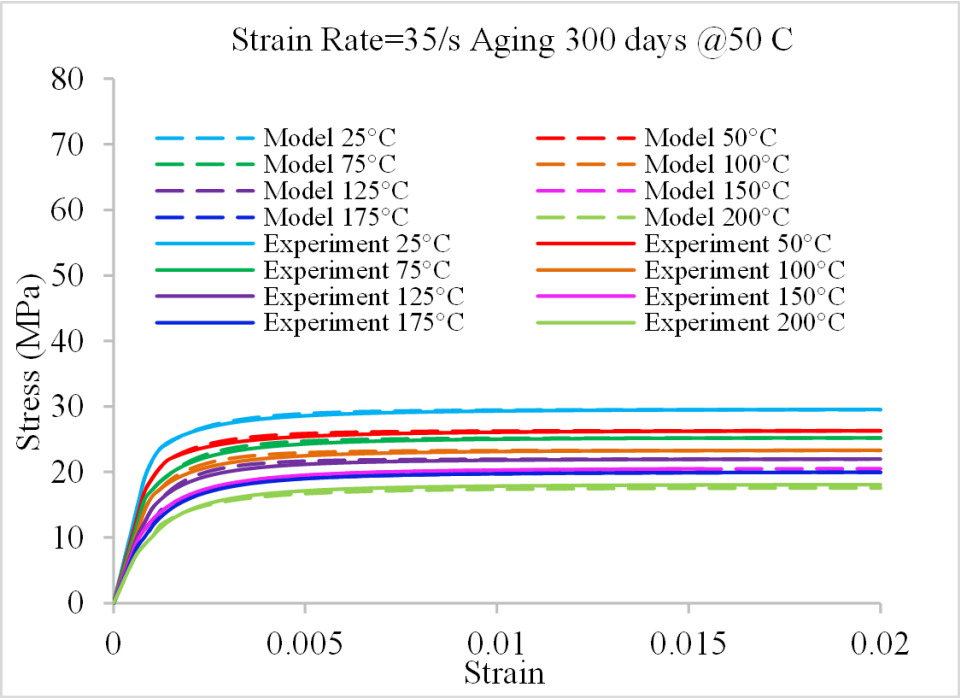

Figure 3.81: Strain rate = 35/s aging 300 days at 50 °C

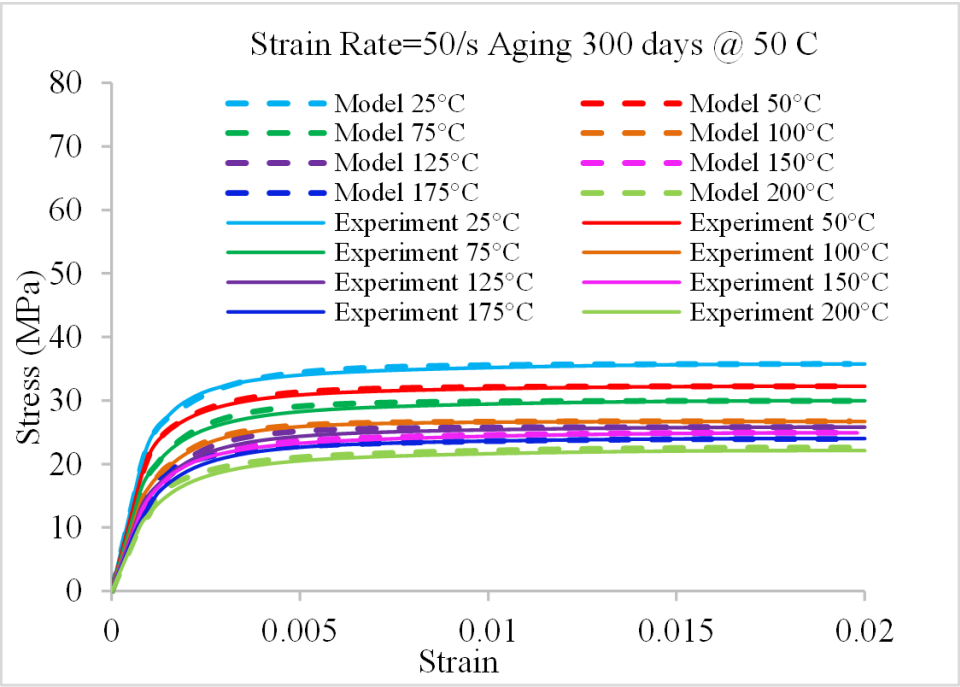

Figure 3.82: Strain rate = 50/s aging 300 days at 50 °C

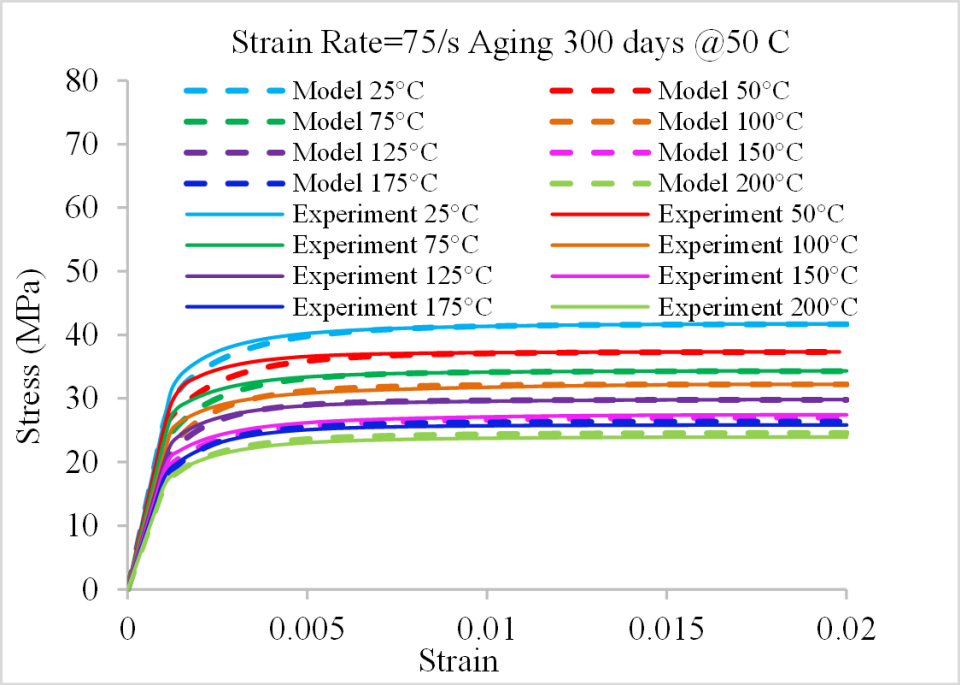

Figure 3.83: Strain rate = 75/s aging 300 days at 50 °C

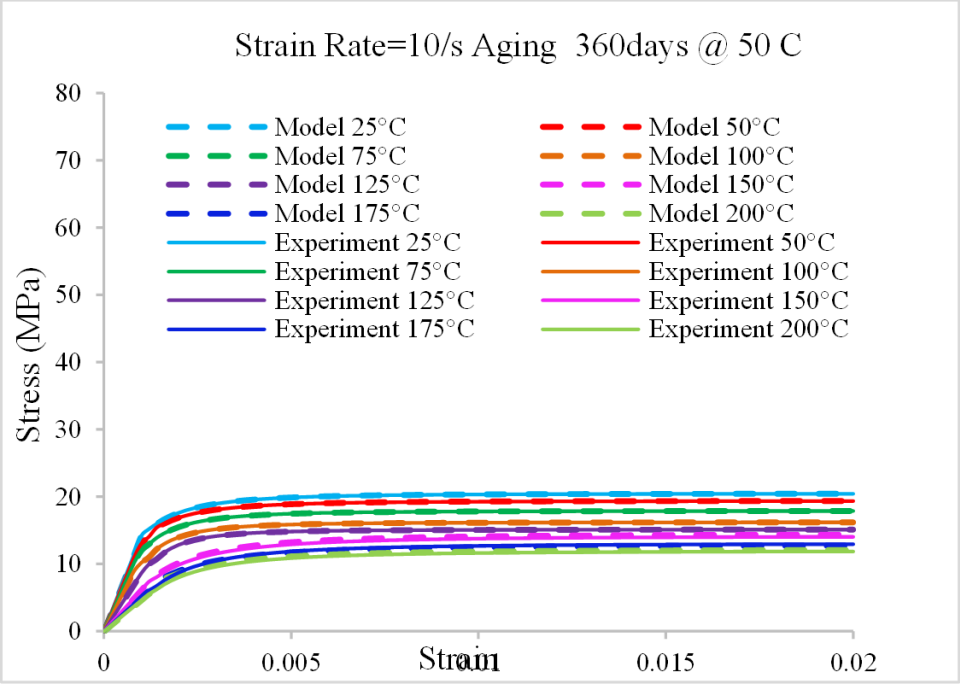

Figure 3.84: Strain rate = 10/s aging 360 days at 50 °C

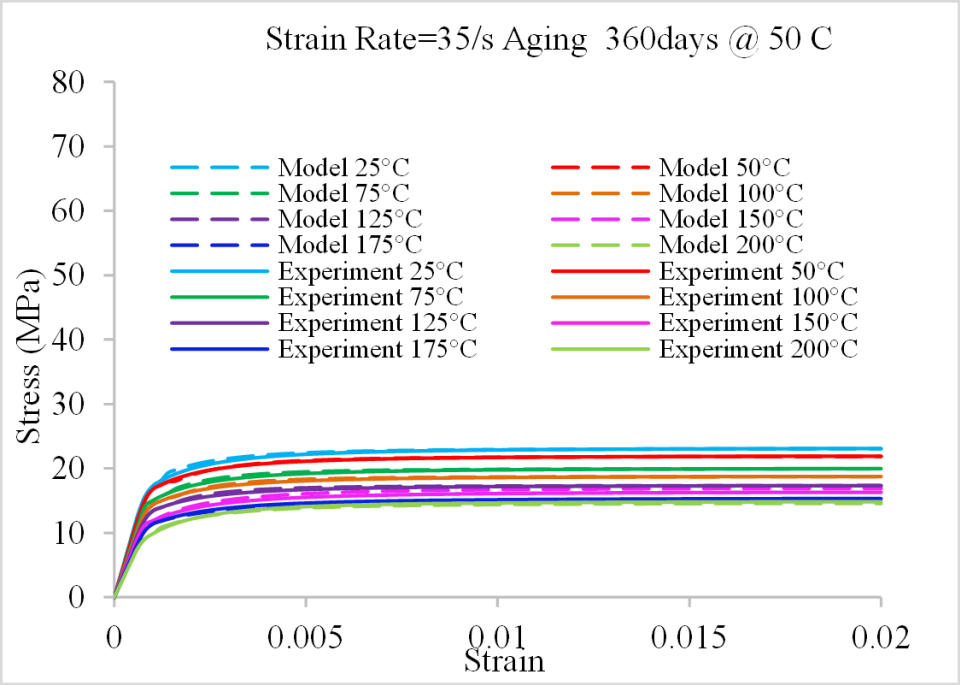

Figure 3.85: Strain rate = 35/s aging 360 days at 50 °C

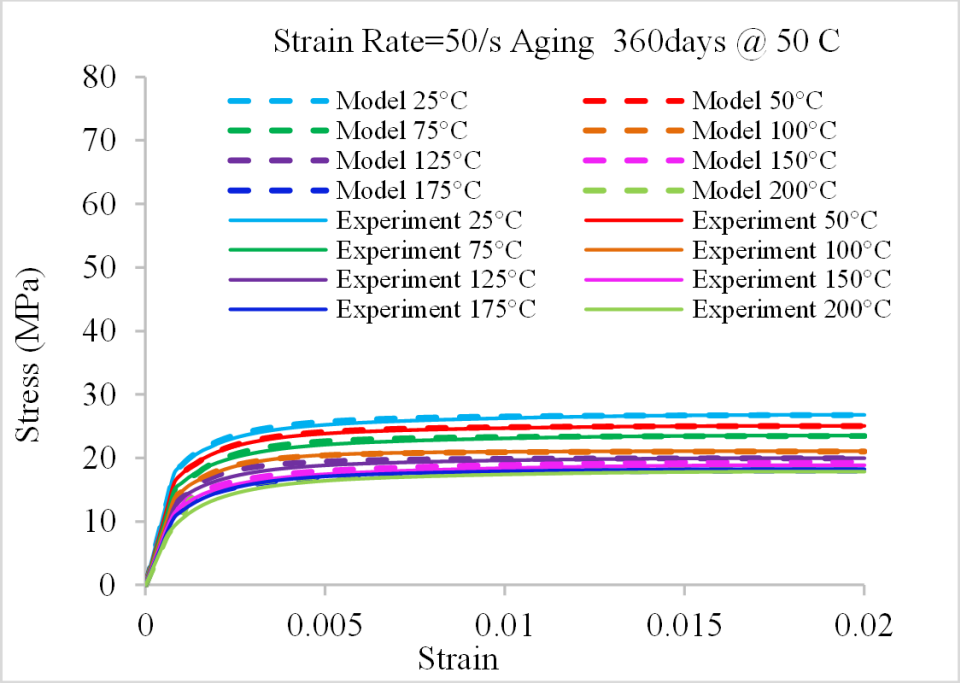

Figure 3.86: Strain rate = 50/s aging 360 days at 50 °C

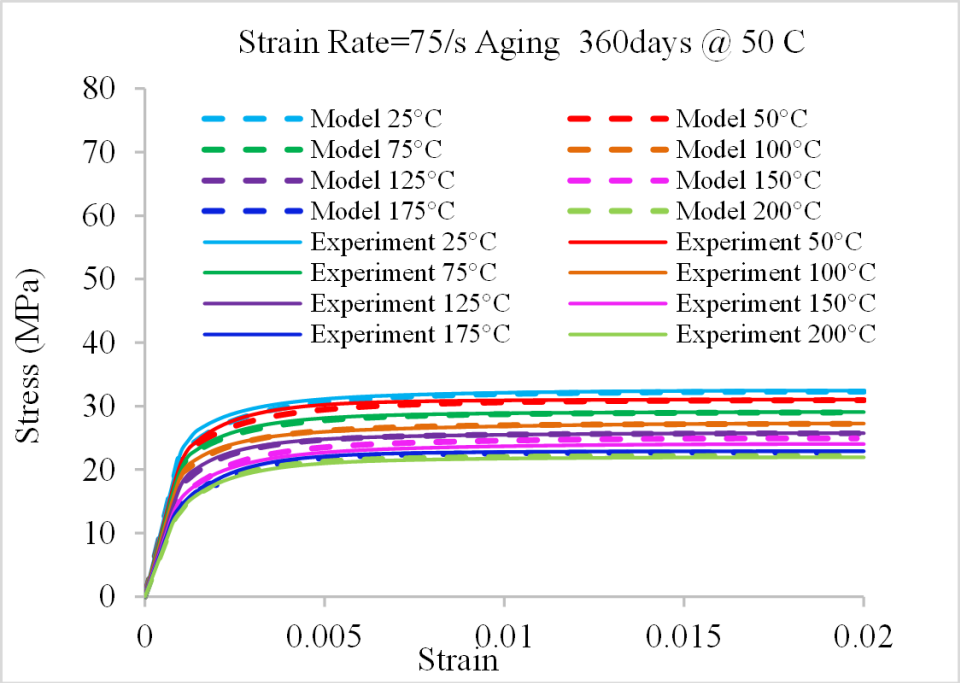

Figure 3.87: Strain rate = 75/s aging 360 days at 50 °C

Table 3.10: Anand constants of SAC305

Constant	Units	Pristine	60 Days	120 Days	180 Days	240 Days	300 Days	360 Days
A	1/s	699.46	778.81	1000	1100	1200	1300	1400
Q/R	1/k	4000	4000	4000	4000	4000	4000	4000
m		0.46	0.45	0.43	0.39	0.36	0.33	0.3
n		0.0011	0.001	0.0009	0.0008	0.0007	0.0006	0.0005
ξ		6	6	6	6	6	6	6
$\hat{s}$	MPa	81	80	76.4	67.62	50.64	42.18	35.12
h_0	MPa	223688.16	204943.1	197652.54	174130	141440	124123	104234
a		1.60	1.63	1.7	1.75	1.88	1.91	2.01
s_0	MPa	58.59	57.90	55.48	32.39	20.00	18.00	15.00

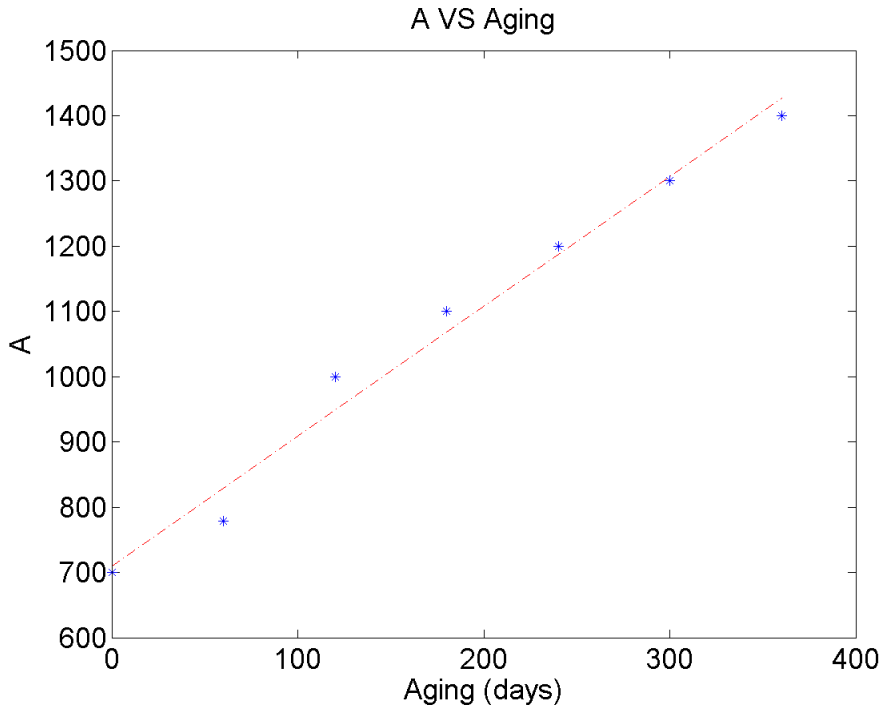

Figure 3.88: Effect of aging on A

two, all the left constants have been effected by aging duration.Parameters such as A, a are increasing with longer aging duration. Parameters such as m, n, $\hat{s}$, h_0, s_0 show reducing in values with increasing of aging time

3.14 Error plot

Good correlation results have been achieved. Figure 3.97 to 3.120 show the percentage of error plot at various testing conditions.

3.15 Summary and conclusion

In this chapter, Stress-strain curves of SAC305 have been has been measured at 8 different temperatures (25, 50, 75, 100, 125, 150, 175, 200 °C), 4 different strain rates (10, 35, 50, 75/s) and 7 aging conditions (Pristine, 60, 120, 180, 240, 300, 360 days). Results show elastic modulus and ultimate tensile strength are both decreased with increasing in aging

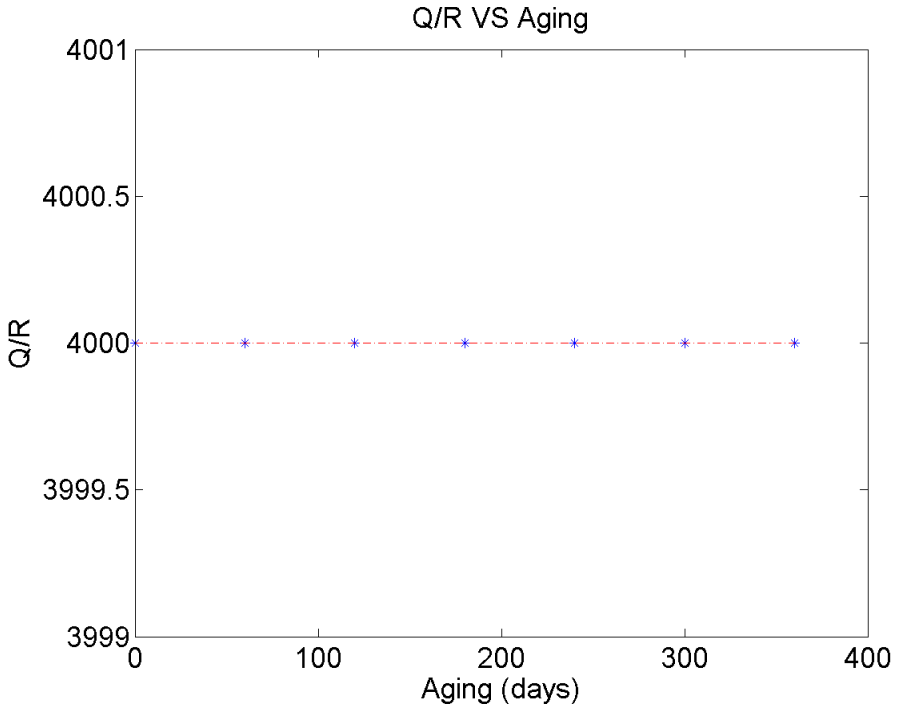

Figure 3.89: Effect of aging on Q/R

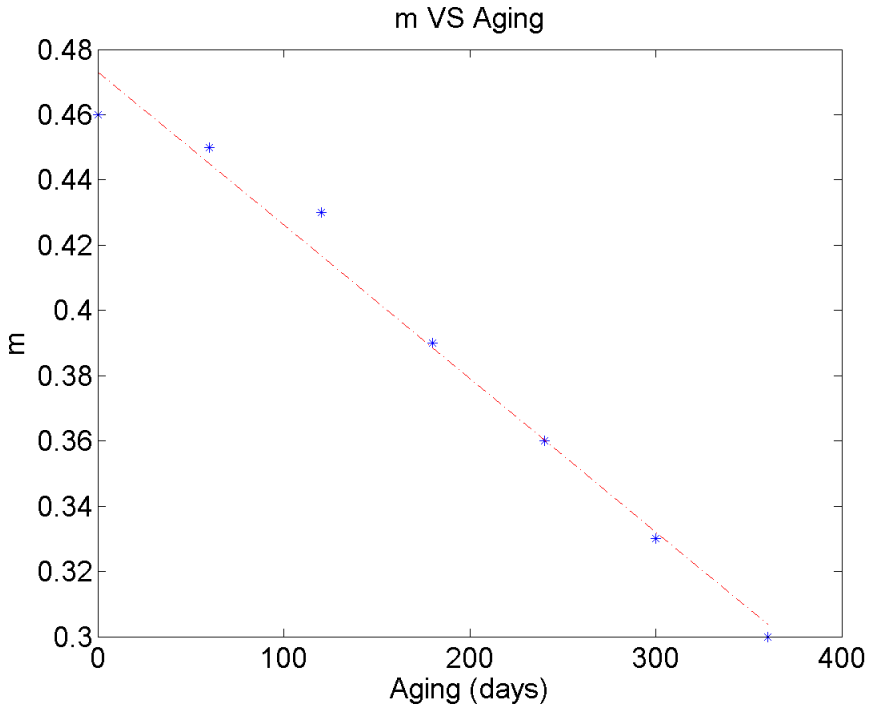

Figure 3.90: Effect of aging on m

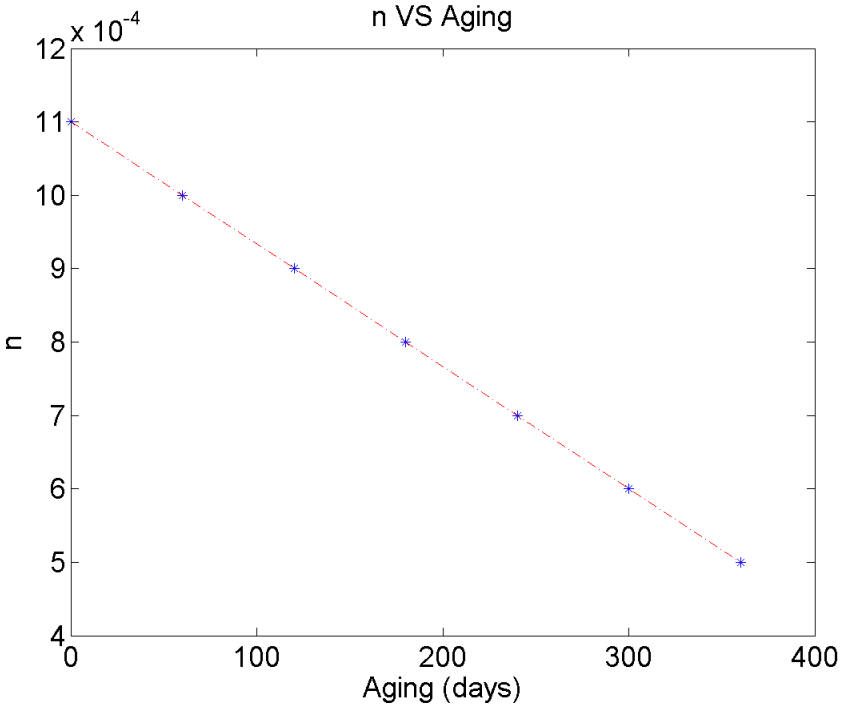

Figure 3.91: Effect of aging on n

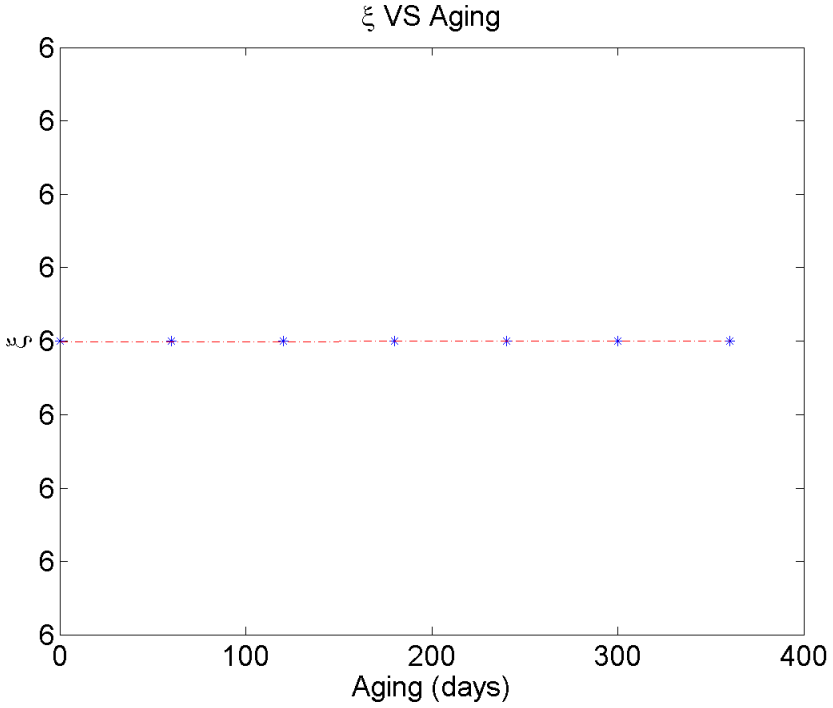

Figure 3.92: Effect of aging on ξ

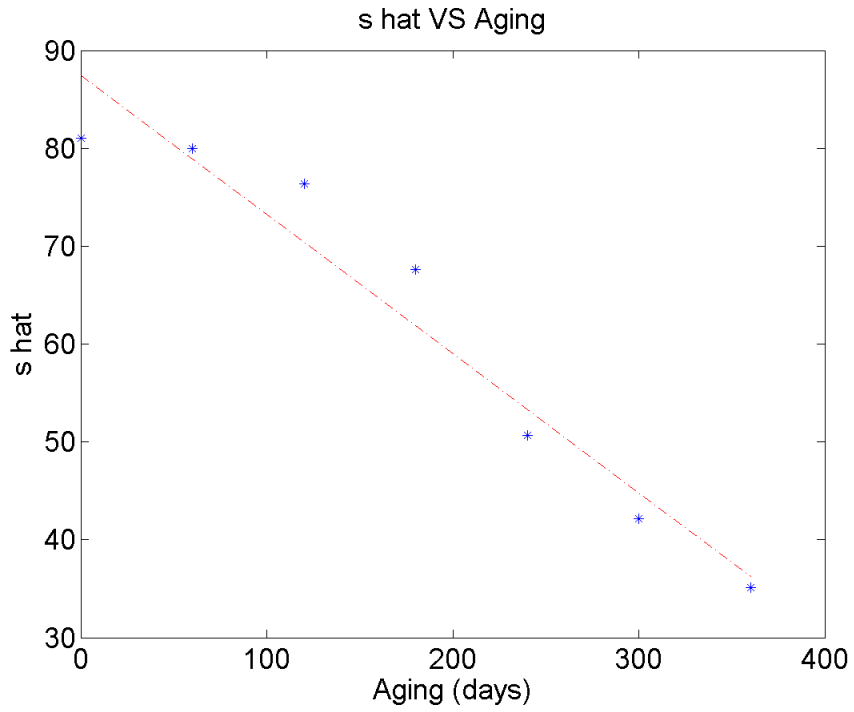

Figure 3.93: Effect of aging on $\hat{s}$

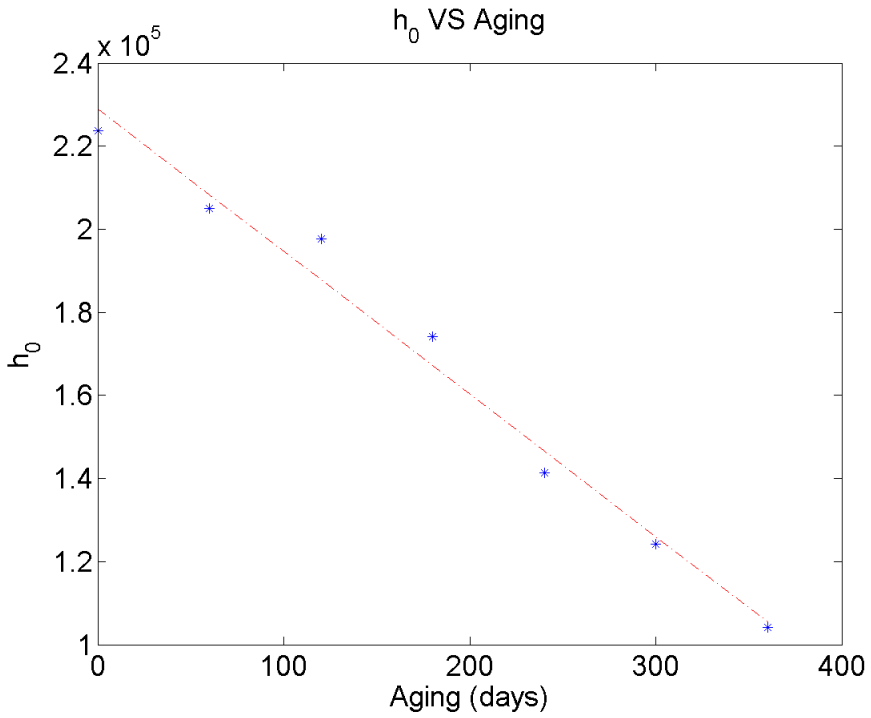

Figure 3.94: Effect of aging on h_0

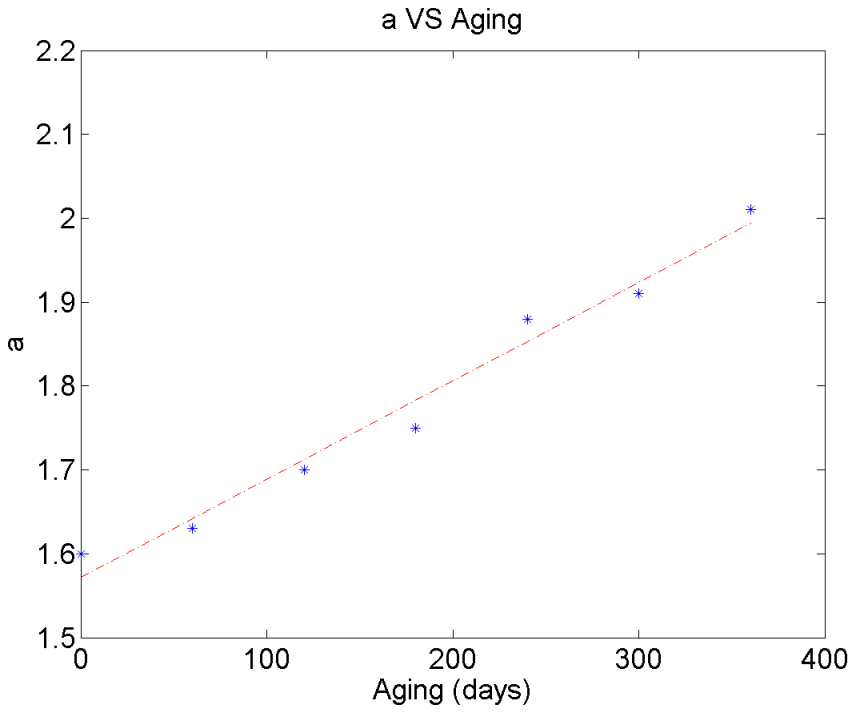

Figure 3.95: Effect of aging on a

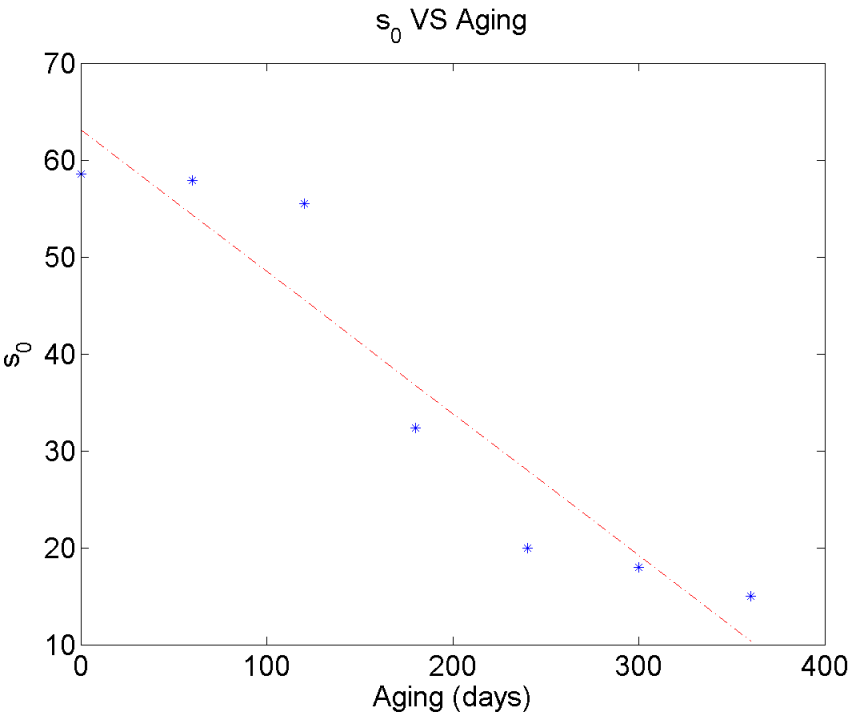

Figure 3.96: Effect of aging on s_0

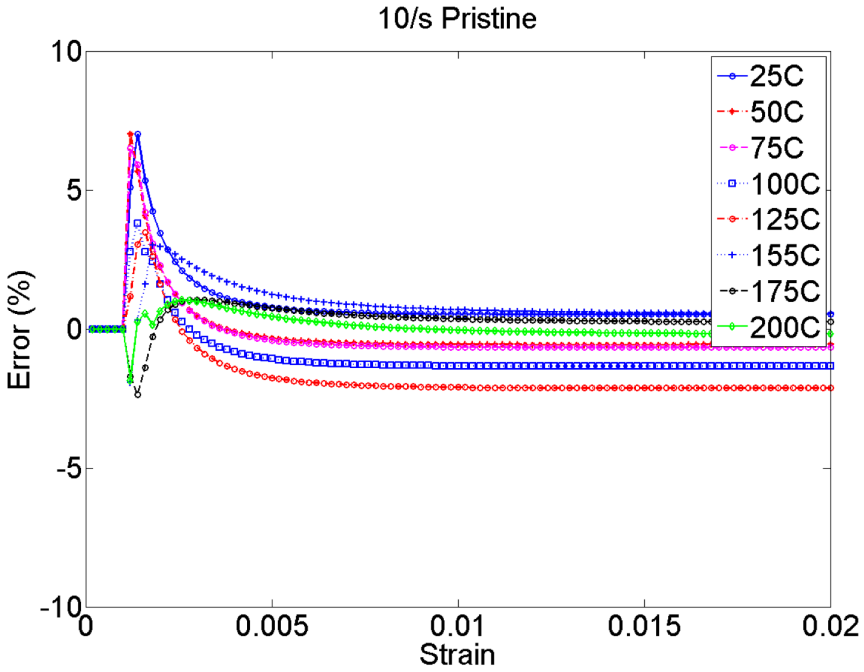

Figure 3.97: Error plot strain rate = 10/s pristine

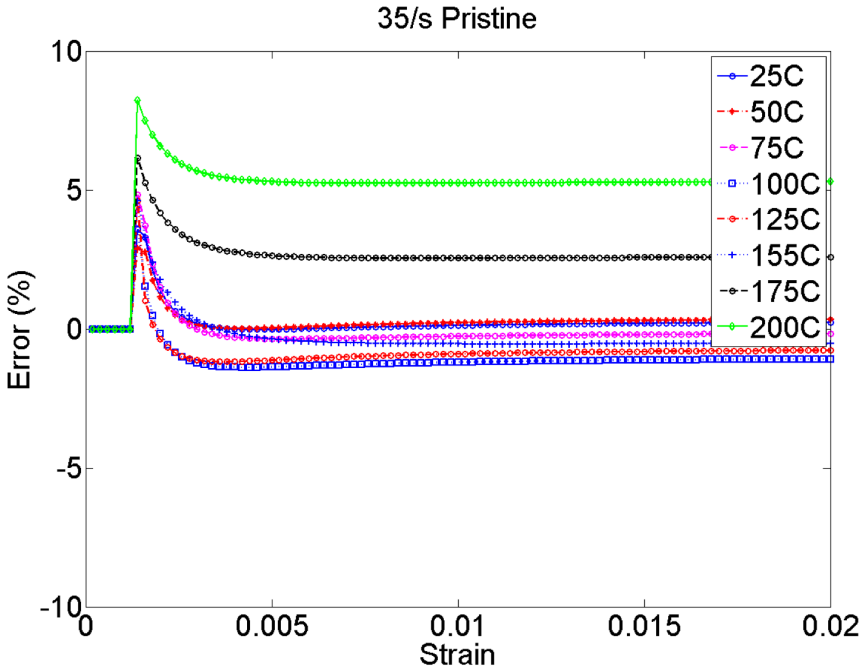

Figure 3.98: Error plot strain rate = 35/s pristine

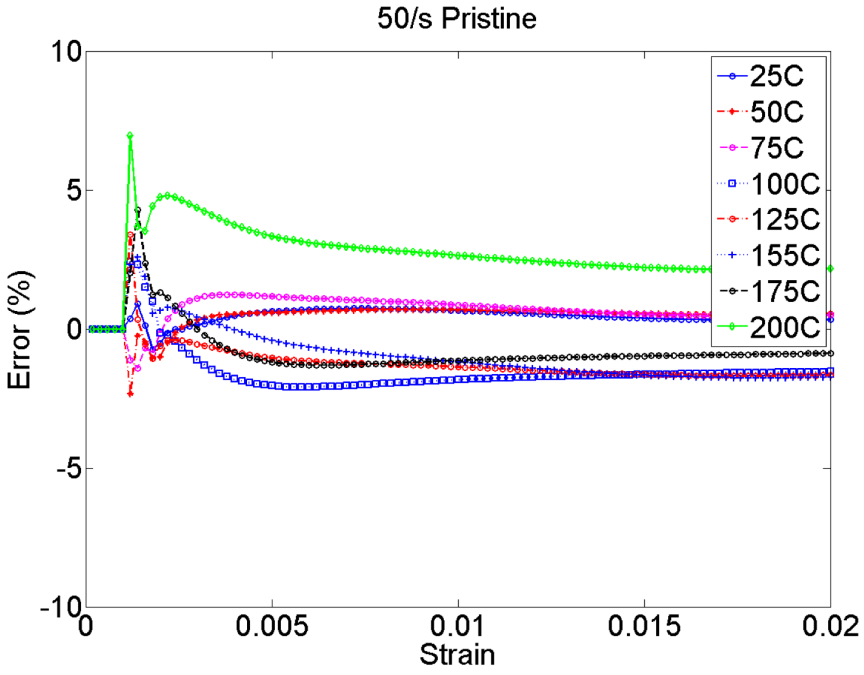

Figure 3.99: Error plot strain rate = 50/s pristine

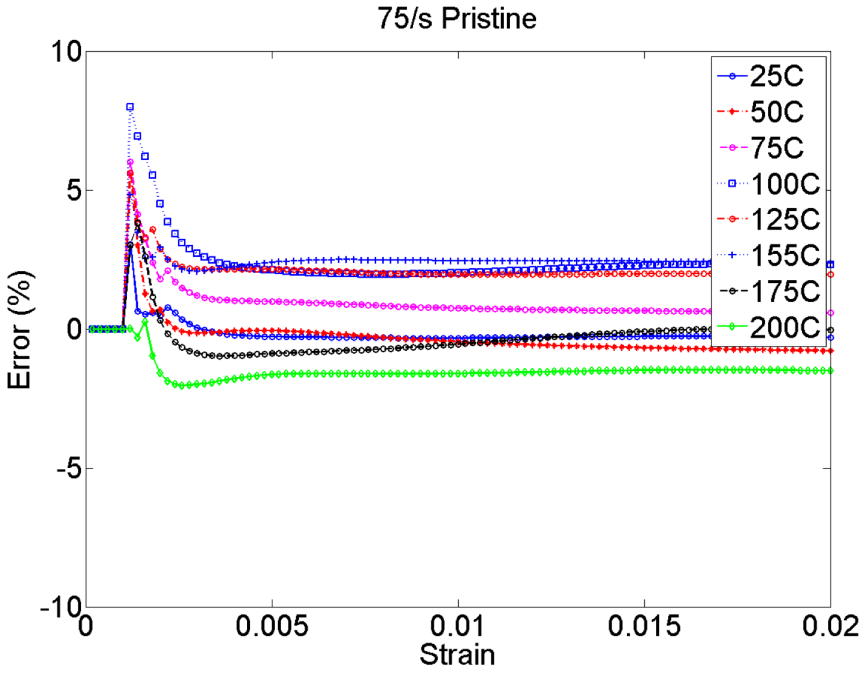

Figure 3.100: Error plot strain rate = 75/s pristine

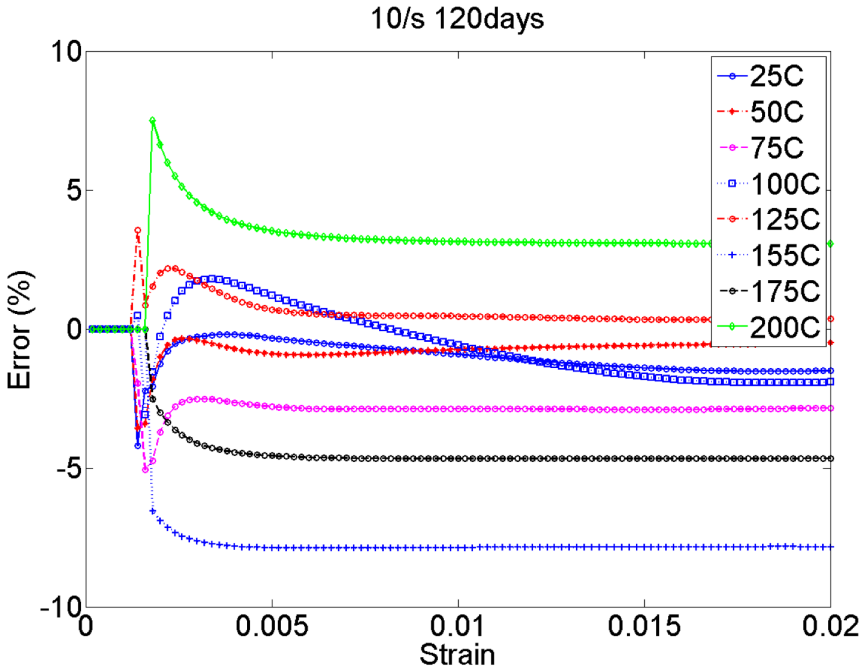

Figure 3.101: Error plot strain rate = 10/s aging 120 days at 50 °C

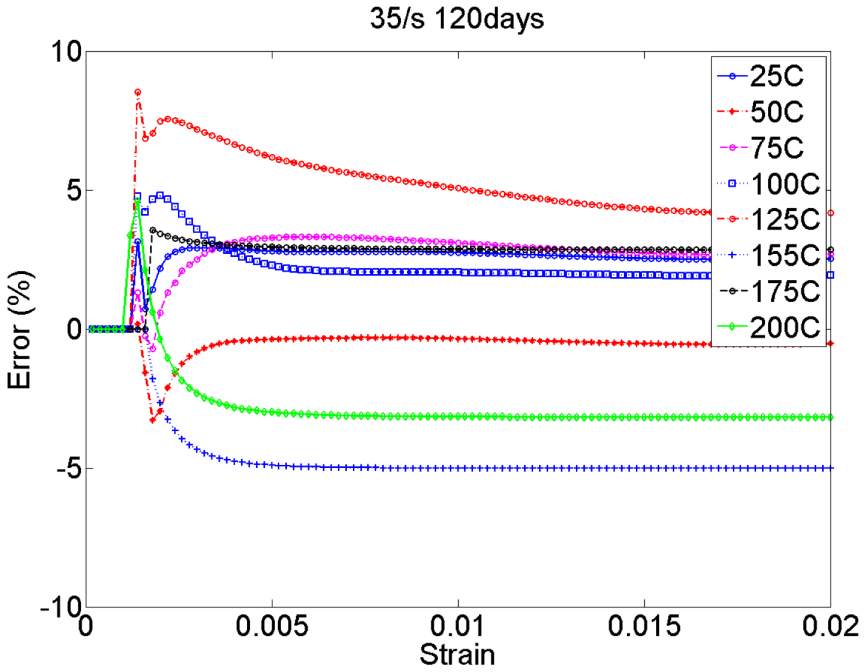

Figure 3.102: Error plot strain rate = 35/s aging 120 days at 50 °C

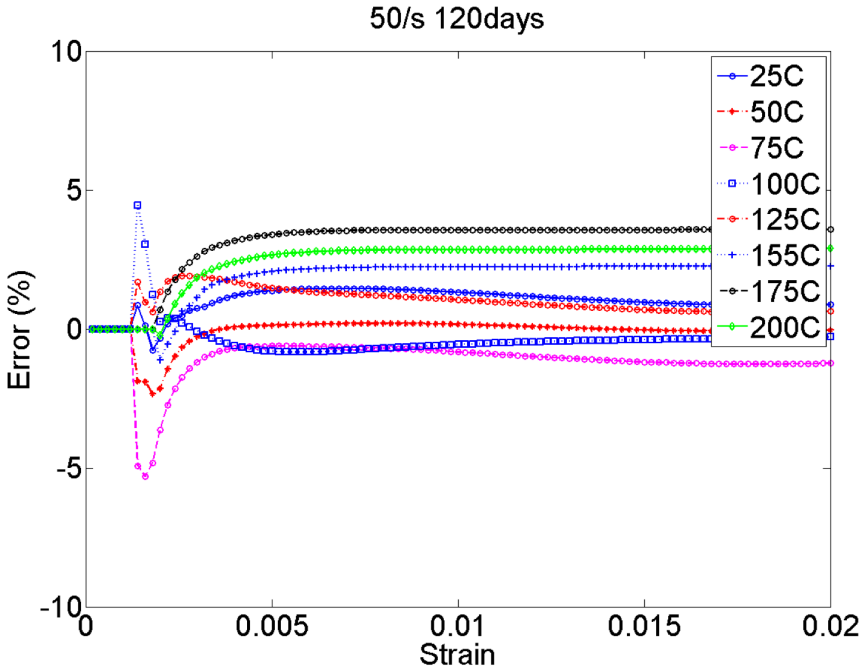

Figure 3.103: Error plot strain rate = 50/s aging 120 days at 50 °C

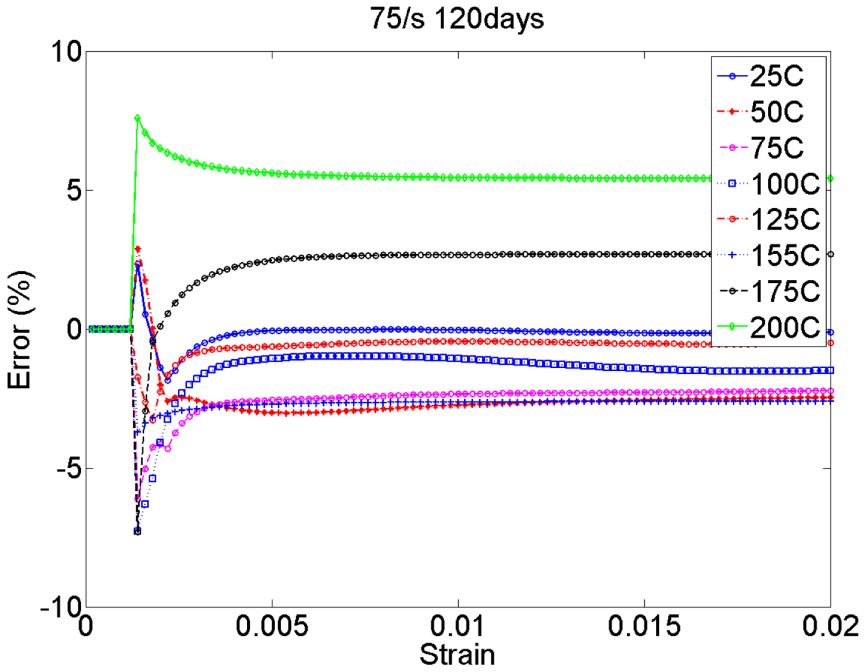

Figure 3.104: Error plot strain rate = 75/s aging 120 days at 50 °C

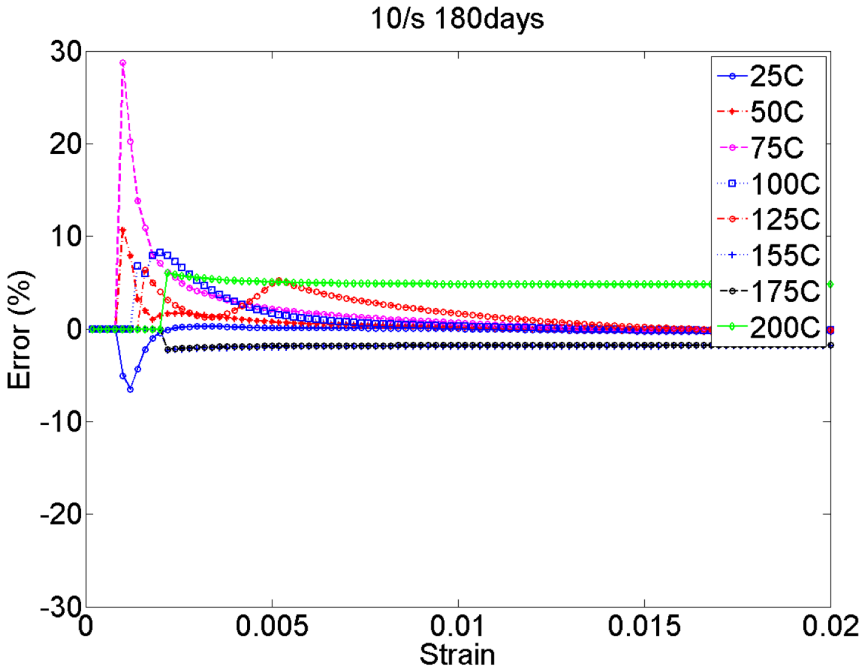

Figure 3.105: Error plot strain rate = 10/s aging 180 days at 50 °C

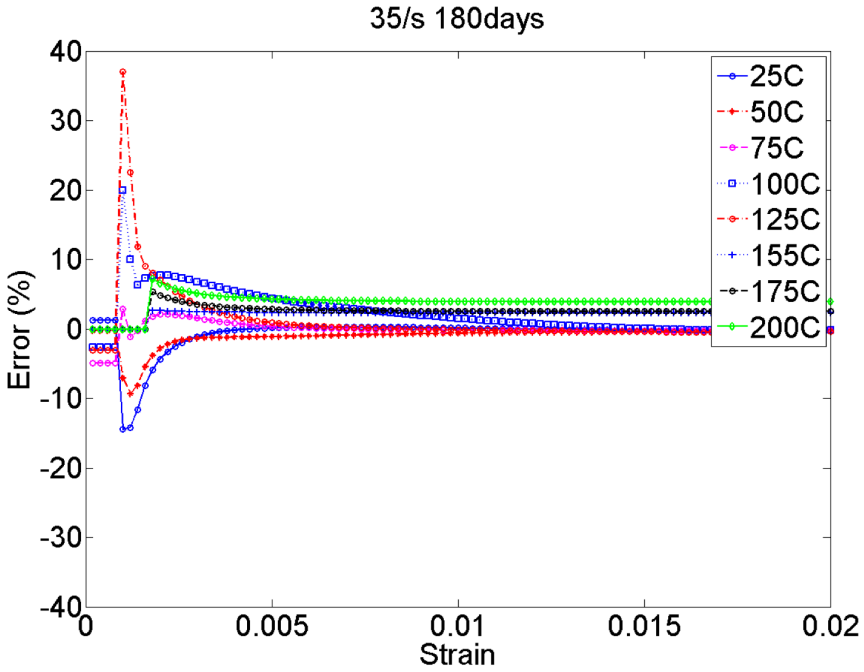

Figure 3.106: Error plot strain rate = 35/s aging 180 days at 50 °C

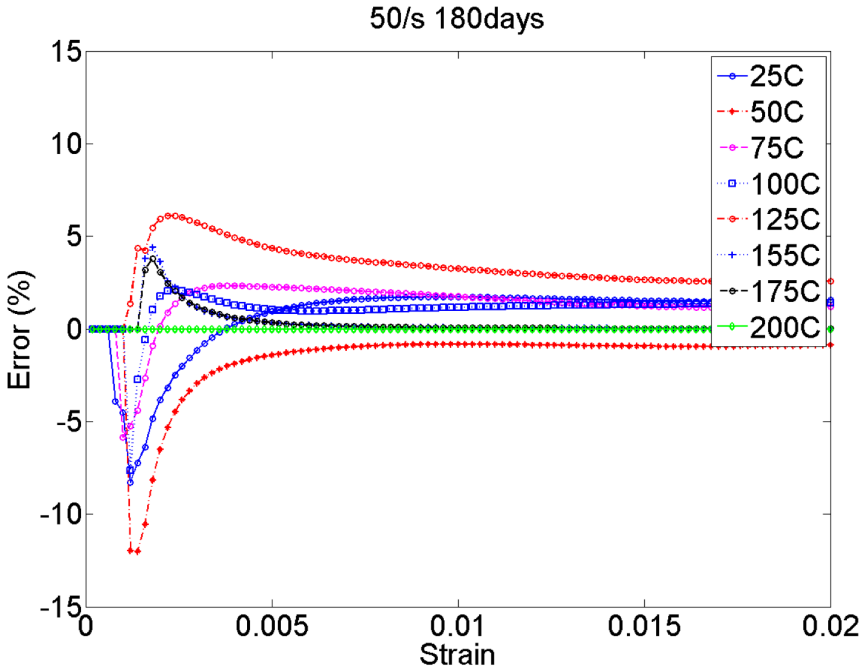

Figure 3.107: Error plot strain rate = 50/s aging 180 days at 50 °C

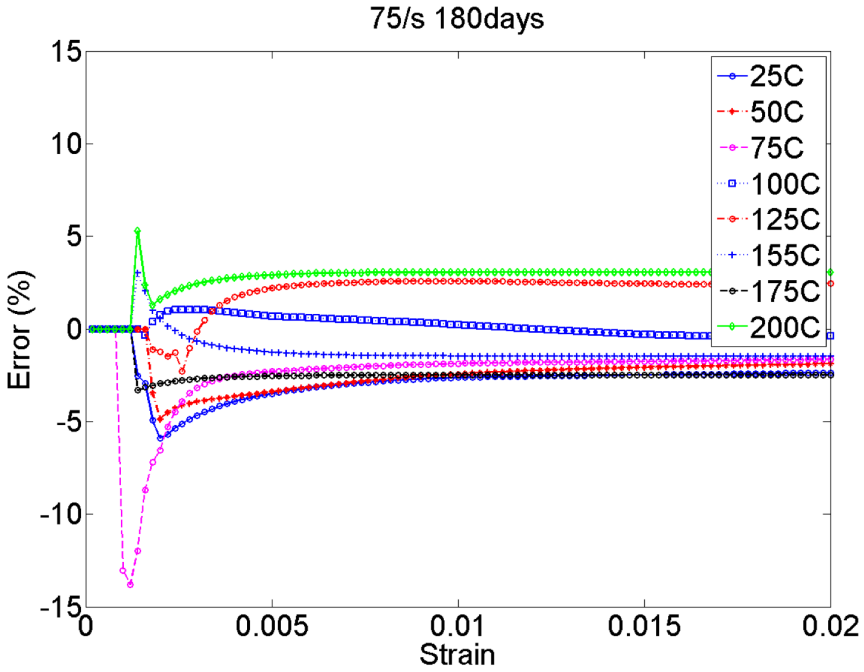

Figure 3.108: Error plot strain rate = 75/s aging 180 days at 50 °C

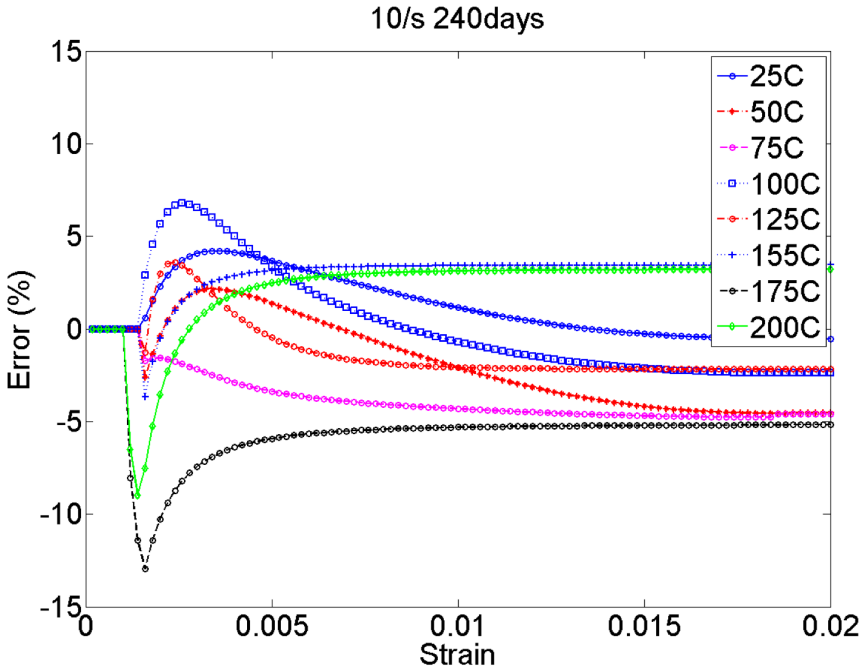

Figure 3.109: Error plot strain rate = 10/s aging 240 days at 50 °C

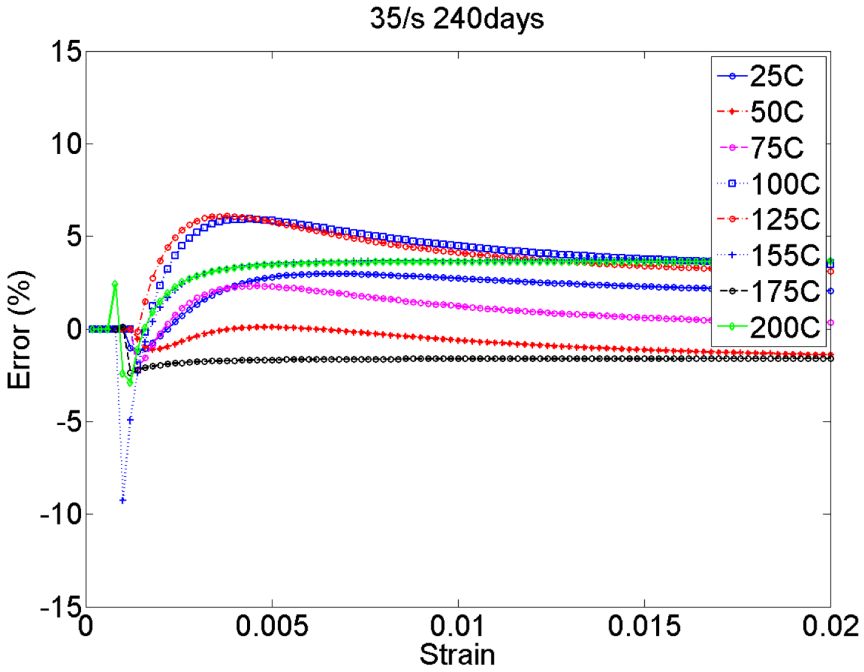

Figure 3.110: Error plot strain rate = 35/s aging 240 days at 50 °C

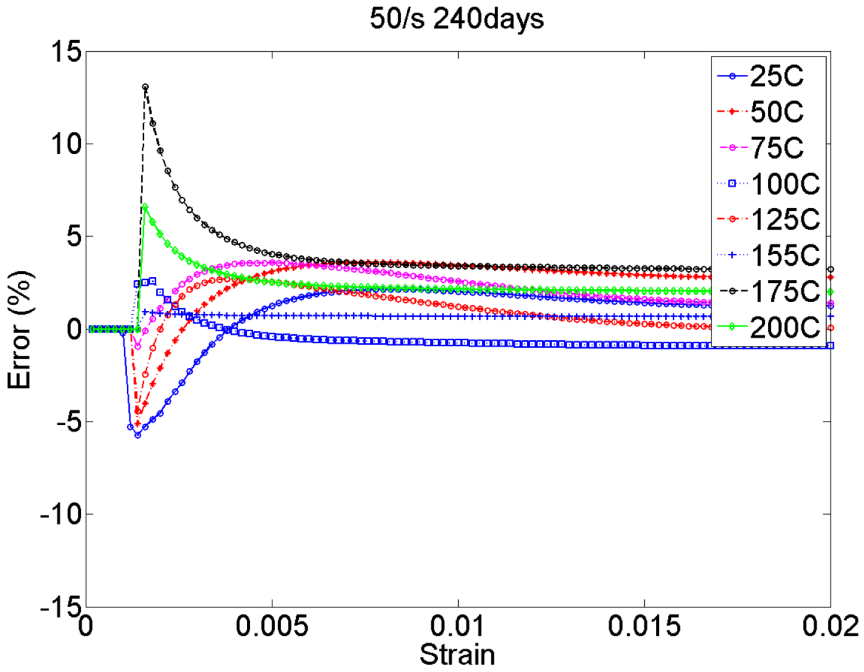

Figure 3.111: Error plot strain rate = 50/s aging 240 days at 50 °C

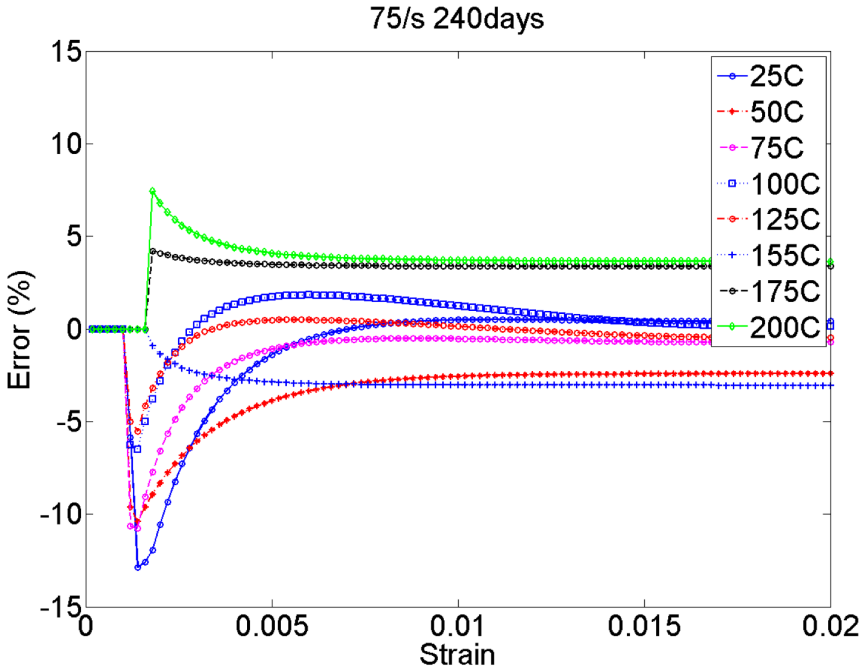

Figure 3.112: Error plot strain rate = 75/s aging 240 days at 50 °C

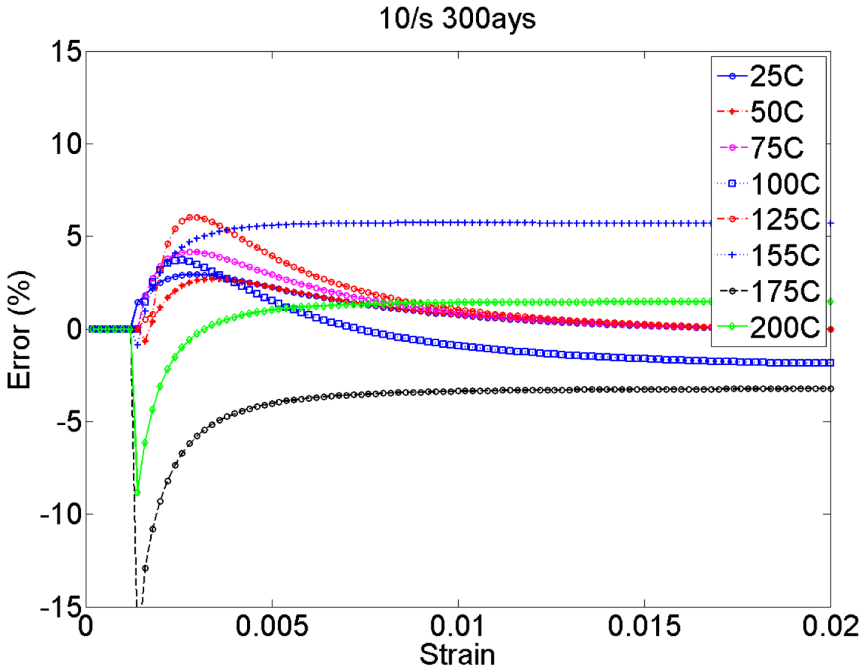

Figure 3.113: Error plot strain rate = 10/s aging 300 days at 50 °C

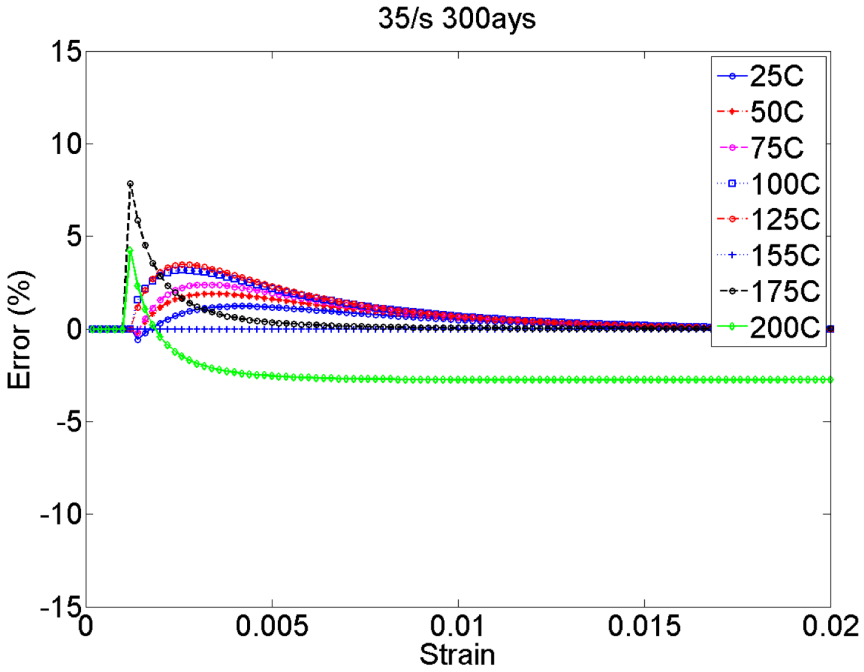

Figure 3.114: Error plot strain rate = 35/s aging 300 days at 50 °C

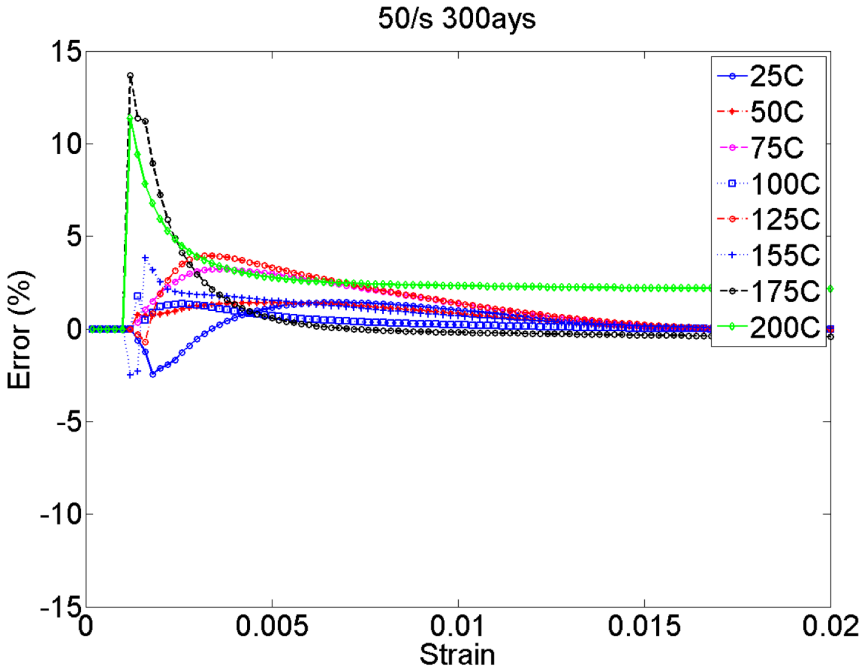

Figure 3.115: Error plot strain rate = 50/s aging 300 days at 50 °C

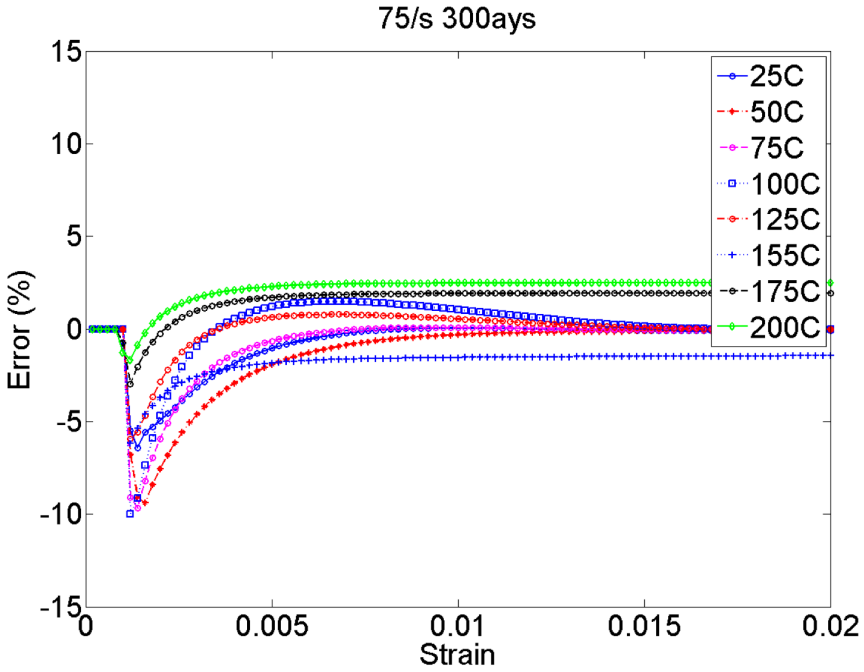

Figure 3.116: Error plot strain rate = 75/s aging 300 days at 50 °C

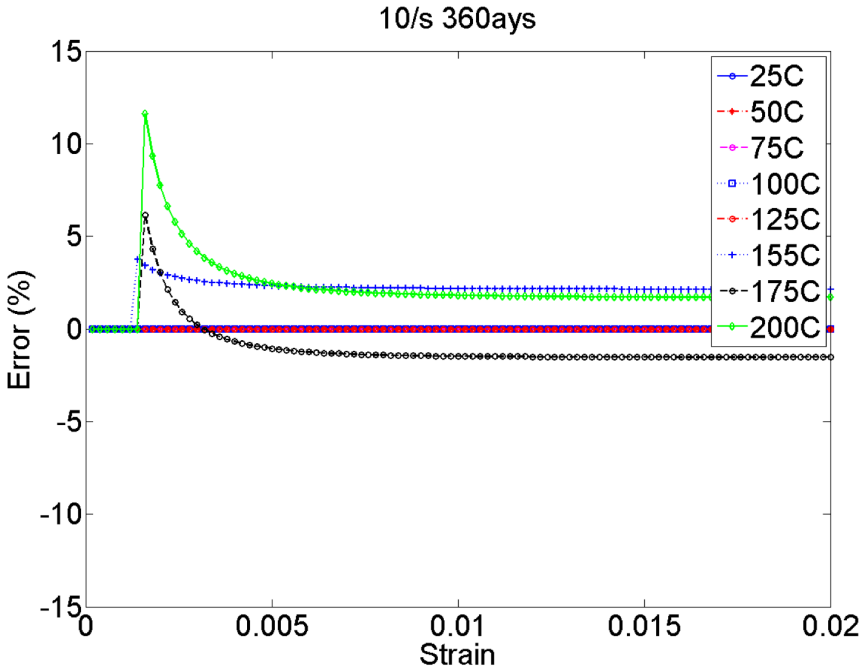

Figure 3.117: Error plot strain rate = 10/s aging 360 days at 50 °C

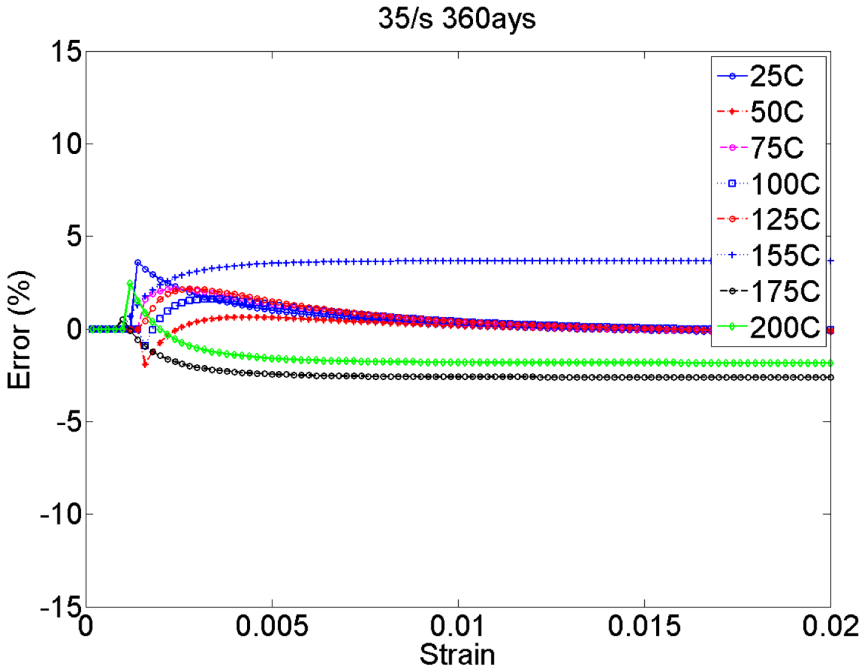

Figure 3.118: Error plot strain rate = 35/s aging 360 days at 50 °C

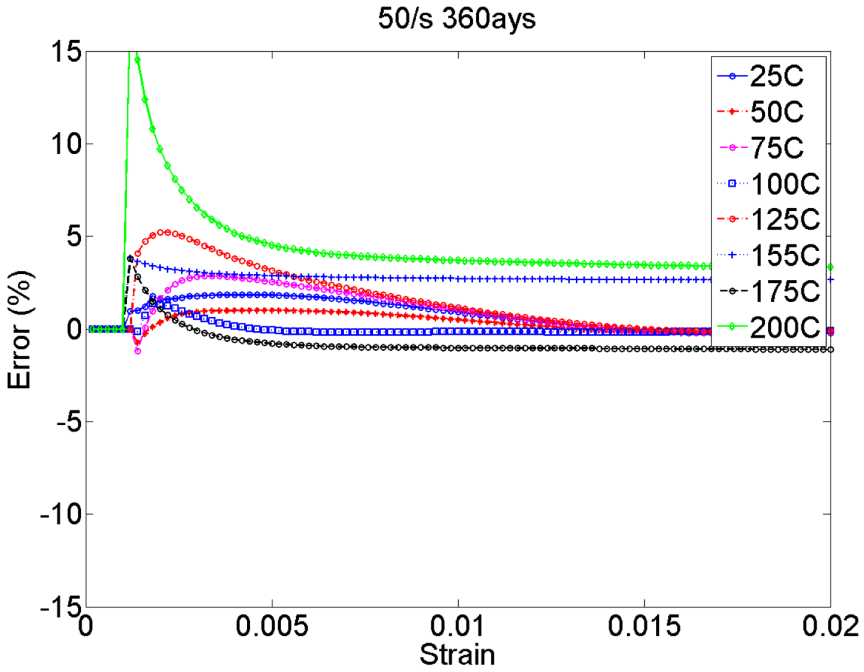

Figure 3.119: Error plot strain rate = 50/s aging 360 days at 50 °C

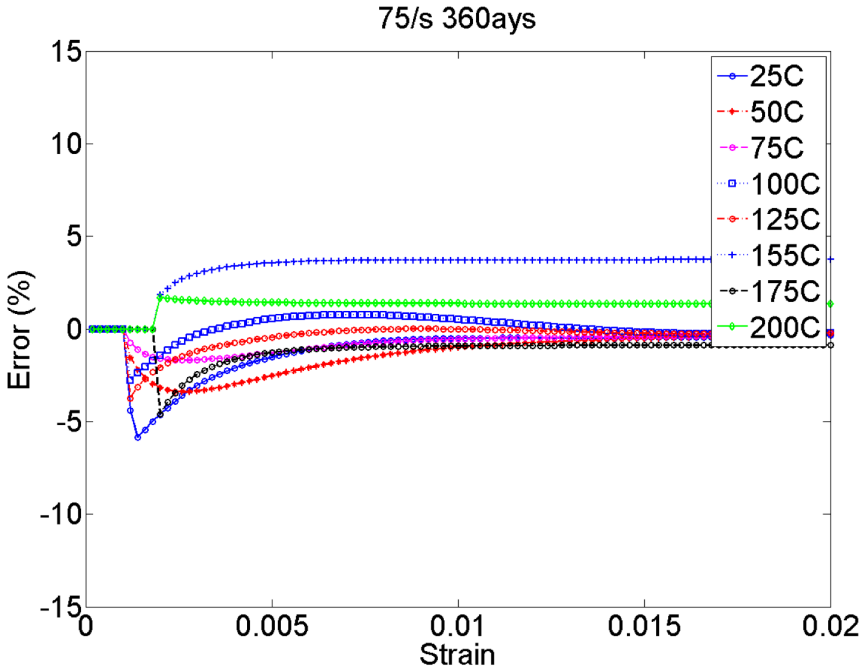

Figure 3.120: Error plot strain rate = 75/s aging 360 days at 50 °C

duration and operating temperature. Both values are increased with larger deformation rate. Various groups of Anand model have been computed and verified at different aging period. Effect of aging on evolution of Anand constants are also studied.

Chapter 4

Applying Anand Model to Board Level Drop Testing

4.1 Introduction to Drop Testing

Electronic products such as smart phone, tablet, personal computer have been populated in recent years, those devices maybe accidentally fall on the ground during normal usage. Therefore, understanding the reliability performance of those devices during impact is very necessary. Previously, JEDEC has published a drop test standard JESD22-B111 [4]. This standard has standardized the test procedures and test conditions. Since board level drop test is a key qualification test for portable electronic devices, lots of researchers have been interested in both experiment and simulation. Since solder joint is one of the weakest link in electronic products, it is important to quantify the stress and strain amplitude of solder joint during drop and shock. However, there is lacking of method to measure the stress and strain of solder joint experimentally, because the pitch size and solder ball is very small. Simulation is a way to approximate the stress and strain values of interconnects during transient deformation. In the literature, the Anand model have been widely used in thermal cycling simulation to characterize the mechanical properties of solder alloys. But it is barely used in drop and shock simulation. In this study, Input-G method with implicit solver was used to simulate the drop test. The Anand model was used to describe the constitutive behavior of lead free solder and compare with linear material. 3-D DIC was used to measure the dynamic full field response of PCB during drop test at different G-level. Further, experimental data was used to compare with simulation results at drop condition of 1500G and 0.5ms. Hysteresis loop and plastic work density were also extracted to evaluate damage to solder joint per impact.

4.1.1 Experimental Method

Figure 4.1 shows a typical setup of drop test. Commercial drop tower is available in the market which enable a repeatable test environment. All the boards mounted on the drop tower must follow a JEDEC dimension and the packages have to be facing down during testing. During the test, the shock pulse is measured by an accelerometer which attached on the base plate, as shown in Figure 4.1. There are two parameters, one is peak acceleration which is decided by drop height. The other is the impact duration which is decided by the matt stiffness and thickness. The more drop height, the higher peak acceleration will be. The thicker of the matt material, the longer the impact duration will be. For the impact pulse, the peak acceleration is 1500 G and impact duration is 0.5 ms. Strain gauges have been used by lots of researchers to measure in-plane strain of PCB during deformation. Other than this method, 3D-DIC is also used by researchers because its easy implementation and capability of capturing large deformation in such a transient time. Lall [18] have used 3D-DIC in-conjunction with strain gauge method to measure in-plane strain.

4.1.2 Method of Simulating Drop Test

Previously, many researchers have carried out different simulation technique to simulate drop test. One of these methods is free fall modeling with explicit solver. Lall ([19] [18] [21]) has carried out board-level free drop modeling using the smeared properties with explicit solver and validated the simulation results with experimental data. Another method is modeling with input acceleration to the board. Tee [23] has introduced the Input-G method to investigate the dynamic response of PCB and stress distribution of critical solder joint during drop and shock event with explicit solver. He also used implicit solver to study board level drop test simulation with input-D method. Meanwhile, Syed [22] has used input-force method to simulate the drop event to investigate the transient deformation of PCB and solder joint.

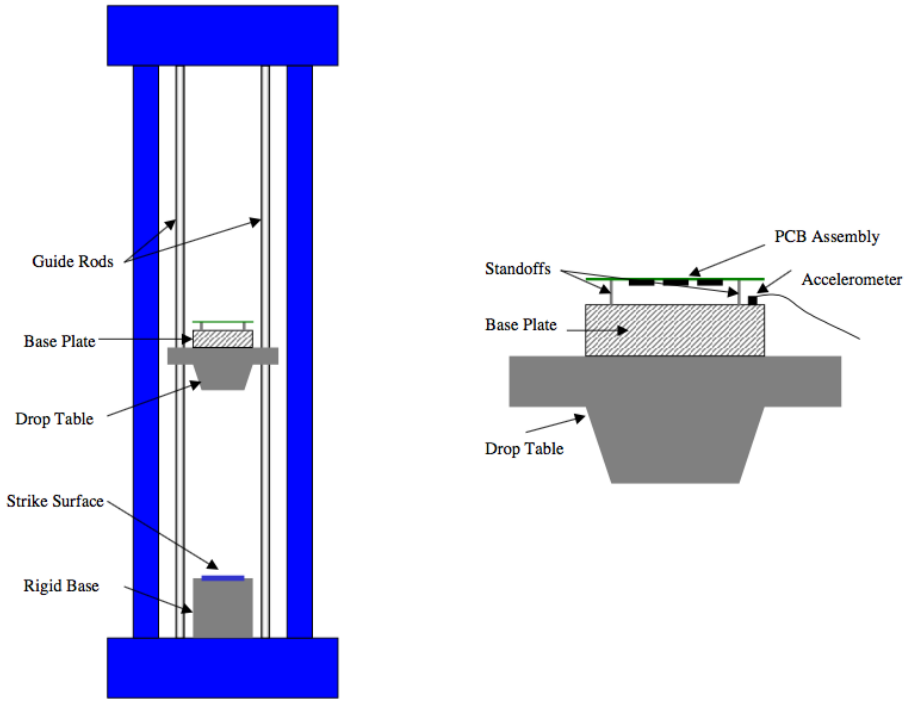

Figure 4.1: Typical drop test apparatus and mounting scheme for PCB assembly

4.1.3 Applying Anand Model to Drop Testing

Solder joint cracking is one of the dominant failure mechanism in electronic devices which subjected to shock and drop environment. Due to functional density increased in portable electronic devices, larger amount of I/O pitches are need. Therefore, the possibility of the package failed will be increased. Solder joint failure occurs due to a combination of PCB bending and mechanical shock during impact. However, experimental drop tests that require much man power in measurement and data analysis are expensive and time-consuming. Meanwhile, due to lacking of method of measuring strain and stress of solder ball during transient deformation event, it is hard to analyze the reliability of solder joint. Therefore, simulation has been considered as a more efficient tool in electronic packaging for design and optimization comparing with actual drop test. In order to better to calculate stress of critical solder joint, an accurate constitutive model is needed. Anand model which is available in ANSYS APDL, has been use by lots of researchers to represent mechanical

Figure 4.2: Test Board PBGA324

properties of solder joint during deformation. Lots of researchers have included it to simulate thermal cycling event, however only few researchers have it applied to transient deformation such as shock and vibration event.

In this study, 3-D DIC was used to measure the dynamic full field response of PCB during drop test at different G-level. Input-G method with implicit solver was used to simulate the drop test. The Anand model was used to describe the constitutive behavior of lead free solder and compared with linear material. Further, experimental data was used to compare with simulation results at drop condition of 1500G and 0.5ms.

4.2 Test Vehicle

Test-board (Figure 4.2) has the dimension 132mm x 77mm x 1.5mm with one PBGA package mounted at the center. The package has 324 I/O count and a pitch of 1mm, as shown Figure 4.3. Other dimensions of the PBGA have been list in Table 4.1. This board has a unique 4 quadrant continuity design as shown in Figure 4.4. The purpose of this continuity design is to track the in-situ failure location within the package with respect to time as the varying quantity.

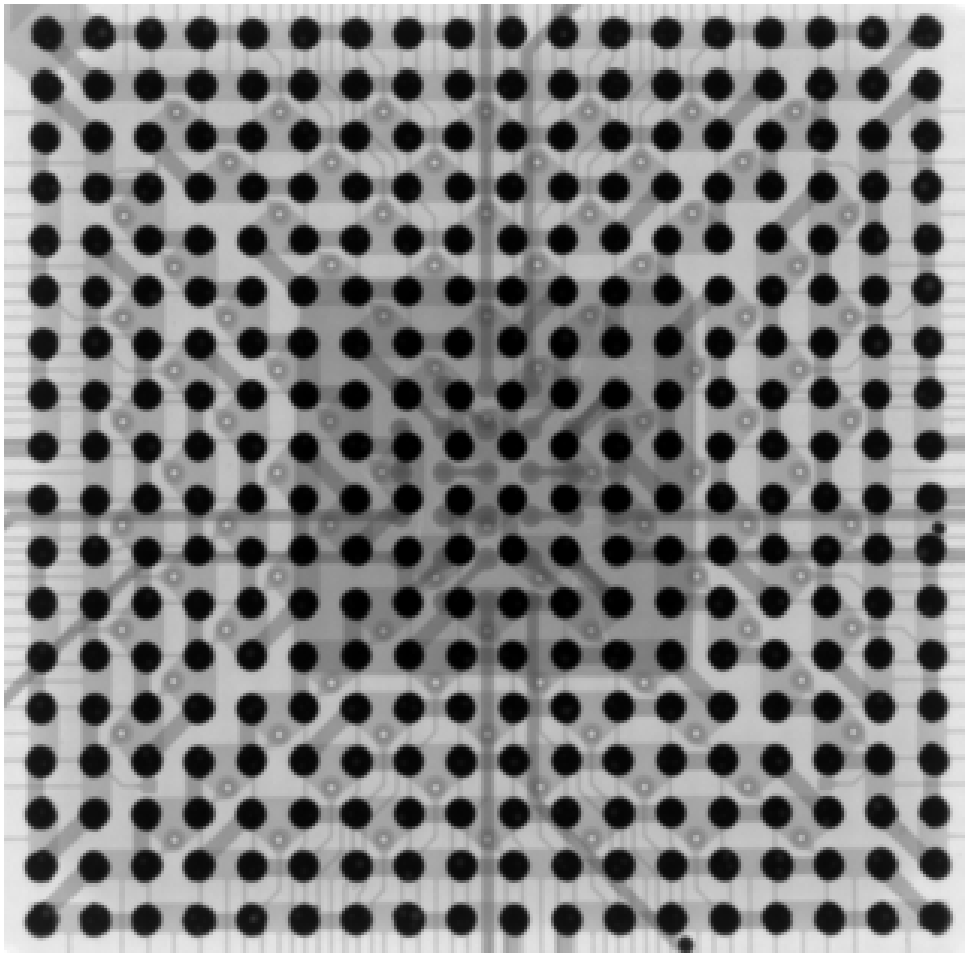

Figure 4.3: X-ray PBGA324

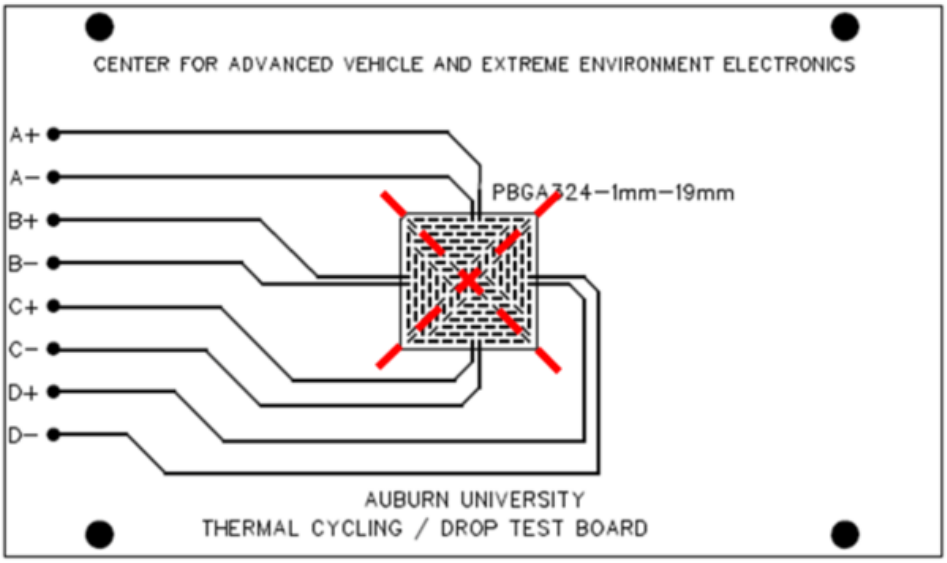

Figure 4.4: Continuity design for PBGA324

Table 4.1: Attributes of PBGA324

I/O Count	324
I/O Pitch	1mm
Body Size	19mm
Ball Matrix	18x18
Ball Alignment	Full Array
Package Type	PBGA
Board Finish	ImAg
Substrate Pad Type	SMD
Solder Ball Material	Sn3Ag0.5Cu
Substrate Pad Die	0.45mm
Ball Diameter	0.4mm
Mold Cap Thickness	1.17mm

4.3 Experimental Setup

The Lansmont Model-23 drop tower has been used for the drop tests. As shown in Figure 4.5. Figure 4.6 shows schematic setup of whole drop testing system. An accelerometer of sensitivity 0.103mv/g attached to the drop tower base was used to attained desired G-level. Proper pulse shape has been achieved through adjusting both the drop height and pulse shaping material between the two surfaces. Previously, Lall ([21], [20]) have successfully tested assemblies subjected to 1500g, half millisecond pulses in accordance with the JESD22-B111 test standard.

4.4 Digital Image Correlation (DIC)

Two High speed cameras running with 15,000 frame/s have been used to record the deformation of speckle patterned PCB during drop test. 3D DIC method was used to analyze full field out-of-plain displacement and in-plain strain. Figure 4.7 shows the high speed camera setup with its controller. In order to achieve higher frame rate, most of time additional light is needed. Figure 4.9 shows the actual camera setup with extra light. The tested printed circuit board should be speckle patterned before taking high speed video. Figure 4.10 shows sample picture before measurement.Two high speed cameras are necessary

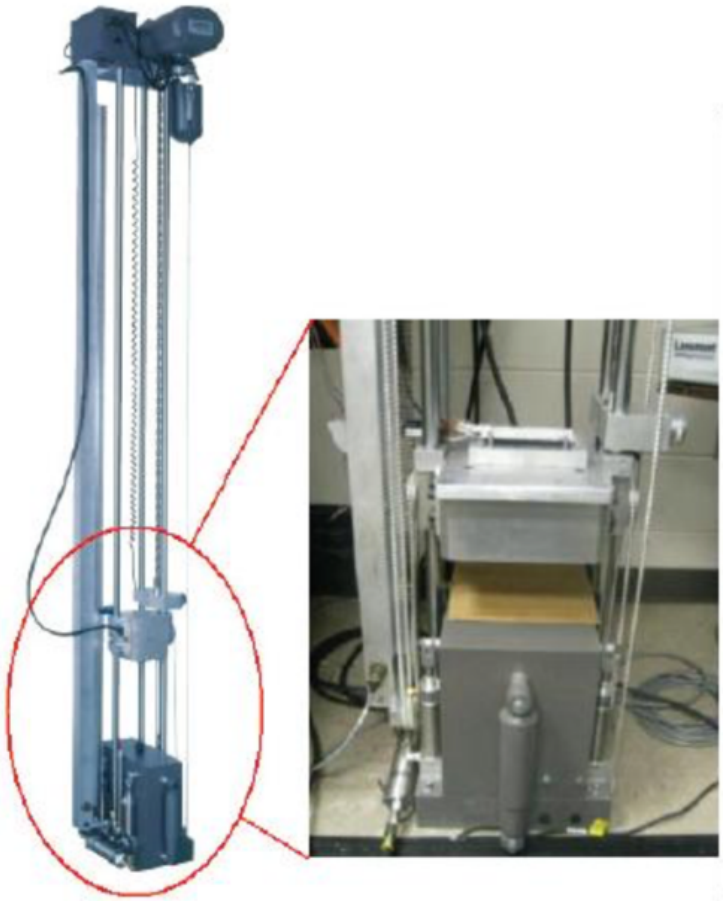

Figure 4.5: Lansmont Model-23

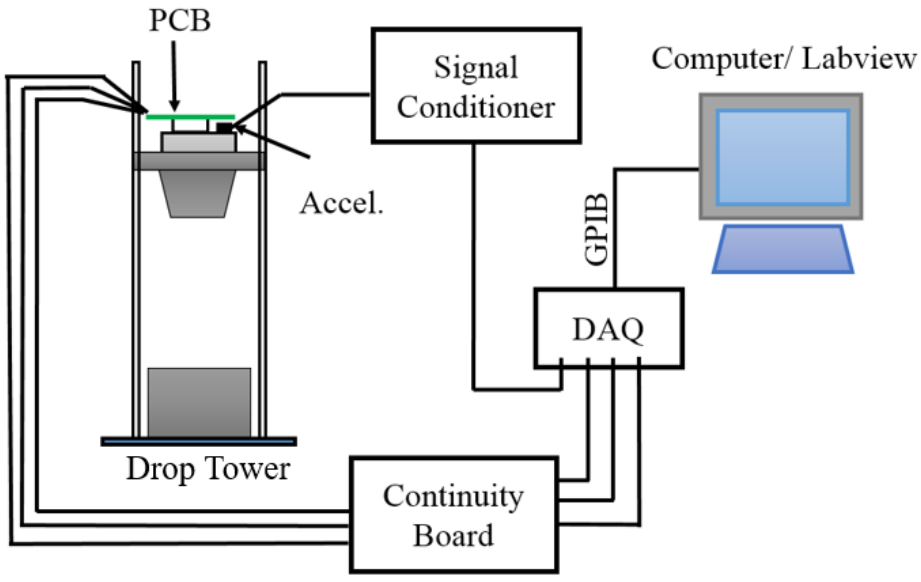

Figure 4.6: Drop testing system

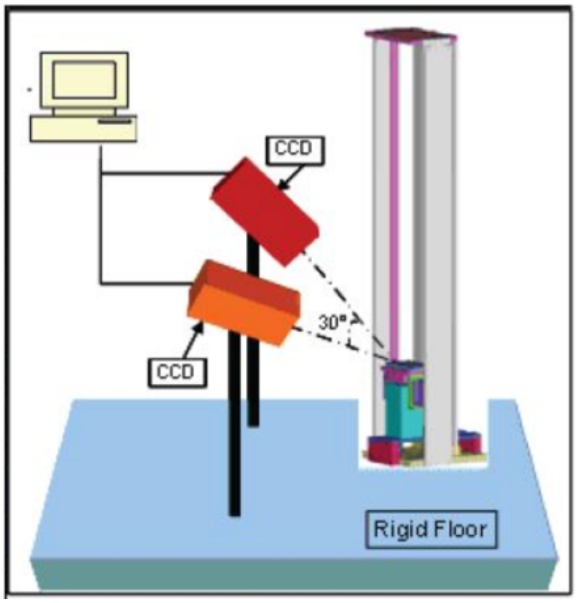

Figure 4.7: Schematic setup of two high speed camera

to perform 3-D DIC measurement. Figure 4.10 and Figure 4.11 show the views of board from two cameras respectively.

Previously, Lall ([39] [40] [17] [3]) has used 3D DIC to measure full field strain and displacement of PCB during drop and shock event. High speed videos have been captured using two high speed cameras. Figure 4.8 shows the basic principle of DIC analysis. In order to calculate the displacement field, the deformed images are compared with the reference image. Since a single pixel is not a unique signature of a point hence a neighboring pixels are used. The collection of pixels are called a subset. Uniqueness of the pattern has been assured by using a non-repetitive random high-contrast speckle pattern. A subset of pixels around a reference pixel O in the reference image has been compared with the subset corresponding to pixels in the deformed image using a predefined correlation function to describe the difference of the two digital sub images. Deformation of the subset during transient deformation has been accomplished through displacement mapping using a subset shape function. The subset has been stepped through the image to measure the displacement of the complete board assembly. An algorithm based on the mutual correlation coefficient or other statistical functions are used to correlate the change in a reference pixel in the original image and the

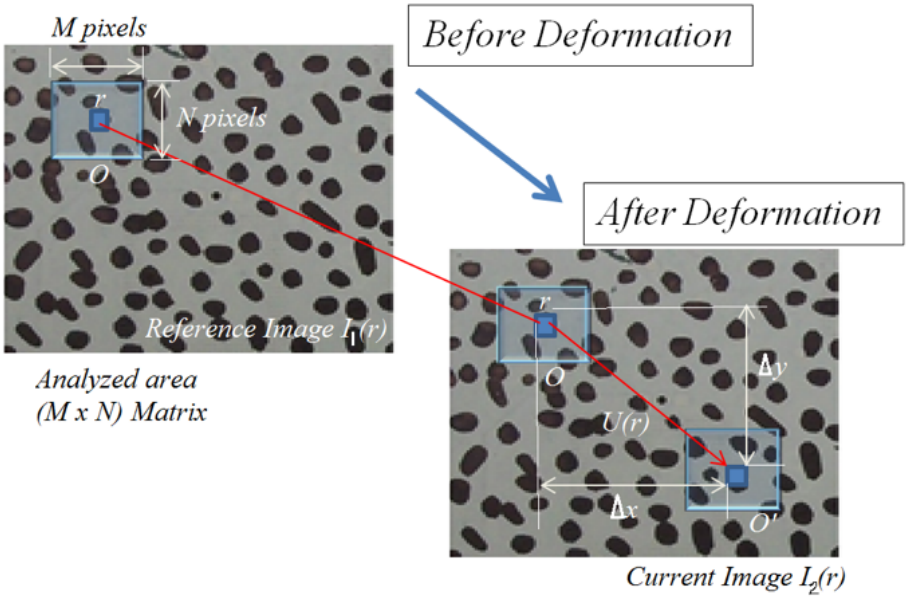

Figure 4.8: Digital Image Correlation Principle

corresponding reference pixel in the deformed image. Three such typical correlations include absolute difference, least square and cross correlation. There are three typical correlation functions which are used and are defined as follows:

Absolute Difference:

$$C_A\left(r'\right) = 1 - \frac{\iint_\Omega \left|I_2\left(r + r'\right) - I_1\left(r\right)\right| \cdot dr}{\iint_\Omega I_1\left(r\right) \cdot dr} \tag{4.1}$$

Least Square

$$C_L\left(r'\right) = 1 - \frac{\iint_\Omega \left[I_2\left(r + r'\right) - I_1\left(r\right)\right]^2 \cdot dr}{\iint_\Omega I_1^2\left(r\right) \cdot dr} \tag{4.2}$$

Cross-Correlation

$$C_C\left(r'\right) = 1 - \frac{\iint_\Omega I_2\left(r + r'\right) \cdot I_1\left(r\right) \cdot dr}{\left[\iint_\Omega I_1^2\left(r\right) \cdot dr \cdot \iint_\Omega I_2^2\left(r\right) \cdot dr\right]^{\frac{1}{2}}} \tag{4.3}$$

where I_1 and I_2 are the original and the deformed images, Ω(M x N) is the area of the sub image around reference pixel r, r' is the current pixel, $C_A(r')$ is the current absolute

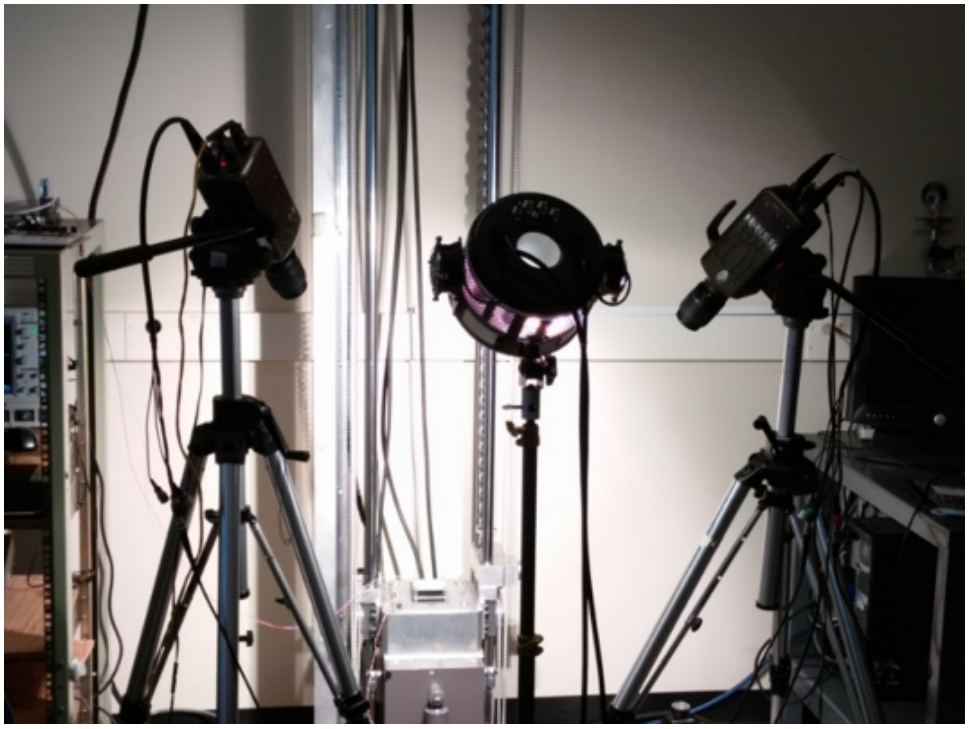

Figure 4.9: High speed camera setup

correlation function, $C_L(r')$ is the current least square correlation function, and $C_C(r')$ is the current cross correlation function.

4.5 Finite Element Analysis of Drop Testing

4.5.1 Meshed Geometry

The solid geometry of PBGA324 is first created in Pro-E and then loaded to Hypermesh. All the solid geometry are mesh part by part. Figure 4.12 and Figure 4.13 show the different view of PBGA324 on a PCB. In order to achieve more accurate results, this finite element model is made without any symmetric geometry assumption. Totally 625740 elements and 697300 nodes are created. Due to computational efficiency, only four corner solder balls have been made with solid elements. Beside the conner solder balls, others are replaced by Timoshenko-beam element. In this way, we can understand the deformation and stress distribution of corner solder joint without too much computation time. Figure 4.13 shows the

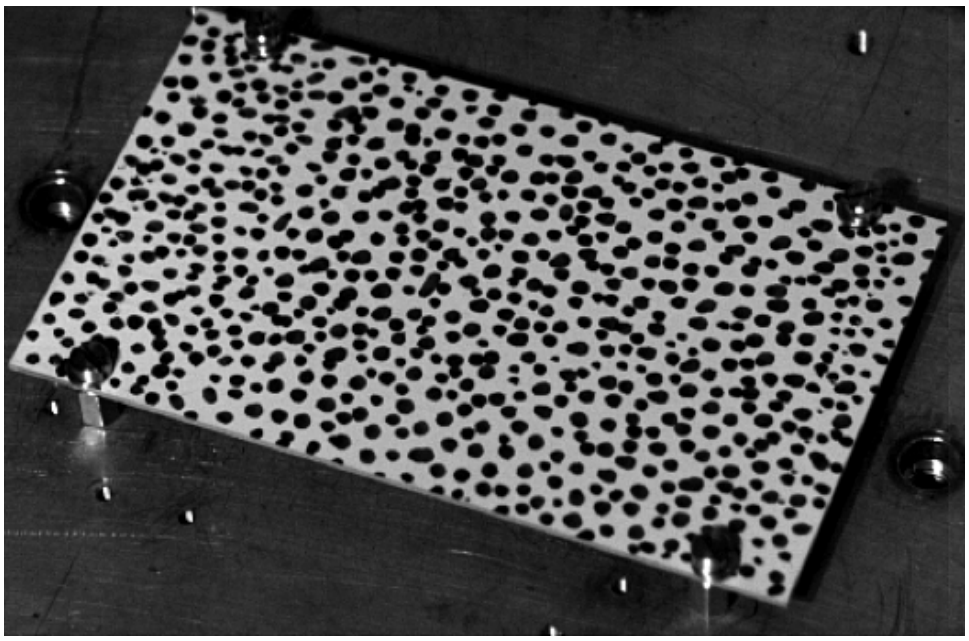

Figure 4.10: View from left high speed camera

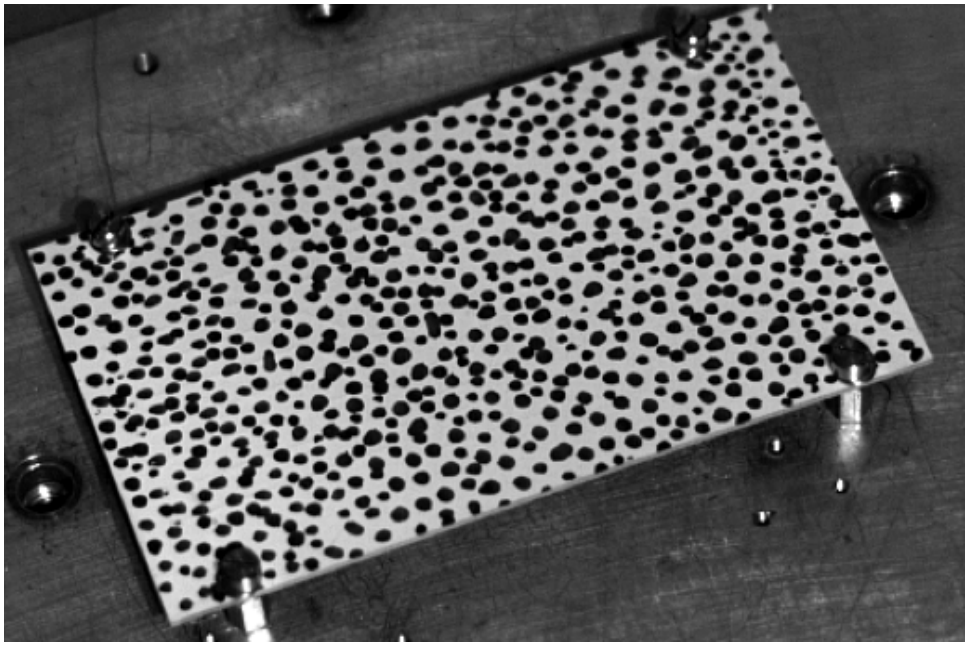

Figure 4.11: View from right high speed camera

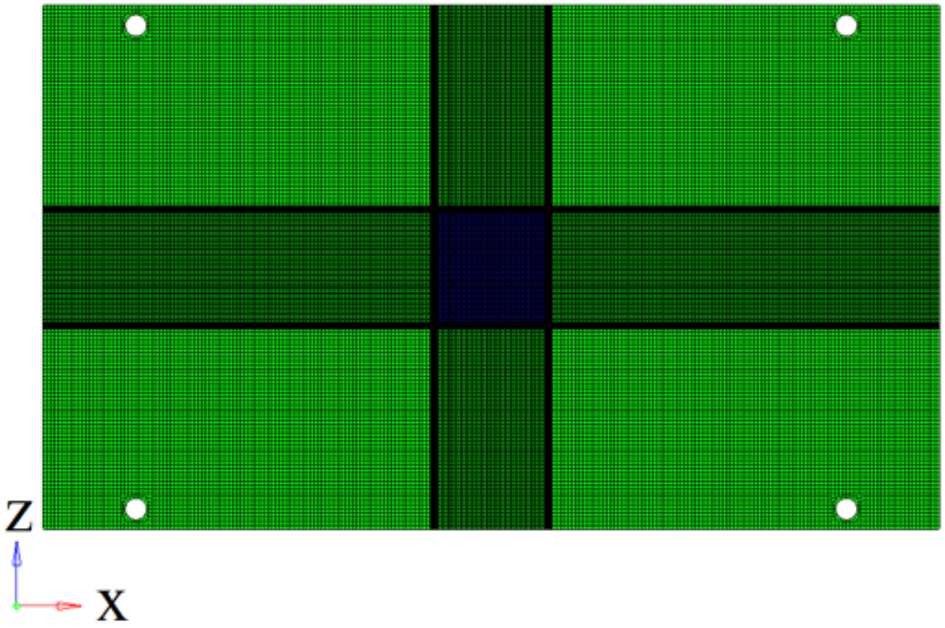

Figure 4.12: Top view of meshed PBGA324

cut-section of PBGA324. The package is modeled with substrate, mold compound, silicon die, adhesive.

4.5.2 Element Types

Totally four types of element have been used to build this model, as shown in 5.1. Two types of element have been used in modeling interconnections. One is VISCO107 which is defined by eight nodes having three degrees of freedom at each node (translations in the nodal x, y and z directions). The element is designed to solve both isotropic rate-independent and rate-dependent large strain plasticity problems. The other is Beam188 which is based on Timoshenko beam theory and includes shear-deformation effects. BEAM188 has six or seven degrees of freedom at each node. These include translations in the x, y, and z directions and rotations about the x, y, and z directions. Besides the interconnection part, others are made of SOLID45, which is used for the 3-D modeling of solid structures. The element is defined by eight nodes having three degrees of freedom at each node: translations in the nodal x,

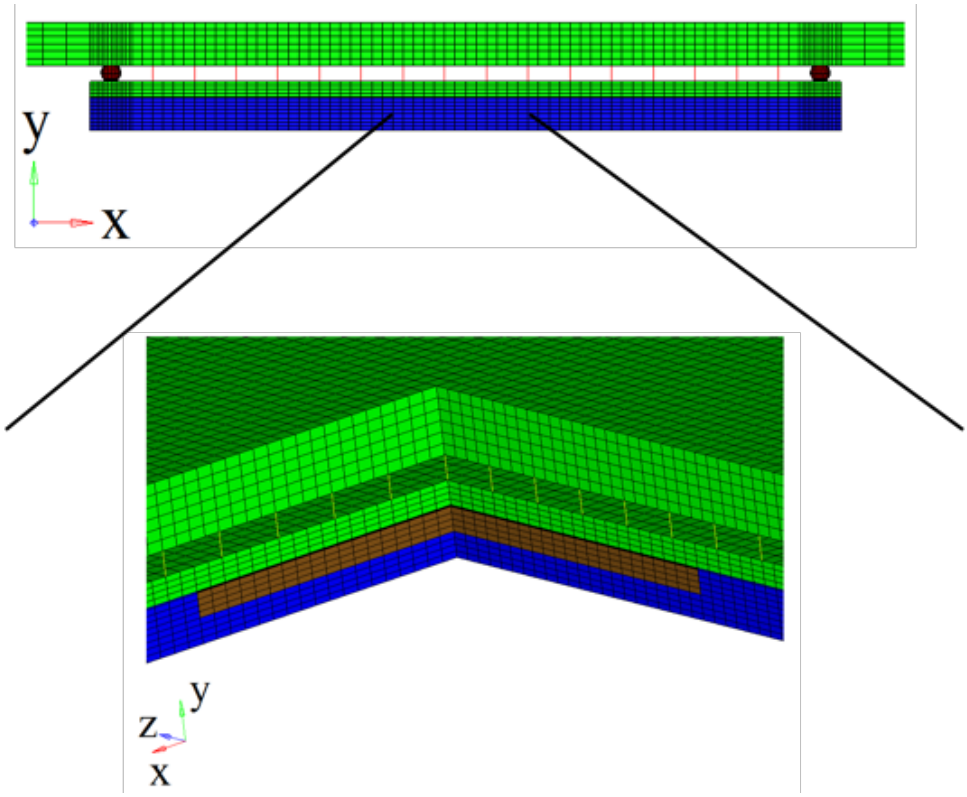

Figure 4.13: Front view of meshed PBGA324

y, and z directions. Mass Element was created at screw holes of PCB where the boundary conditions were applied.

4.5.3 Material Properties

Previously, lots of researchers have used Anand model [13] to characterized the constitutive behavior of solder alloys. This constitutive law has been used by researchers to develop the damage relationship (Darveaux [14], Motalab [6], Basit [15]). In the last chapter, the high rate mechanical properties of SAC305 at high temperature have been discussed. The Anand model which used to describe constitutive behavior of solder has been formulated. Other material such as mold compound, silicon die, die attach, die attach, BT substrate and copper pad are modeled as liner material. PCB are characterized as orthotropic material(Lall [18]). The detail values have been listed in Table 4.3.

Table 4.2: Elements of PBGA324

Board Assembly	Element Type
PCB	SOLID45
Copper Pad	SOLID45
Mold Compound	SOLID45
Silicon Die	SOLID45
Die Attach	SOLID45
BT substrate	SOLID45
Solder Joints	VISCO107
Solder Beams	BEAM188
Mass Element	MASS21

Table 4.3: Material Properties of Package Assembly

Package Assembly	Elastic Modulus(MPa)	Poisson's Ratio	Density (tonne/mmˆ3)
Solder Jonits	42000	0.34	8.40E-09
Mold Compound	23500	0.25	1.65E-09
Silcon Die	162000	0.28	2.33E-09
Die Attach	2760	0.35	7.80E-09
BT Substrate	17400	0.28	1.80E-09
Copper Pad	129000	0.34	8.82E-09
PCB	20800	0.39	1.80E-09
	20800	0.39	
	9000	0.11	

4.5.4 Boundary Conditions

Input-G method with Anand model has been used to analyze board-level drop test event. However, unlike ANSYS Ls-dyna (explicit solver without Anand model), the acceleration degree of freedom is not available in implicit solver. Some researchers have come out with a few ideas to solve this problem. Previously, Syed [22] has used input-force method to simulate the drop event. In this method, a large mass element is attached to the nodes around the screw holes using rigid elements. The acceleration input which is compulsorily monitored by oscilloscope following the JEDEC standard. By multiplying the acceleration with a large mass, the input-force at the large mass node can be achieved. In this study, the simulation board is subjected to JEDEC standard with specified 1500G and 0.5ms. As shown in Figure 4.14. This acceleration plot is converted to force data by multiplying a large mass. The mass of this mass element is typically five orders of magnitude higher than the total mass of board assembly including packages. A force tabular data changing with time was generated and those data points were input as boundary condition to the mass element in order to get desired acceleration output as shown in Figure 4.14. Furthermore, in order to satisfy connection between BEAM188 and SOLID elements, all the Timoshenko-beam elements need to be fixed at three rotational degree of freedom.

4.6 Experimental Measurement

Due to the inertia effect, the PCB subjected to drop test will move up and down. This causes the corner solder joints suffered tension and compression, as shown in Figure 4.15. Crack will be happened to solder joint, due to the effect of fatigue and impact loading. Therefore the deflection of PCB and contact load has a great impact on the reliability of solder joints. Figure 4.16 and Figure 4.17 show the maximum downward and upward displacement field of PCB from experiment. Based on 3D-DIC measurements, the peak downward and upward deflection happened at the center of the board and the peak amplitudes are around

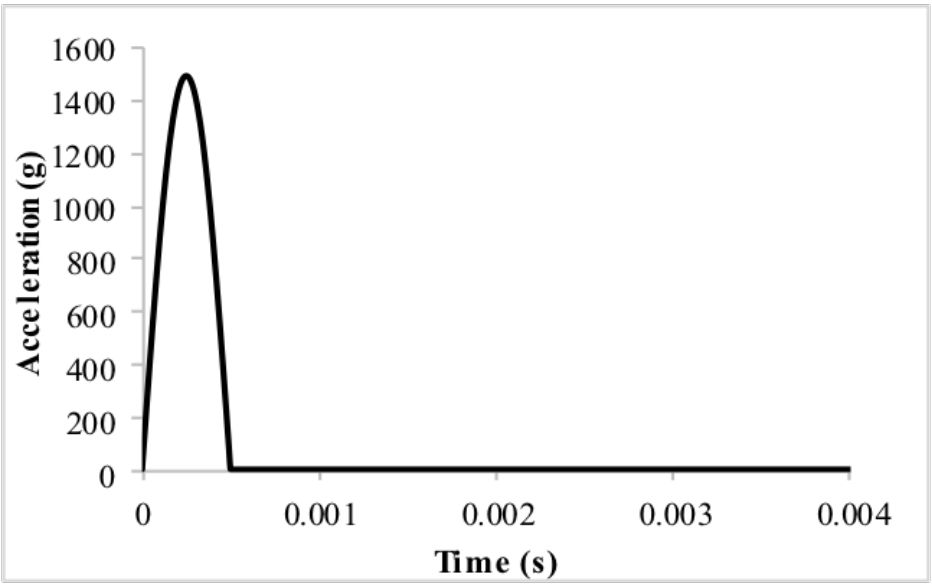

Figure 4.14: Desired Input Acceleration

3mm. Figure 4.20 shows the relative displacement history plot at center of PCB during impact. Figure 4.21 shows longitude-strain history plot and the peak longitude-strain at center of PCB is around 0.003.

4.7 Correlation Between Experimental data and Simulation results

Figure 4.18 and Figure 4.19 show the maximum displacement contour comparison. The contour from experiments are well correlated with simulation results. The peak values at the center of PCB from both downward and upward are matched very well. Figure 4.20 and Figure 4.21 shows the relative displacement history values at center of PCB from experiment and simulation. Those two figures shows the great matches between experiment and simulation not only on amplitude but also on time domain.

4.8 Solder Joint Stress and Strain

Figure 4.22 and Figure 4.23 show the pealing stress (Syy) distribution of solder joint at the time when maximum downward and upward displacement happened. The maximum

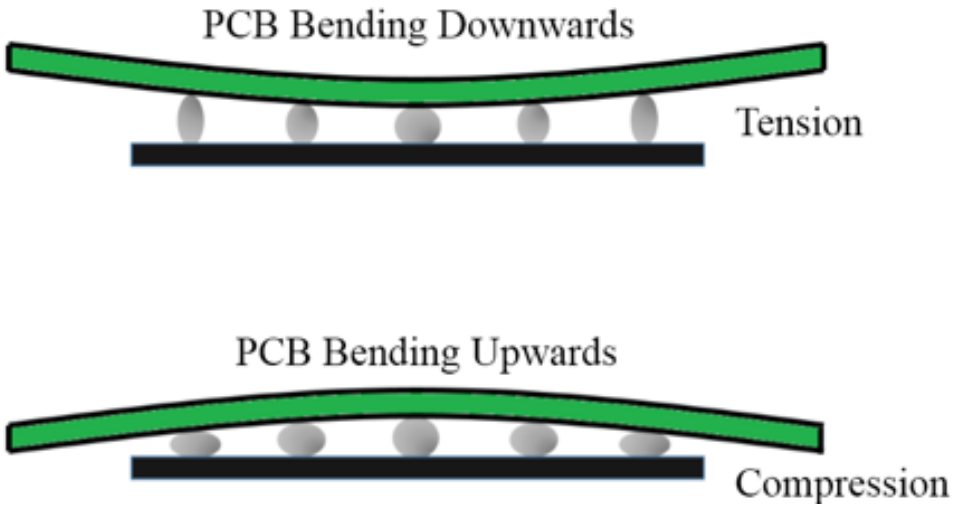

Figure 4.15: Effect of PCB Bending on Solder Joint

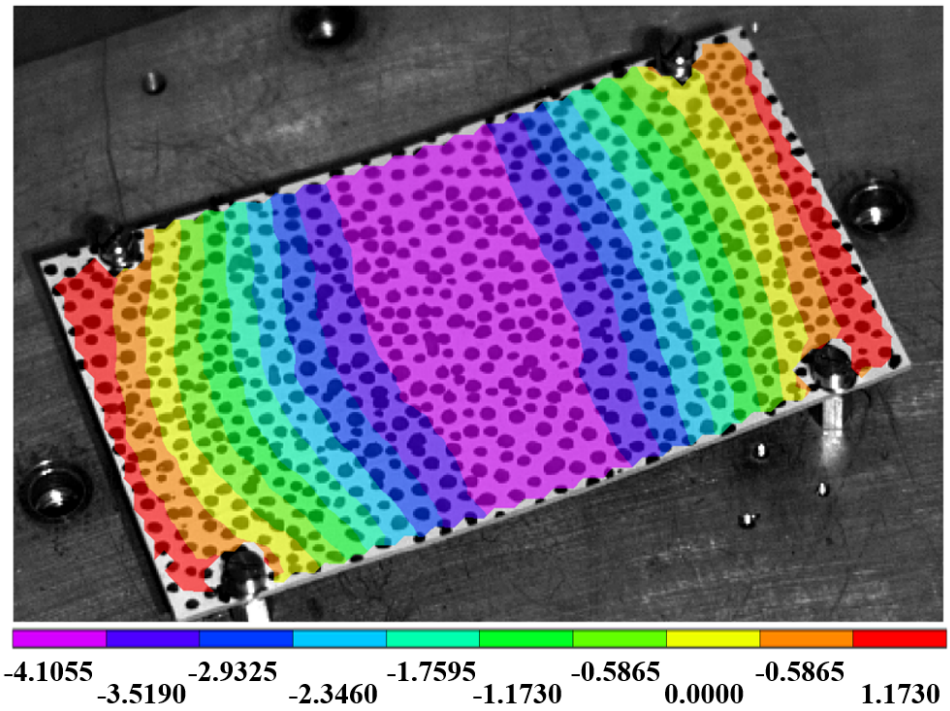

Figure 4.16: Maximum Downward Displacement Distribution of PCB in Experiment

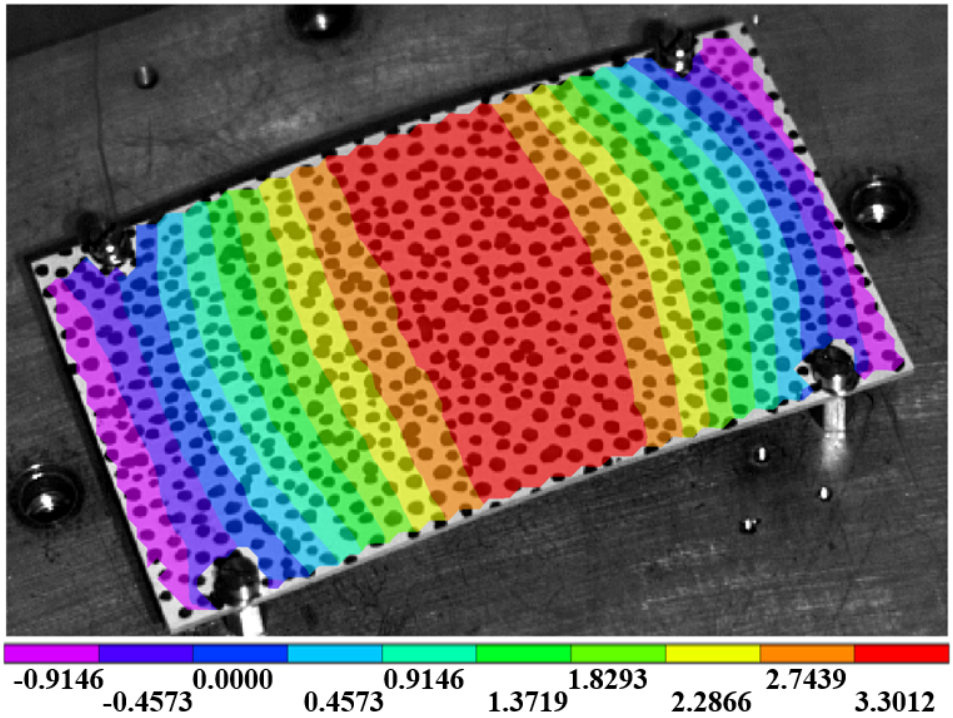

Figure 4.17: Maximum Upward Displacement Distribution of PCB in Experiment

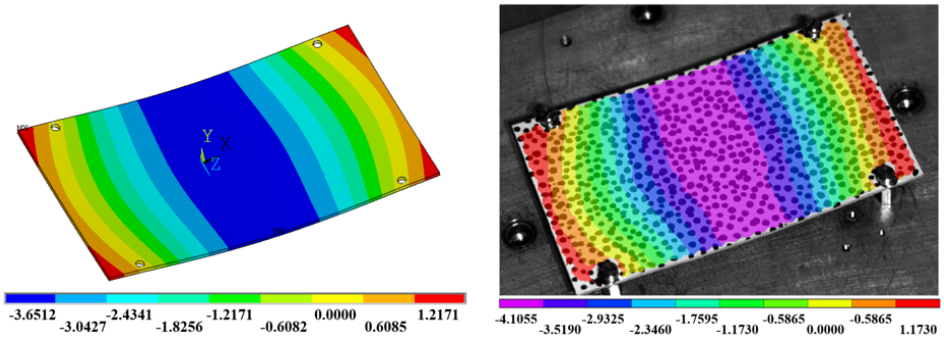

Figure 4.18: Maximum Downward Displacement Contour at Center of PCB (Left Simulation, Right Experiment)

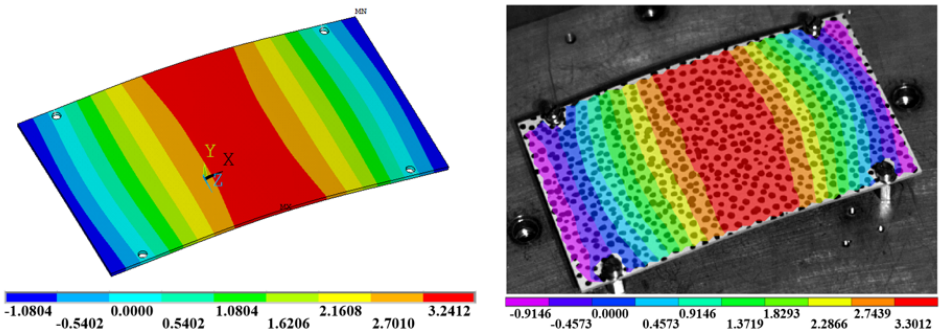

Figure 4.19: Maximum Upward Displacement Contour at Center of PCB (Left Simulation, Right Experiment

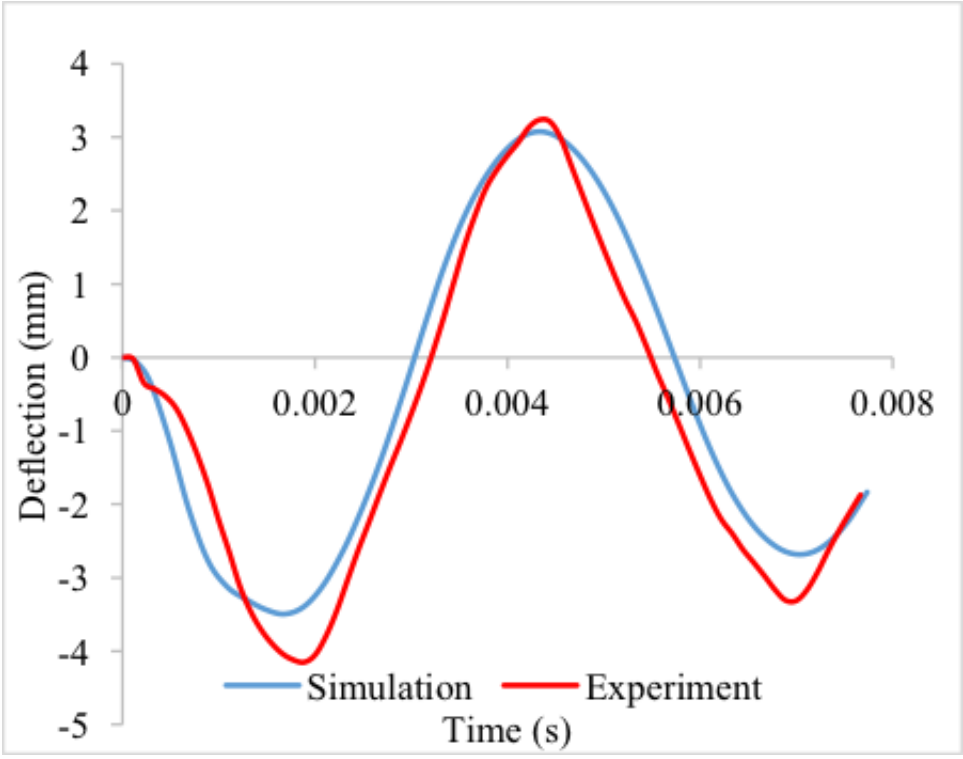

Figure 4.20: Displacement History at the center of PCB

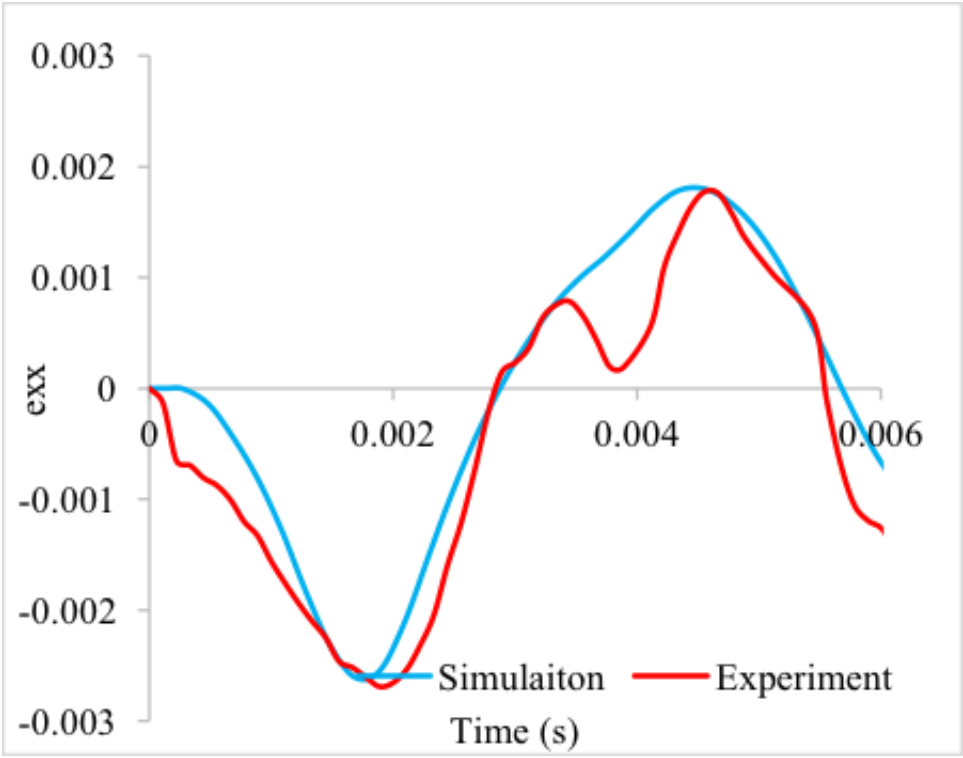

Figure 4.21: Strain History at the center of PCB

normal stress happened at the corner of solder joint and the stress concentration located at interface between solder ball and copper pad, as shown in Figure 4.22 and Figure 4.23.

Three method were used to calculate normal stress and strain. The first one is based on critical element of the critical solder ball. All the stress and strain value have been extracted from the critical element and plot with time. The second method is based on center on solder joint. All the stress and strain value were from center of critical solder joint. The third method was from volume averaging technique, which was used to reduce the sensitivity to meshing. The volume of the element normalizes the stress and strain value at each element. Only the top layer of the critical solder joint was used to calculate the average values by using Equation 5.1 and 5.2

$$\sigma_{ave} = \frac{\sum_{i=1}^{n} \sigma_i \cdot V_i}{\sum_{i=1}^{n} V_i} \tag{4.4}$$

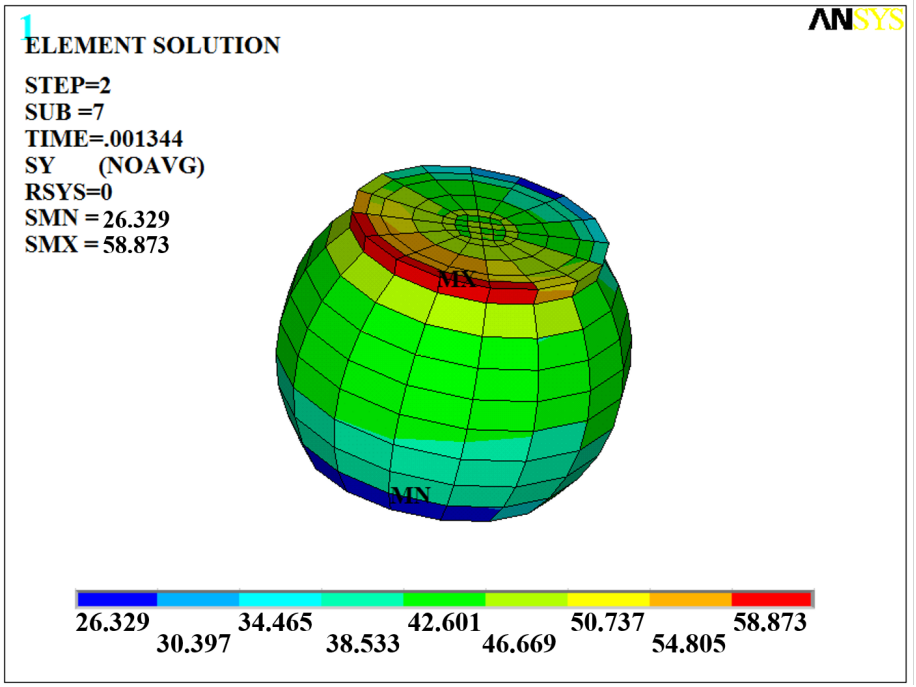

Figure 4.22: Stress Distribution of Critical Solder Ball at Maximum downward Deformation of PCB

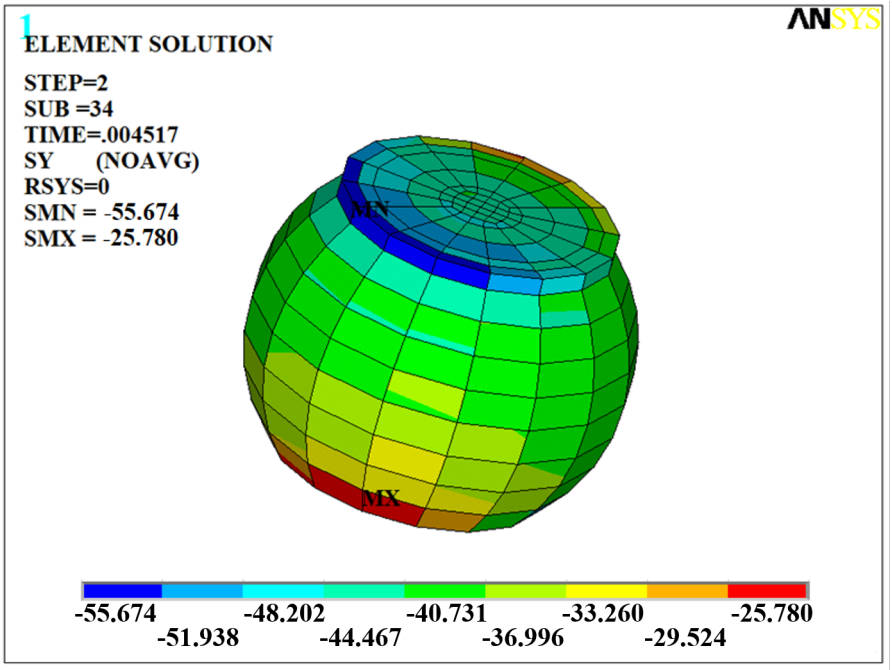

Figure 4.23: Stress Distribution of Critical Solder Ball at Maximum Upward Deformation of PCB

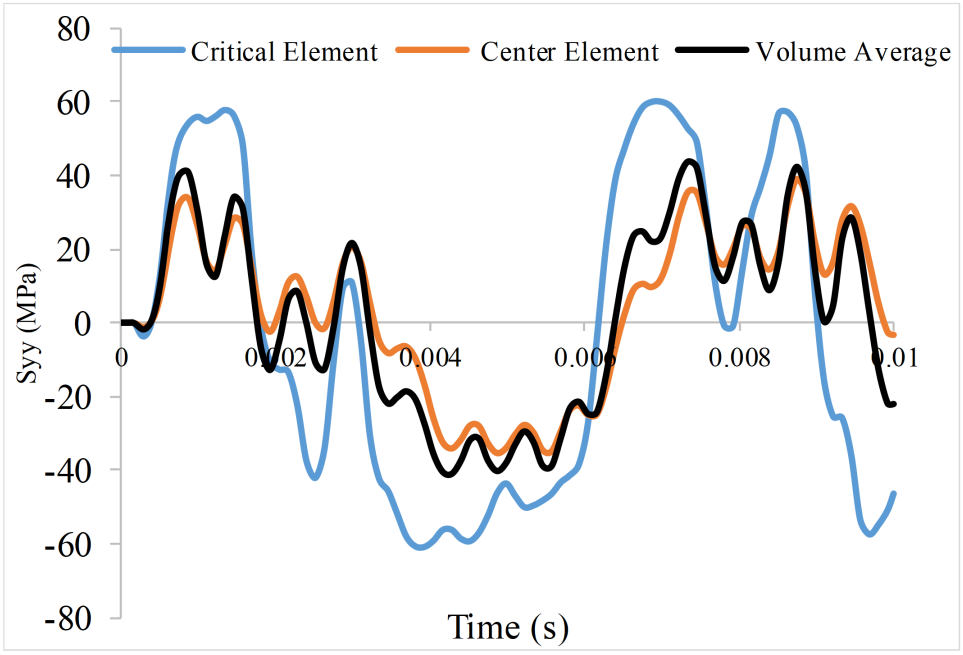

Figure 4.24: Stress History of the Critical Solder Ball

$$\varepsilon_{ave} = \frac{\sum_{i=1}^{n} \varepsilon_i \cdot V_i}{\sum_{i=1}^{n} V_i} \tag{4.5}$$

Where σ_{ave} and ε_{ave} are average stress and strain along the normal direction. V is the volume of i th element. σ_i and ε_i are stress and strain value of i th element along the normal direction. Figure 4.24 and Figure 4.25 show the comparison of stress and strain of the critical solder joint based on the above three methods. Volume averaging method is more reasonable than other two methods. For example, in Figure 4.24, the maximum stress at the critical element is almost two times of the UTS of SAC 305. Based on this condition, the solder would be broken at the first 1500g drop. It is nonsense to use this value to represent the actual stress value of solder ball. Further, with decreasing in size of elements, the amplitude of stress and strain will be increased. Therefore, by using volume average technique, the mesh sensitivity effect can be reduced.

Hysteresis loop is also plotted based on volume average method by combining the above stress and strain data together (Figure 4.26). The area of this plot shows plastic work density stored in solder ball per bending cycle. Figure 4.27 shows the accumulated plastic

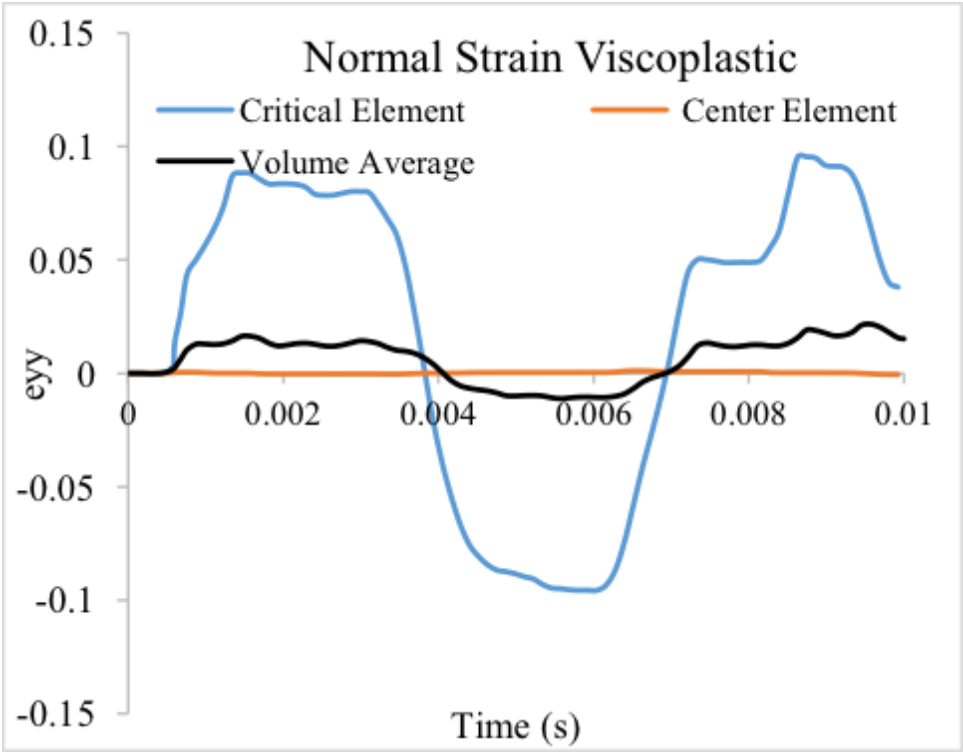

Figure 4.25: Strain History of the Critical Solder Ball

work density stored in solder joint with increasing of bending cycles which is computed by Equation 5.3 . With adding more energy, this finally will lead to the failure of packages.

$$W_{ave} = \frac{\sum_{i=1}^{n} W_i \cdot V_i}{\sum_{i=1}^{n} V_i} \tag{4.6}$$

4.9 Effect of Solder Material Properties on Simulation Results

In this section, the linear elastic material property is used to describe solder material. All of data including stress, strain, and displacement extracted from simulation results were compared between elastic and visco-plastic model based on volume average method from Equation 4.4, 4.5 and 4.6. Figure 4.28 and 4.29 show the defection and strain at center of PCB of these two groups of simulation are almost identical, only in amplitude but also in time domain. Thus, these two different constitutive model of SAC 305 have little impact on the deformation PCB.

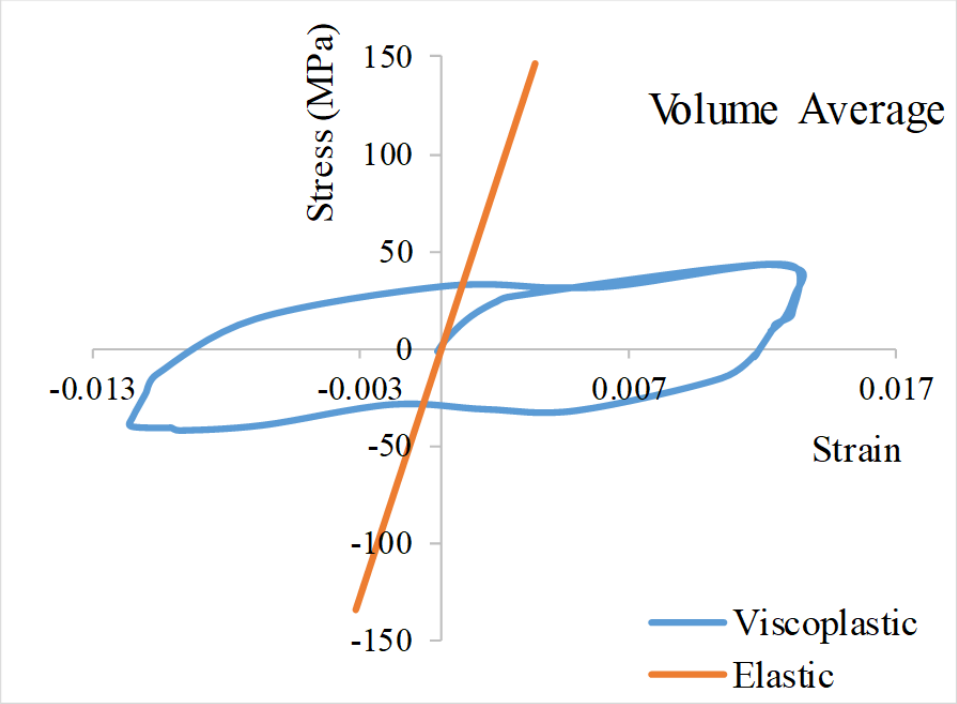

Figure 4.26: Hysteresis Loop of the Critical Solder Ball

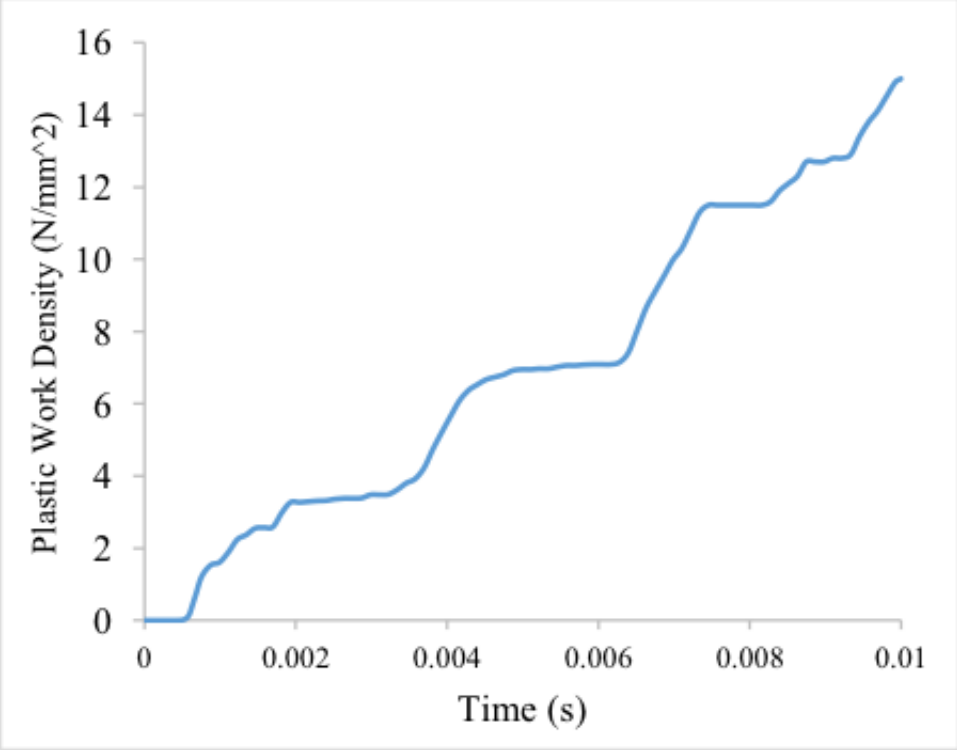

Figure 4.27: Plastic Work Density of the Critical Solder Ball

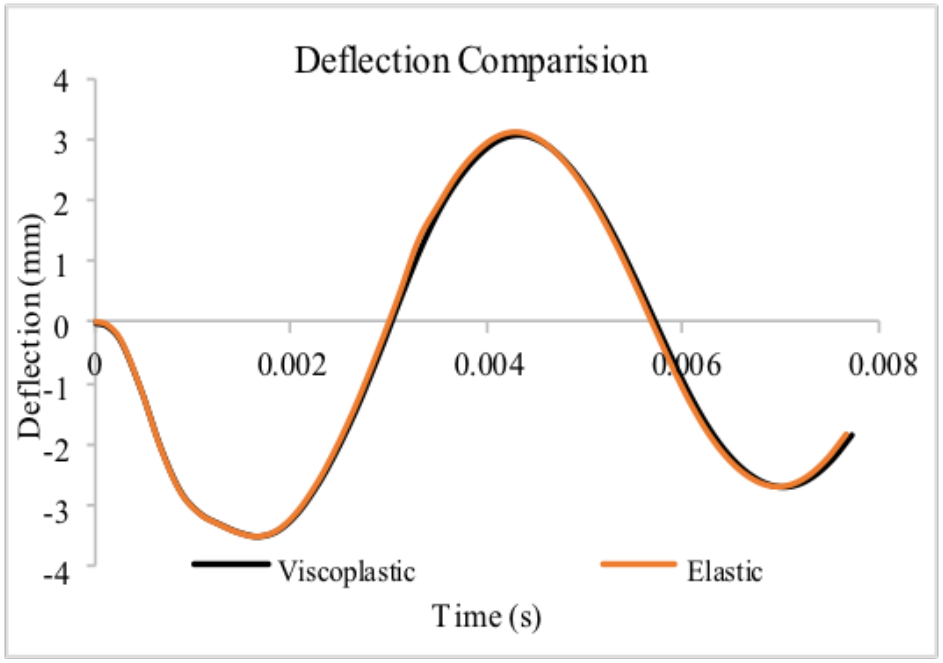

Figure 4.28: Deflection of at Center of PCB under 1500G (Elastic vs. Viscoplastic)

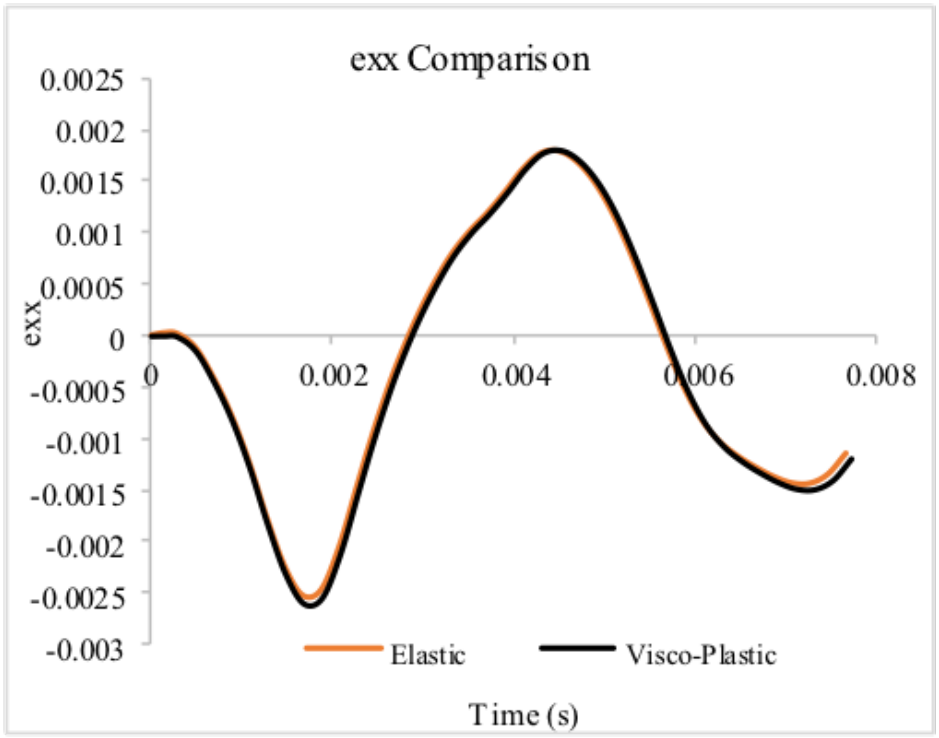

Figure 4.29: Strain of at Center of PCB under 1500G (Elastic vs. Viscoplastic)

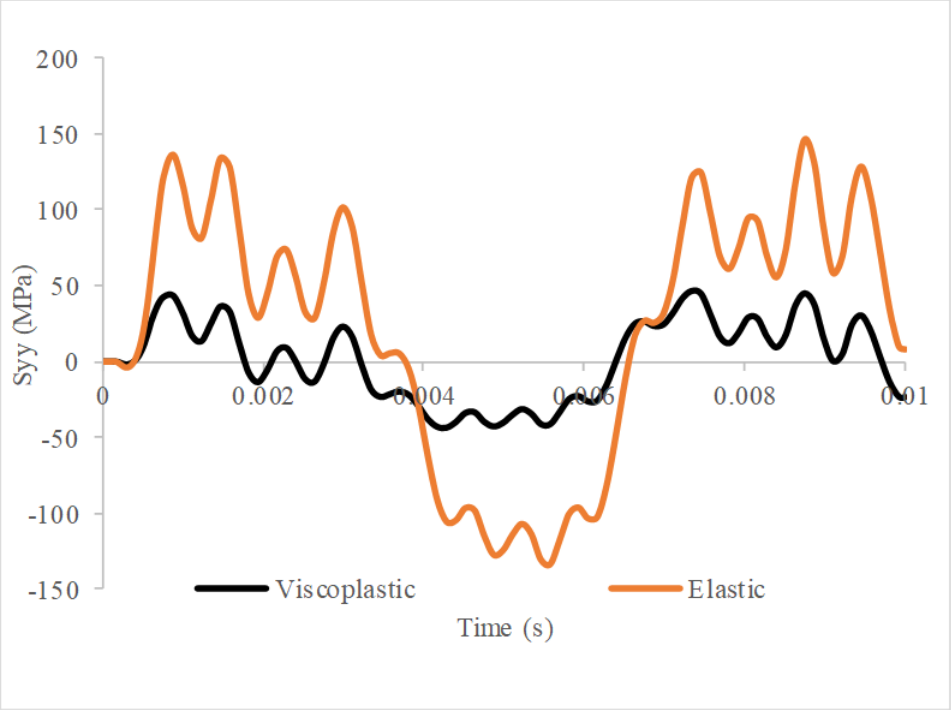

Figure 4.30: Stress of Critical Solder Joint under 1500G (Elastic vs. Viscoplastic)

Figure 4.31 and 4.30 show the strain and stress history of critical solder ball based on elastic constitutive equation. Theoretically, elastic model provides more stiffness than visco-plastic model, because there is no plastic deformation happened. Thus, the stress values in elastic solder should be higher than visco-plastic solder. Although the time domain is the same for both, the peak stress value of elastic model is almost two times of visco-plastic model. The Maximum of normal stress value from elastic model is way above the failure stress of solder ball. Therefore, by applying visco-plastic model to second-level interconnection can more accurately predict the stress distribution of solder joint rather than by using unreasonable linear-elastic material properties.

4.10 Deformation Rate of Critical Solder Joint

Deformation rate of critical solder joint can be achieved by differentiate the strain history plot. Figure 4.32 shows the strain rate plot of critical solder joint with visco-plastic material properties. The peak value is around 50 s^{-1}.

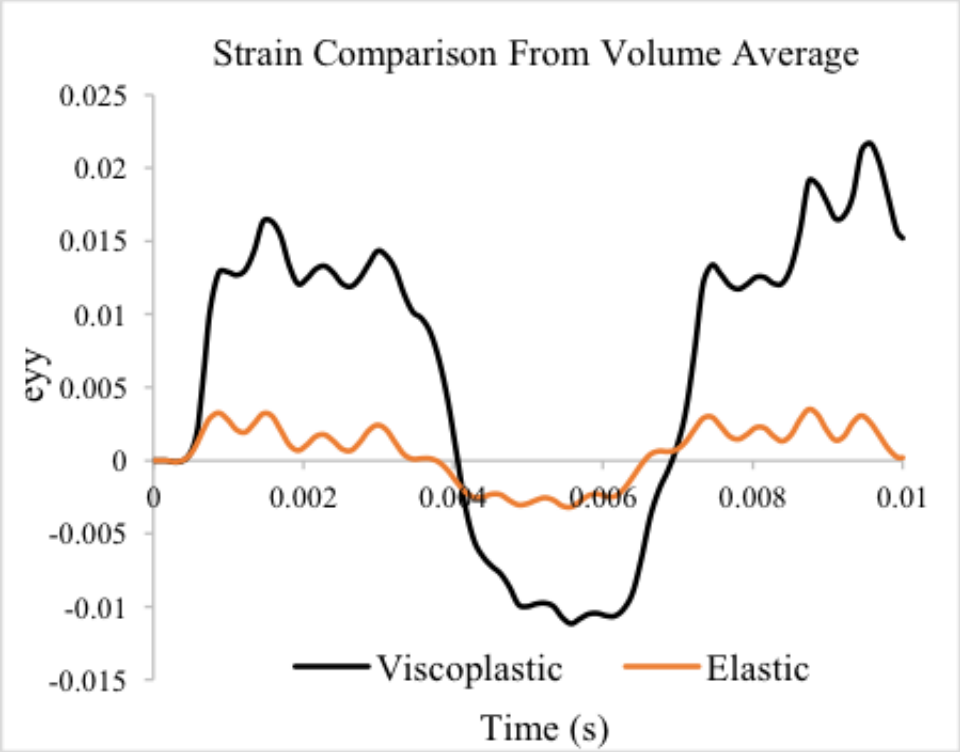

Figure 4.31: Strain of Critical Solder Joint under 1500G (Elastic vs. Viscoplastic)

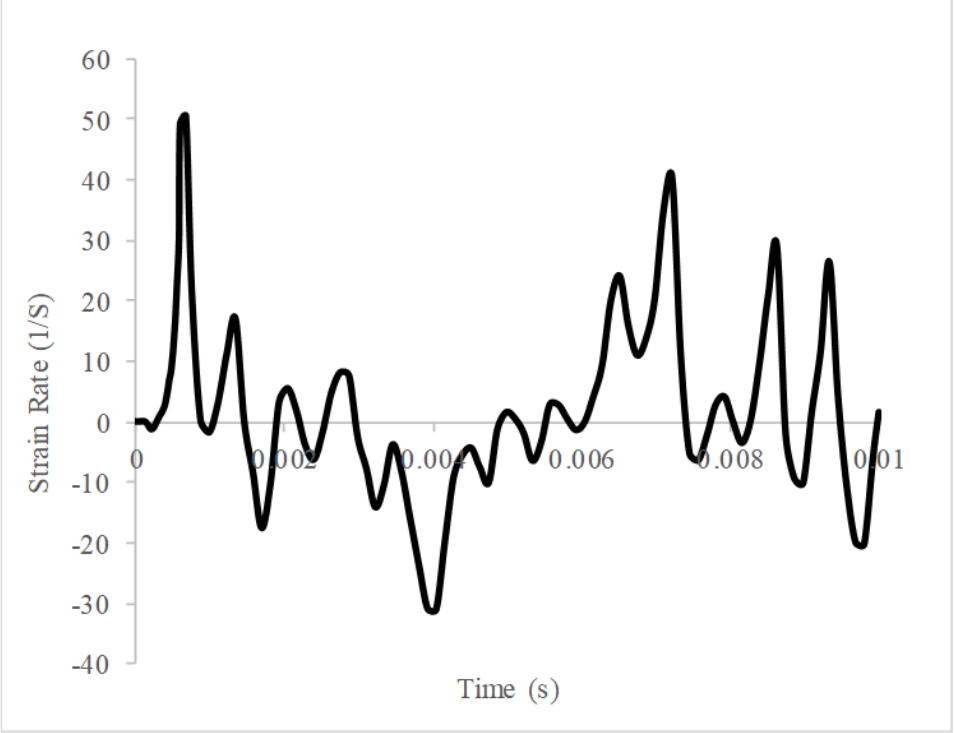

Figure 4.32: Strain of Critical Solder Joint under 1500G (Elastic vs. Viscoplastic)

4.11 Summary and conclusion

In this chapter, board level drop testing is executed with 1500G and impact pulse duration 0.5ms. Digital image correlation method is used to measurement full field displacement and strain. Finite element method is also used to simulate this drop event with input G method and Anand model. Hysteresis loop and plastic work density have also been calculated by FEM to see the damage accumulated by bending cycle.

Chapter 5

Reliability of Electronic Packages Subjected to High Temperature Vibration

5.1 Introduction

In automotive applications, electronic system can get exposed to high temperature and vibration during their life cycles. Simultaneously high temperature and vibration can cause failure in electronic system (Barker [29], Basaran [30], Qi [31]). Johnson [24] has studied the reliability of electronic products with temperature upto 140°C and vibration G-level upto 10G in automotive applications. The reliability of electronic products can be improved through understanding of solder interconnects in the electronic system. Presently, the literature on mechanical behavior of lead-free alloys under simultaneous harsh environment of high-temperature vibration is sparse. Most of the prior researches are focused on thermal-mechanical reliability of solder joint which is low-cycle fatigue. Tavernelli [41] has developed the life prediction models for solder joint fatigue subjected to thermal cycling. Solder joint reliability under random vibration can also be found in current literature (Lau [42], Upadhyayul [43], Li [44]). The theory for life prediction and accelerated testing is also well formalized for leaded solders at room temperature (Steinberg [45], Hu [27], Henderson [26]). However, relatively few researchers have studied the reliability of solder joint under simultaneous high temperature and vibration (Barker [29], Basaran [30], Qi [31]). Solder joint crack is one of dominant failure mechanism in temperature vibration. Wong [46] has demonstrated multiple failure modes of solder joint interconnects and the crack locations.

Previously, finite element method has been used to quantify deformation of solder joint during transient deformation (Pittaresi [47] [48], Lall [49]). It also has been developed to predict fatigue life of electronic components under random vibration. Chen [50] has derived a fatigue life prediction model of electronic components which combined the vibration

test data with simulation results. The deformation of 63Sn/37Pb solder joints under high temperature vibration has been studied with finite element method by Zhao [51]. In order to improve computational efficiency, finite element based global-local method has been widely used to simulate the solder joint deformation. Global model with smeared properties has been used to investigate the deformation of whole board (Ciech [52], Lall [19], Gu [53]). Sub-modeling technique has been used to investigate the deformation of solder joints (Lall [49], Syed [22]). The component deformation is governed by the PCB deflection. Material properties of PCB are changing at various operating temperature. It changes dramatically when the operating temperature is close to its glass transition temperature. Lall [49] has used dynamic mechanical analysis to analyze temperature dependent mechanical properties of PCB. This has been demonstrated by measuring the change in natural frequency as a function of temperature. Furthermore, deformations of PCB when subjected to drop and shock has been accurately measure using DIC technique (Lall [20], Miller [54], Park [55], [56]). Prior researchers have plotted S-N curves for SAC alloys using a combination of fatigue life data and solder joint stress amplitude (Al-Yafawi [57], Lall [49]). This technique can be used to predict the remaining useful life of electronic components. In this study, test vehicles have been subjected to elevated temperature and vibration load at its first nature frequency at same time. The reliability of SAC305 solder interconnects for test vehicles have been studied. Experimental modal analysis as well as FE based modal analysis have been conducted for test board to determine the natural frequencies, mode shapes. An image express method has been used to extract the out of plane displacement of PCB which is used to validate simulation results. Finite element method based global and local method has been used to extract hysteresis loop and plastic work density of critical solder joint. A life prediction model for electronic components has been derived based on experimental data and simulation results. Finally, failure mode analysis has been performed to show the failure mechanism.

Figure 5.1: Test Vehicle

5.2 Test Vehicles

Figure 5.1 shows the test board studied in this research. The test board is a dummy board for engine control unit of an agriculture equipment, which has 12 CABGA288 packages mounted on the board. All the packages in this board have been daisy chained in order to check the continuity during testing. SAC305 has been used as the interconnect material. Dimensions of this board following the JEDEC standard ([4]) is 132mm x 77mm x 1.6mm. This testing board has a 8 layered (FR4) laminated PCB with silver immersion finish. The PCB pads were non solder mask defined (NSMD). Figure 5.2 shows the footprint of solder joint.

5.3 Experiment Setup

A LDS Shaker V722 with an isothermal oven has been used to test the test vehicles at elevated temperature vibration. The isothermal oven has a glass window on top to acquire high speed video of the PCB deformation. The test vehicles are subjected to vibration at their first natural frequency with stress level of 1G, 5G, 10G and 14G. The deformation of PCB has been measured at those G-levels under its resonant frequency. Resistance data

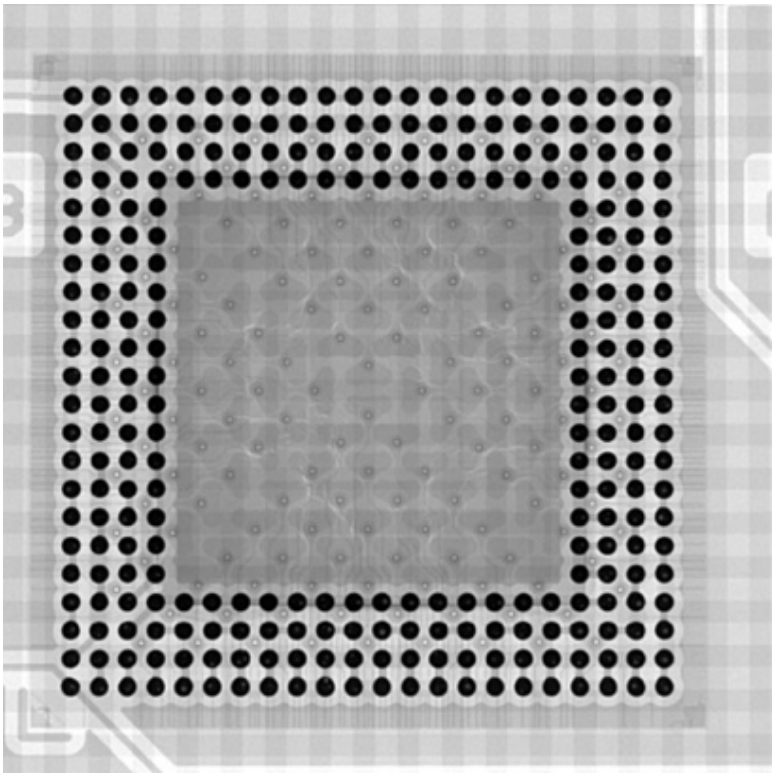

Figure 5.2: X-ray Image of CABGA288

across daisy chained packages for test vehicles were captured using high speed data logger (Figure 5.5). Each test board was attached to high speed data acquisition system using wires. Figure 5.4 shows the board mounted on the shaker with wires. A 20 percent increasing in resistance for 7 consecutive cycles defined as failure of package. The test is continued till the packages have failed or running for 12000 mins. The time to failure is converted to cycles to failure. The complete experimental setup shown in Figure 5.3. The resistance of different daisy chained packages have been monitored using high speed data logger.

5.4 Finite Element Model

The transient dynamic response of the board assemblies during the vibration event has been simulated with implicit finite element method. Figure 5.6 shows the general view of this assembly with 12 packages mounted on the top. For this global model, all the solder joints are replaced by Timoshenko beam elements in order to improve computation efficiency.

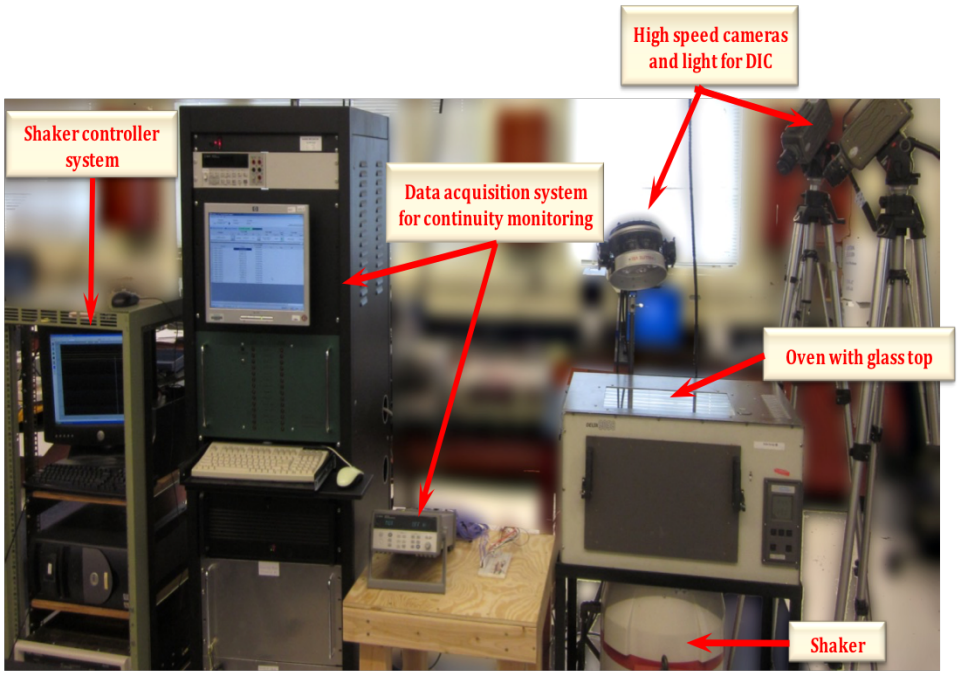

Figure 5.3: Equipment Setup

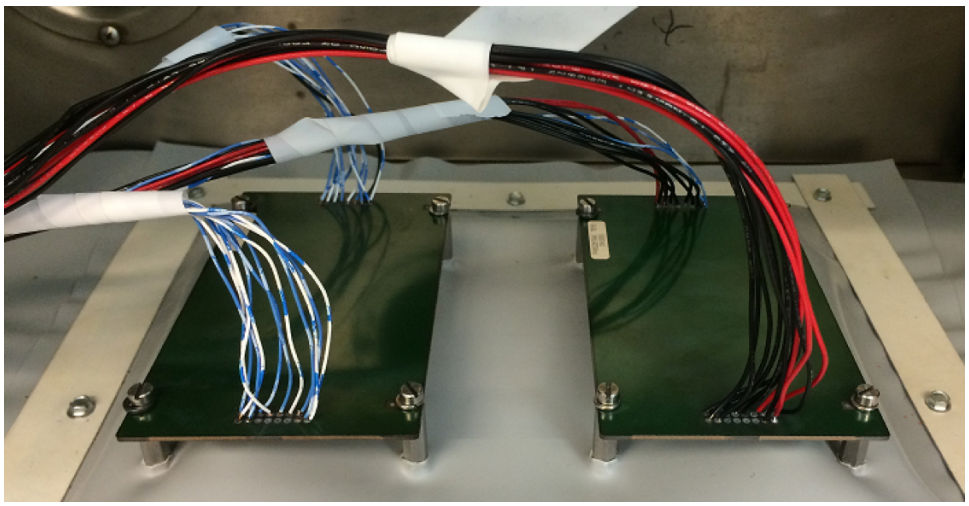

Figure 5.4: Test Board with Wires

Figure 5.5: Data Logger

Table 5.1: Elements Table of Global CABGA288

Board Assembly	Element Type
PCB	SOLID45
Copper Pad	SOLID45
Mold Compound	SOLID45
Silicon Die	SOLID45
Die Attach	SOLID45
BT substrate	SOLID45
Solder Beams	BEAM188
Mass Element	MASS21

Figure 5.7 shows the cut-section of meshed model. The package is modeled with substrate, mold compound, silicon die, adhesive. Totally three types of element have been used to build the model, as shown in Figure 5.1. SOLID45 is used to mesh solid structure. In order to apply the boundary conditions with Input-G method, four mass elements are also needed to create at screw holes of PCB. For the global model all the material are model with linear elastic. Table 5.2 shows the detail values of each material.

Stresses in solder interconnects have been extracted from sub-model. Anand model (discussed in chapter 3) has been used to define the constitutive equation of solder joints. stress amplitudes are plotted against cycles to failure at all the test temperatures and G-levels. Furthermore, model predictions have been correlated with experimental data.

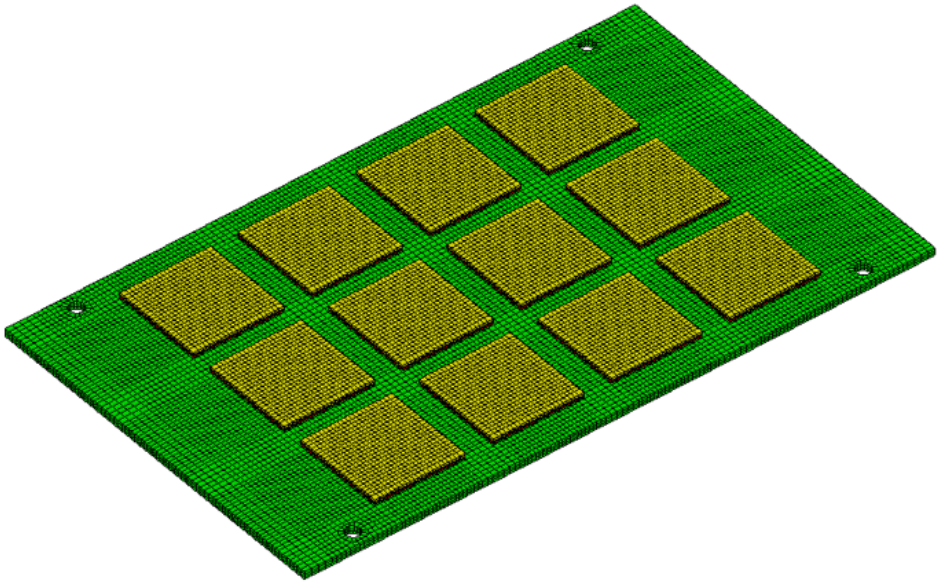

Figure 5.6: Global Model of Test Vehicle

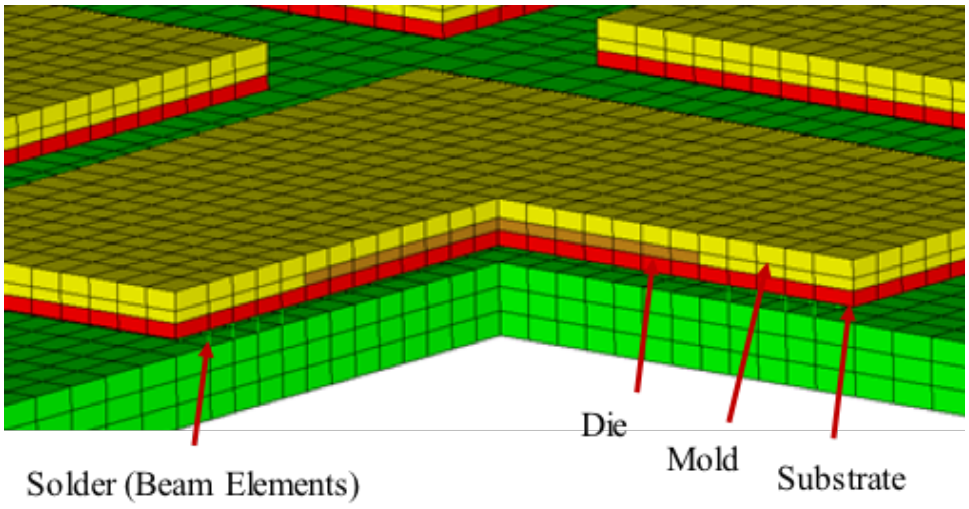

Figure 5.7: Cut-Section View of CABGA288

Table 5.2: Material Properties of Test Vehicle

Package Assembly	Elastic Modulus(MPa)	Poisson's Ratio	Density (tonne/mmˆ3)
Solder Jonits	42000	0.34	8.40E-09
Mold Compound	23500	0.25	1.65E-09
Silcon Die	162000	0.28	2.33E-09
Die Attach	2760	0.35	7.80E-09
BT Substrate	17400	0.28	1.80E-09
Copper Pad	129000	0.34	8.82E-09
PCB	23800 (25C)	0.12	1.80E-09
	22880 (55C)		
	19480 (155C)		

5.5 Modal Analysis

5.5.1 Experimental Measurement of First Natural Frequency

Experimental modal analysis (EMA) is conducted on test vehicle to measure the 1^{st} Natural frequency (NF). The test vehicle was subjected to harmonic vibration at their 1^{st} NF at elevated temperatures. Two accelerometers have been used to perform EMA as shown in Figure 5.8. One accelerometer is attached to shaker table and other one is attached at center of test board as shown in Figure 5.8. Accelerometer 1 measures the excitation signal and accelerometer 2 measures the response. The test board with packages facing down is mounted on four standoffs. A sine sweep profile from 5 Hz to 2000 Hz with constant amplitude of 10 G is used. A transmissibility plot is obtained from EMA test as shown in Figure 5.9. The excitation frequency corresponding to each peak in the transmissibility plot denotes the natural frequency of test board. For this test board, the first natural frequency is around 360Hz.

5.5.2 Modal Analysis in Simulation

Modal analysis was running in ANSYS APDL. The meshed geometry and material properties have been discussed above. Figure 5.11 shows weight of the meshed geometry calculate by Hypermesh which is close to its actual weight measured by scale shown in

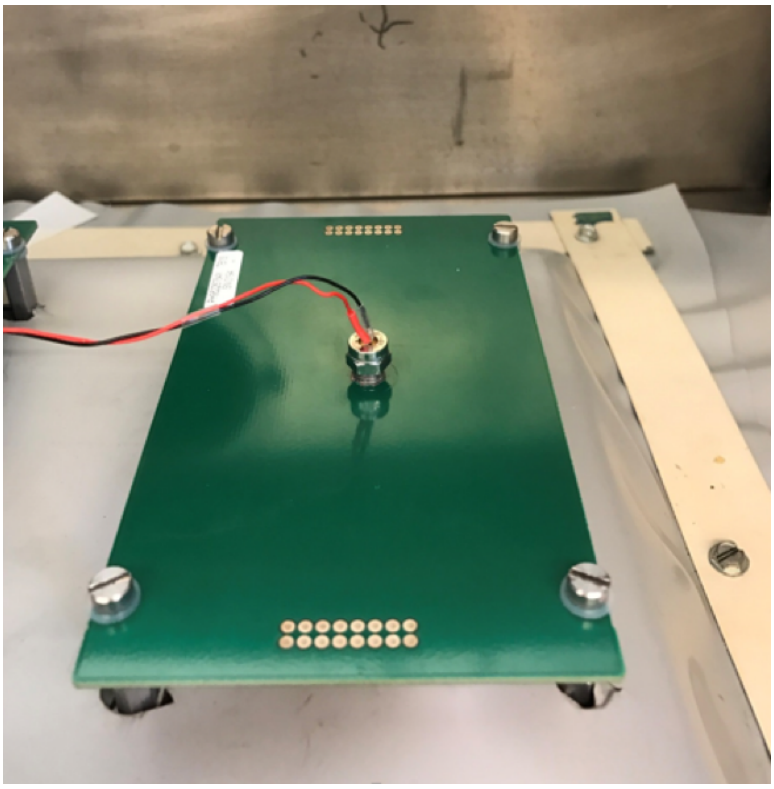

Figure 5.8: Natural Frequency Measurement Setup

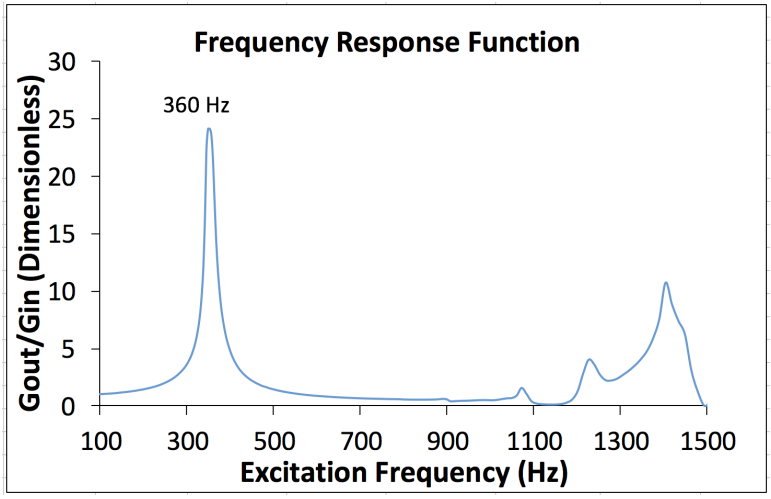

Figure 5.9: Trasmissbility Plot

Figure 5.10: Actual Weight of Test Vehicle

Figure 5.10. The first natural frequency from simulation is 360.1Hz which matches very well matched with the experimental measurement. The error is less than 1 percent. Figure 5.12 to Figure 5.15 show four mode shapes of this testing assemblies. Those modal shapes show the deformation of assembly vibrating at its corresponding frequency.

5.5.3 Effect of Operating Temperature on First Natural Frequency

A thermalcouple is attached to the surface of PCB to measure the actual temperature of the board during measurement. Three temperatures (25, 55, 155 °C) are chosen to evaluate the temperature influence on its 1^{st} Natural Frequency. Table 5.3 shows measured frequencies at different evaluated temperatures. Figure 5.16 shows the natural frequency changing with temperature increasing. A linear line is used to fit the experimental results. It is observed that the changing rate is about 0.53 Hz/°C.

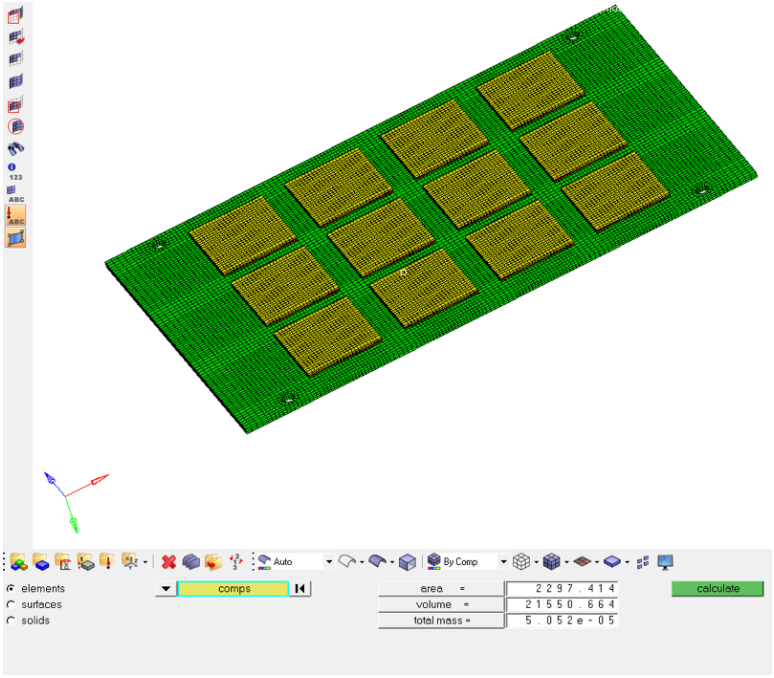

Figure 5.11: Simulation Weight of Test Vehicle

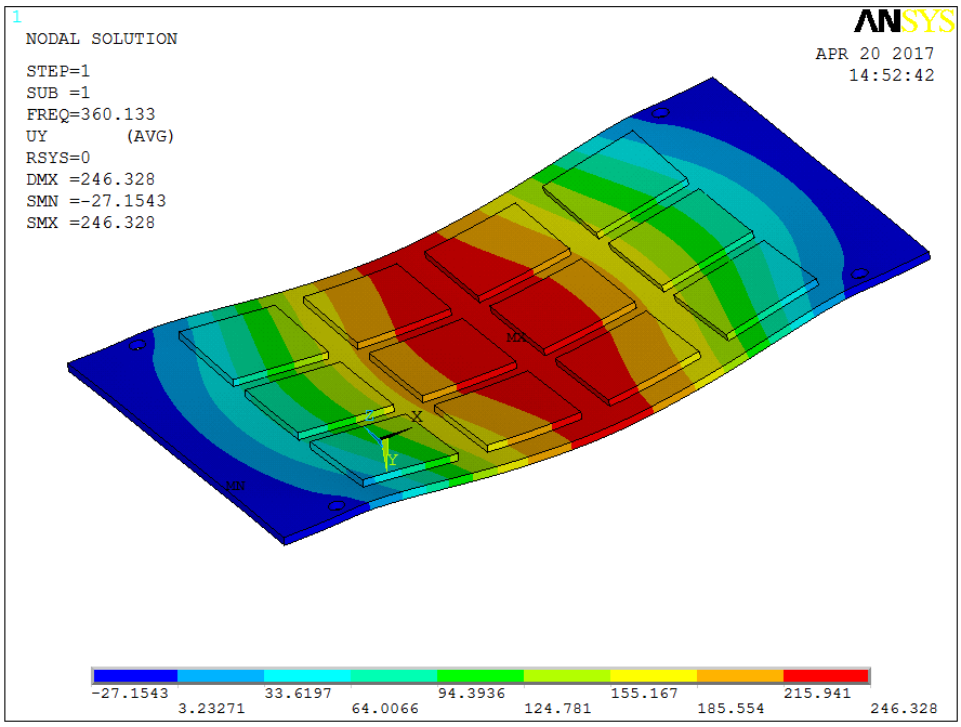

Figure 5.12: Mode Shape 1 of Test Vehicle

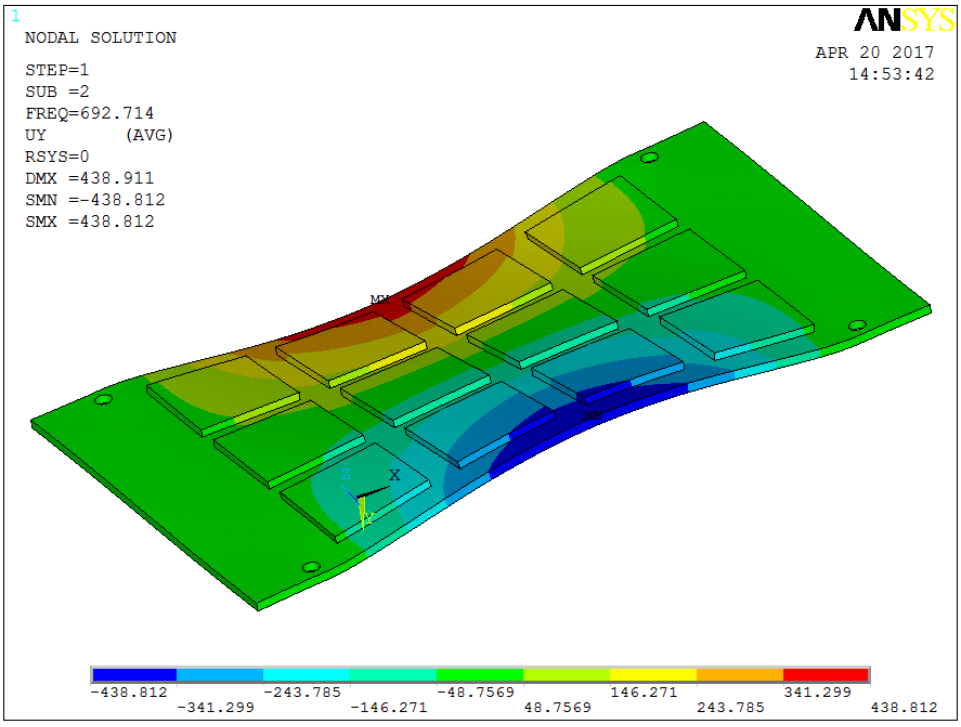

Figure 5.13: Mode Shape 2 of Test Vehicle

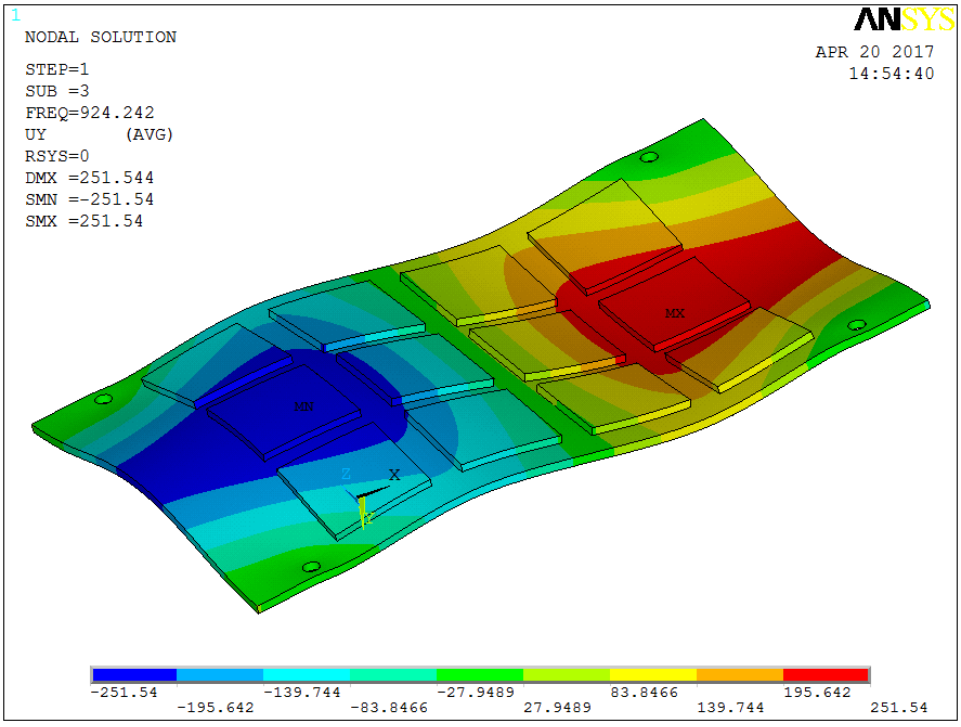

Figure 5.14: Mode Shape 3 of Test Vehicle

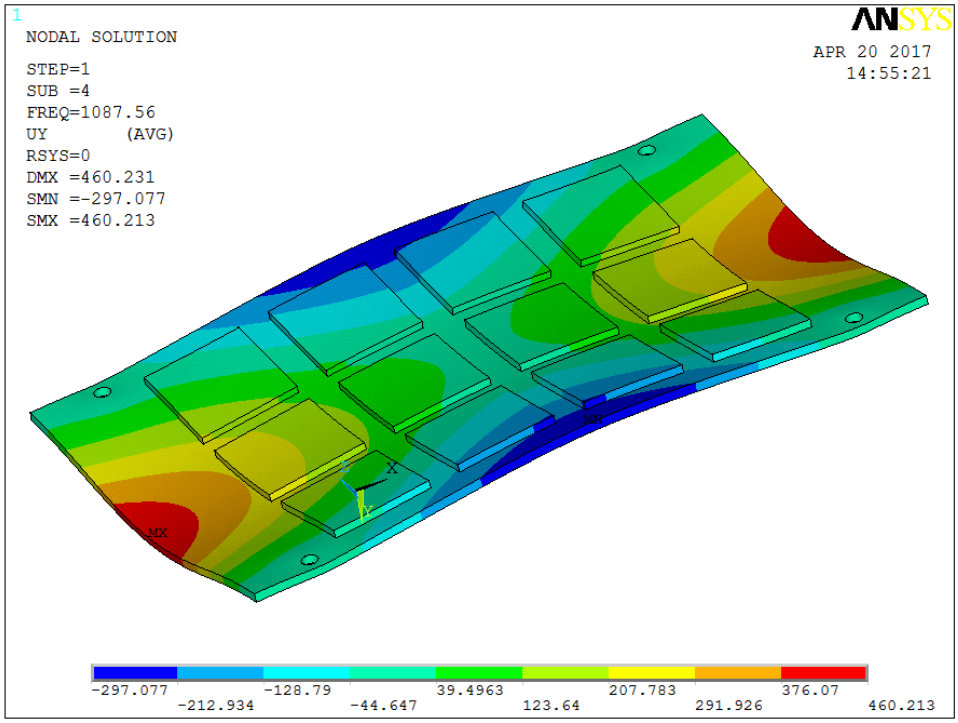

Figure 5.15: Mode Shape 4 of Test Vehicle

Table 5.3: 1^{st} Natural Frequency from experiment and simulation

Operating Temperature	Experiment	Simulation
25 °C	360 Hz	360.1 Hz
55 °C	342 Hz	345.9 Hz
155 °C	291 Hz	297.6 Hz

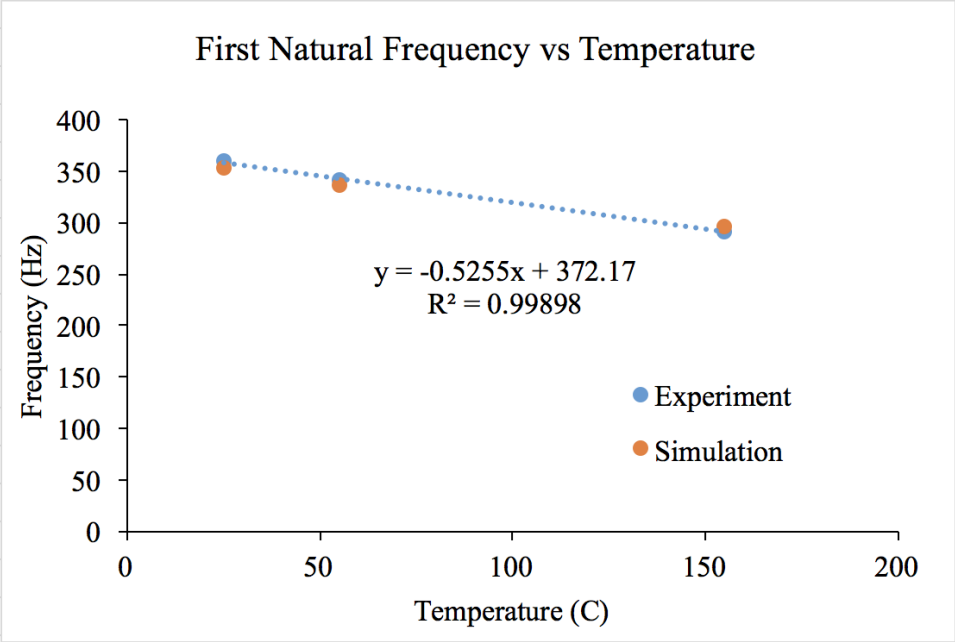

Figure 5.16: Effect of Operating Temperature on 1^{st} Natural Frequency

The temperature dependence for simulation is achieved by the temperature dependence of the elastic modulus, which is measured by dynamic mechanical analysis (DMA) (Geeta [49]). Figure 5.16 shows the good correlation between simulation results and experimental measurement. It is also observed that with increasing in operating temperature, the peak to peak displacement is also increasing. Figure 5.17 to Figure 5.18 show the model shape 1 of testing board at 55°C and 155°C.

5.6 Experimental Results

5.6.1 Displacement, Velocity and Acceleration Measurement of PCB during Vibration

Figure 5.19 shows the experimental measurement setup for PCB during vibration at its first natural frequency. There is one high speed camera sitting in front of the chamber to capture the high speed video of PCB during deflection. Figure 5.20 shows the front view of the test setup. There are totally 5 targets mounted on the surface of on the PCB and stand off. Figure 5.21 indicates the numbering of the target in the software. Target 4 and 5 are

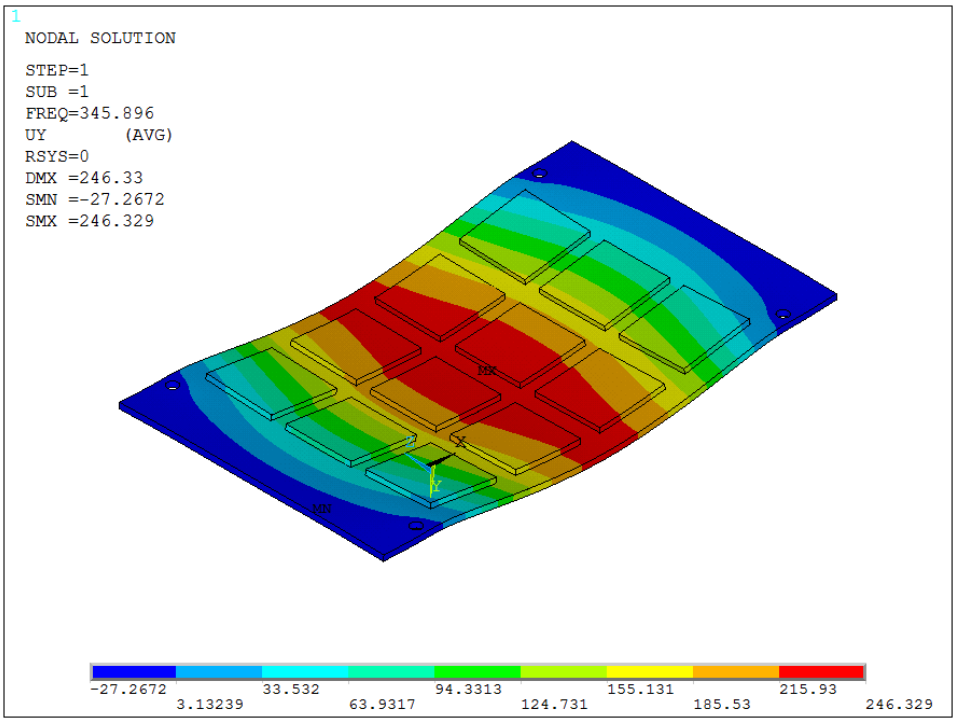

Figure 5.17: Mode Shape 1 of Test Vehicle at 55°C

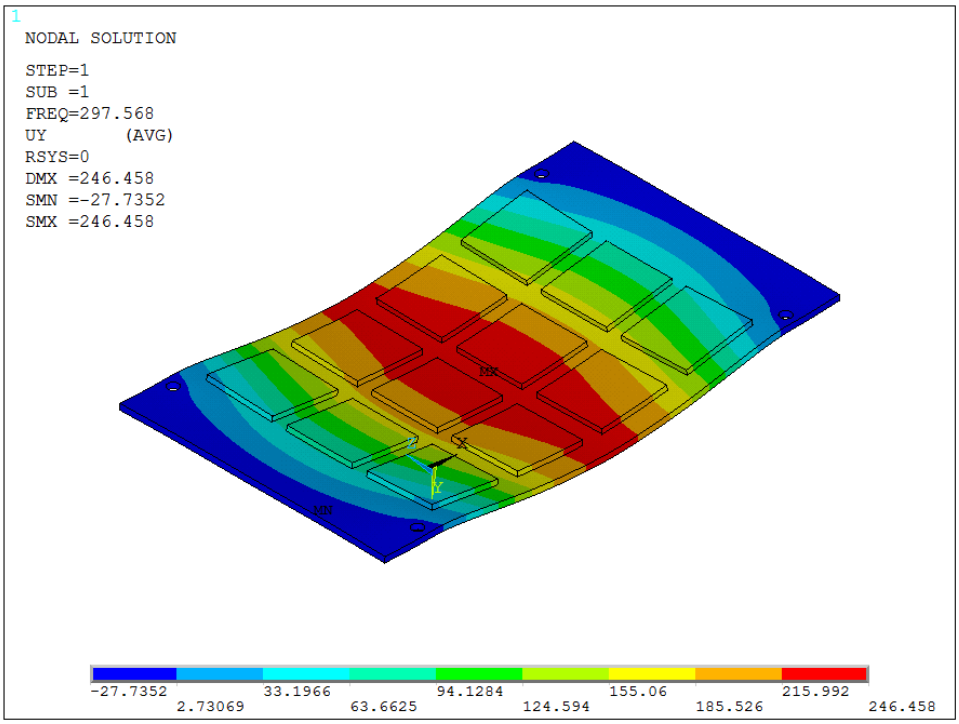

Figure 5.18: Mode Shape 1 of Test Vehicle at 155°C

Figure 5.19: Experiment Setup of High Speed Camera

the reference targets which are used for calibration. Target 1 to 3 are used to monitor the deflection of PCB during vibration. The high speed camera is running 8000 frame/s with 0.35s capture duration and resolution 512x512. A software named motion plus is used to analyze this high speed video and track the movement of targets. the output results are the displacement, velocity and acceleration of PCB where the targets locate. Figure 5.23 shows the deflection of PCB during deformation with sinusoidal vibration at its first natural frequency. The G amplitude is 14G with testing at room temperature. Figure 5.24 and 5.25 shows the output velocity and acceleration history plot respectively. During vibration, the PCB is continuing to move up and down which can cause the fatigue failure of solder joints. Figure 5.22 shows the deformation images of PCB during vibration at different time frame. The top one is the maximum upward deformation of PCB. The middle one and bottom one show the unbended PCB and maximum downward movement of PCB. The peak values for upward and downward are as shown in Figure 5.23.

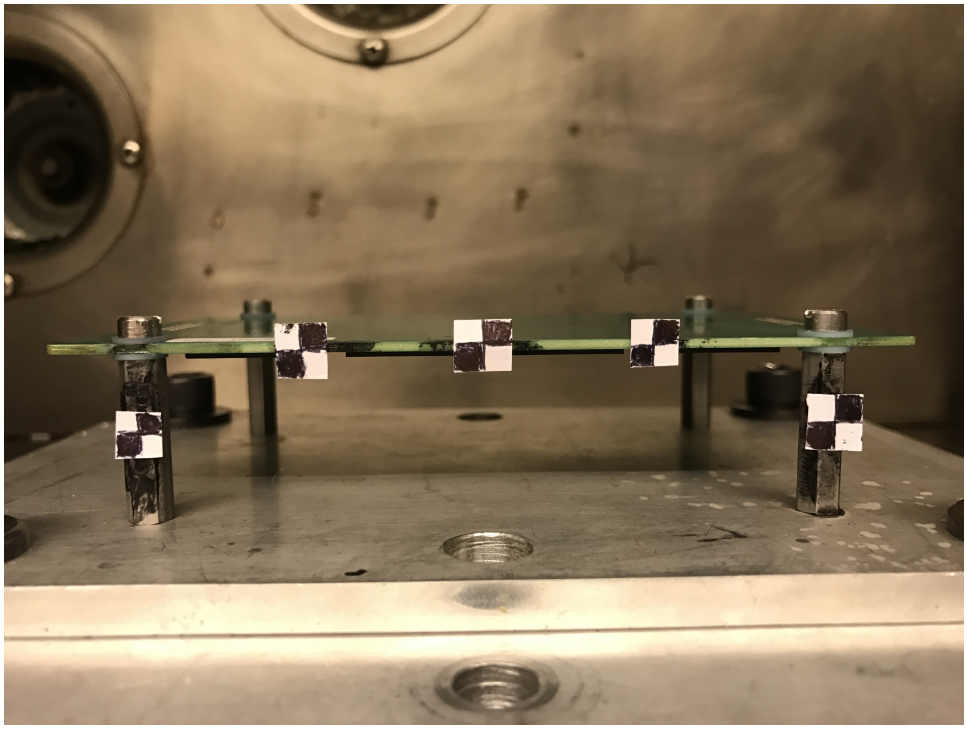

Figure 5.20: Front View of Experiment Setup

5.6.2 Effect of Vibration G-Level on Deformation of PCB from Experiment

The same PCB is tested at G-level of 1, 5, 10, 14g dwelling at its first natural frequency 360Hz at room temperature. Figure 5.26 shows the displacement history of target 2 at different G-level. it is easily observed with decreasing in input G-level, the displacement amplitude is also reduced. From 14g to 10g, the peak values are decreased by 10 percent.

Figure 5.28 and 5.30 show the effect of G-level on velocity and acceleration of PCB at target 2. All the peak values have been extracted and plot against G-level, shown in Figure 5.29 and 5.31. With reducing amplitude in G-level, the peak velocity and acceleration are decreasing.

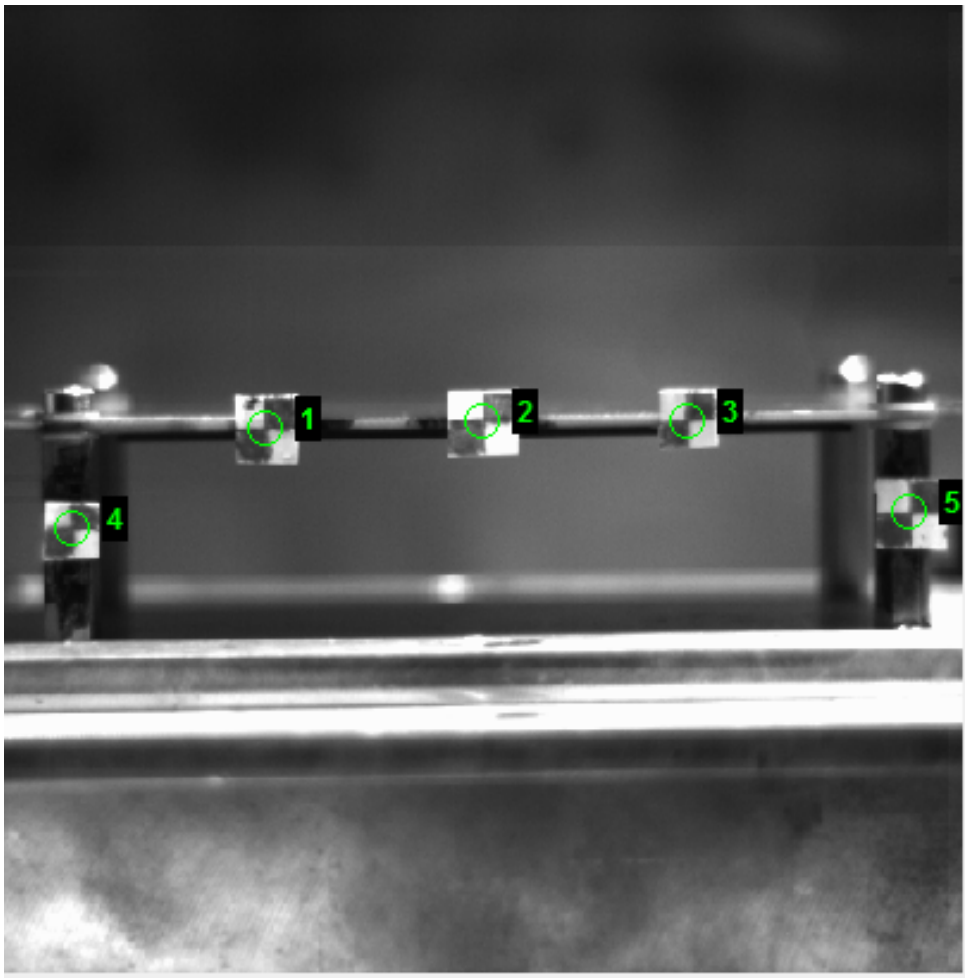

Figure 5.21: Target Numbering and View from High Speed Camera

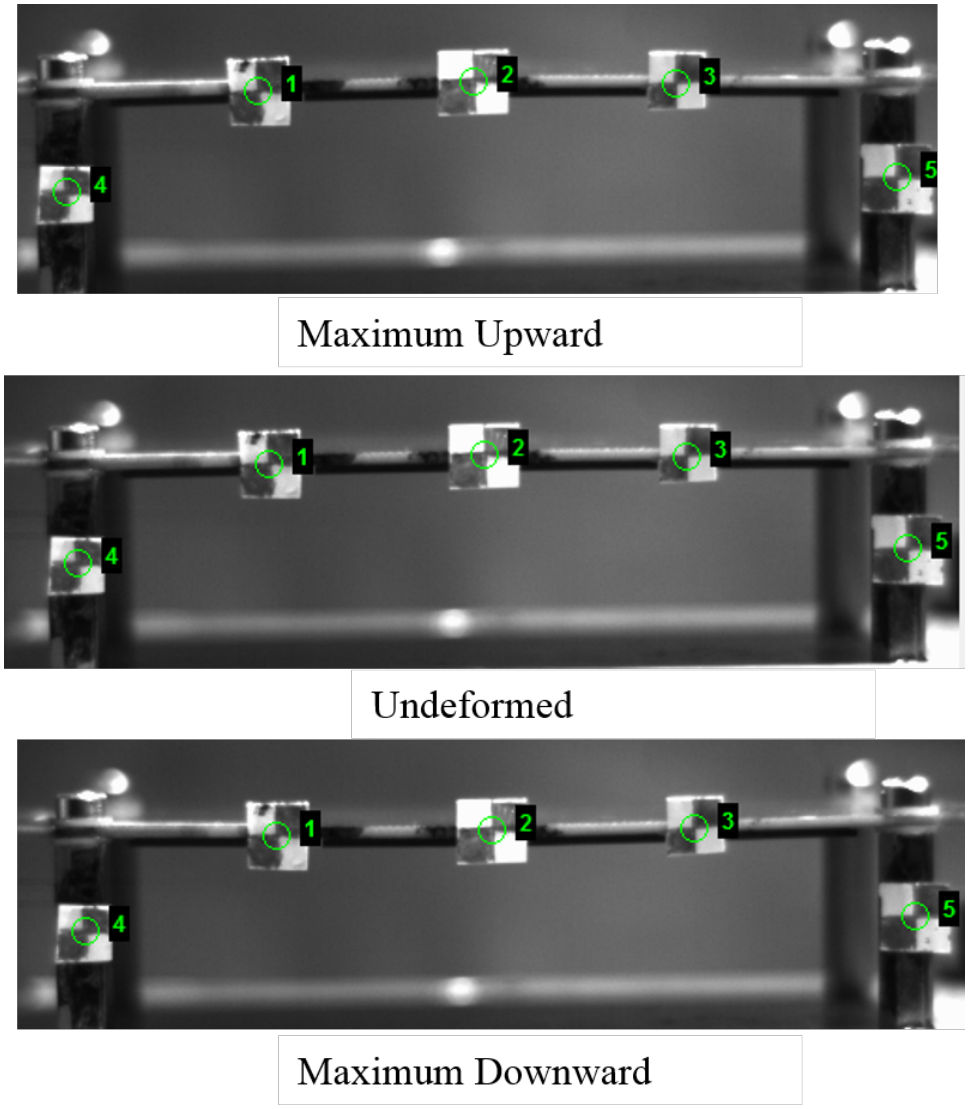

Figure 5.22: Deformation of PCB Capturing by High Speed Camera

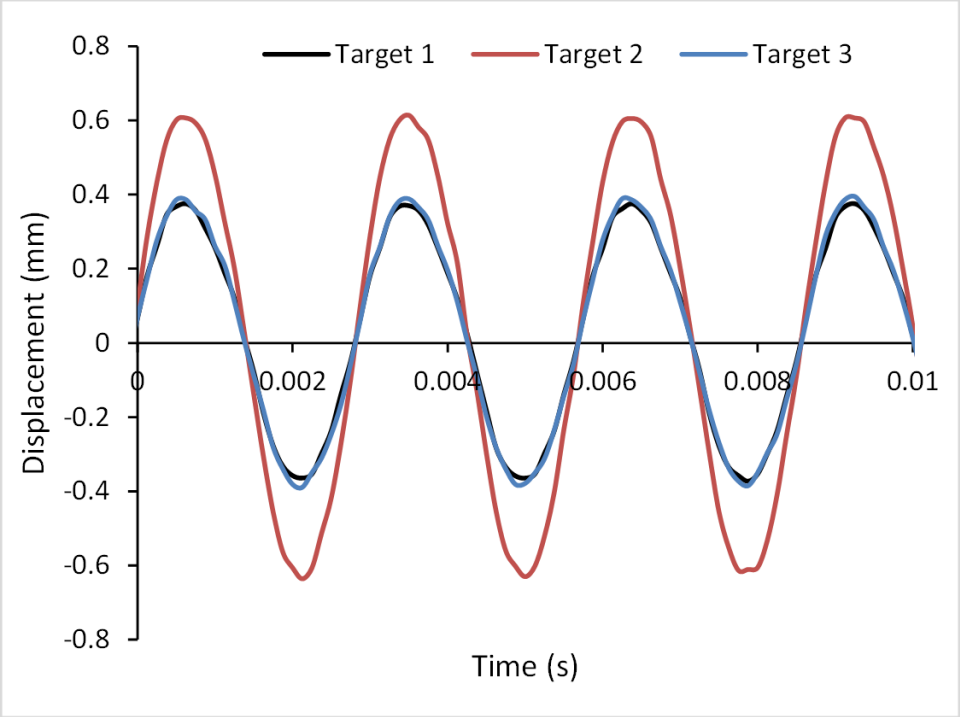

Figure 5.23: Target Displacement History of PCB Vibrating at 14G

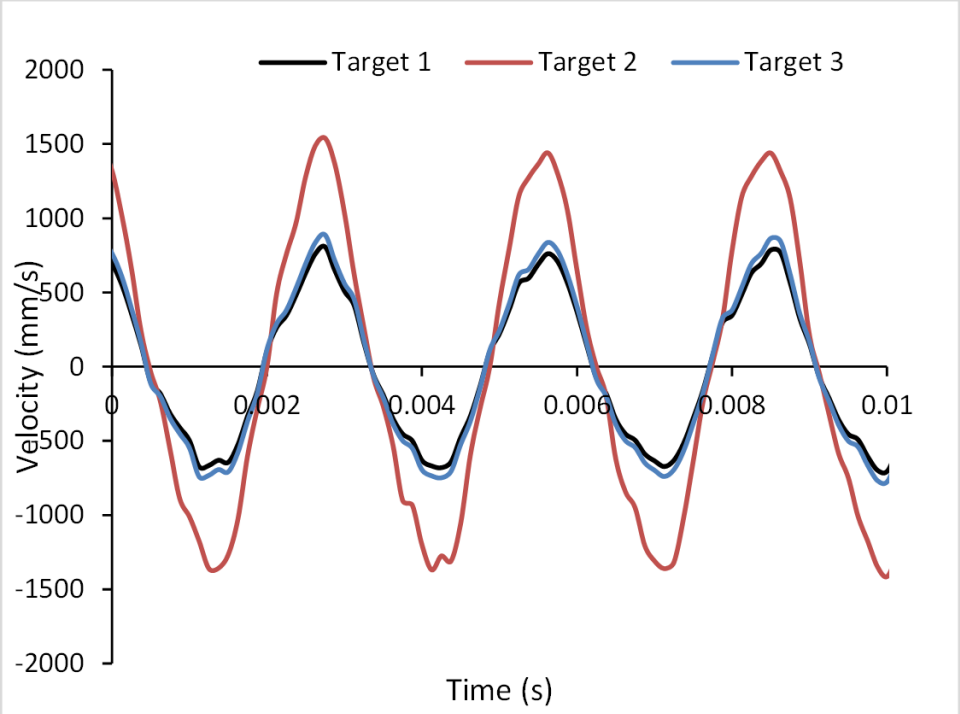

Figure 5.24: Target Velocity History of PCB Vibrating at 14G

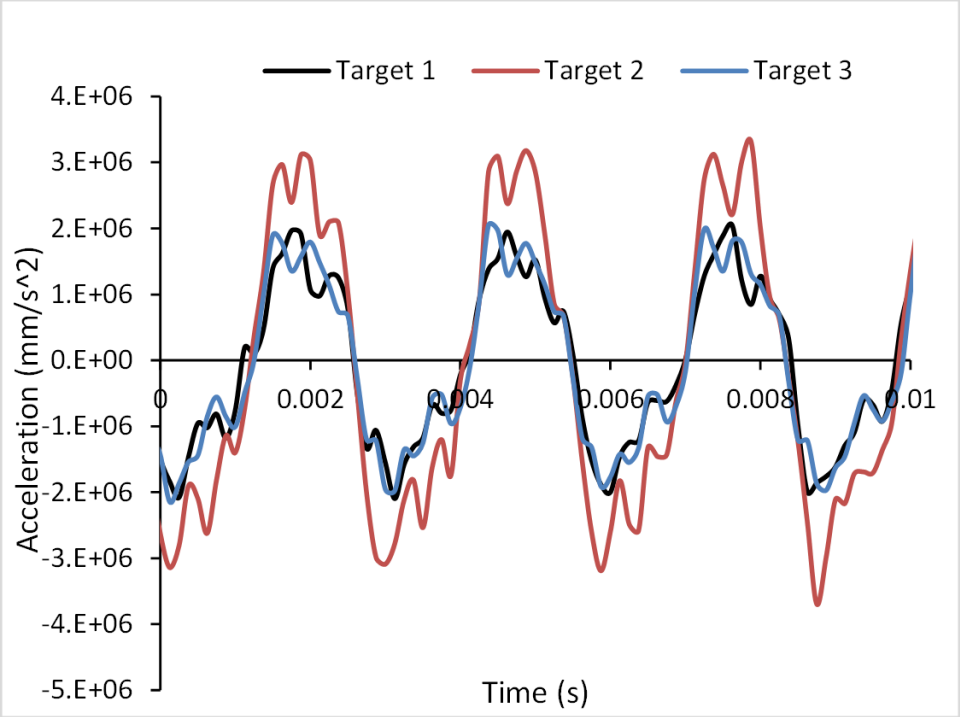

Figure 5.25: Target Acceleration History of PCB Vibrating at 14G

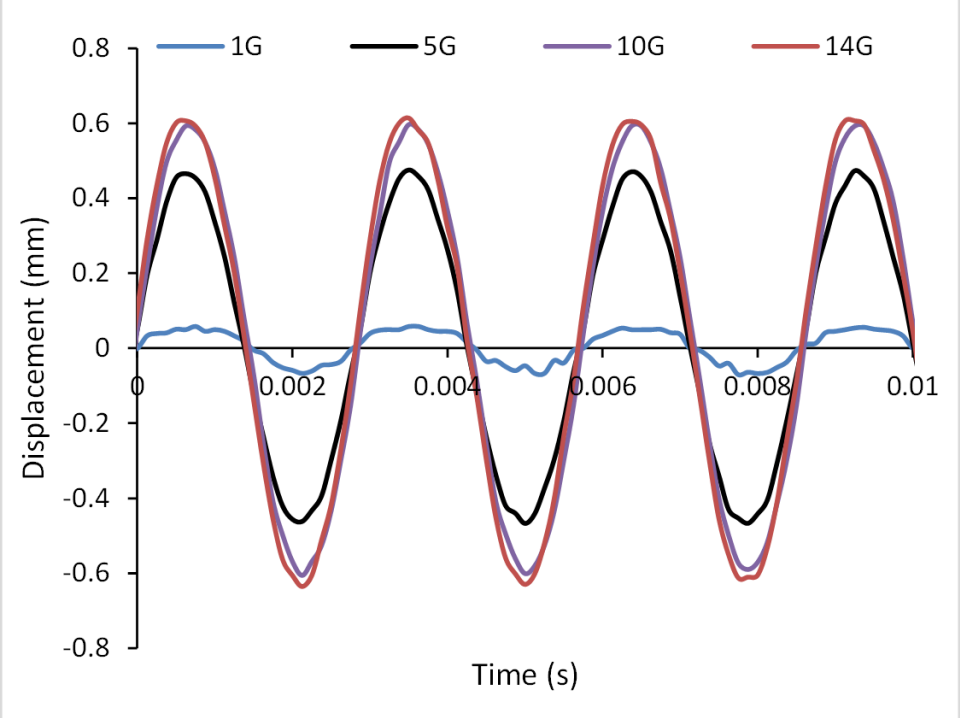

Figure 5.26: Effect of G-level on Displacement History of Target 2

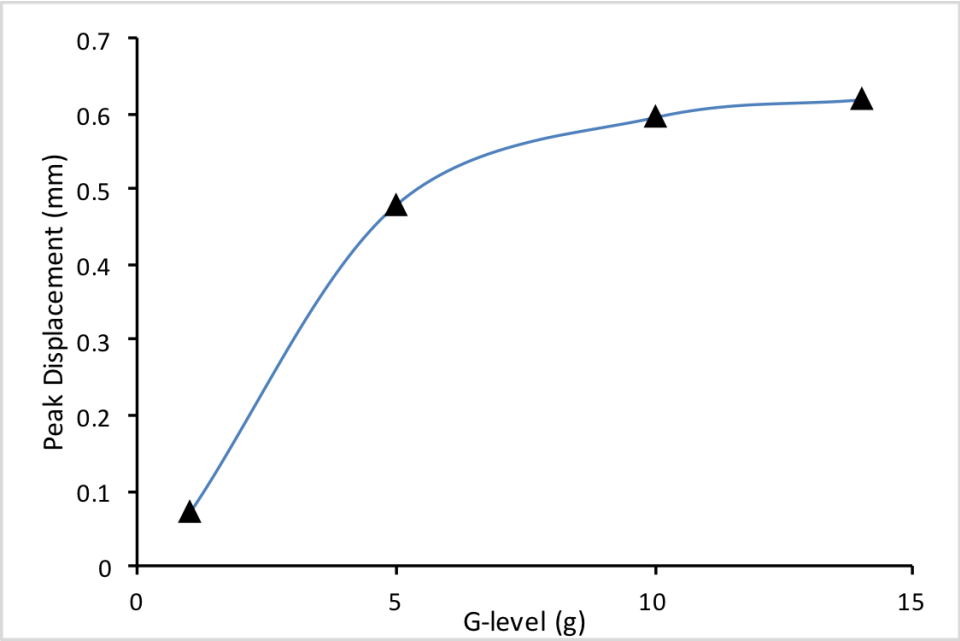

Figure 5.27: Effect of G-level on Peak Displacement of Target 2

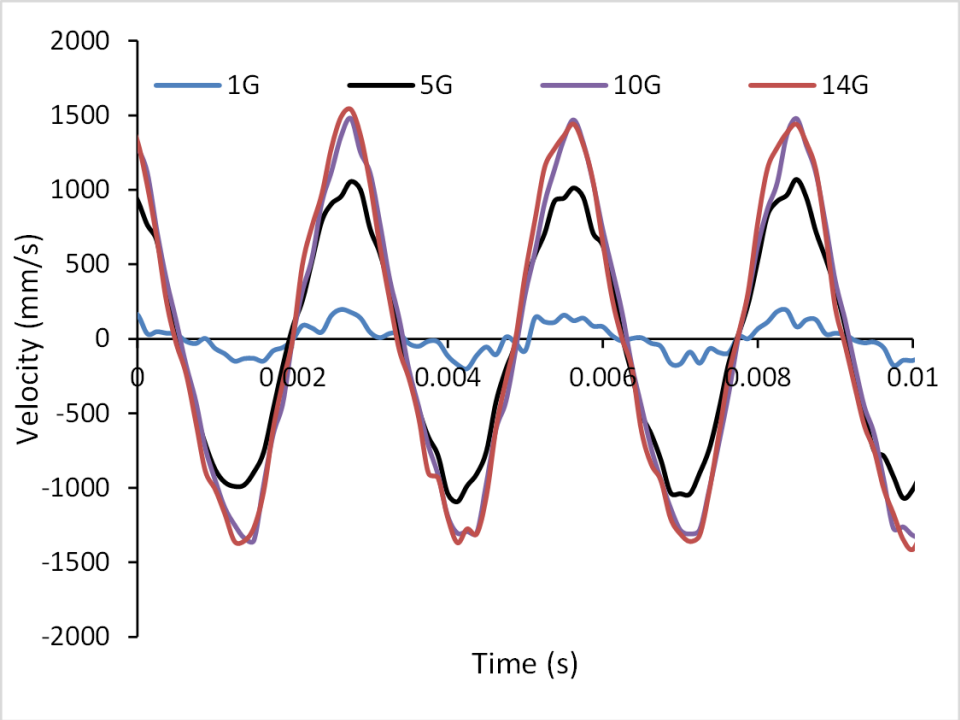

Figure 5.28: Effect of G-level on Velocity History of Target 2

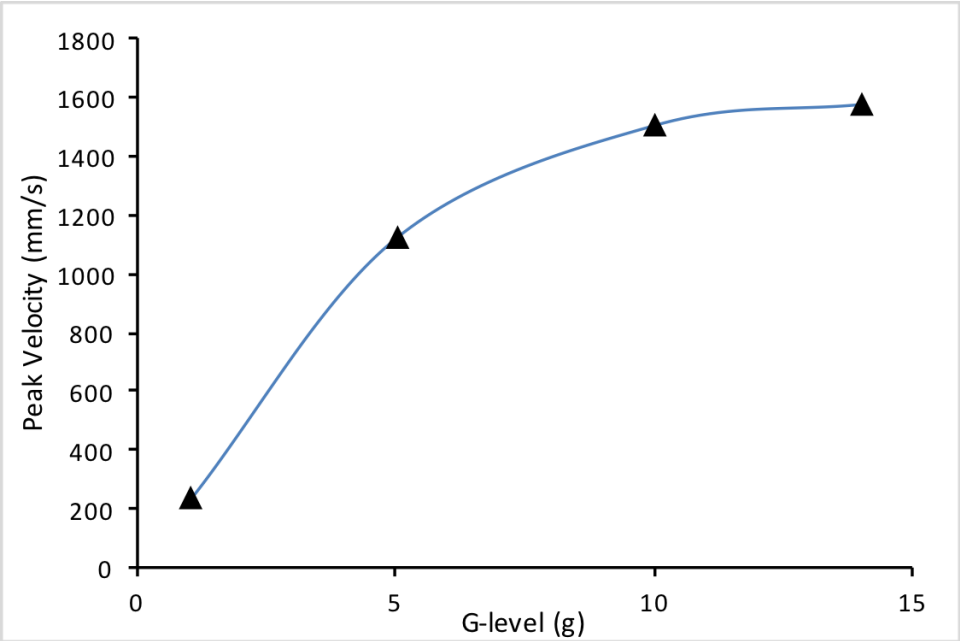

Figure 5.29: Effect of G-level on Peak Velocity of Target 2

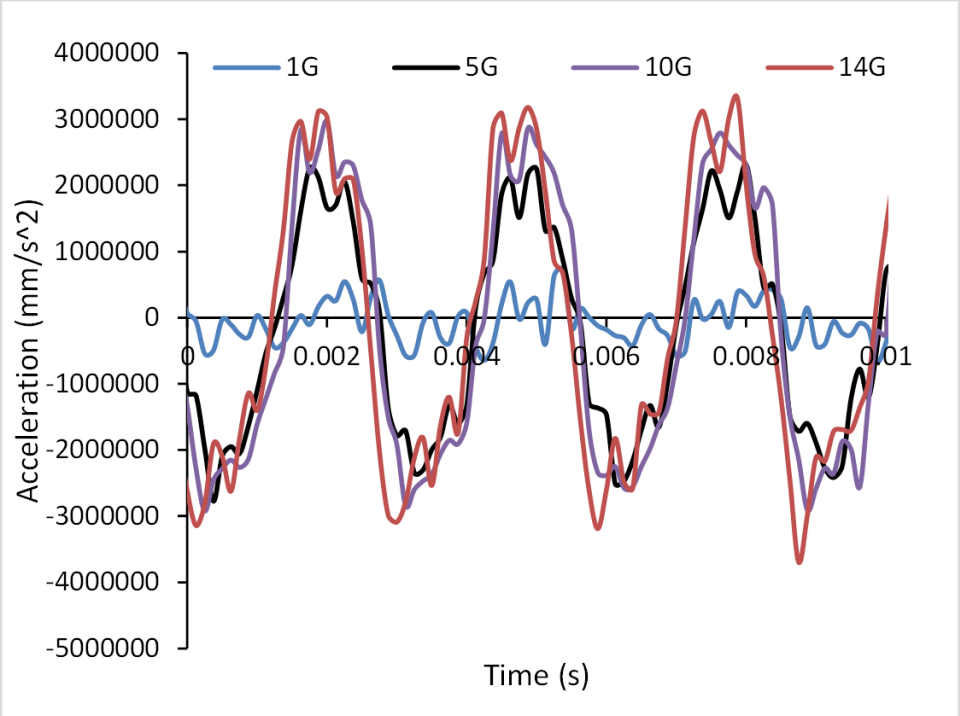

Figure 5.30: Effect of G-level on Acceleration History of Target 2

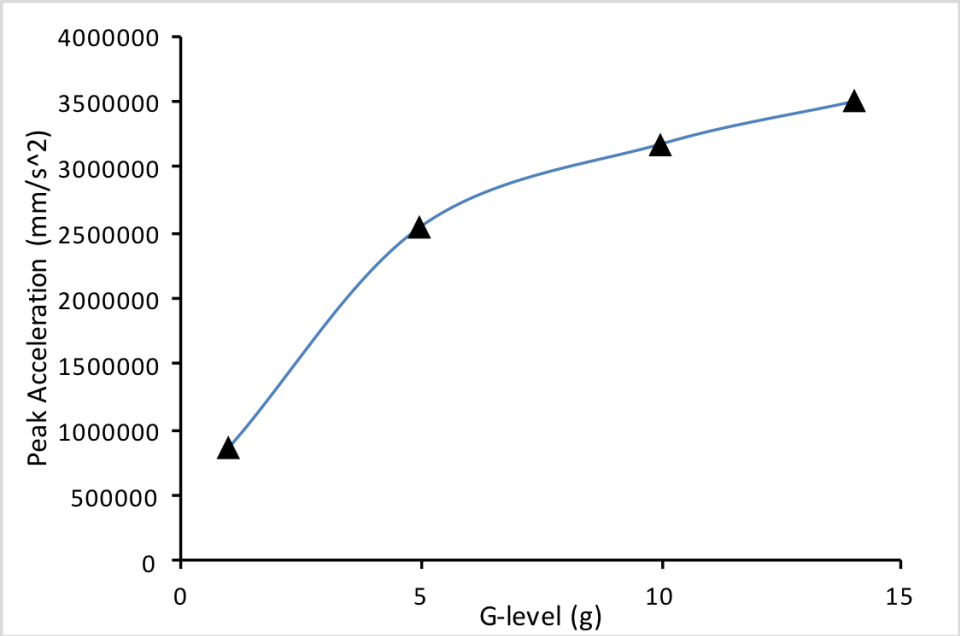

Figure 5.31: Effect of G-level on Peak Acceleration of Target 2

5.7 Finite Element Results of Global Model

Input-G method has been used to simulate this vibration event at its first natural frequency with different G-level and operating temperature. In order to perform this methodology, four mass elements are needed to be created at the center of screw holes. In this way, desired input acceleration values can be converted to force data by applying force to the mass elements. Figure 5.32 shows the mass element created at center of screw holes of PCB. The mass of this element is five order magnitude larger than the actual weight of the test vehicle. And also rigid elements have been created to connect the mass element to PCB around screw holes. Figure 5.33 indicates the desired input excitation from stand off at different G-level. The amplitude and period indicate the G-level and frequency. Based on Newton's Second Law ($F = m \cdot a$), the acceleration data can be converted to force by multiplying the mass. Figure 5.34 shows the input force data changing with time at different G-level. Then a tabular input force is generated based on this data. This tabular force data is applied at the mass node along the normal direction of PCB. A nonlinear transient

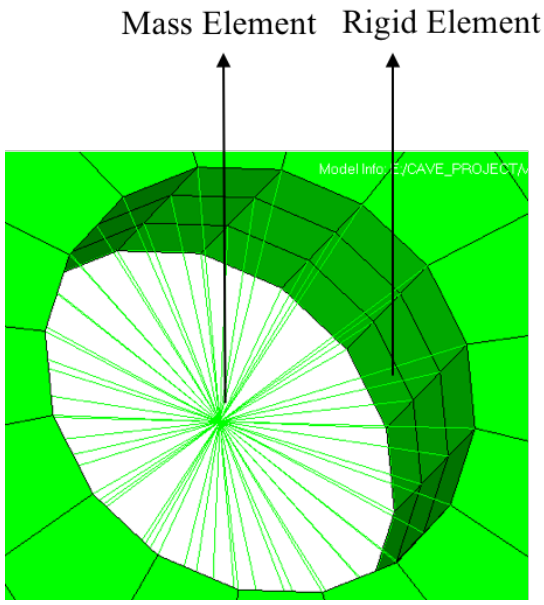

Figure 5.32: Mass and Rigid Element at Screw holes of PCB

analysis is used to analyzed this vibration event. Figure 5.35 shows the acceleration history output at the mass node vibrating at 14g and 360Hz which matches with the desired output values (Figure 5.33).

5.7.1 Displacement at Center of PCB From Simulation

Simulation was running at 14g with 360Hz. Displacement history have been extract at the center of PCB and mass node. The relative displacement at center of PCB is calculated by subtracting the rigid body motion from mass node. Figure 5.36 shows the relative displacement history plot at enter of PCB. The peak value is 0.62mm which is very close the experiment results. Figure 5.37 to Figure 5.39 shows the maximum upward and downward displacement contour of PCB.

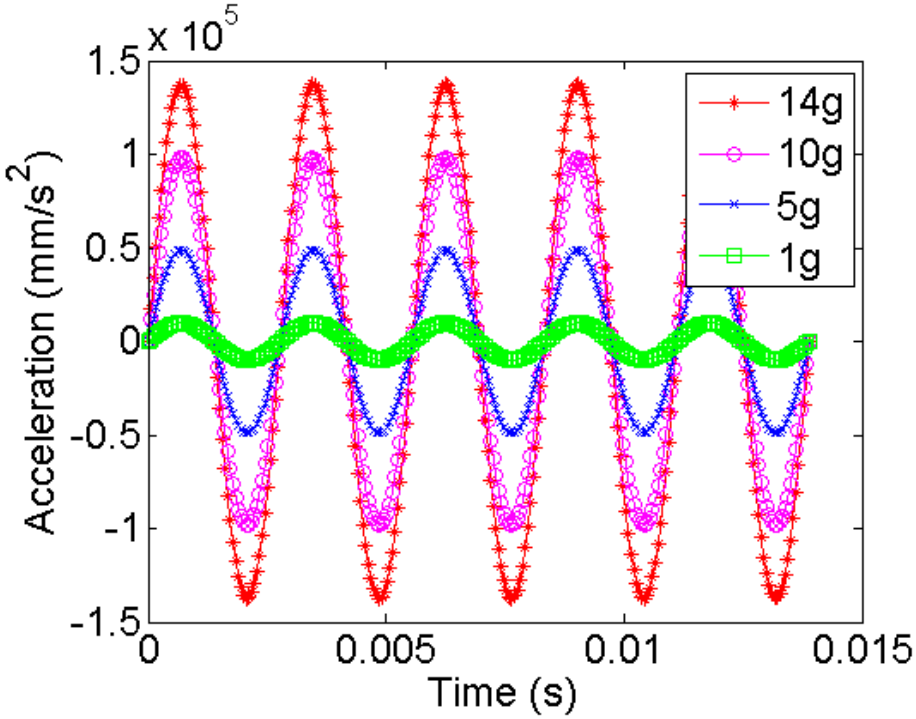

Figure 5.33: Desired Input Excitation

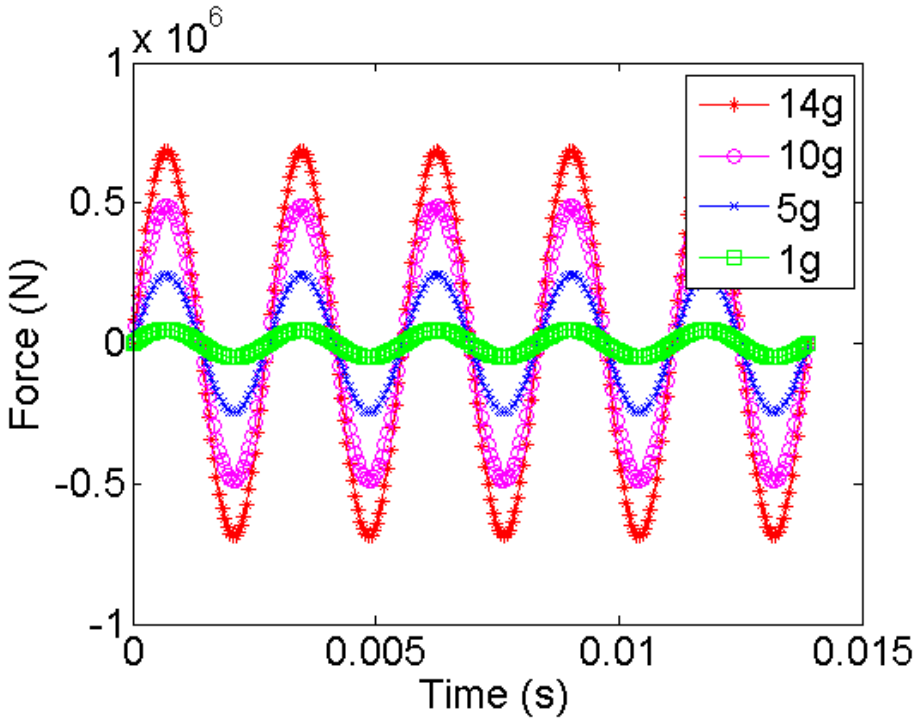

Figure 5.34: Input Tabular Force Data

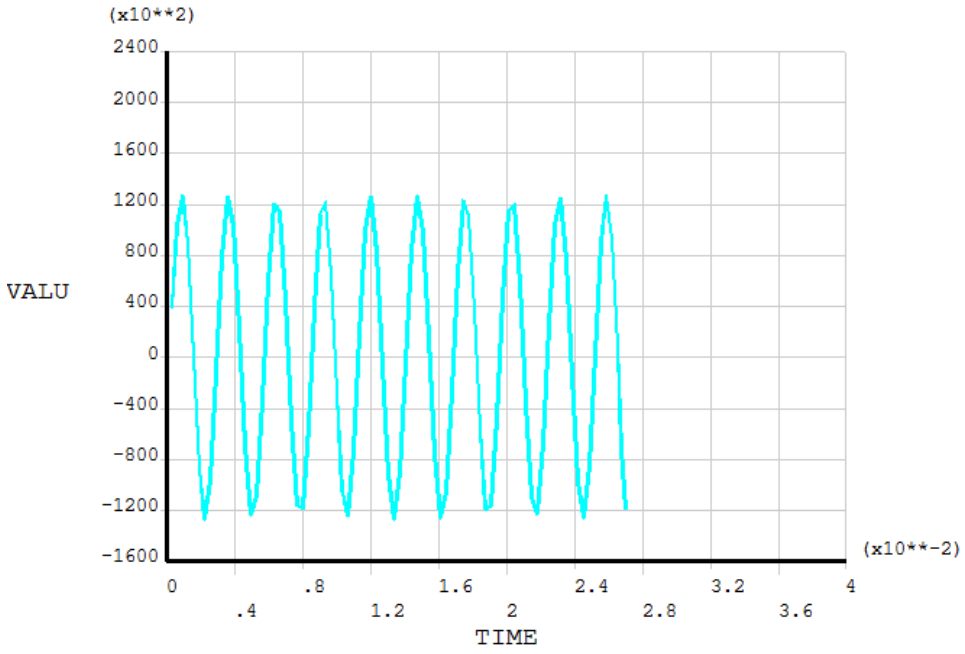

Figure 5.35: Output Acceleration from the Mass node at 14g and 360Hz

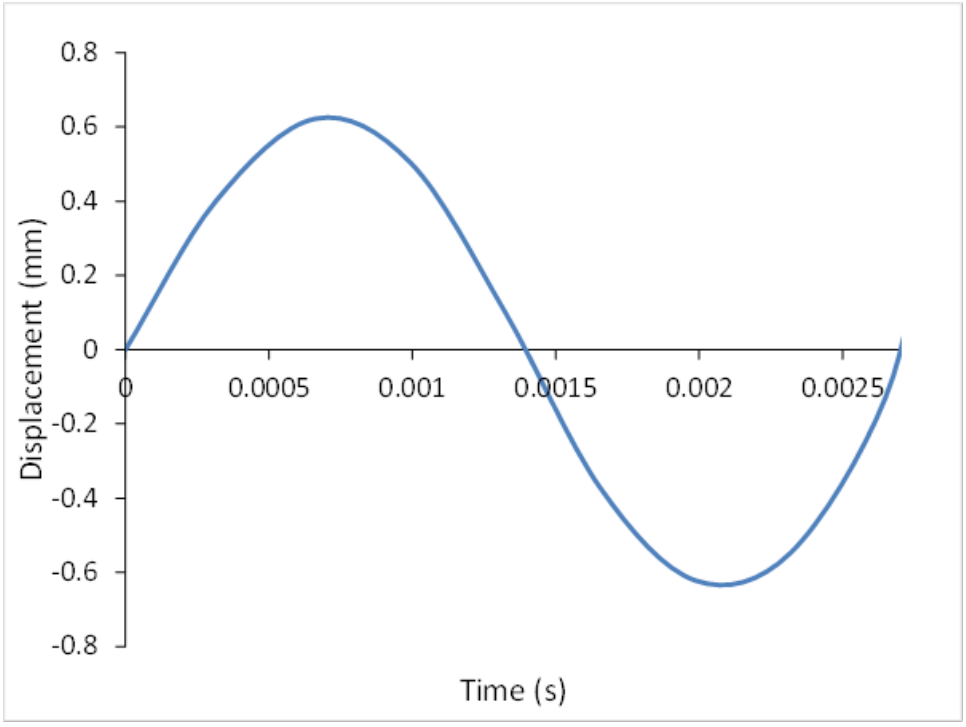

Figure 5.36: Displacement History at Center of PCB at 14g and 25C

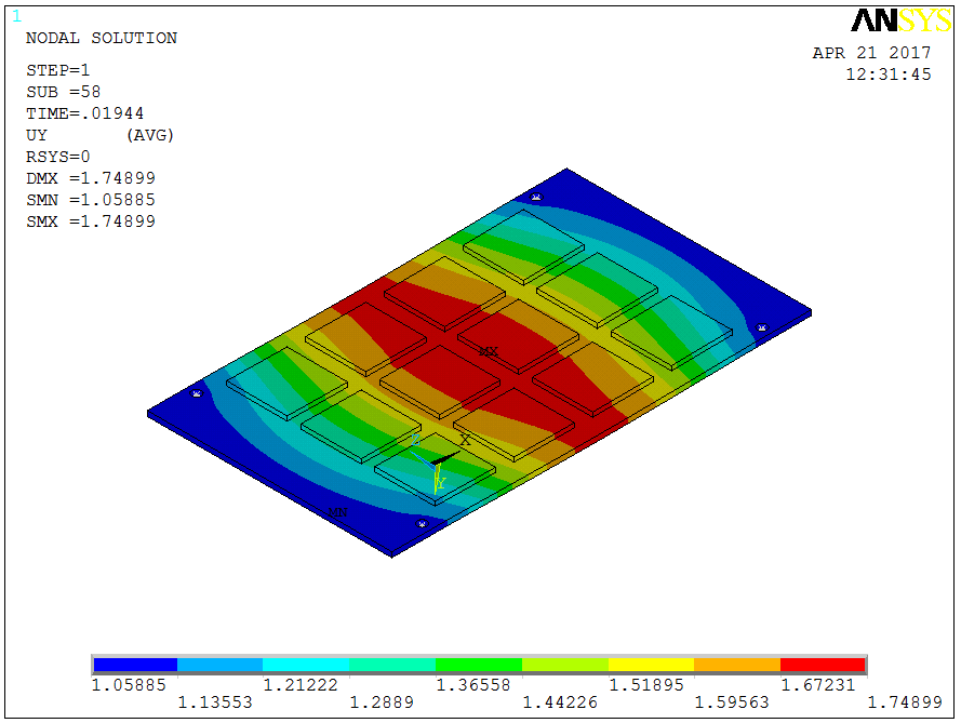

Figure 5.37: Maximum Upward Displacement Contour Plot at 14g and 25C

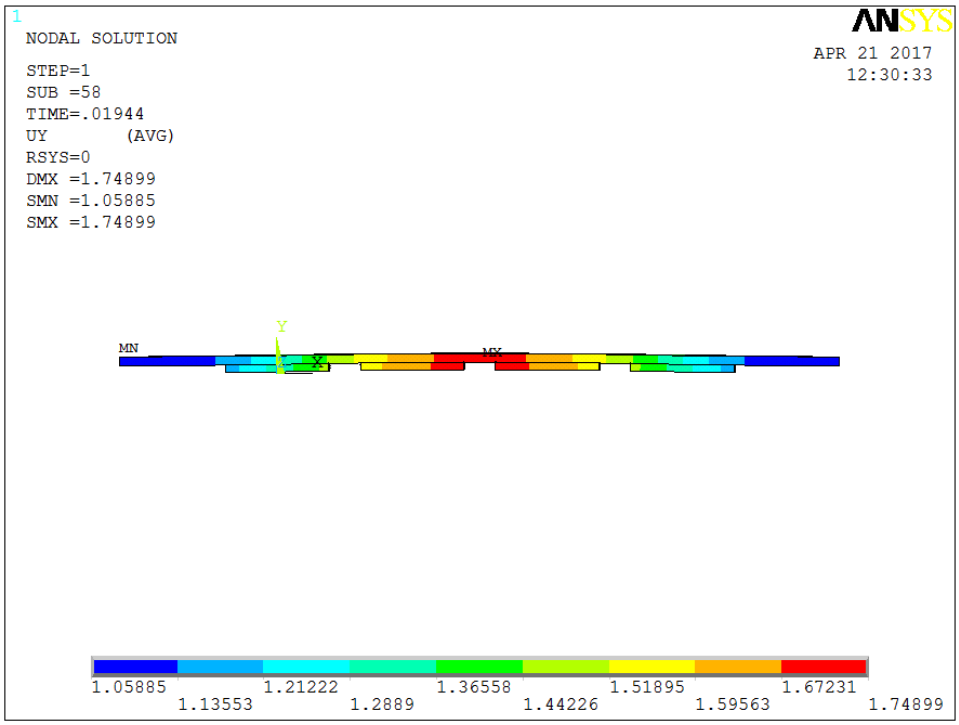

Figure 5.38: Maximum Upward Displacement Contour Plot at 14g and 25C(Front View)

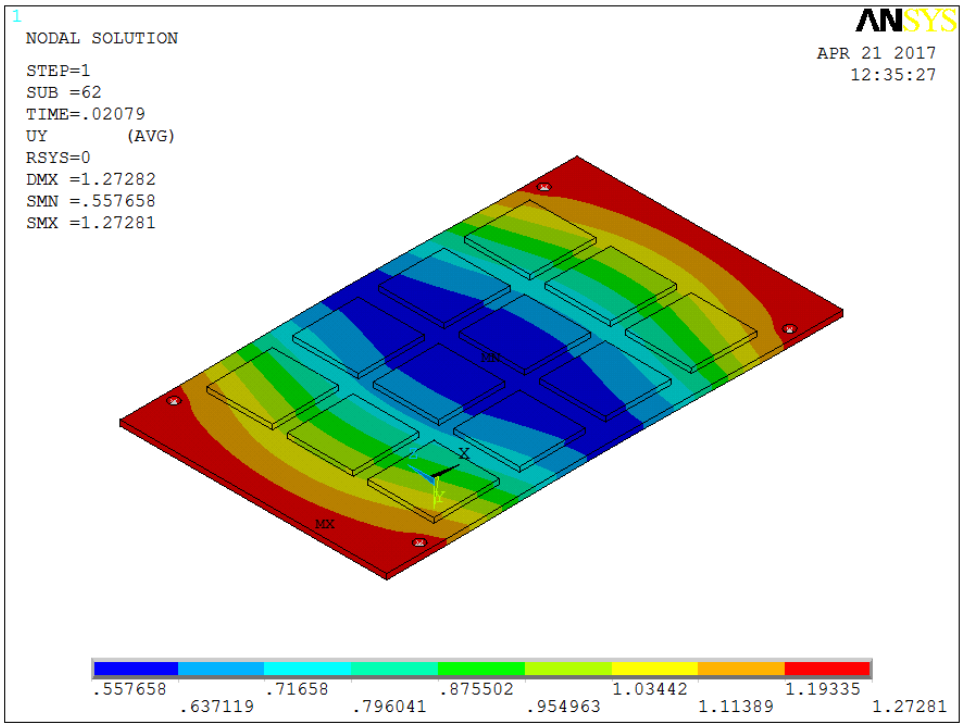

Figure 5.39: Maximum Downward Displacement Contour Plot at 14g and 25C

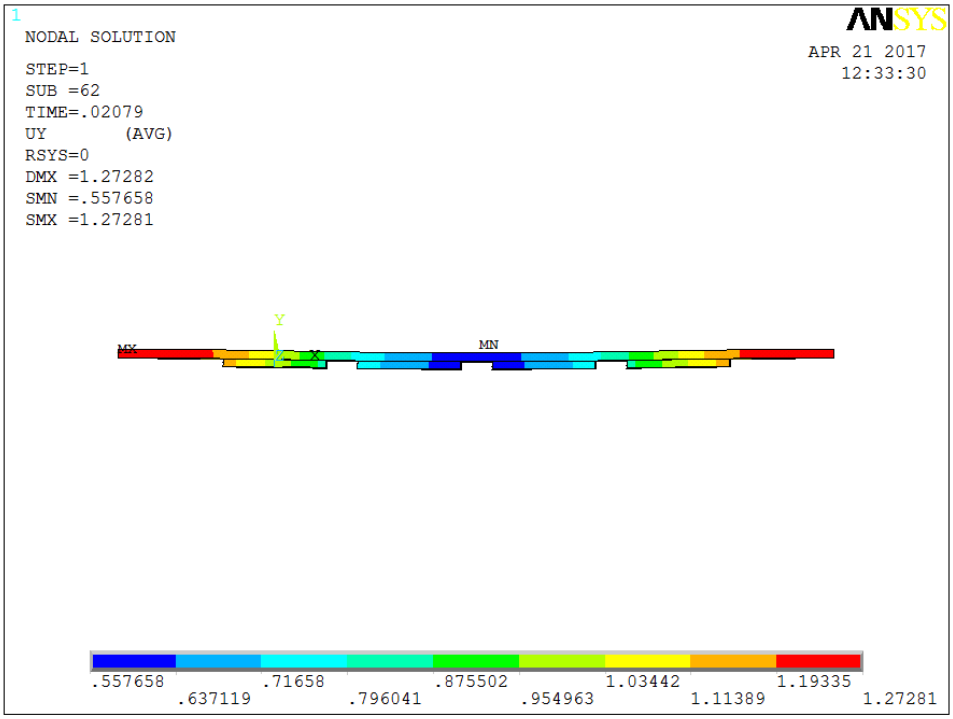

Figure 5.40: Maximum Downward Displacement Contour Plot at 14g and 25C(Front View)

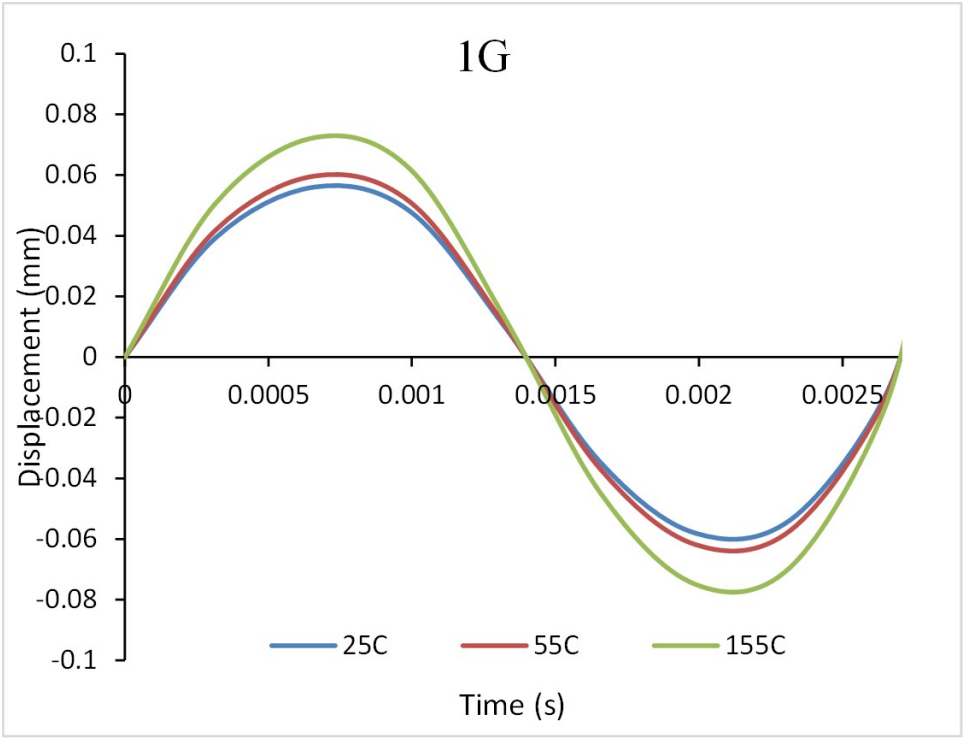

Figure 5.41: Effect of Temperature on Displacement History at Center of PCB at 1g

5.7.2 Effect of Operating Temperatures on Deformation of PCB from Simulation

Since the material properties of PCB are changing with temperature, at different operating temperature, the deformation of PCB subjected to vibration environment is different. Geeta [49] has performed DMA analysis to measure the temperature dependent mechanical properties of PCB. In this section, different groups of vibration simulations are running at various testing temperature (25, 55, 155 °C) and G-level (1, 5, 10, 14G). Figure 5.41 to Figure 5.44 show the displacement history at different temperature at each specific G-level. It is observed that with increasing in operating temperature, the peak displacement of PCB is also increasing. All the peak displacement have extracted from this figure and replotted against operating temperature. Figure 5.45 shows the effect of temperature on peak deflection of PCB at various G-level. From 25 °C to 155 °C, the peak values are increasing by 30 percent.

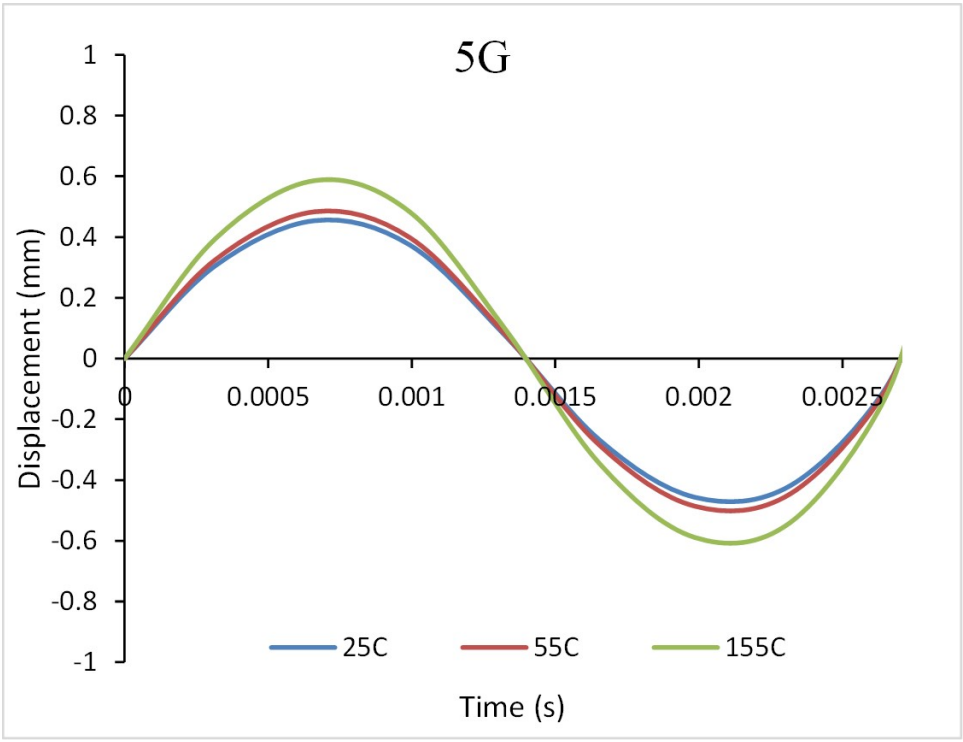

Figure 5.42: Effect of Temperature on Displacement History at Center of PCB at 5g

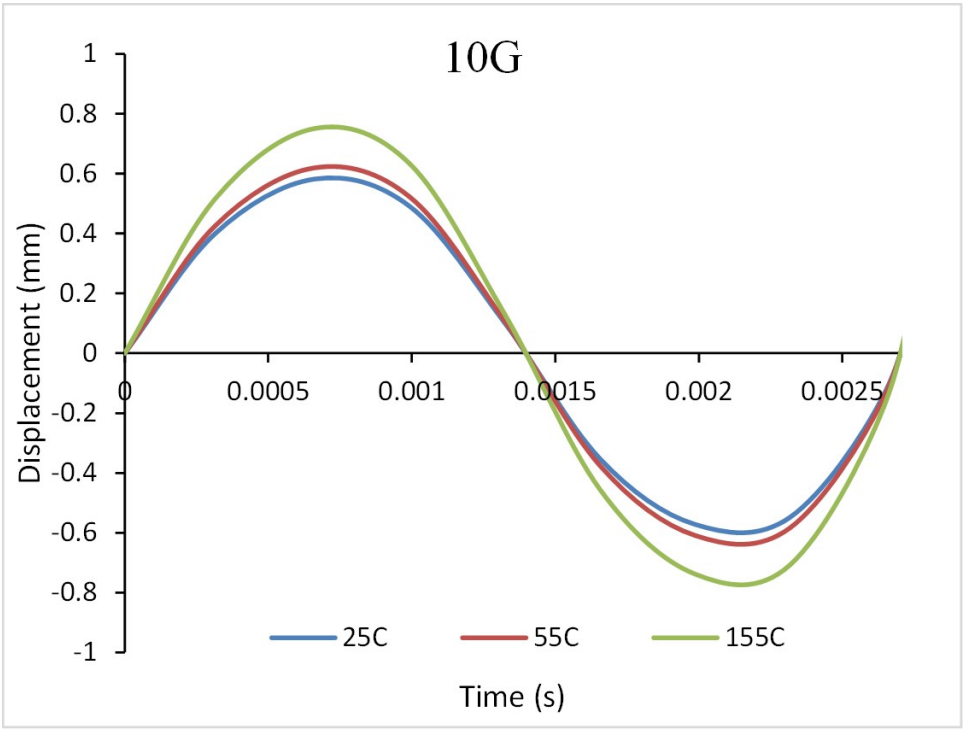

Figure 5.43: Effect of Temperature on Displacement History at Center of PCB at 10g

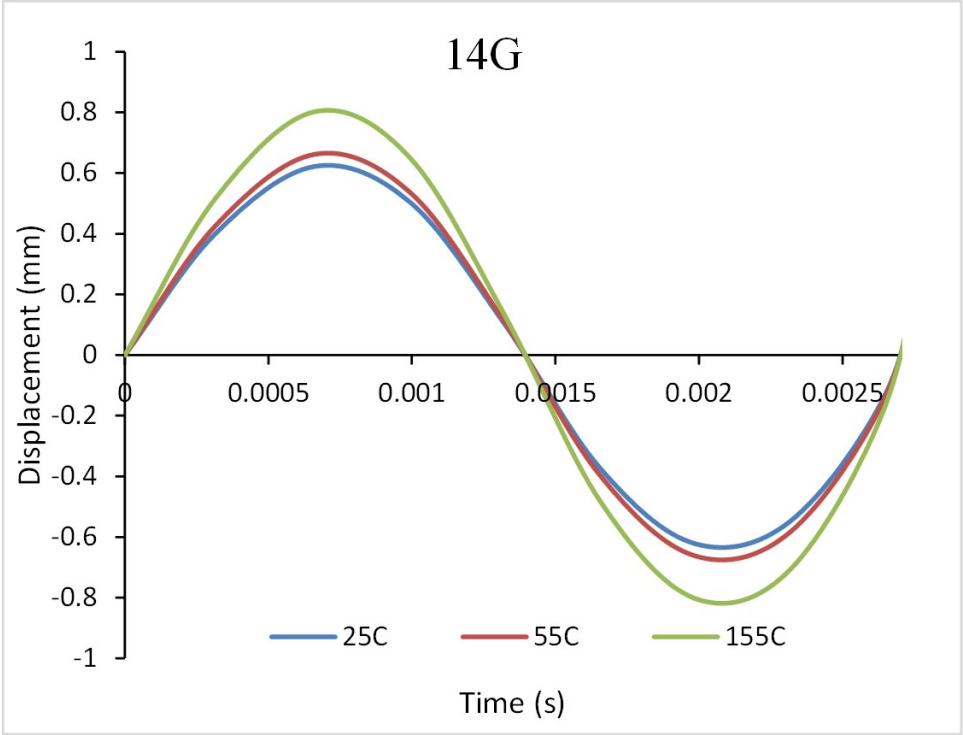

Figure 5.44: Effect of Temperature on Displacement History at Center of PCB at 14g

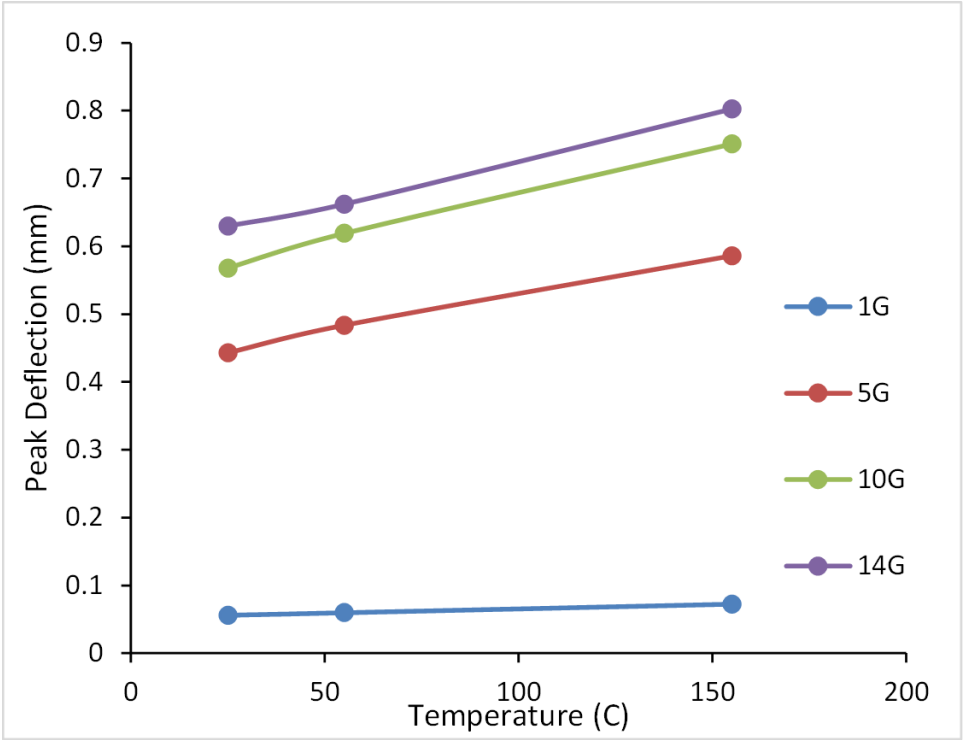

Figure 5.45: Effect of temperature peak displacement at center of PCB

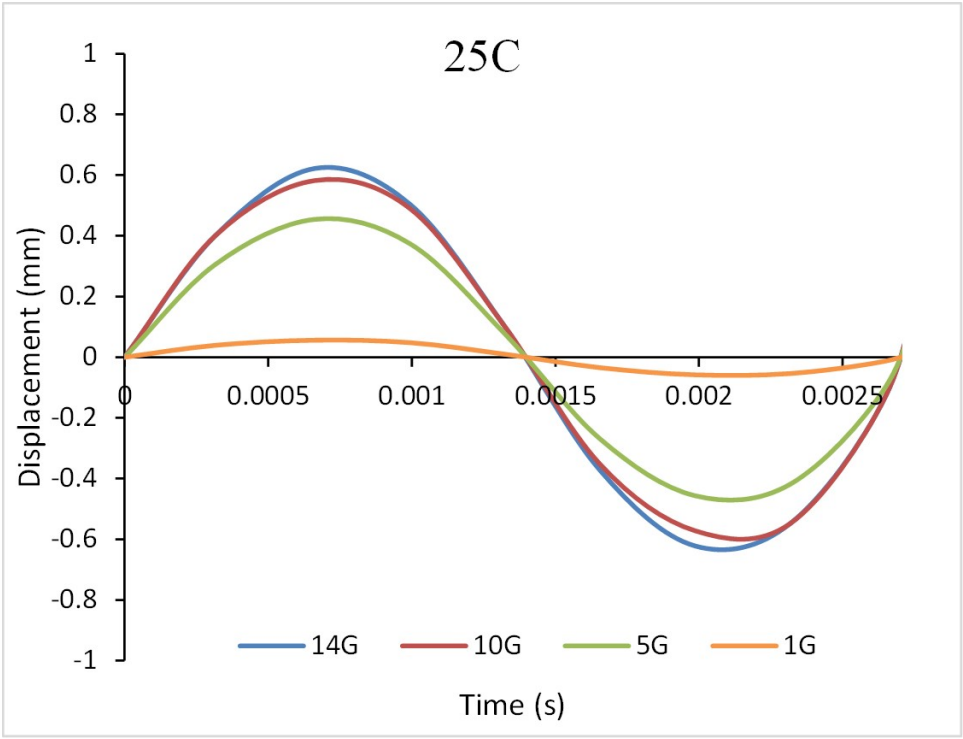

Figure 5.46: Effect of G-level on Displacement History at Center of PCB (25°C)

5.7.3 Effect of Vibration G-Level on Deformation of PCB from Simulation

The above figures have been replotted, in order to study deflection of PCB at different G-level. Figure 5.46 to Figure 5.48 shows the comparison results of at center of PCB at different G-level. it is observed with decreasing in excitation G-level, the displacement amplitude is also reduced. From 14g to 10g, the peak values are decreased by 10 percent. Figure 5.49 shows the relationship between input G-level and peak output displacement.

5.8 Validation of Simulation Results

The displacement histories from simulation at different G-level have been compared with experimental results at Target 4. Figure 5.50 to 5.53 shows the deflection comparing results at different G-level. It is obvious that the experiment results match very well with the simulation results. Figure 5.54 shows the peak displacement correlations.

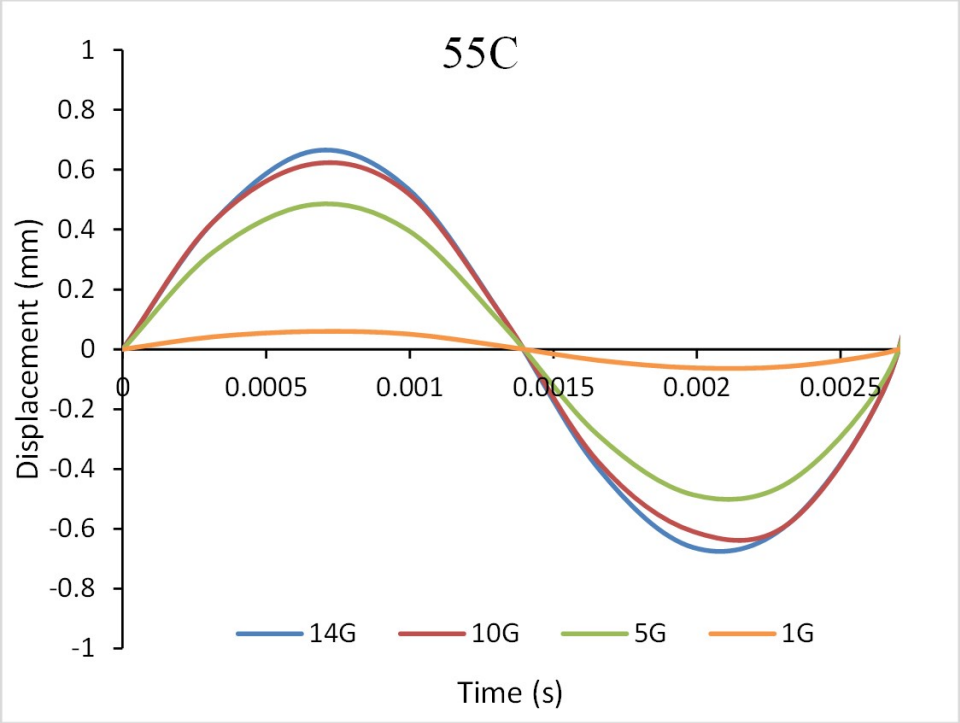

Figure 5.47: Effect of G-level on Displacement History at Center of PCB (55°C)

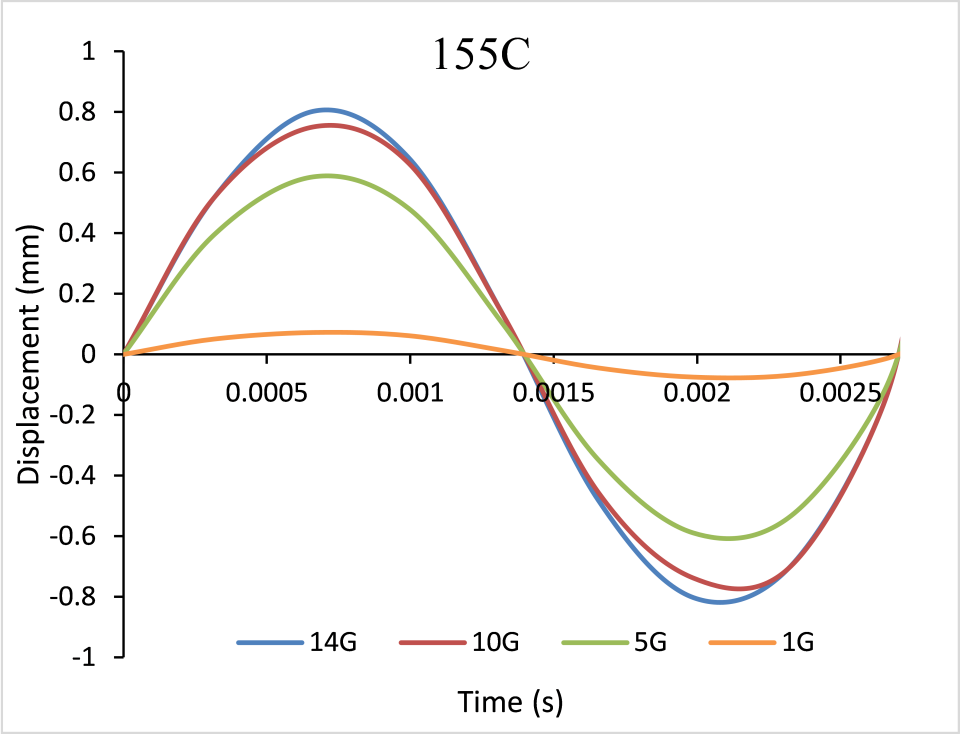

Figure 5.48: Effect of G-level on Displacement History at Center of PCB (155°C)

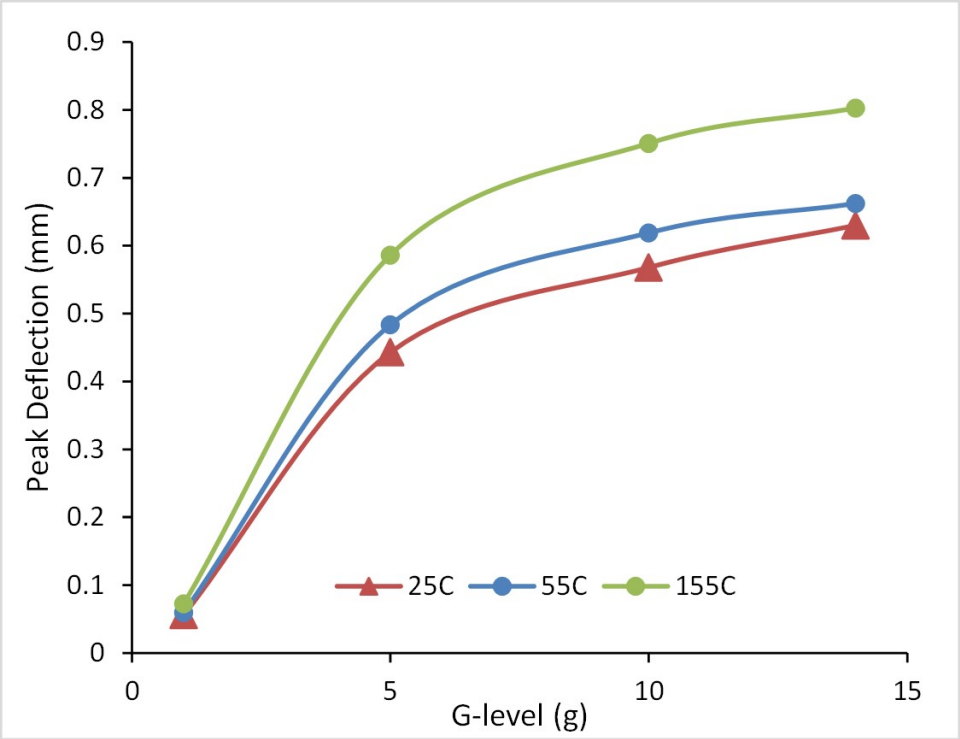

Figure 5.49: Effect of G-level on Peak Displacement at Center of PCB

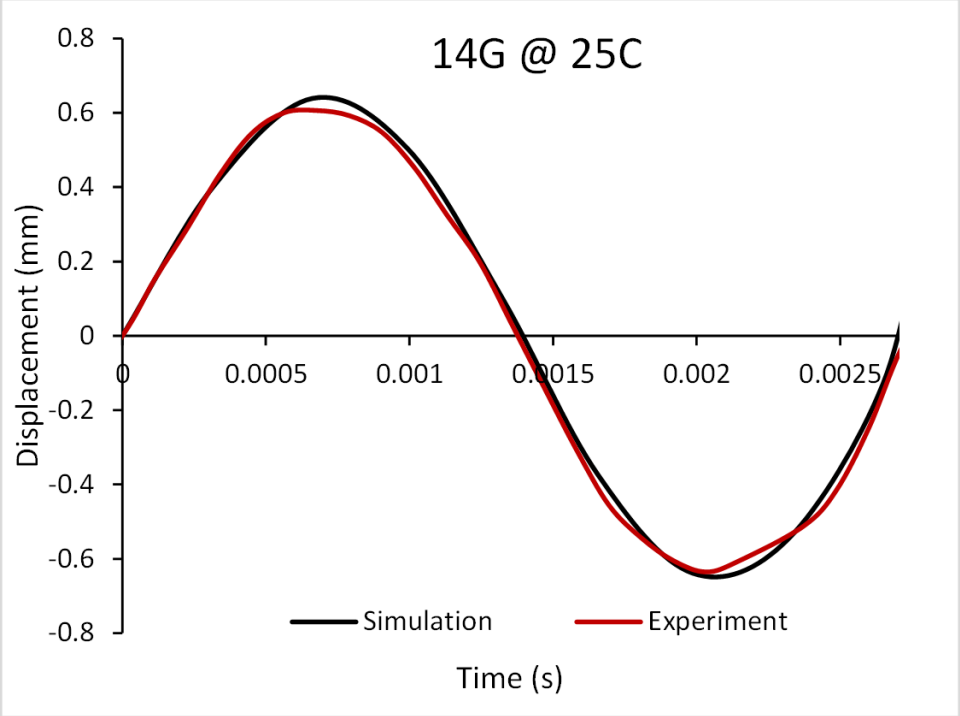

Figure 5.50: Displacement History Correlation at Target 4 between Experiment and Simulation at 14g

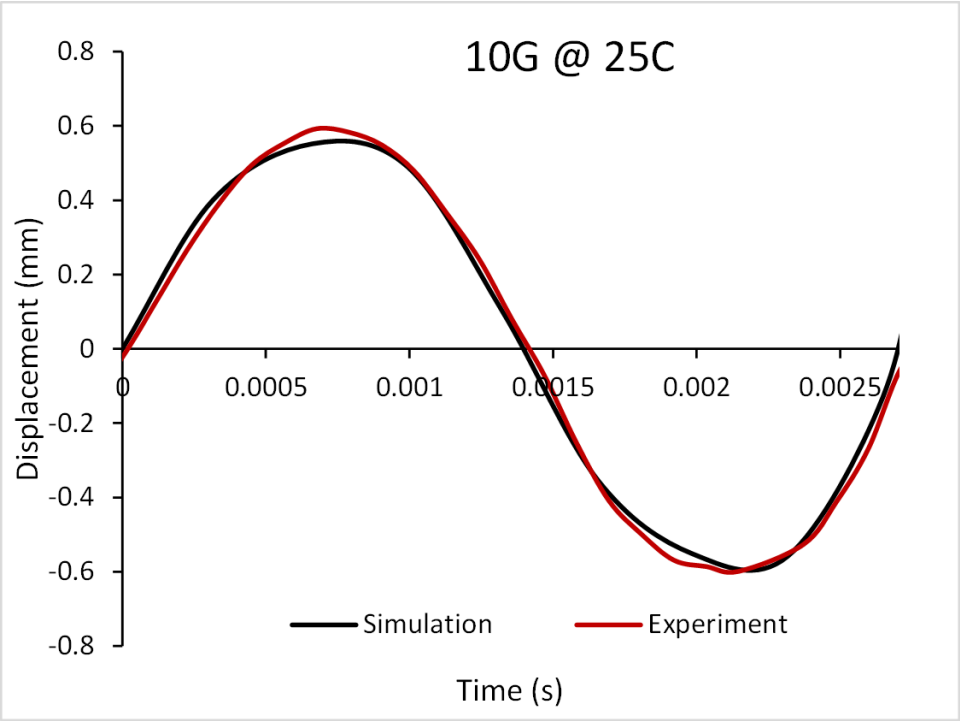

Figure 5.51: Displacement History Correlation at Target 4 between Experiment and Simulation at 10g

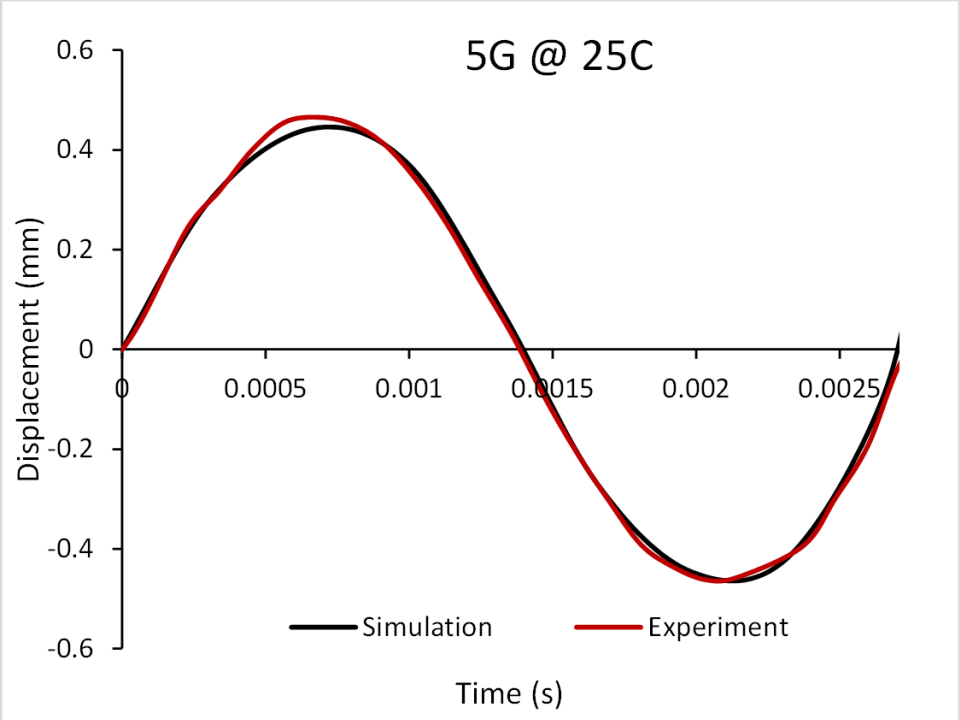

Figure 5.52: Displacement History Correlation at Target 4 between Experiment and Simulation at 5g

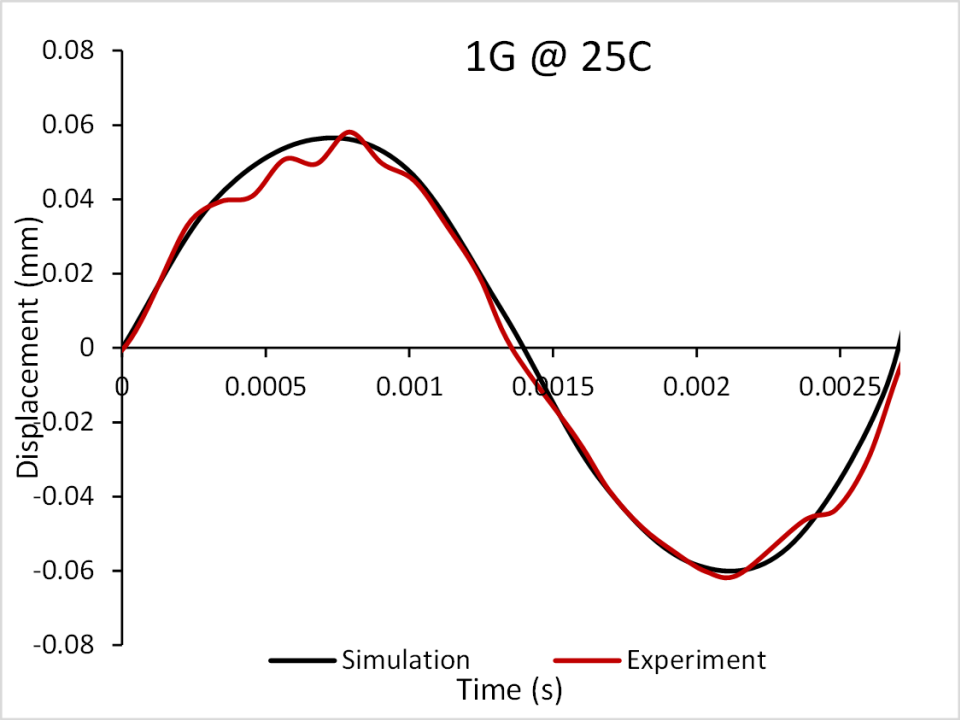

Figure 5.53: Displacement History Correlation at Target 4 between Experiment and Simulation at 1g

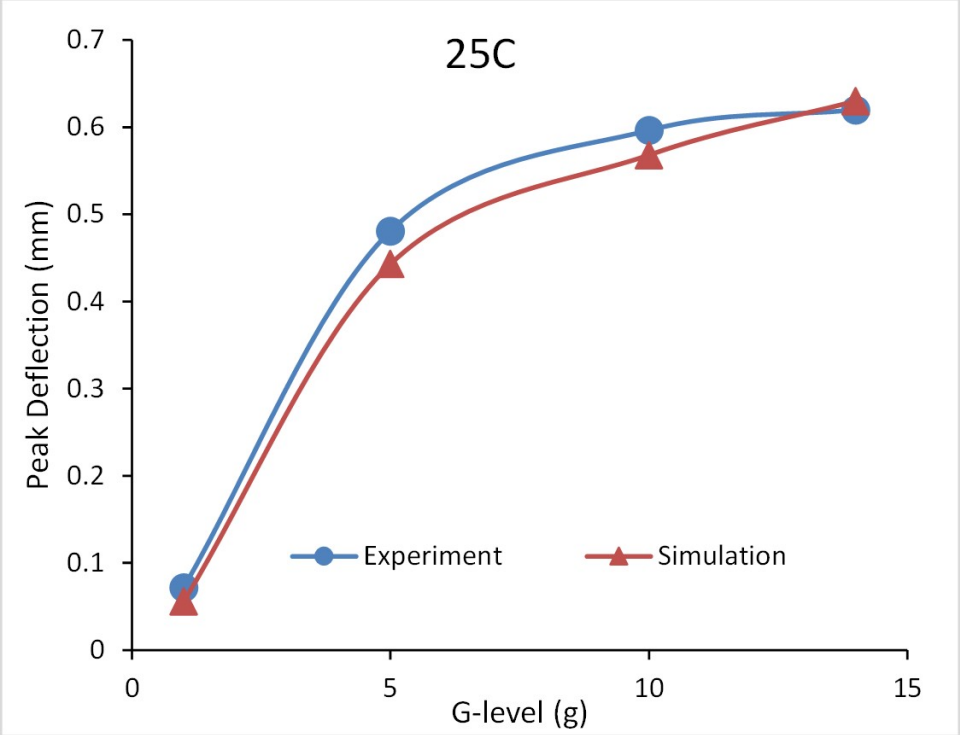

Figure 5.54: Peak Displacement Correlation at Target 4 between Experiment and Simulation

5.9 Nonlinear Sub-modeling

5.9.1 Introduction to Sub-modeling

Sub-modeling has been used by researchers to obtain solutions at local areas. Although sub-modeling may be commonly thought of as being applicable to linear static structural solutions, it can also be applied to nonlinear and transient analyses. Lall [35] has used node based method to perform nonlinear submodeling by input experiment displacement to simulation as boundary conditions. Submodeling technique can be used for nonlinear analysis, but it need more work to get it running. Generally, there are two kinds of nonlinear simulaiton, one is path-dependent and another is path-indepednent. For path-dependent problems, such as nonlinear constitutive equation, contact analysis, the energy is conservative, the traditional way of submodeling is not working properly. In order to solve this problem, Sheldon (ANSYS Tips and Tricks) has proposed a method named nonlinear submodeling method. By using this concept, sub-modeling with nonlinearity can be solved. There are basic some steps to perform nonlinear submodeling. Figure 5.55 shows the detail procedures how to implement non-linear submodeling in ANSYS.

5.9.2 Submodel of Test Vehicle

Based the global model, a submodel is generated at same coordinate system. Figure 5.56 and Figure 5.57 show the submodel of CABGA288 at different views, the four corner solder ball are created and meshed with VISCO107. Figure 5.58 shows the meshed details of solder joint. Based on above discussion about procedures of nonlinear sub-modeling, this method has been used for running simulation. Figure 5.59 shows the meshed geometry with tabular cutting boundary displacement history applied in ANSYS APDL.

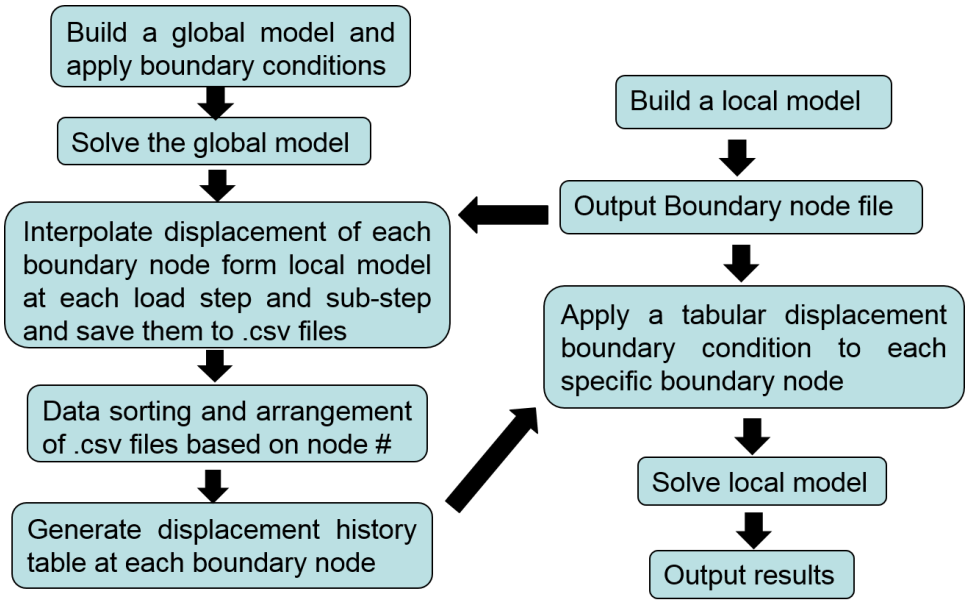

Figure 5.55: Flow Chart of Nonlinear Submodeling Technique

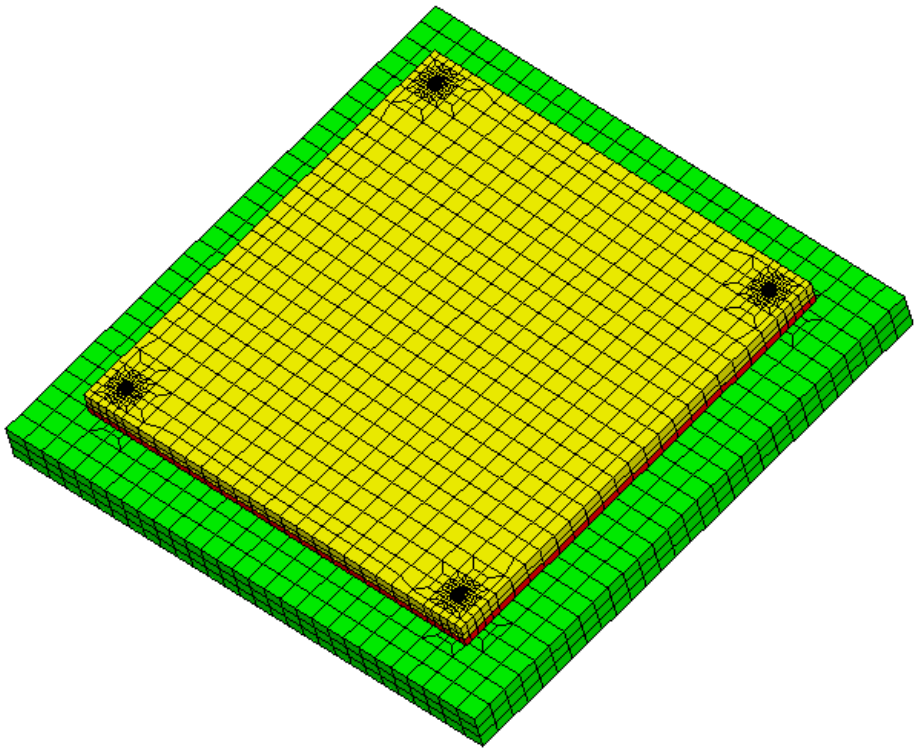

Figure 5.56: General View of CABGA288

Figure 5.57: Front View of CABGA288

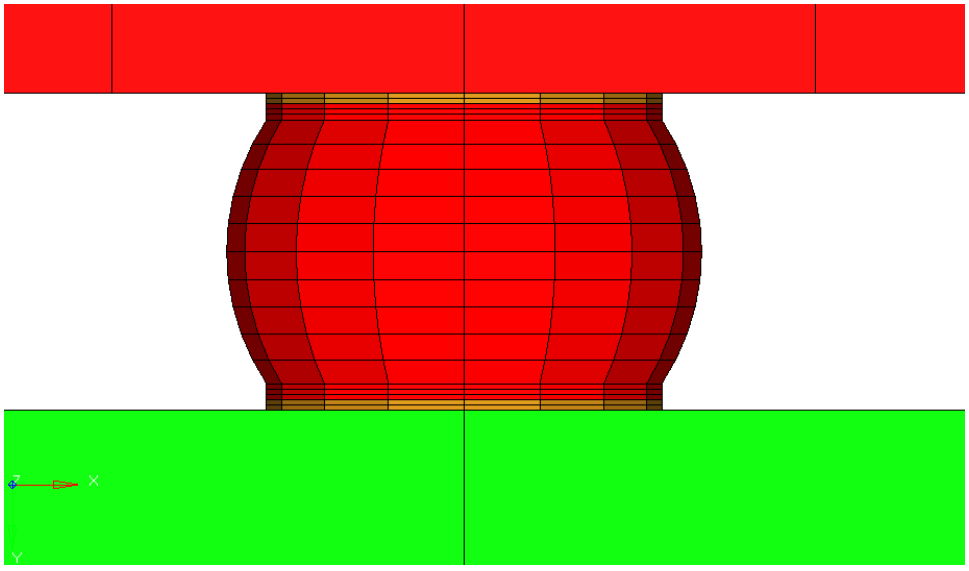

Figure 5.58: Solder Ball Details of CABGA288

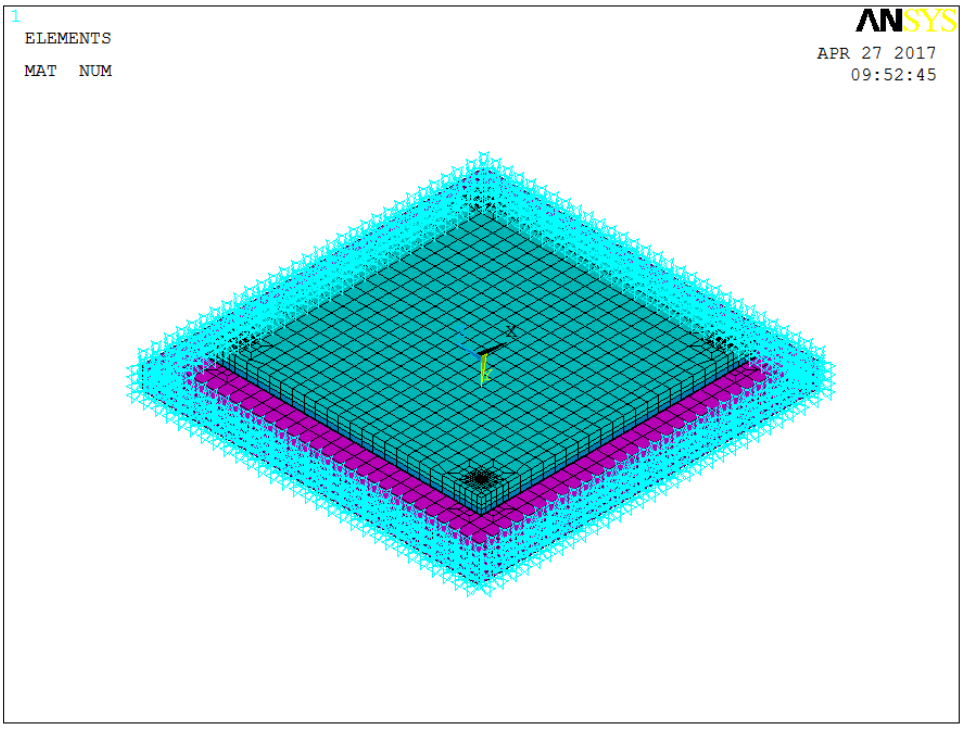

Figure 5.59: Boundary Condition of CABGA288 in ANSYS

5.9.3 Stress of Critical Solder Joint

Critical solder joint is observed at the corner of the package from the simulation results. Figure 5.60 and Figure 5.61 show the solder joint stress distribution of U6 at maximum upward and downward deformation of PCB at 25°C and 14G. Figure 5.68 and Figure 5.69 show stress contour plot of critical solder joint of U6 at 25°C and 14G. It is observed the maximum stress happened between the solder joint and the copper pad.

5.9.4 Hysteresis Loop of Critical Solder Joint

Stress and strain data of critical solder joint is calculated based on volume average technique which can help to eliminate the mesh density effect on finite element results (Equation 5.1 and 5.2). The top layer of solder joint is used to calculate average stress and strain values. Hysteresis loop is also plotted based on stress and strain data of critical solder joint. Figure

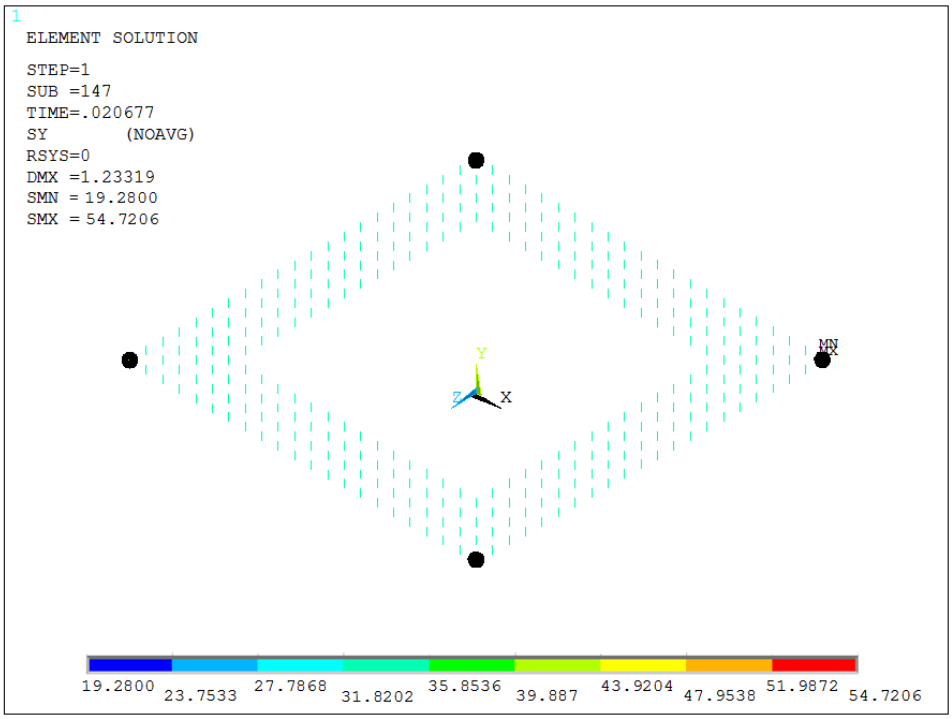

Figure 5.60: Solder Joint Stress Distribution of U6 at Maximum Downward Deformation of PCB (14g, 25°C)

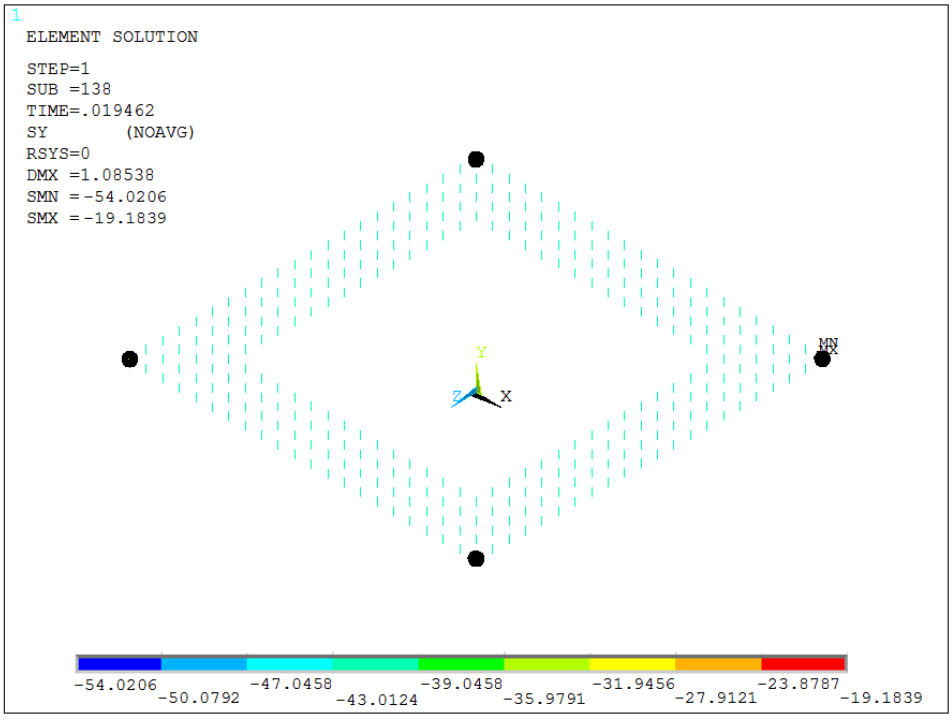

Figure 5.61: Solder Stress Distribution of U6 at Maximum Upward Deformation of PCB (14g, 25°C)

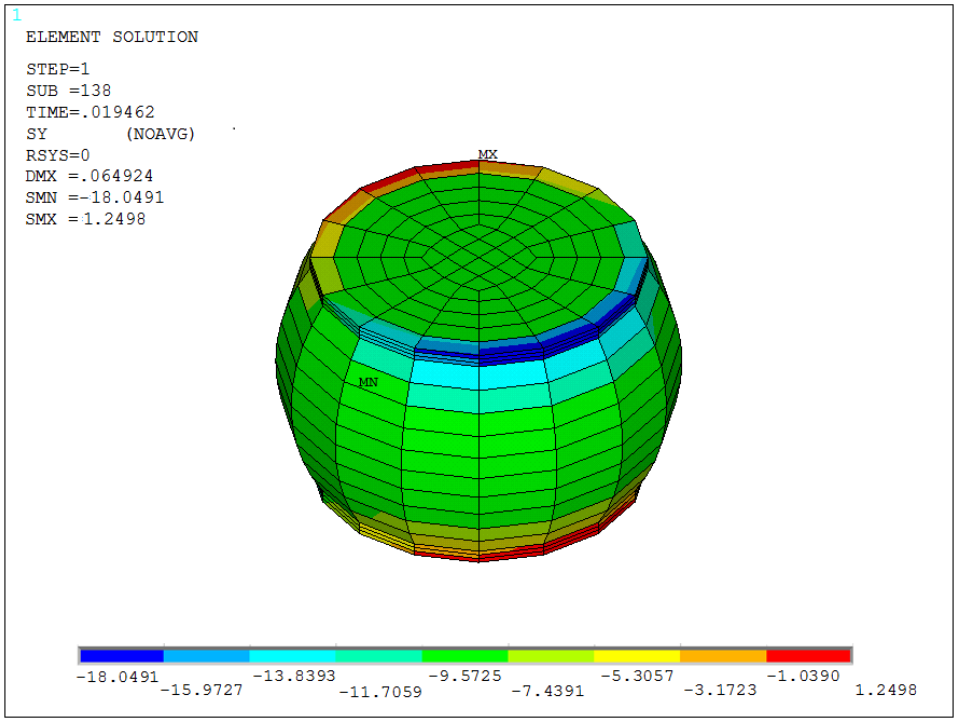

Figure 5.62: Critical Solder Joint Stress Contour of U6 at Maximum Upward Deformation of PCB (1g, 25°C)

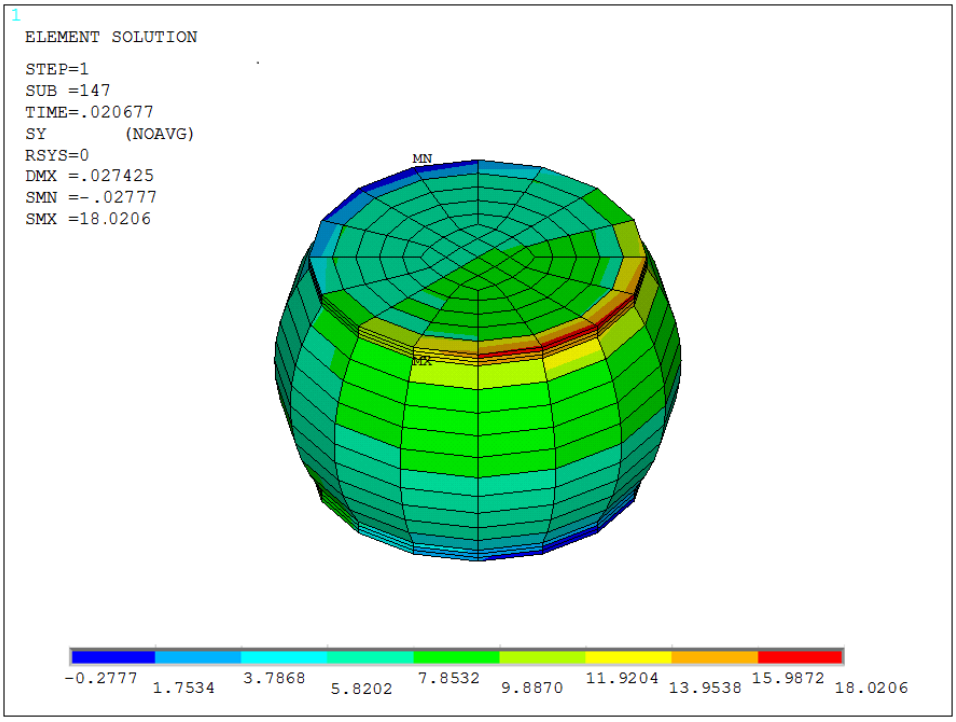

Figure 5.63: Critical Solder Joint Stress Contour of U6 at Maximum Downward Deformation of PCB (1g, 25°C)

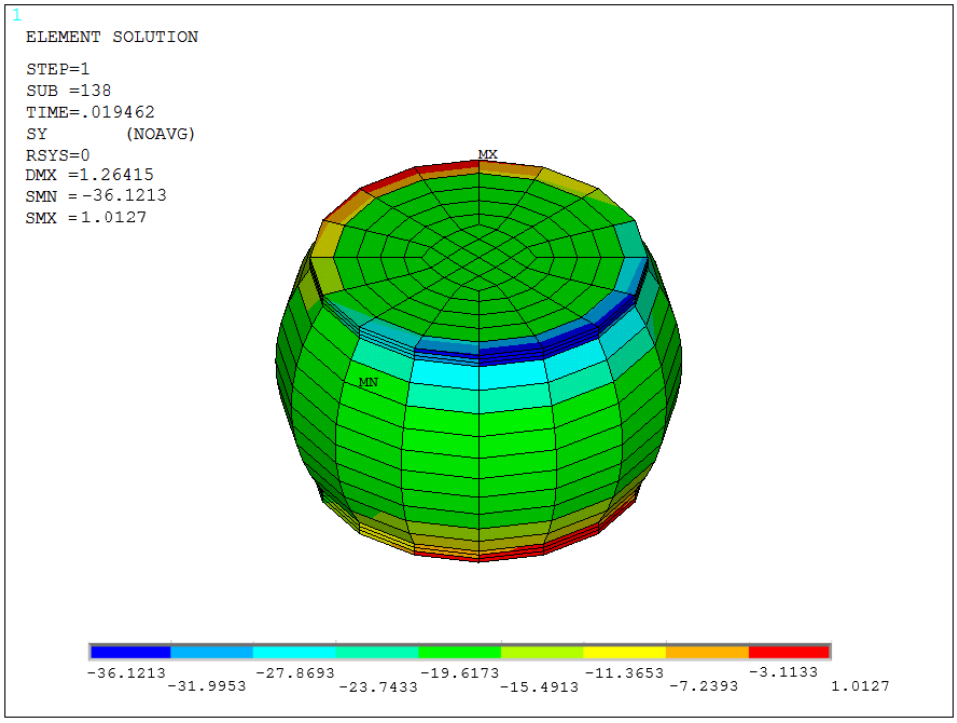

Figure 5.64: Critical Solder Joint Stress Contour of U6 at Maximum Upward Deformation of PCB (5g, 25°C)

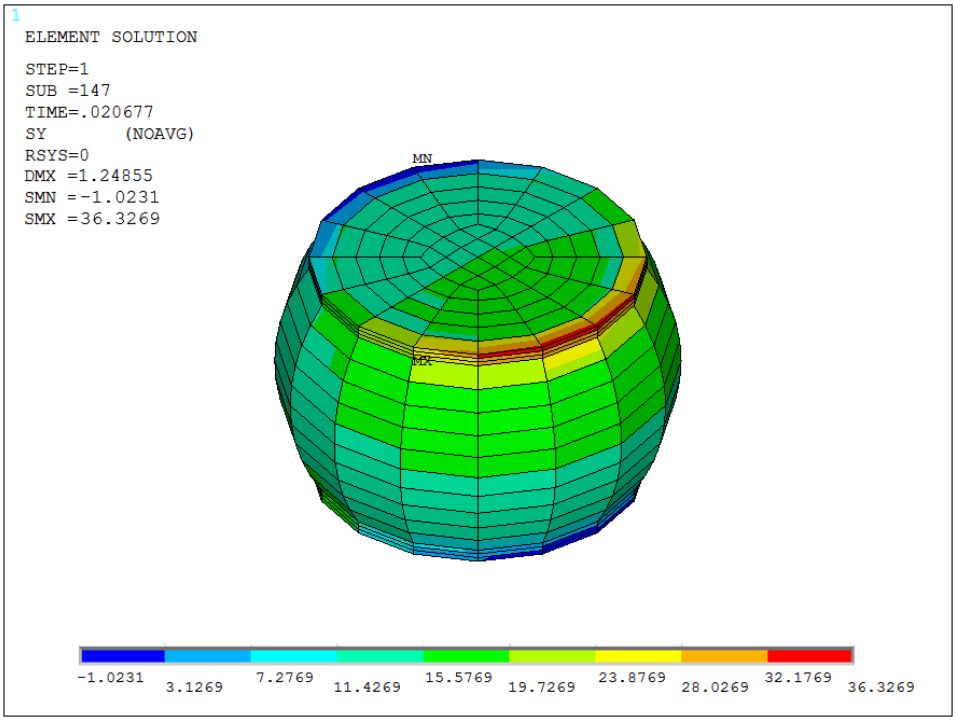

Figure 5.65: Critical Solder Joint Stress Contour of U6 at Maximum Downward Deformation of PCB (5g, 25°C)

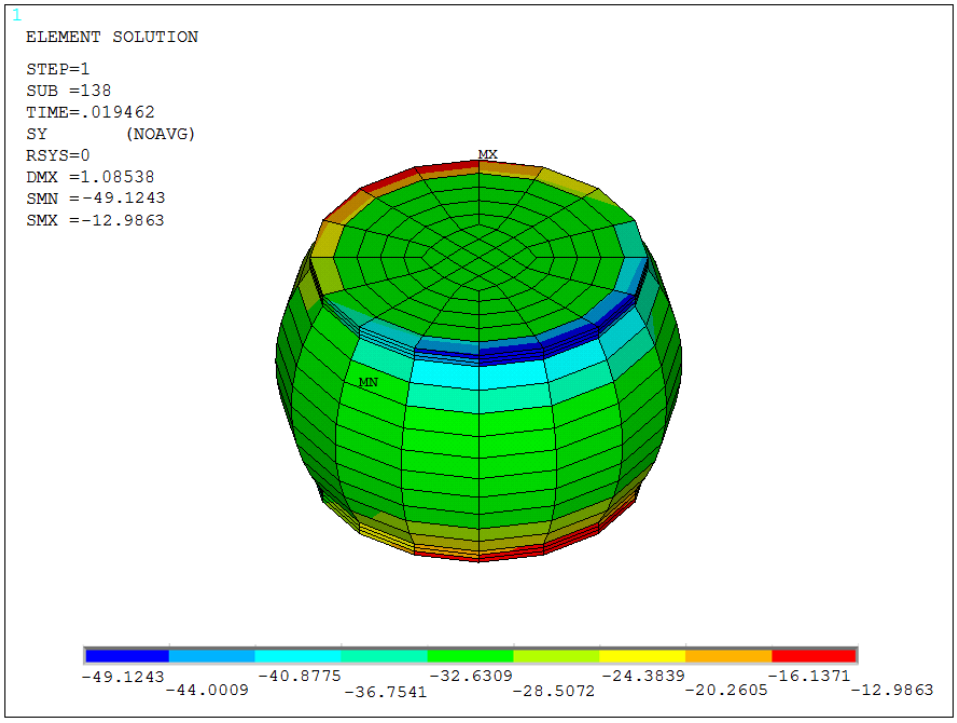

Figure 5.66: Critical Solder Joint Stress Contour of U6 at Maximum Upward Deformation of PCB (10g, 25°C)

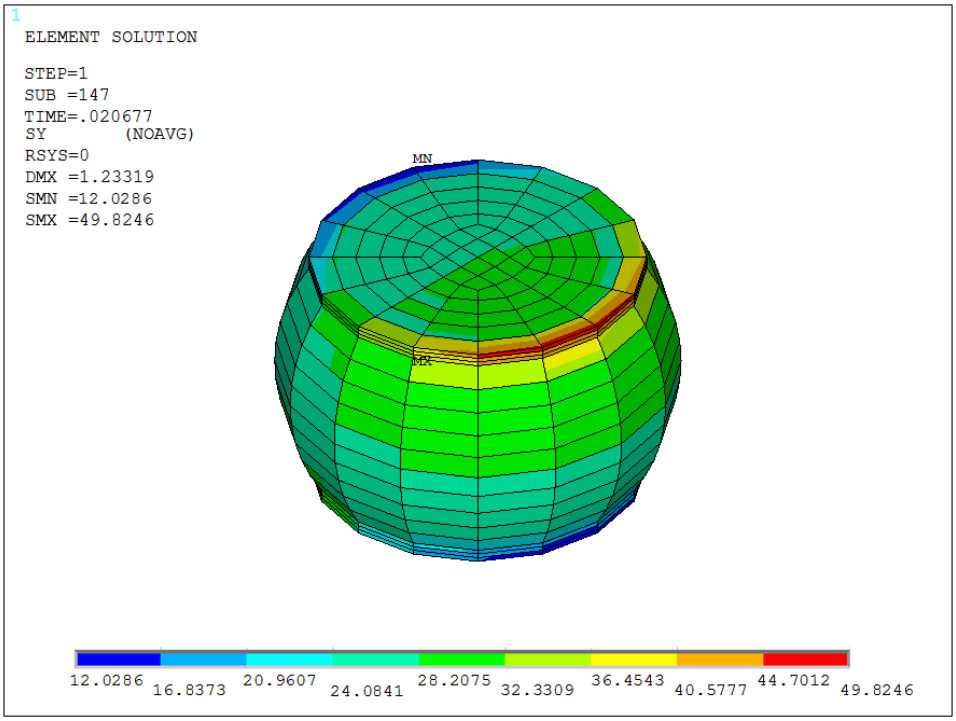

Figure 5.67: Critical Solder Joint Stress Contour of U6 at Maximum Downward Deformation of PCB (10g, 25°C)

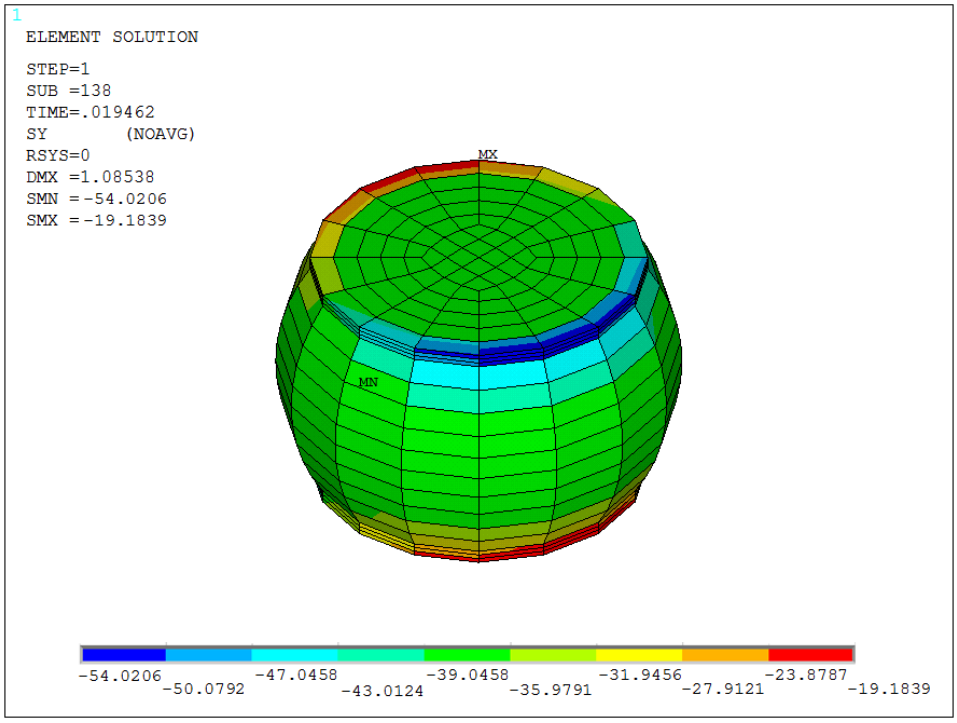

Figure 5.68: Critical Solder Joint Stress Contour of U6 at Maximum Upward Deformation of PCB (14g, 25°C)

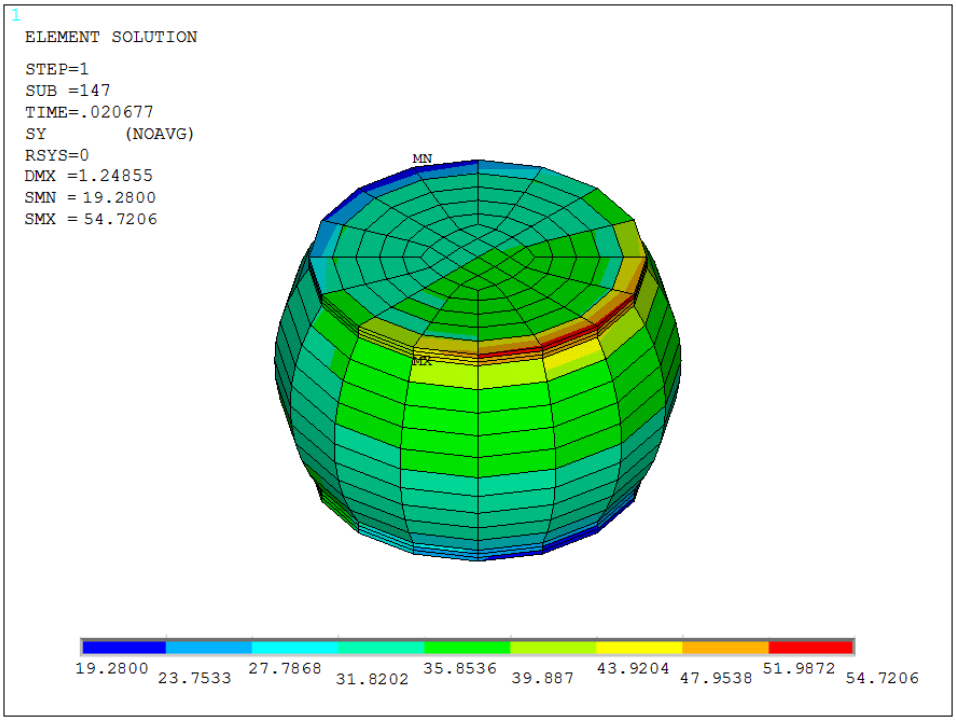

Figure 5.69: Critical Solder Joint Stress Contour of U6 at Maximum Downward Deformation of PCB (14g, 25°C)

5.70 to Figure 5.85 show the hysteresis loops at different G-level and operating temperature. The area of hysteresis plot shows plastic work density stored in solder ball per bending cycle.

$$\sigma_{ave} = \frac{\sum_{i=1}^{n} \sigma_i \cdot V_i}{\sum_{i=1}^{n} V_i} \tag{5.1}$$

$$\varepsilon_{ave} = \frac{\sum_{i=1}^{n} \varepsilon_i \cdot V_i}{\sum_{i=1}^{n} V_i} \tag{5.2}$$

5.9.5 Effect of G-level and Package Locations on Hysteresis Loop of Critical Solder Joint

Hysteresis loops are extracted from different four locations (U1, U2, U5, U6) and different G-levels (1, 5, 10 and 14G). Figure 5.70 to 5.73 show the effect of G-level on the area of hysteresis loop of U6. The area is increasing with larger input of G-level. The trend is the same for other locations. As shown from Figure 5.74 to 5.85. Furthermore, the packages located at the center of PCB have maximum area of hysteresis loop than other locations which is because the center packages are subjected to larger deformation.

5.9.6 Accumulative Plastic Work Density of Critical Solder Joint

Figure 5.86 to Figure 5.89 show the accumulated plastic work density stored in critical solder joint, which is computed by Equation 5.3. It is observed that with increasing in fatigue cycles, the accumulated plastic work density is increasing.

$$W_{ave} = \frac{\sum_{i=1}^{n} W_i \cdot V_i}{\sum_{i=1}^{n} V_i} \tag{5.3}$$

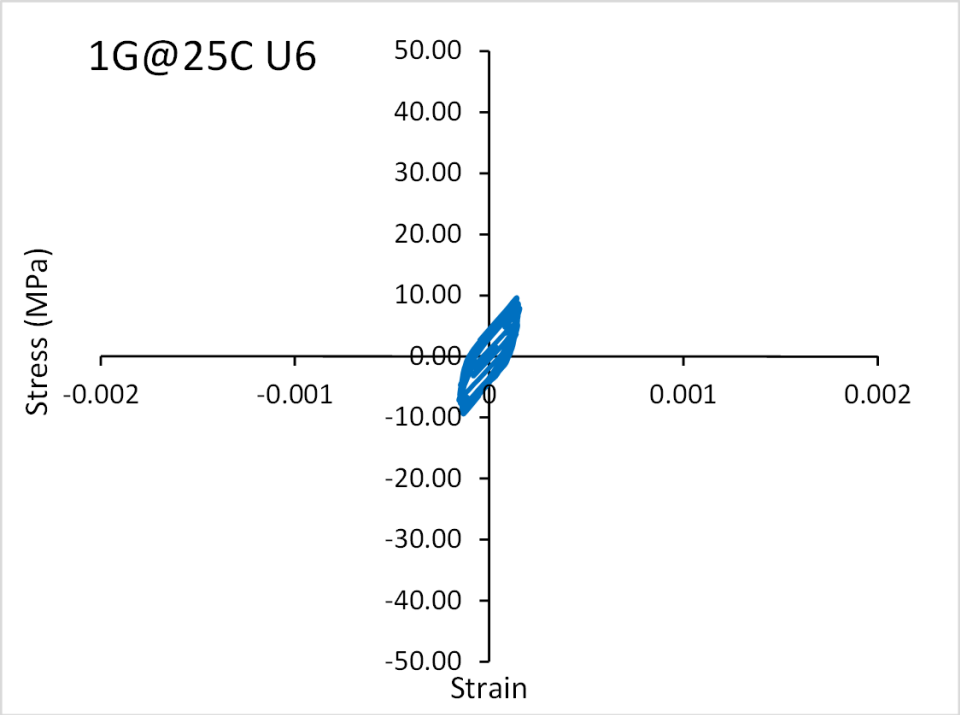

Figure 5.70: Hysteresis loop of critical solder joint (U6 @ 25°C 1G)

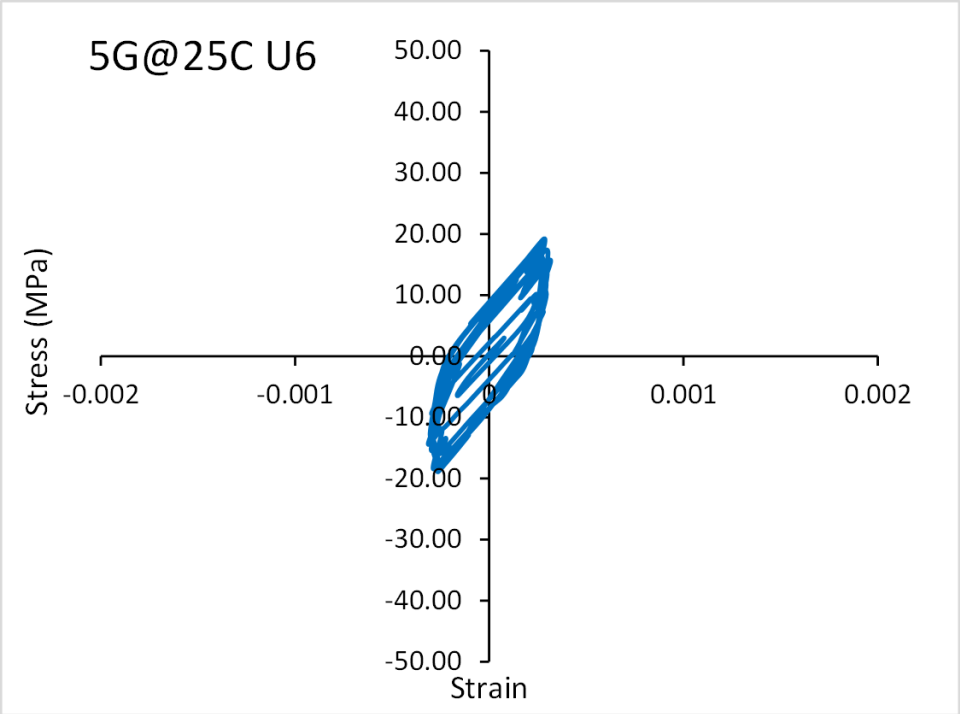

Figure 5.71: Hysteresis loop of critical solder joint (U6 @ 25°C 5g)

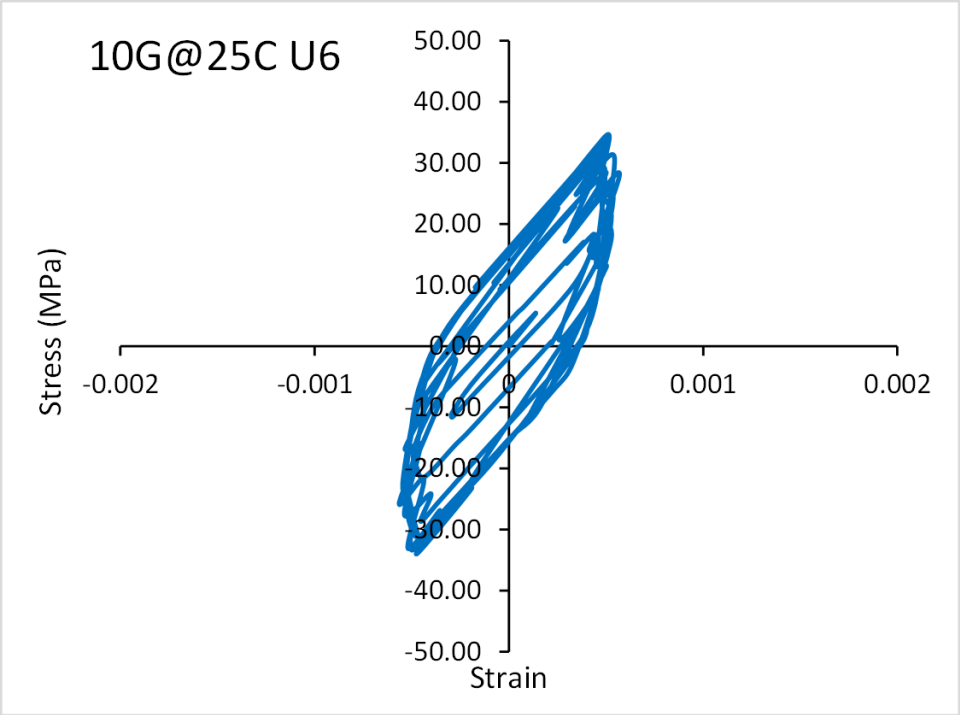

Figure 5.72: Hysteresis loop of critical solder joint (U6 @ 25°C 10g)

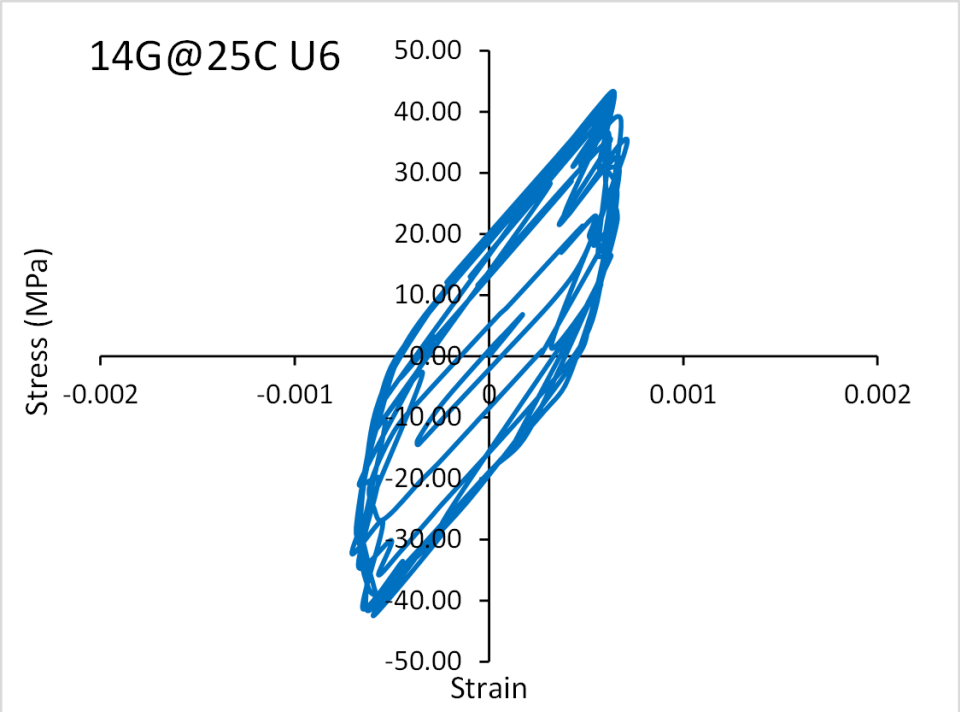

Figure 5.73: Hysteresis loop of critical solder joint (U6 @ 25°C 14g)

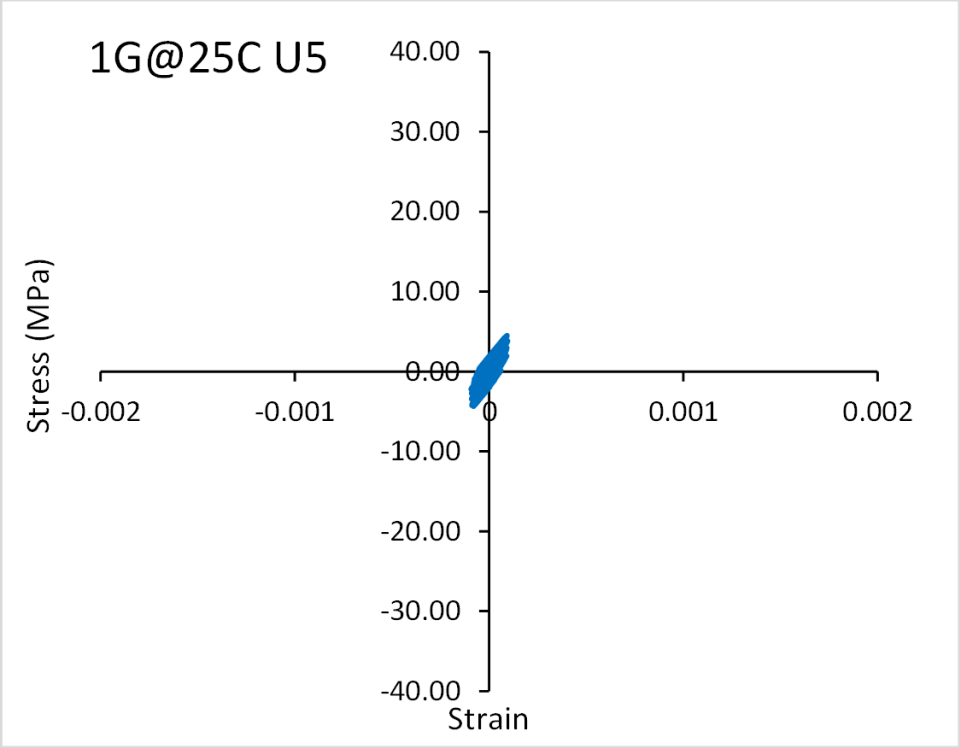

Figure 5.74: Hysteresis loop of critical solder joint (U5 @ 25°C 1G)

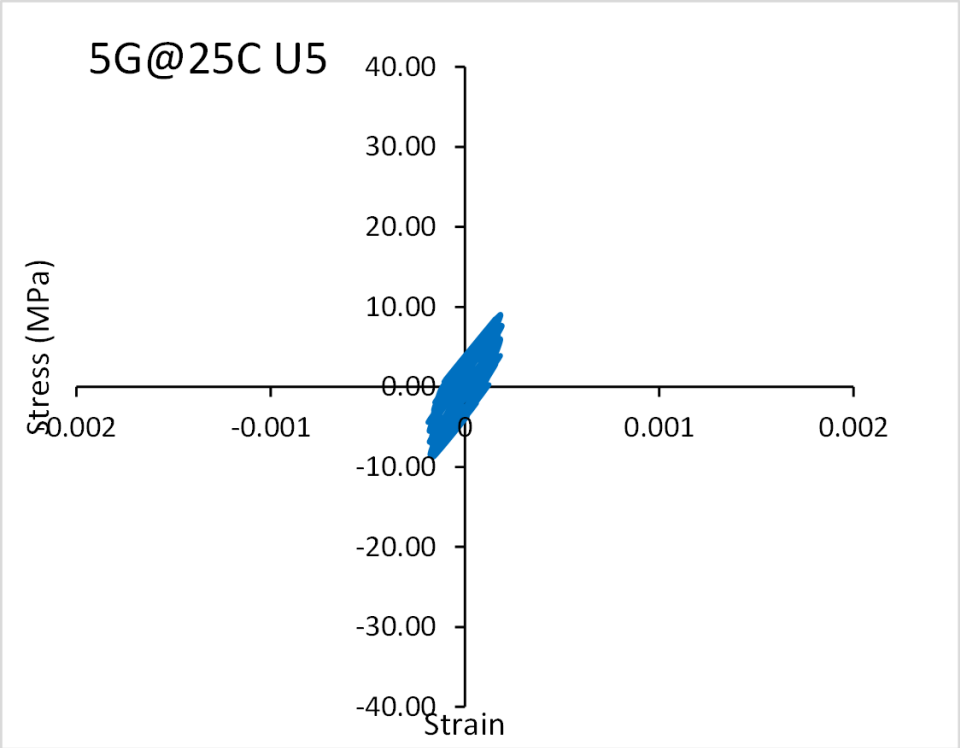

Figure 5.75: Hysteresis loop of critical solder joint (U5 @ 25°C 5g)

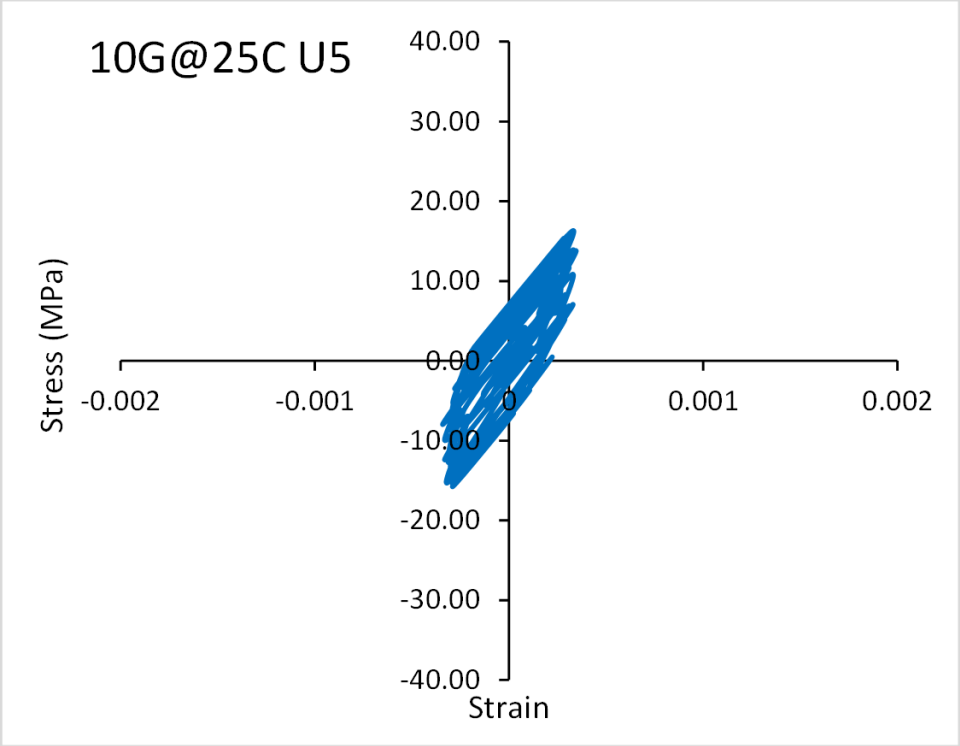

Figure 5.76: Hysteresis loop of critical solder joint (U5 @ 25°C 10g)

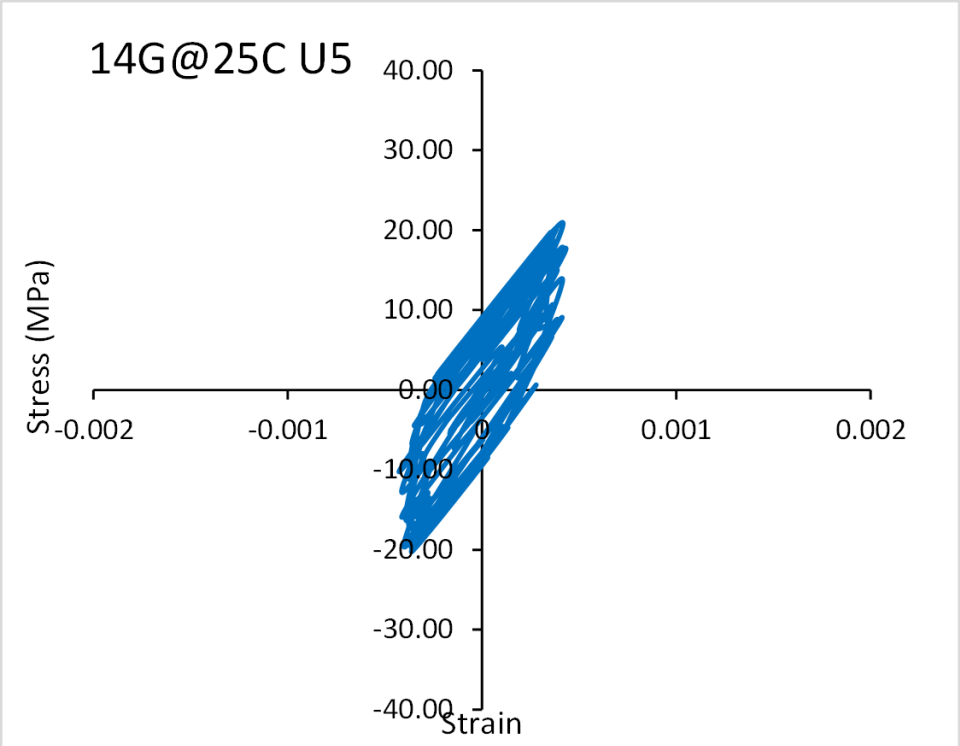

Figure 5.77: Hysteresis loop of critical solder joint (U5 @ 25°C 14g)

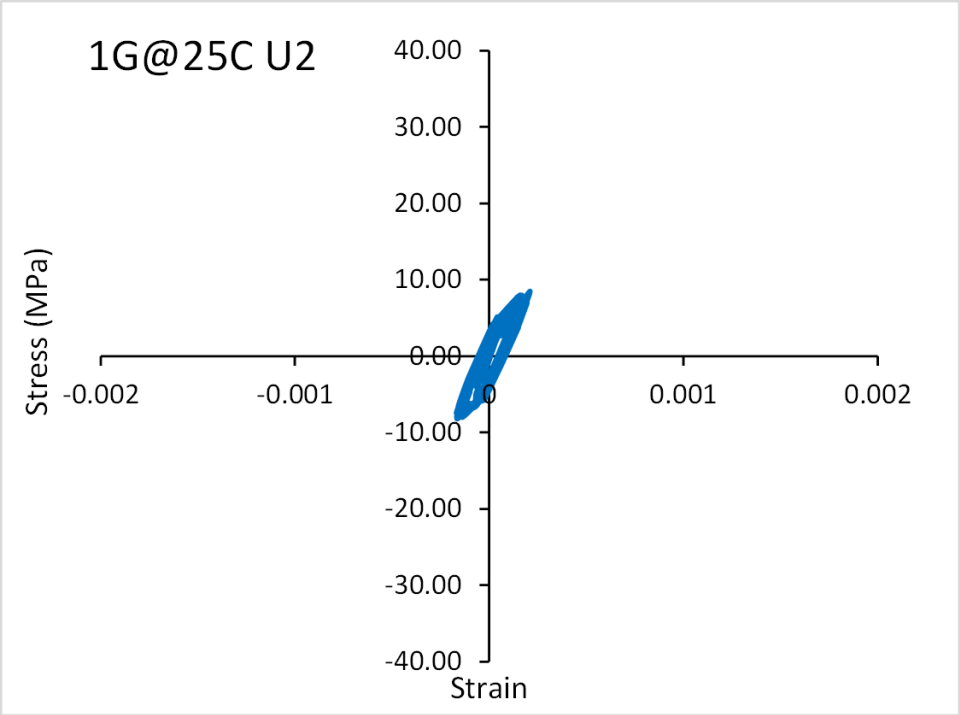

Figure 5.78: Hysteresis loop of critical solder joint (U2 @ 25°C 1G)

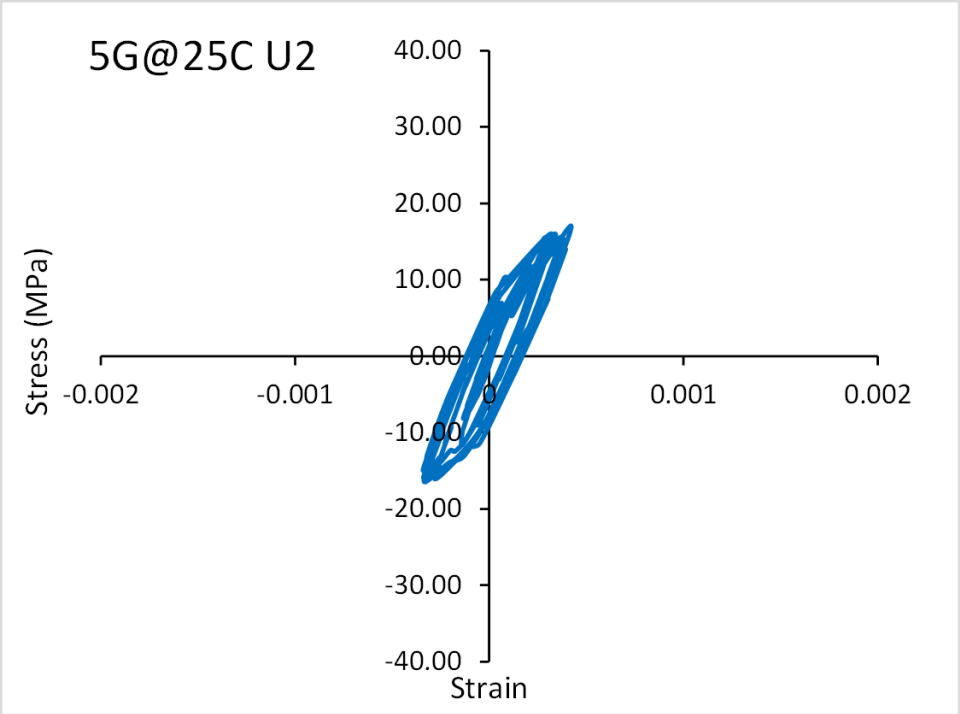

Figure 5.79: Hysteresis loop of critical solder joint (U2 @ 25°C 5g)

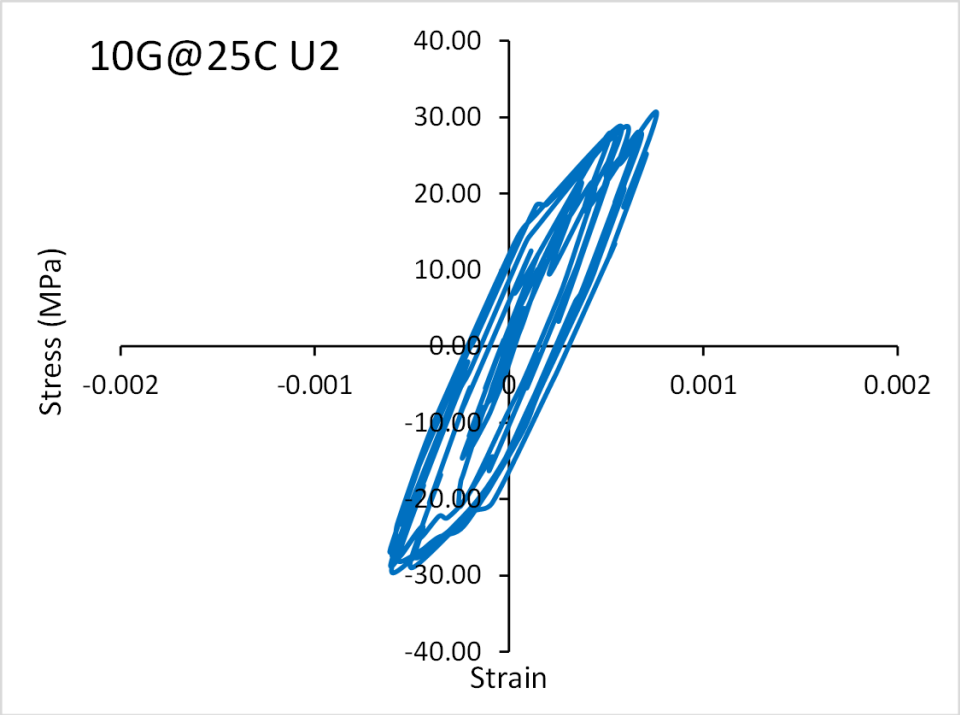

Figure 5.80: Hysteresis loop of critical solder joint (U2 @ 25°C 10g)

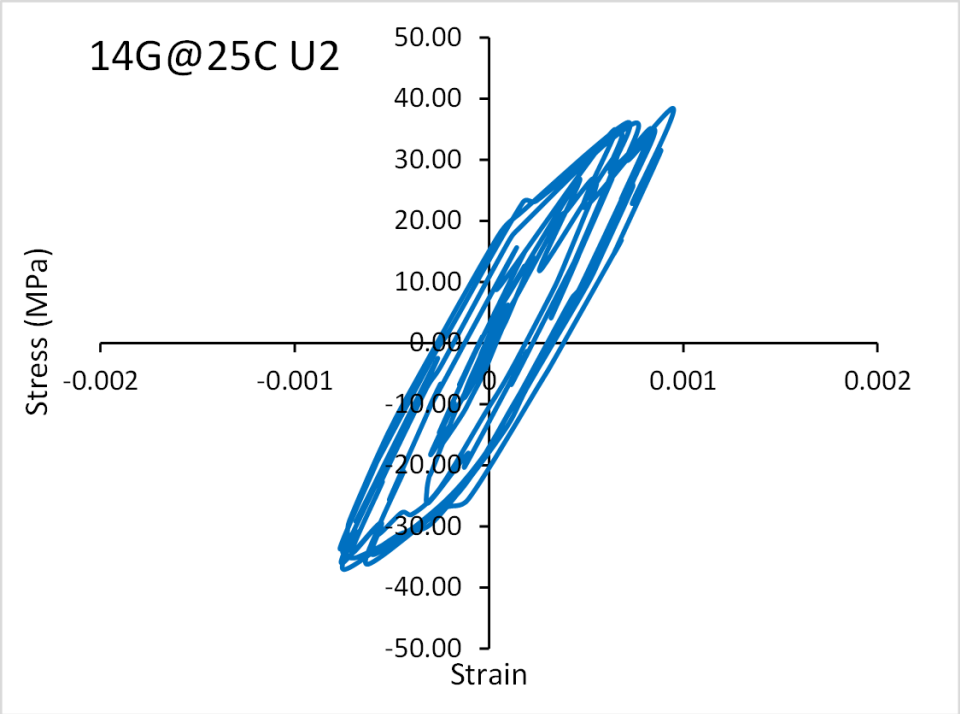

Figure 5.81: Hysteresis loop of critical solder joint (U2 @ 25°C 14g)

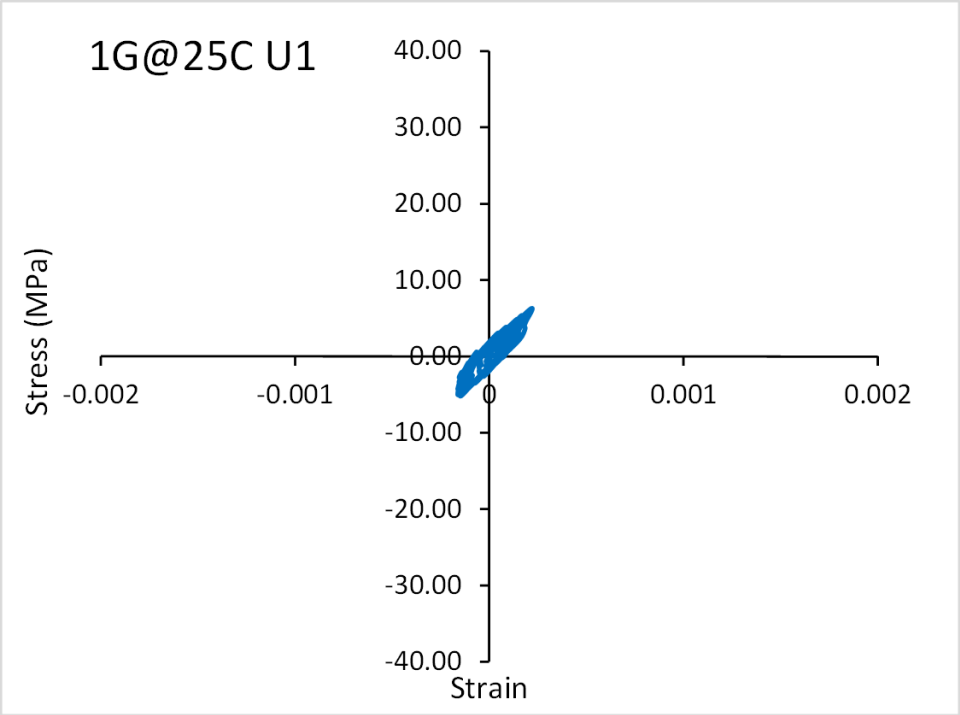

Figure 5.82: Hysteresis loop of critical solder joint (U1 @ 25°C 1G)

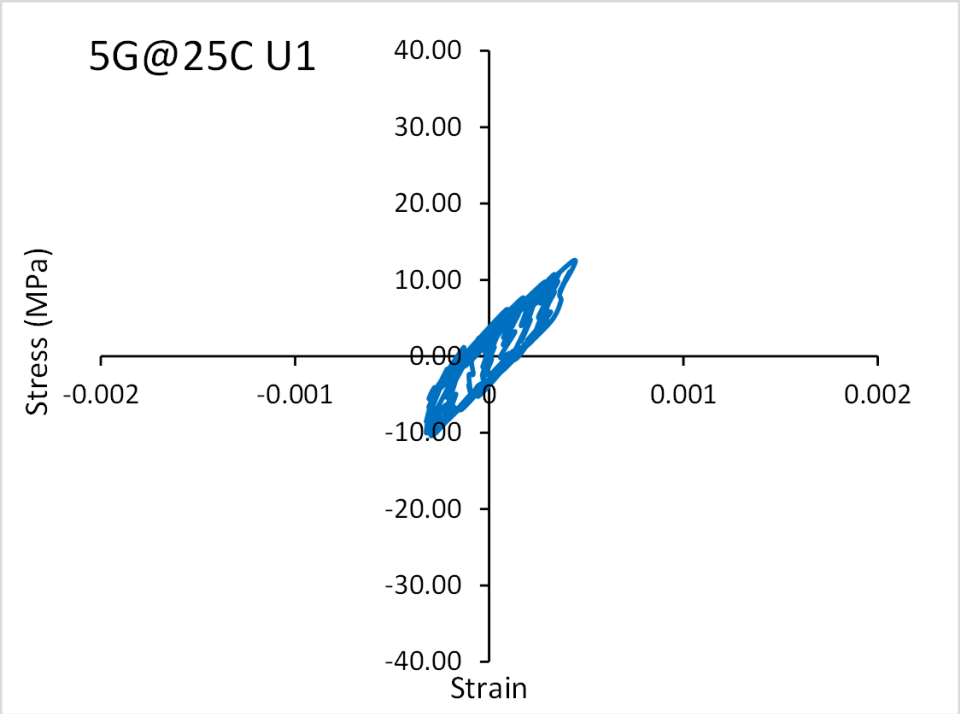

Figure 5.83: Hysteresis loop of critical solder joint (U1 @ 25°C 5g)

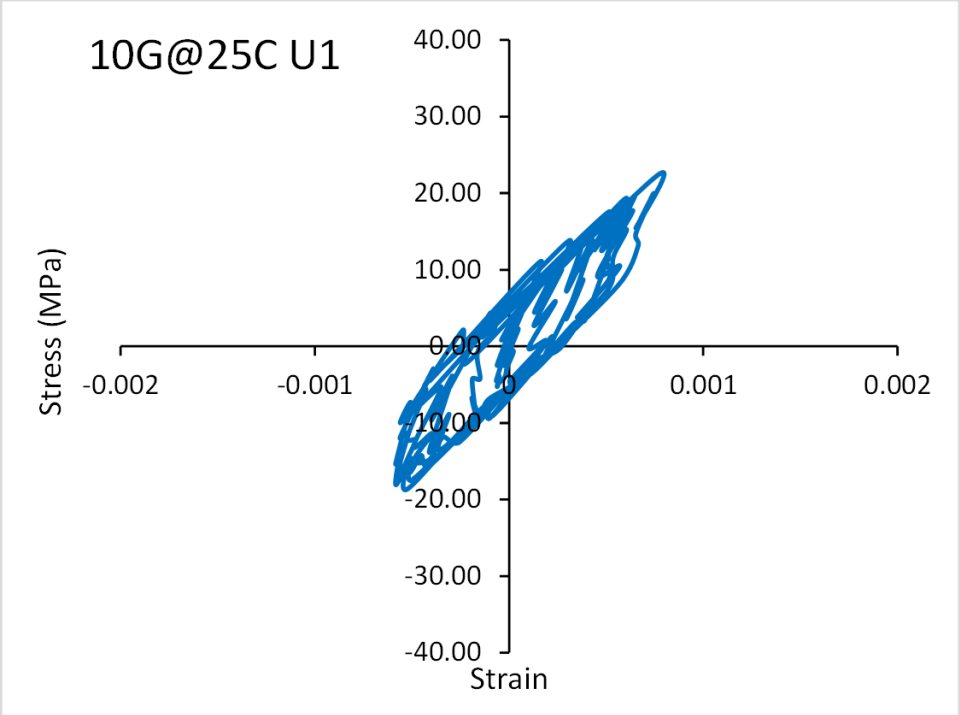

Figure 5.84: Hysteresis loop of critical solder joint (U1 @ 25°C 10g)

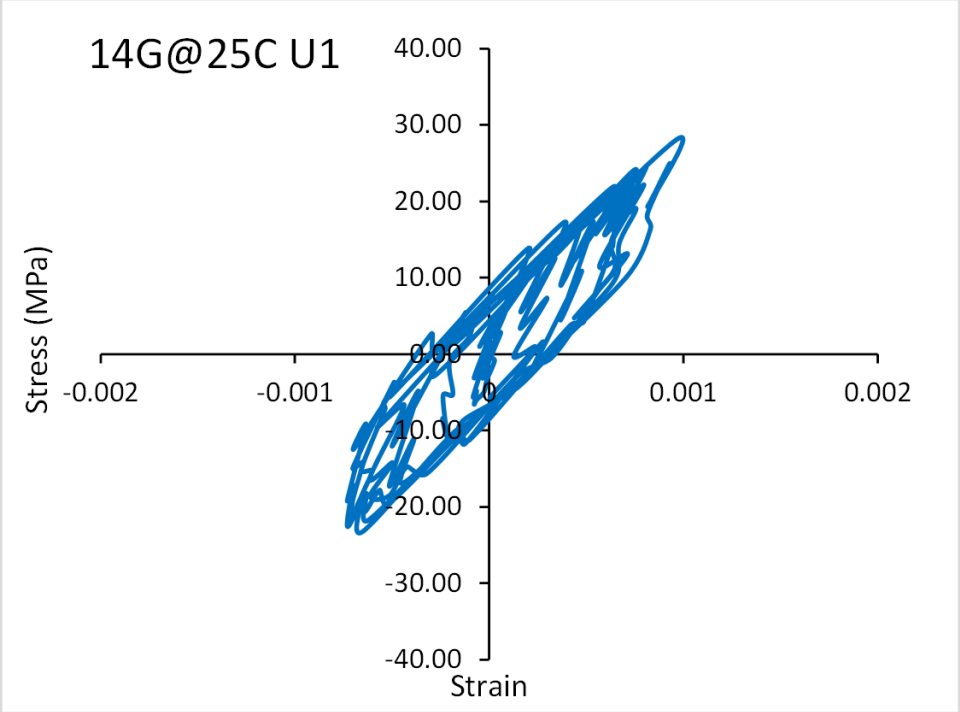

Figure 5.85: Hysteresis loop of critical solder joint (U1 @ 25°C 14g)

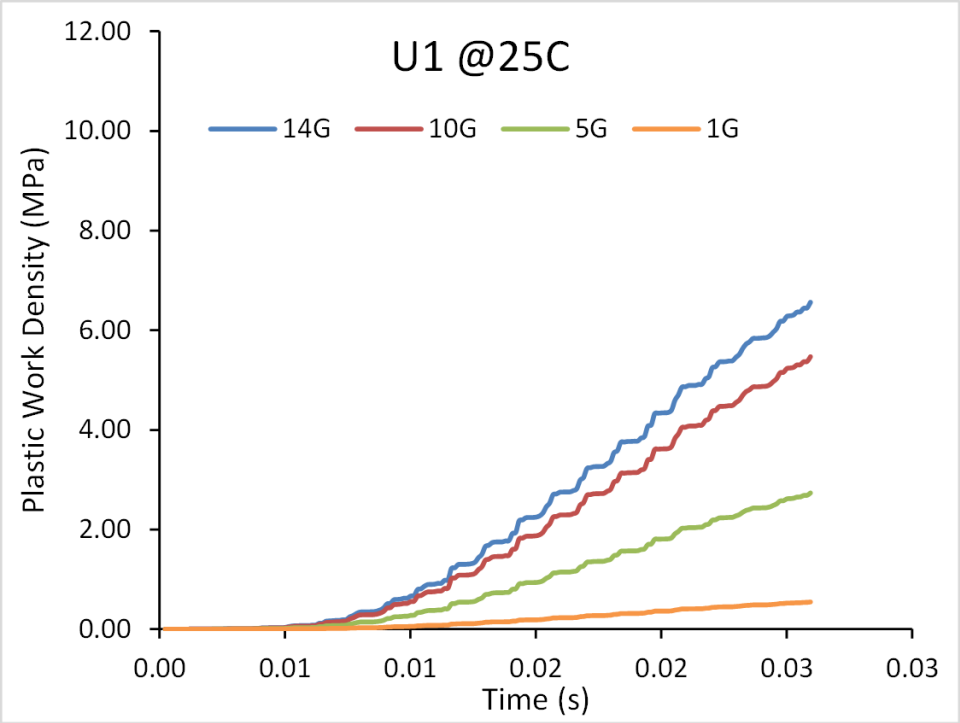

Figure 5.86: Accumulative plastic work density of critical solder joint (U1, 25°C)

5.9.7 Effect of G-level on Accumulative Plastic Work Density of Critical Solder Joint

Figure 5.86 to Figure 5.89 show results of accumulative plastic work density of critical solder joint at different G-level (1, 5, 10 and 14g) and different package locations (U1, U2, U5, U6). For example, Figure 5.89 shows that with increasing in vibration G-level, the accumulative plastic work density is increasing.

5.9.8 Effect of Package Location on Accumulative Plastic Work Density of Critical Solder Joint

The above graphs have been replotted in order to study package location effects (Figure 5.90 to Figure 5.93). Figure 5.93 shows that at the same environmental conditions U6 has larger accumulative plastic work density values than other packages, which can lead to a earlier failure of packages.

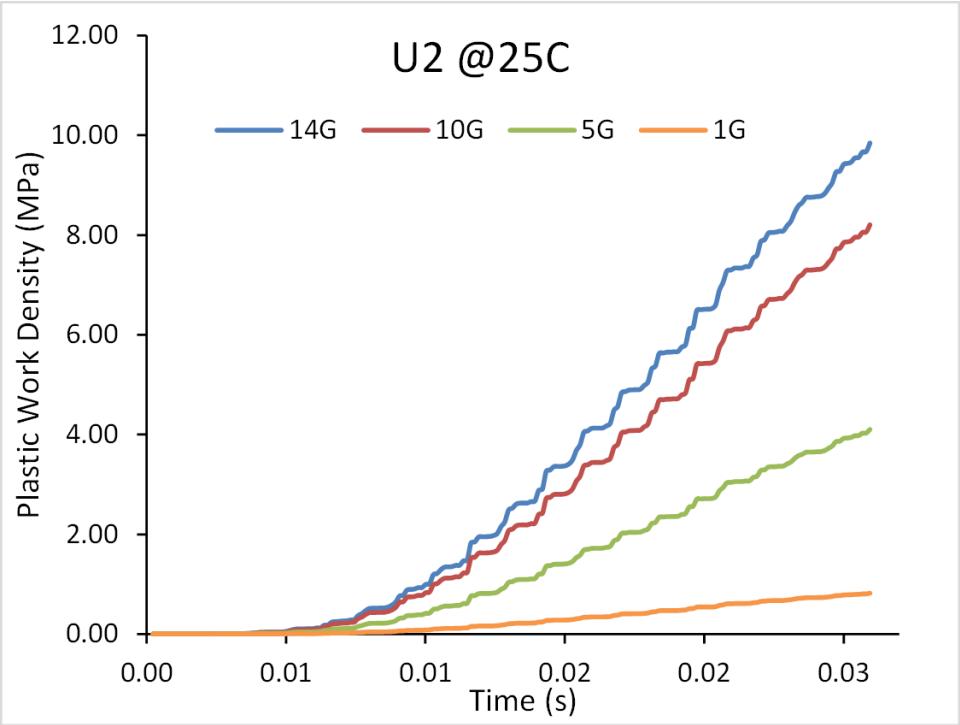

Figure 5.87: Accumulative plastic work density of critical solder joint (U2, 25°C)

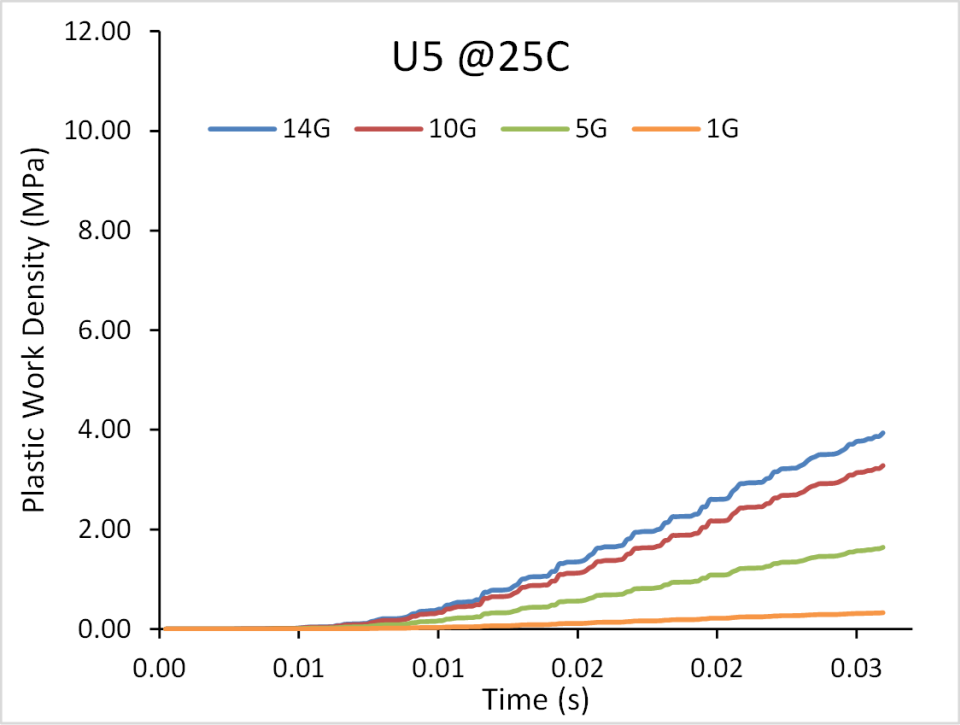

Figure 5.88: Accumulative plastic work density of critical solder joint (U5, 25°C)

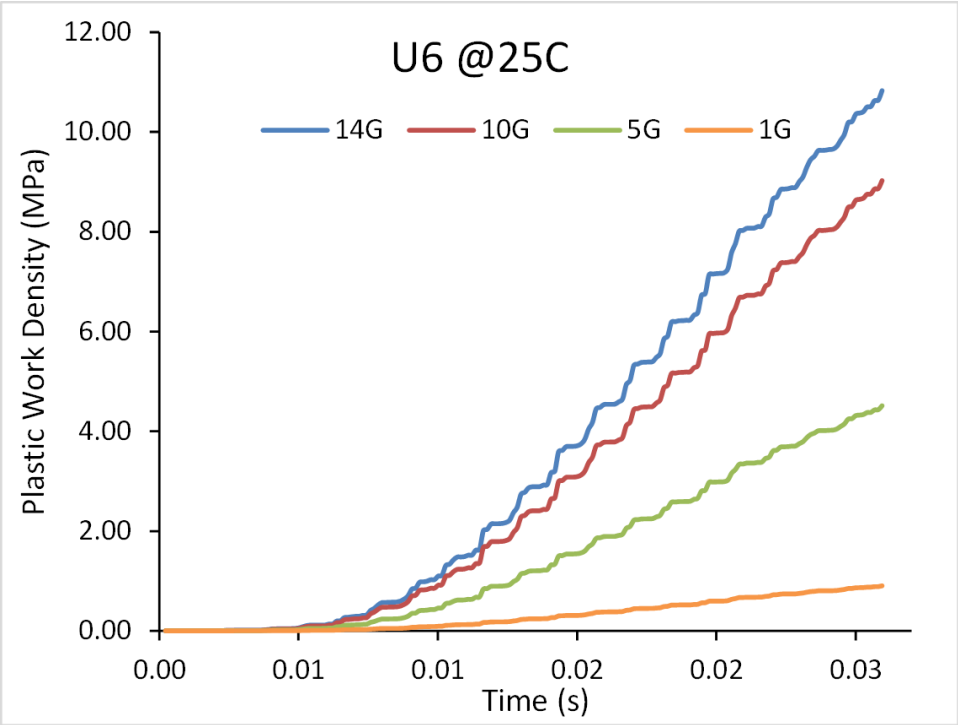

Figure 5.89: Accumulative plastic work density of critical solder joint (U6, 25°C)

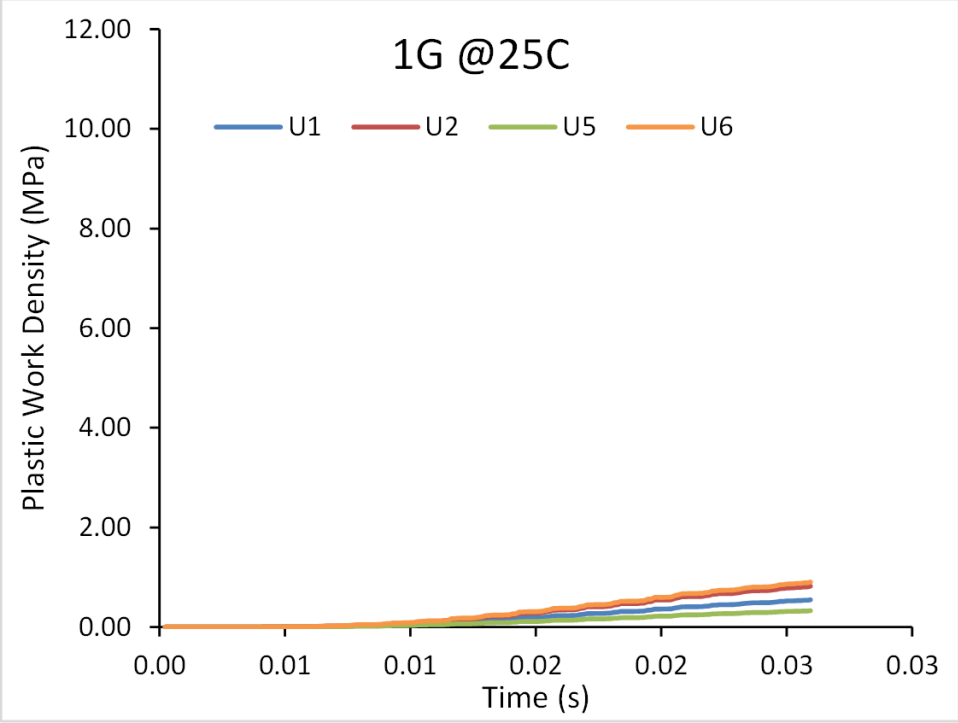

Figure 5.90: Accumulative plastic work density of critical solder joint (25°C, 1g)

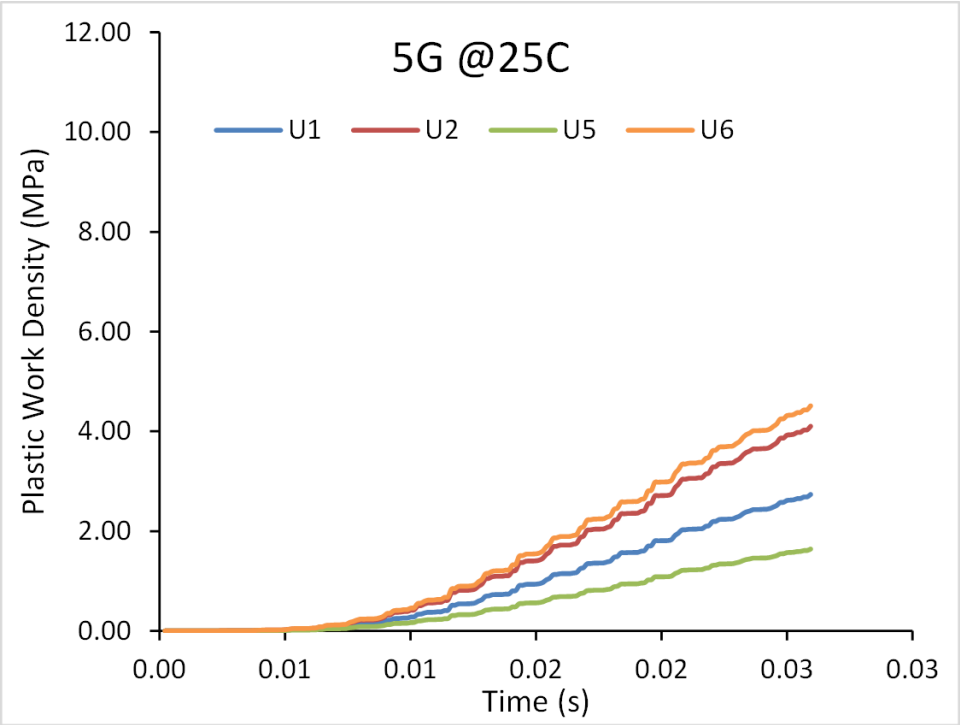

Figure 5.91: Accumulative plastic work density of critical solder joint (25°C, 5g)

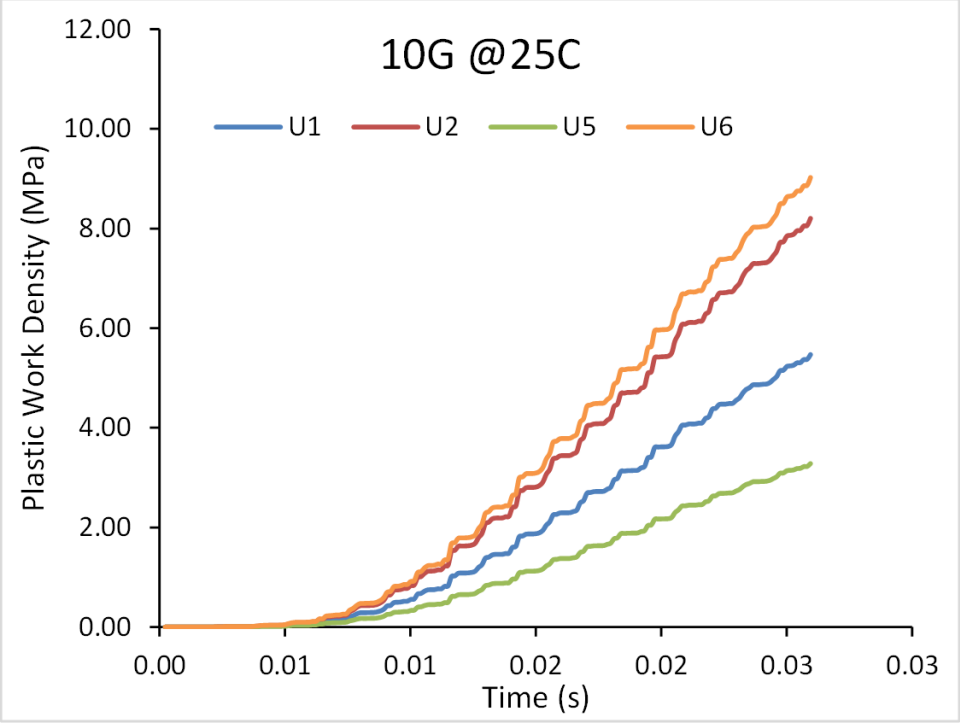

Figure 5.92: Accumulative plastic work density of critical solder joint (25°C, 10g)

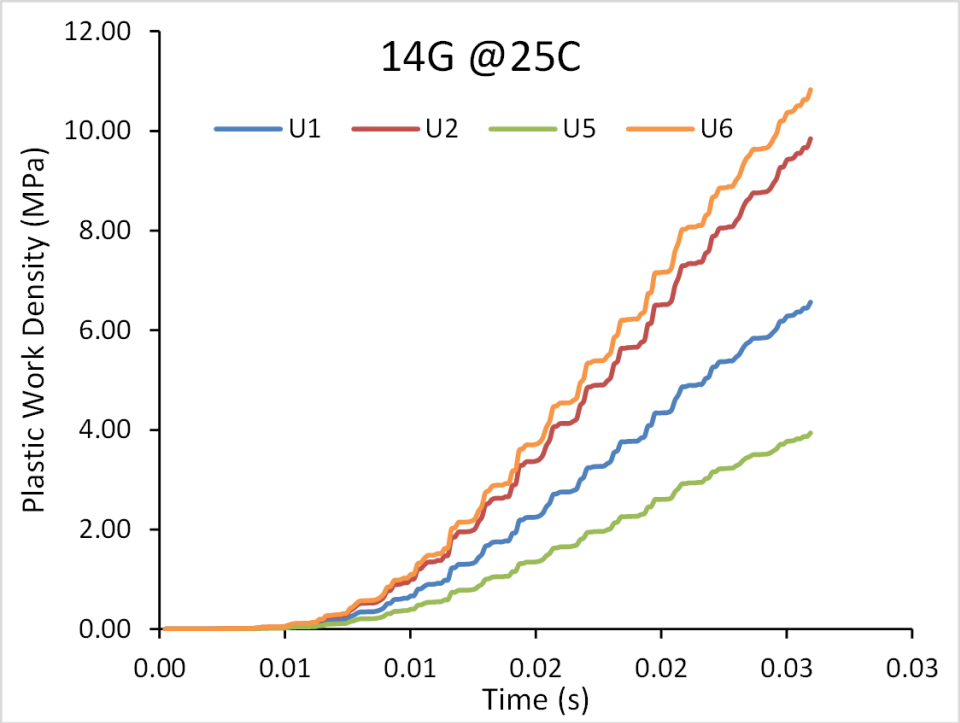

Figure 5.93: Accumulative plastic work density of critical solder joint (25°C, 14g)

5.9.9 Effect of Operating Temperature on Accumulative Plastic Work Density of Critical Solder Joint

In order to study the temperature effect on accumulative plastic work density, simulations have been run at different temperature (25, 55, 155°C) at 5g. Figure 5.94 to Figure 5.97 show the simulation results. The results show that with increasing operating temperature, the accumulative plastic work density values is increasing, which can lead to a faster failure rate.

5.10 Life Data Analysis

All the packages are daisy chained before testing. An Agilent switch unit (Figure 5.5) is used to continue to monitor the resistance change of packages. The cycles to failure have been calculated by multiplying the time to failure by frequency of base excitation which is constant throughout the test. Figure 5.98 to Figure 5.103 show the typical plot

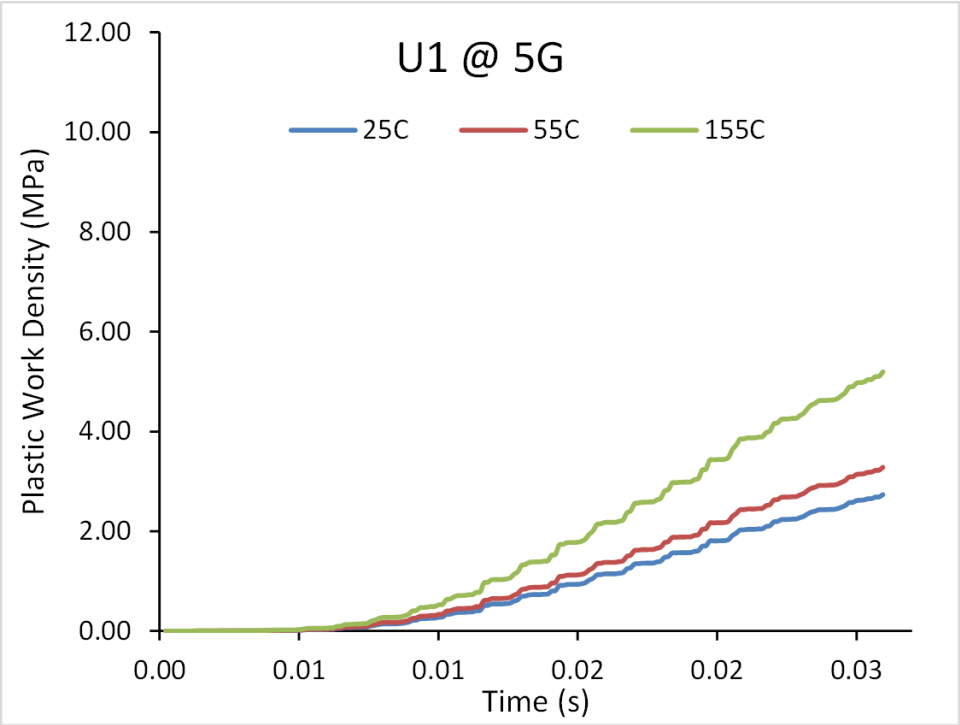

Figure 5.94: Accumulative plastic work density of critical solder joint (U1, 5g)

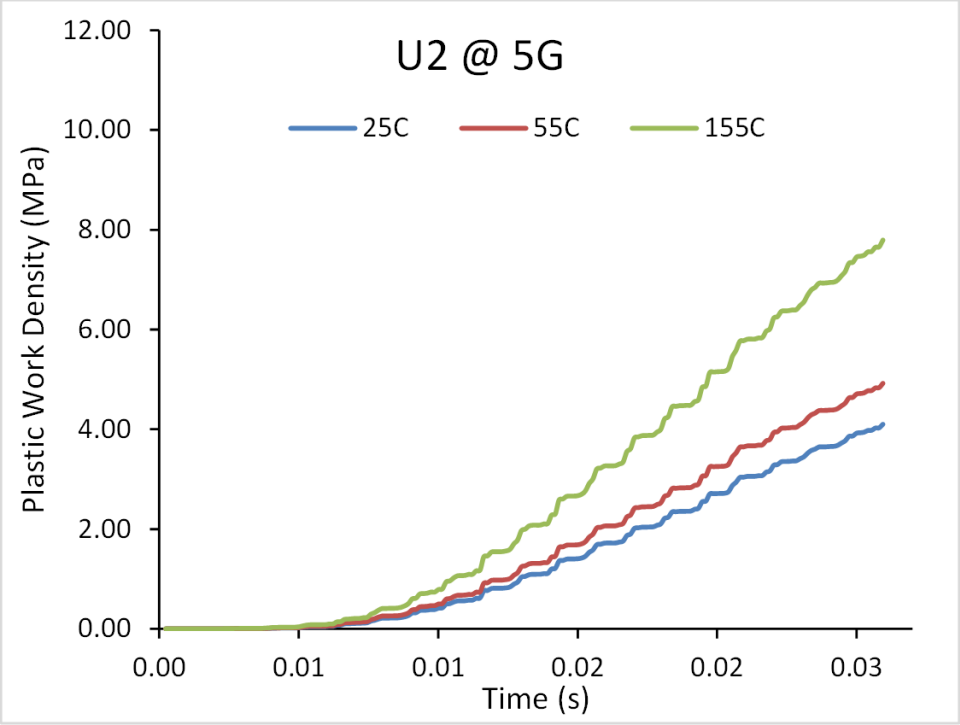

Figure 5.95: Accumulative plastic work density of critical solder joint (U2, 5g)

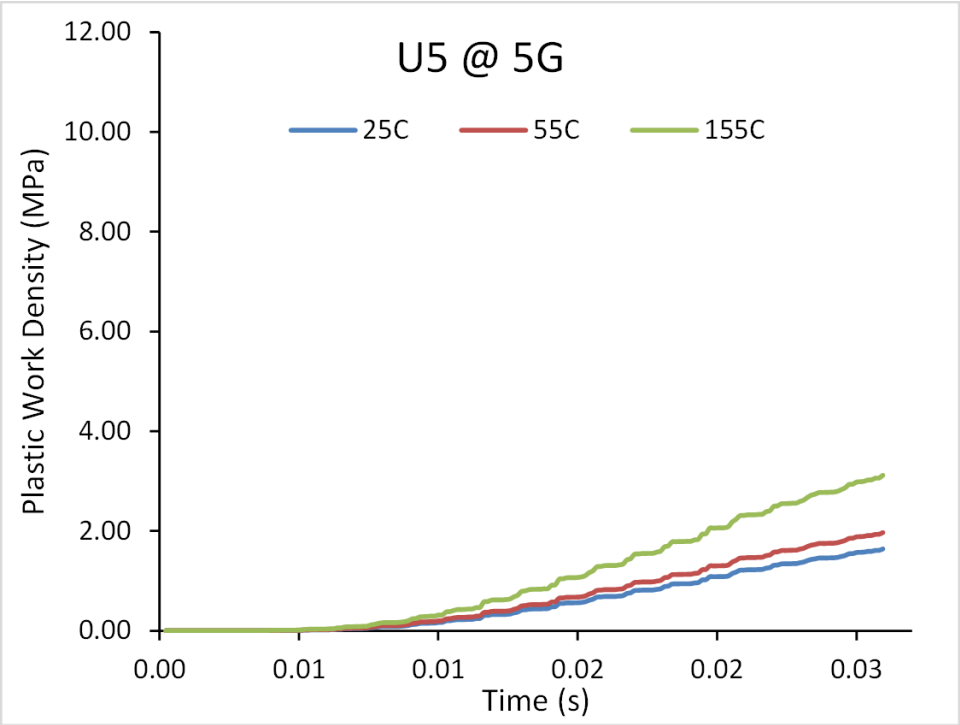

Figure 5.96: Accumulative plastic work density of critical solder joint (U5, 5g)

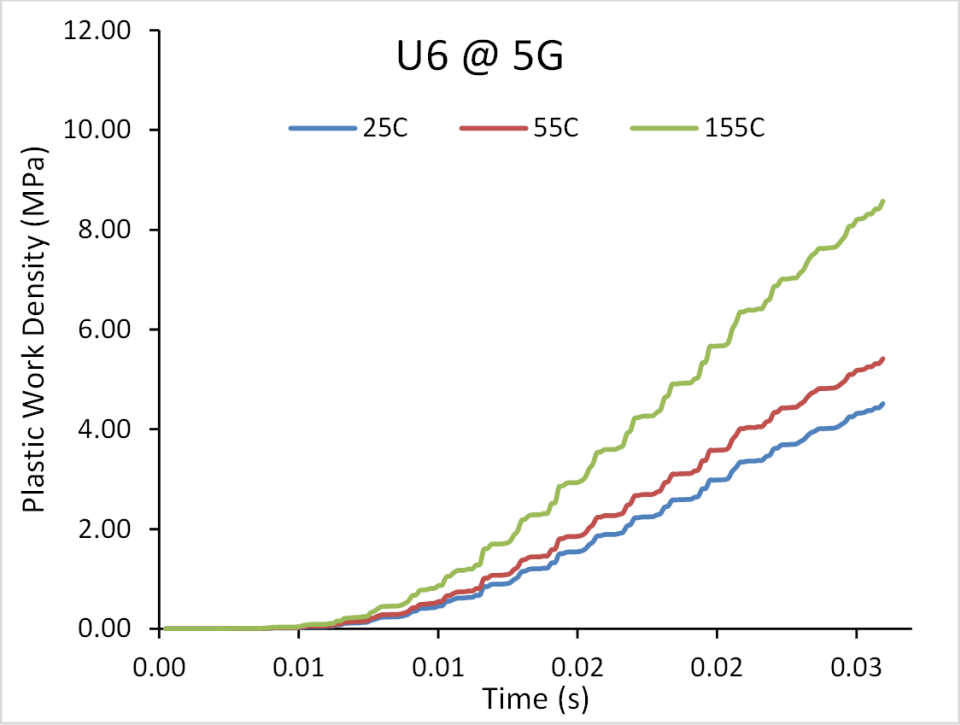

Figure 5.97: Accumulative plastic work density of critical solder joint (U6, 5g)

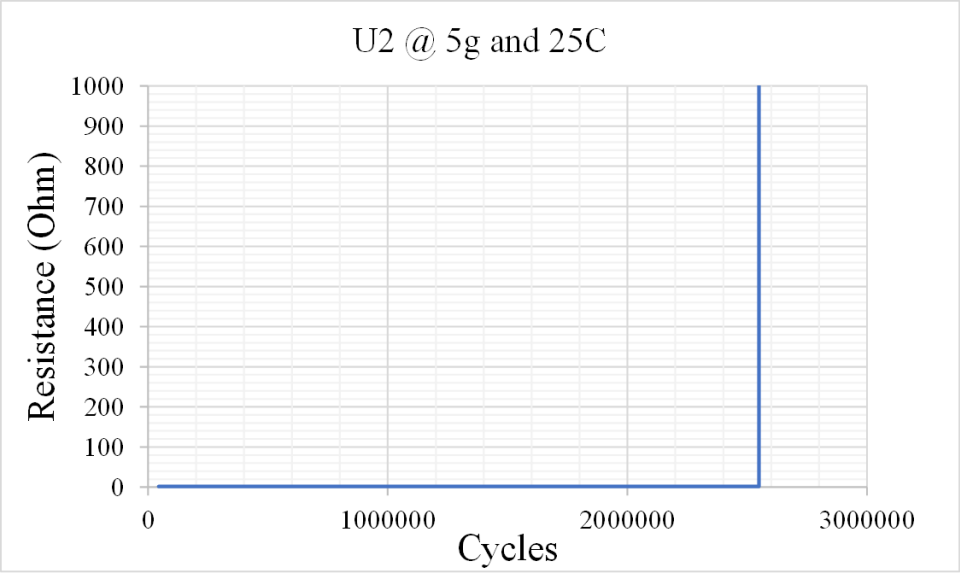

Figure 5.98: Typical resistance plot (U2 @ 5G and 25 °C)

of resistance vs. cycles to failure. All the resistance vs. cycles at different conditions have been analyzed and extracted. Two-parameter Weibull analysis has been used to analyze failure data. Equation 5.4 is cumulative distribution function which is used to compute characteristic life of packages. Cycles to failure are different in the same board because at different locations packages are subjected to different strain amplitude. Since the test board is symmetric, it is considered to have four different locations (U1, U2, U5, U6).

$$f(t) = 1 - e^{-\left(\frac{t}{\eta}\right)^{\beta}} \tag{5.4}$$

where t is time, η is characteristic life, β is the shape parameter. Figure 5.104 to Figure 5.106 show the Weibull plots of packages at three locations (U1, U2, U6) and three temperatures (25 , 55 , 155 °C) at 5G. 63.2% of failures are considered as the characteristic life η.

5.10.1 Effect of Operating Temperature on Fatigue Life of CABGA288

Figure 5.104 to Figure 5.106 show the effect of temperature on characteristic life of CABGA288. The mean time to failure is decreasing with increasing in operating temperature. The characteristic life has been extracted and reploted in Figure 5.107. It is easily

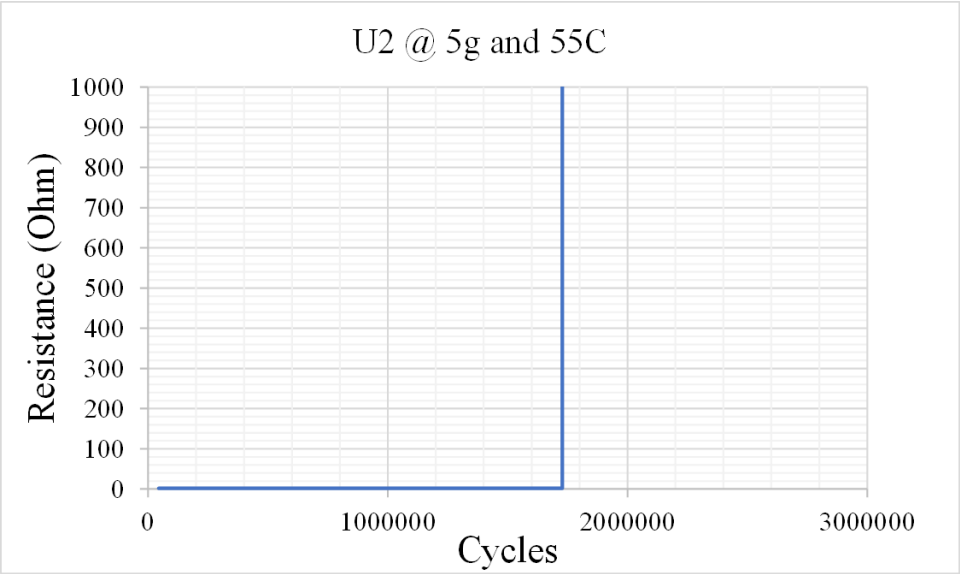

Figure 5.99: Typical resistance plot (U2 @ 5G and 55 °C)

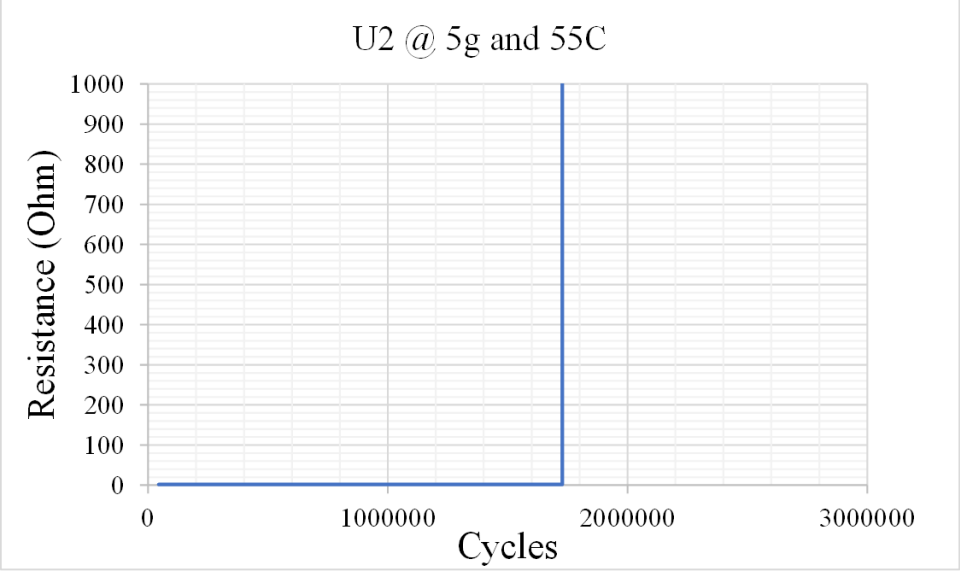

Figure 5.100: Typical resistance plot (U2 @ 5G and 155 °C)

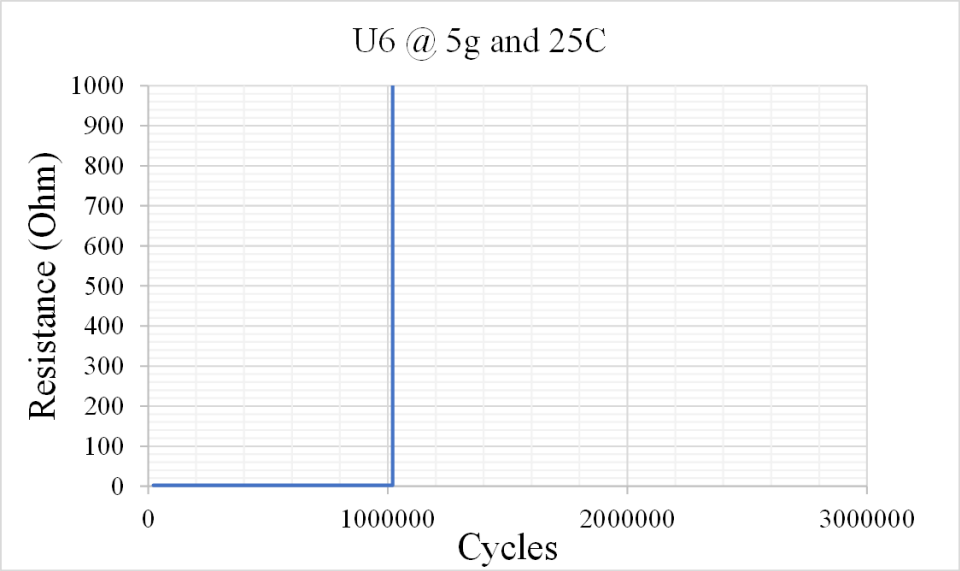

Figure 5.101: Typical resistance plot (U6 @ 5G and 25 °C)

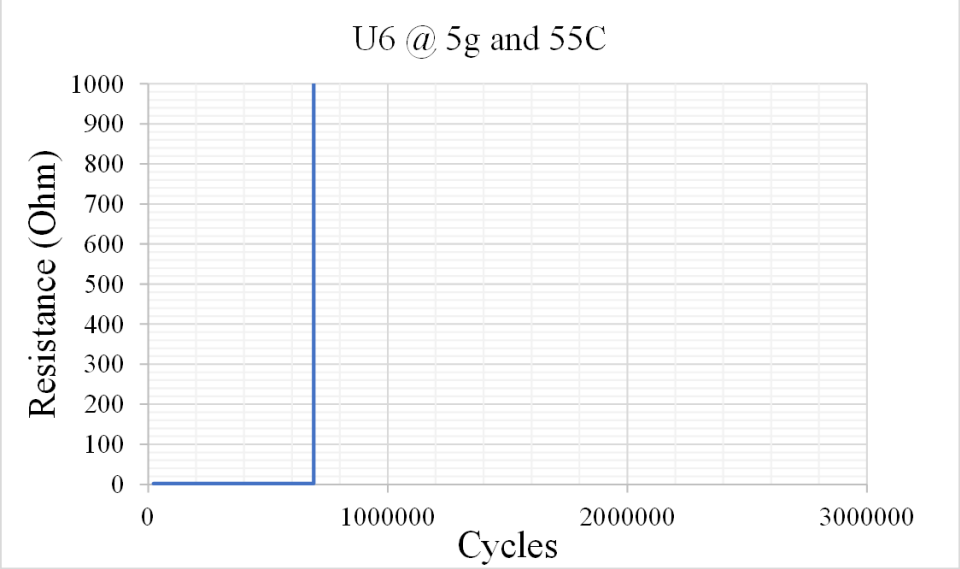

Figure 5.102: Typical resistance plot (U6 @ 5G and 55 °C)

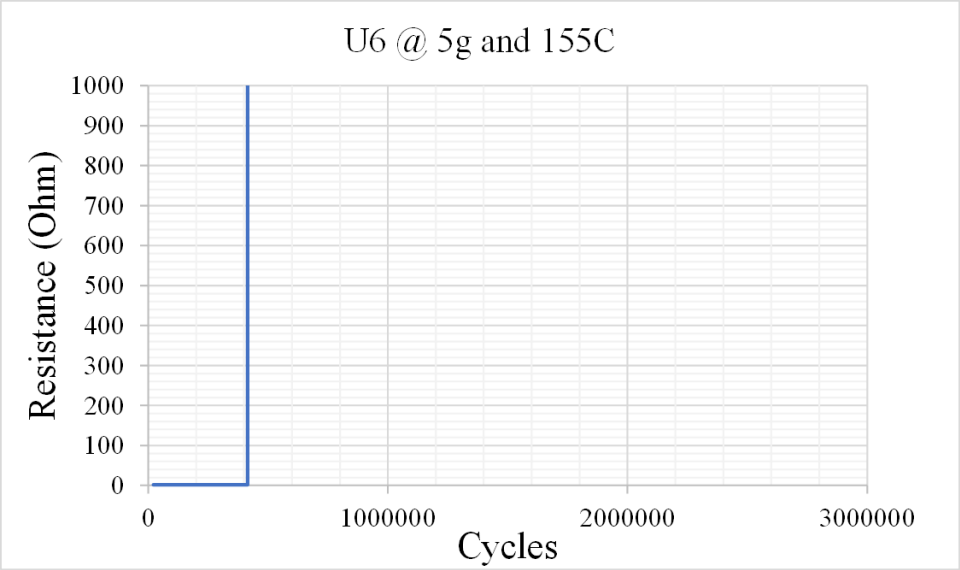

Figure 5.103: Typical resistance plot (U6 @ 5G and 155 °C)

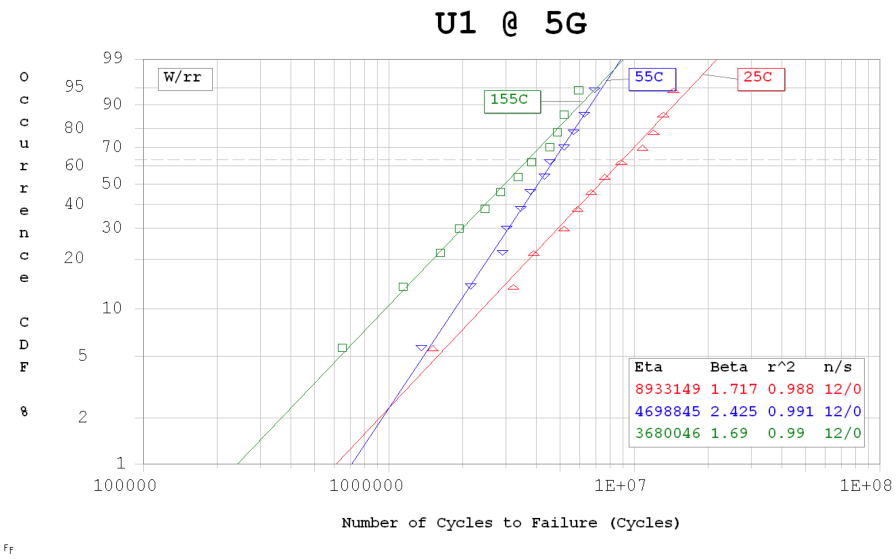

Figure 5.104: Weibull plot (U1 @ 5G)

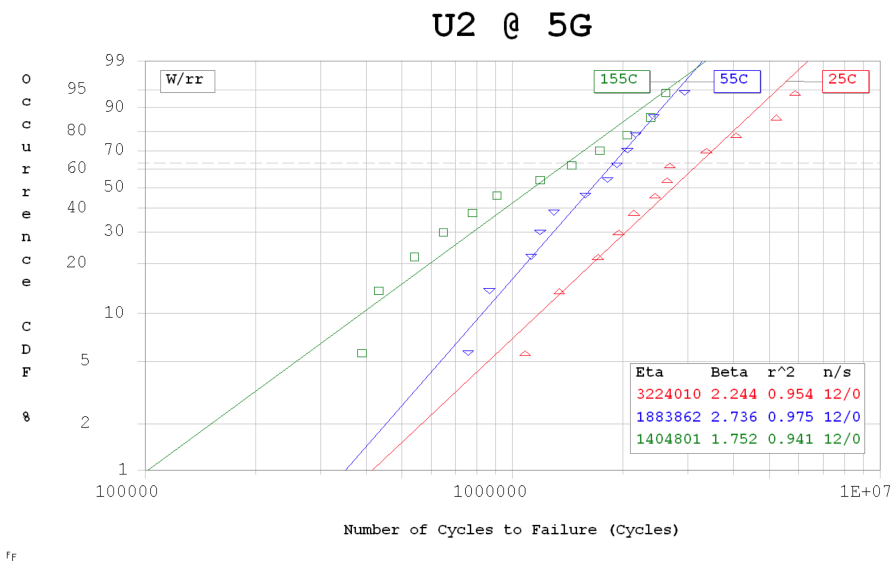

Figure 5.105: Weibull plot (U2 @ 5G)

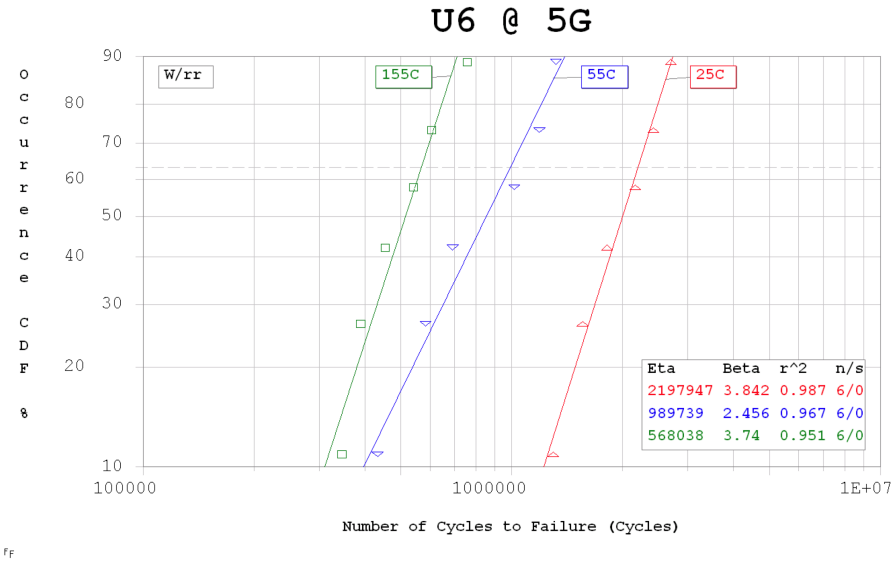

Figure 5.106: Weibull plot (U6 @ 5G)

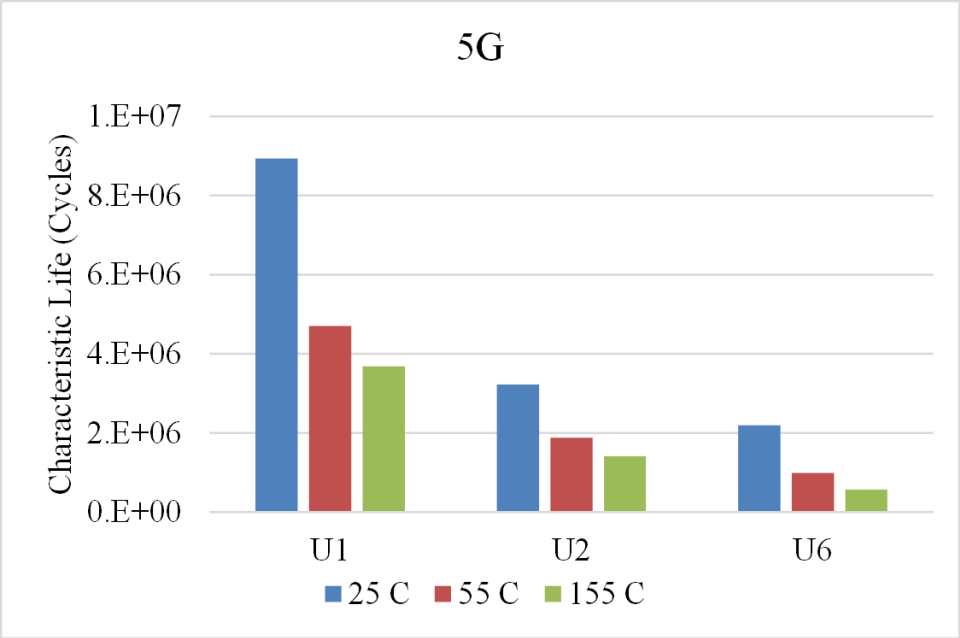

Figure 5.107: Characteristic life chart (5G)

observed that by increasing in operating temperature from 25 °C to 155 °C, the characteristic life dropped more than 50% at various locations.

5.11 Energy Based Fatigue Life Prediction Model

The plastic work density can be used to evaluate the damage to solder joint per bending cycle. When the accumulative plastic work density is larger than the threshold value of solder joint, it leads to failure in second-level interconnect. Previous, power law equation (Equation 5.5) has been used to predict fatigue life of solder joints.

$$N_f = a \cdot (\Delta W_{ave})^{-b} \tag{5.5}$$

where N_f is characteristic life, ΔW_{ave} is the plastic work density accumulated per bending cycles. a and b are fatigue constants.

Table 5.4 shows the plastic work density values at 5G. All those values are extracted from simulation. Table 5.5 shows the extracted characteristic life of CABGA288 from Weibull

Table 5.4: Plastic work density @ 5G

5G			
ΔW_{ave}	25 °C	55 °C	155 °C
U1	0.21	0.29	0.42
U2	0.38	0.41	0.67
U5	0.16	0.19	0.27
U6	0.42	0.53	0.84

Table 5.5: Characteristic Life @ 5G

5G			
Characteristic Life	25 °C	55 °C	155 °C
U1	8933149	4698845	3680046
U2	3224010	1883862	1404801
U5	NF	NF	NF
U6	2197947	989739	568038

analysis. Figure 5.108 shows the plot of ΔW_{ave} vs. N_f. Three curves have been generated at different temperature 25, 55, 155 °C. Equation 5.5 has been used to compute fatigue constants and fatigue exponent. Table 5.6 shows the constant values extracted from Figure 5.108 at various temperature.

The fatigue constants and fatigue exponents have been extracted and plotted against operating temperature. Figure 5.109 and 5.110 show the effect of operating temperature on fatigue coefficients and fatigue exponents. The famous Arrhenius equation 5.6 has been used to study the effect of temperature on fatigue constants and fatigue exponents.

$$R = A \cdot e^{-\frac{Q}{K \cdot T}} \tag{5.6}$$

Where A is scaling factor. Q is activation energy. K is the Boltzmann constant. T is temperature in Kelvin. Figure 5.109 and Figure 5.110 show the fitting results with

Table 5.6: Fatigue constants table

Constant	25 °C	55 °C	155 °C
a	931378	528050	314550
b	1.194	1.379	1.408

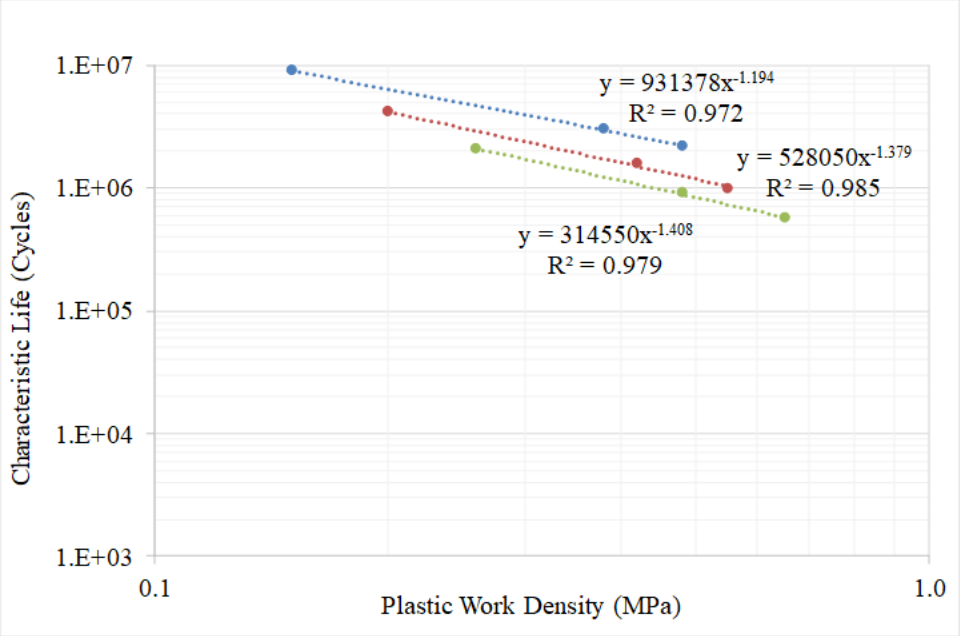

Figure 5.108: Characteristic life vs. plastic work density

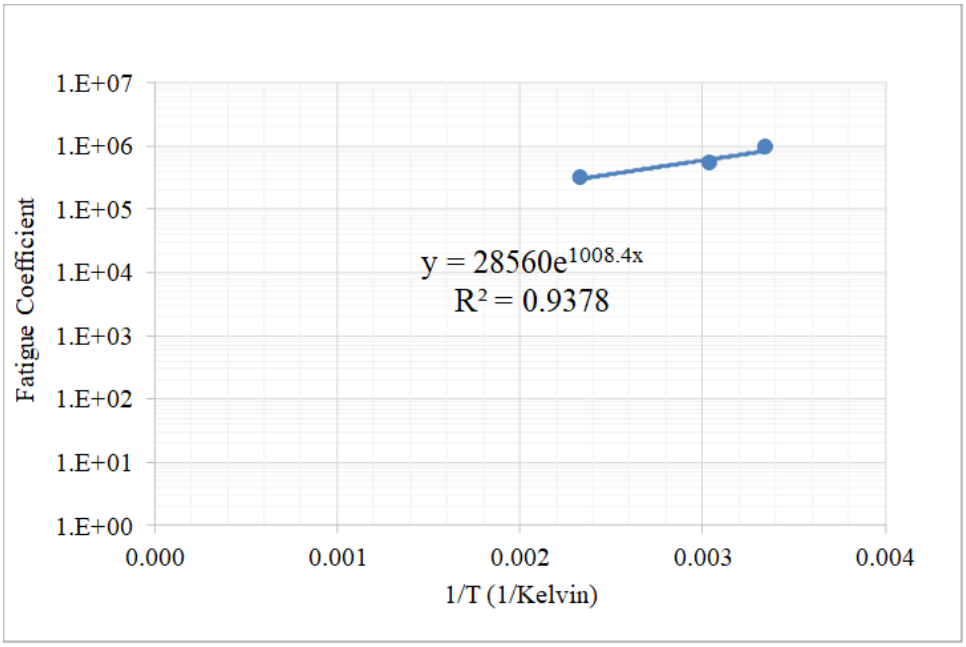

Figure 5.109: Fatigue constant vs. T

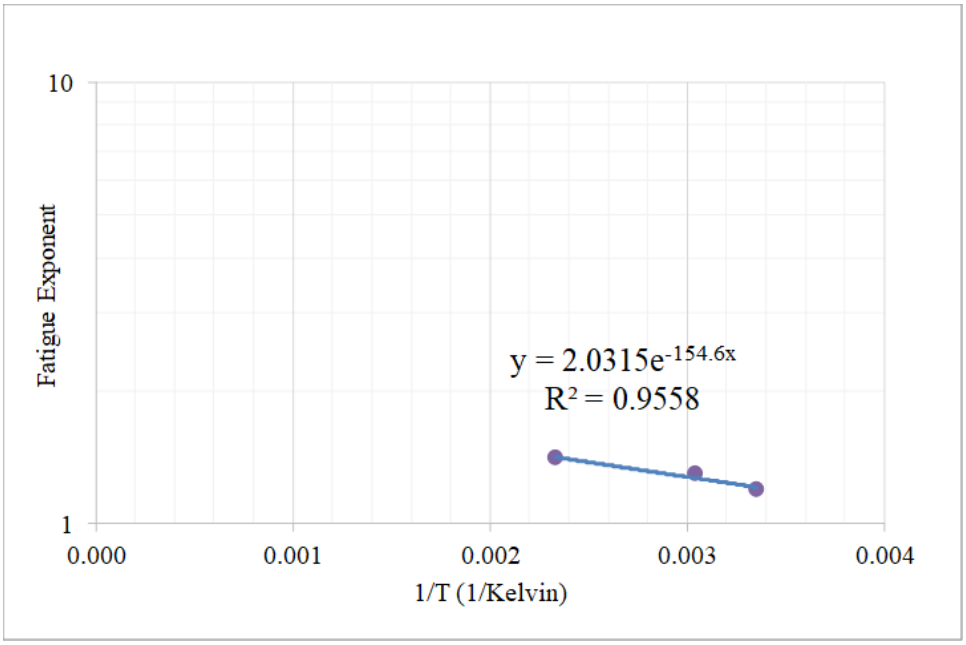

Figure 5.110: Fatigue exponent vs. T

Arrhenius model. It is observed very good correlations have been achieved. Equation 5.7 and 5.8 show fatigue constants and fatigue exponents in terms of temperature. Fatigue exponent is increasing with increasing in temperature, while fatigue constants is decreasing with increasing in temperature. By substituting these two equations into the power law equation 5.5, the life prediction can be formulated as Equation 5.9.

$$a\left(T\right) = 28560 \cdot e^{\frac{1008.4}{T}} \tag{5.7}$$

$$b\left(T\right) = 2.0315 \cdot e^{-\frac{154.6}{T}} \tag{5.8}$$

$$N_f = \left(28560 \cdot e^{\frac{1008.4}{T}}\right) \cdot \left(\Delta W_{ave}\right)^{-\left(2.0315 \cdot e^{-\frac{154.6}{T}}\right)} \tag{5.9}$$

This equation can be used to predict the fatigue life of solder joint subjected to high temperature vibration by substituting the plastic work density value from simulation and operating temperature condition.

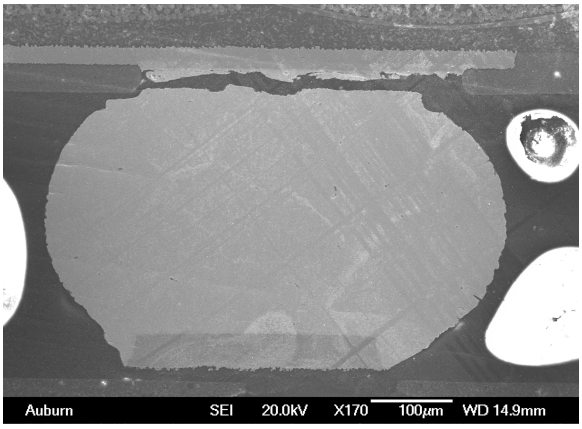

Figure 5.111: Solder joint crack on package-side

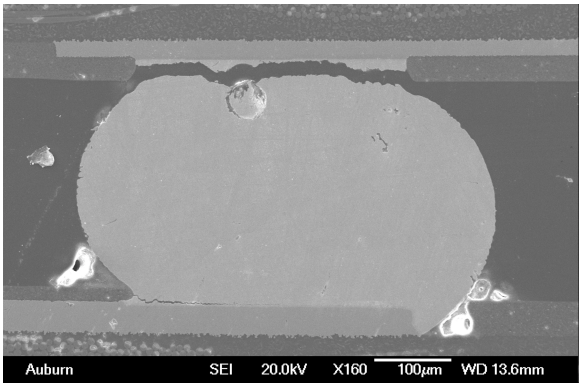

Figure 5.112: Solder joint crack on package-side and PCB-side

5.12 Failure Mode Analysis

Failure analysis has been performed on CABGA288 after reliability test. Figure 5.111 and 5.112 show the cross-sectioning image of solder joint after it failed. Multiple failure modes have been observed. The crack occurred at solder-copper interface on package-side and PCB-side as shown in Figure 5.111 and Figure 5.112. Furthermore, it is observed that corner solder joints have more possibilities of failing than other locations.

5.13 Summary and Conclusion

This chapter mainly focuses on effect of high temperature vibration on reliability of electronic packages. JEDEC dimension boards with 12 packages mounted are tested at

its first natural frequency with different G-level and operating temperature. Digital image correlation method is used to measurement displacement and strain of the PCB during deformation. Finite element method is also used to simulate vibration event with Input-G method combining with Anand model. In order to increase the computational efficiency, a nonlinear sub-modeling technique is carried out to running simulation. Displacement and strain results were also extracted from simulation and verified with experimental results. Hysteresis loop and plastic work density have also been calculated from simulation. Weibull analysis was used to analyze characteristic life of electronic packages subjected high temperature vibration. Effect of temperature and vibration G-level on fatigue life of CABGA288 have been discussed. Based on the characteristic life, plastic work density and characteristic life of solder joint, life prediction models were carried out to predict the useful life of packages on board. Failure analysis was performed to find the failure mode.

Chapter 6

Summary

In this work, the author has characterized high strain strain mechanical properties of lead-free solder. Stress-strain curves of SAC305 have been has been measured at eight different temperatures (25, 50, 75, 100, 125, 150, 175, 200 °C), four different strain rates (10, 35, 50, 75/s) and seven aging conditions (Pristine, 60, 120, 180, 240, 300, 360 days). Results show elastic modulus and ultimate tensile strength are both decreased with increasing in aging duration and operating temperature. Both values are increased with larger deformation rate. Various groups of Anand model have been computed and verified at different aging period. Effect of aging on evolution of Anand constants are also studied.

Secondly, board level drop testing has been executed with 1500G and impact pulse duration 0.5ms. Digital image correlation method is used to measurement full field displacement and strain. Finite element method is also used to simulate this drop event with input G method and Anand model. Hysteresis loop and plastic work density have also been calculated by FEM to see the damage accumulated by bending cycle.

Finally, effect of high temperature vibration on reliability of electronic packages has also been discussed. JEDEC dimension boards with 12 packages mounted are tested at its first natural frequency with different G-level and operating temperature. Digital image correlation method is used to measurement displacement and strain of the PCB during deformation. Finite element method is also used to simulate vibration event with Input-G method combining with Anand model. In order to increase the computational efficiency, a nonlinear sub-modeling technique is carried out to running simulation. Displacement and strain results were also extracted from simulation and verified with experimental results. Hysteresis loop and plastic work density have also been calculated from simulation. Weibull analysis

was used to analyze characteristic life of electronic packages subjected high temperature vibration. Effect of temperature and vibration G-level on fatigue life of CABGA288 have been discussed. Based on the characteristic life, plastic work density and characteristic life of solder joint, life prediction models were carried out to predict the useful life of packages on board. Failure analysis was performed to find the failure mode.

Bibliography

[1] P. Lall, S. Shantaram, and D. Locker, "High strain rate properties of sac105 and sac305 leadfree alloys after extended high temperature storage," Journal of the SMTA, vol. 27, no. 1, pp. 13–27, 2014.

[2] P. Lall, D. Zhang, V. Yadav, and D. Locker, "High strain-rate constitutive behavior of sac105 and sac305 leadfree solder during operation at high temperature," in Thermal, Mechanical and Multi-Physics Simulation and Experiments in Microelectronics and Microsystems (EuroSimE), 2015 16th International Conference on, pp. 1–11, IEEE, 2015.

[3] P. Lall, D. Zhang, V. i. Yadav, and D. Locker, "High strain rate constitutive behavior of sac105 and sac305 leadfree solder during operation at high temperature," Microelectronics Reliability, vol. 62, pp. 4–17, 2016.

[4] JEDEC Standard JESD22-B111, Board Level Drop Test Method of Components for Handheld Electronic Products, July 2003.

[5] J. C. Suhling and P. Lall, "Electronic packaging applications," in Springer Handbook of Experimental Solid Mechanics, pp. 1015–1044, Springer, 2008.

[6] M. Motalab, Z. Cai, J. C. Suhling, and P. Lall, "Determination of anand constants for sac solders using stress-strain or creep data," in Thermal and Thermomechanical Phenomena in Electronic Systems (ITherm), 2012 13th IEEE Intersociety Conference on, pp. 910–922, IEEE, 2012.

[7] M. Motalab, Z. Cai, J. C. Suhling, J. Zhang, J. L. Evans, M. J. Bozack, and P. Lall, "Improved predictions of lead free solder joint reliability that include aging effects," in Electronic Components and Technology Conference (ECTC), 2012 IEEE 62nd, pp. 513–531, IEEE, 2012.

[8] A. Medvedev, "Aging of tin-lead solders and joints soldered by them," Metallovedenie i Obrabotka Metallov, no. 7, pp. 16–23, 1956.

[9] P. Lall, S. Shantaram, J. Suhling, and D. Locker, "Effect of aging on the high strain rate mechanical properties of sac105 and sac305 leadfree alloys," in Electronic Components and Technology Conference (ECTC), 2013 IEEE 63rd, pp. 1277–1293, IEEE, 2013.

[10] Y. Ding, C. Wang, Y. Tian, and M. Li, "Influence of aging treatment on deformation behavior of 96.5 sn3. 5ag lead-free solder alloy during in situ tensile tests," Journal of Alloys and Compounds, vol. 428, no. 1, pp. 274–285, 2007.

[11] S.-T. Jenq, H.-H. Chang, Y.-S. Lai, and T.-Y. Tsai, "High strain rate compression behavior for sn–37pb eutectic alloy, lead-free sn–1ag–0.5 cu and sn–3ag–0.5 cu alloys," Microelectronics Reliability, vol. 49, no. 3, pp. 310–317, 2009.

[12] C. R. Siviour, High strain rate properties of materials using Hopkinson bar techniques. PhD thesis, University of Cambridge, 2005.

[13] S. B. Brown, K. H. Kim, and L. Anand, "An internal variable constitutive model for hot working of metals," International journal of plasticity, vol. 5, no. 2, pp. 95–130, 1989.

[14] R. Darveaux and K. Banerji, "Constitutive relations for tin-based solder joints," IEEE Transactions on Components, Hybrids, and Manufacturing Technology, vol. 15, no. 6, pp. 1013–1024, 1992.

[15] M. M. Basit, M. Motalab, J. C. Suhling, and P. Lall, "The effects of aging on the anand viscoplastic constitutive model for sac305 solder," in Thermal and Thermomechanical Phenomena in Electronic Systems (ITherm), 2014 IEEE Intersociety Conference on, pp. 112–126, IEEE, 2014.

[16] W. Ramberg and W. R. Osgood, "Description of stress-strain curves by three parameters," 1943.

[17] P. Lall, S. Shantaram, J. Suhling, and D. Locker, "Effect of high strain-rate on mechanical properties of sac105 and sac305 leadfree alloys," in Electronic Components and Technology Conference (ECTC), 2012 IEEE 62nd, pp. 1312–1326, IEEE, 2012.

[18] P. Lall, S. Shantaram, A. Angral, and M. Kulkarni, "Explicit submodeling and digital image correlation based life-prediction of leadfree electronics under shock-impact," in Electronic Components and Technology Conference, 2009. ECTC 2009. 59th, pp. 542–555, IEEE, 2009.

[19] P. Lall, D. Panchagade, Y. Liu, W. Johnson, and J. Suhling, "Smeared-property models for shock-impact reliability of area-array packages," Journal of Electronic Packaging, vol. 129, no. 4, pp. 373–381, 2007.

[20] P. Lall, S. Shantaram, and D. Panchagade, "Peridynamic-models using finite elements for shock and vibration reliability of leadfree electronics," in Thermal and Thermomechanical Phenomena in Electronic Systems (ITherm), 2010 12th IEEE Intersociety Conference on, pp. 1–12, IEEE, 2010.

[21] P. Lall, K. Dornala, D. Zhang, D. Xie, and A. Zhang, "Transient dynamics model and 3d-dic analysis of new-candidate for jedec jesd22-b111 test board," in Electronic Components and Technology Conference (ECTC), 2014 IEEE 64th, pp. 85–99, IEEE, 2014.

[22] A. Syed, S. M. Kim, W. Lin, J. Y. Kim, E. S. Sohn, and J. H. Shin, "A methodology for drop performance modeling and application for design optimization of chip-scale packages," IEEE transactions on electronics packaging manufacturing, vol. 30, no. 1, pp. 42–48, 2007.

[23] J.-e. Luan and T. Y. Tee, "Novel board level drop test simulation using implicit transient analysis with input-g method," in Electronics Packaging Technology Conference, 2004. EPTC 2004. Proceedings of 6th, pp. 671–677, IEEE, 2004.

[24] R. W. Johnson, J. L. Evans, P. Jacobsen, J. R. Thompson, and M. Christopher, "The changing automotive environment: high-temperature electronics," IEEE Transactions on Electronics Packaging Manufacturing, vol. 27, no. 3, pp. 164–176, 2004.

[25] D. S. Steinberg, Vibration analysis for electronic equipment. John Wiley & Sons, 2000.

[26] G. R. Henderson and A. G. Piersol, "Fatigue damage related descriptor for random vibration test environments," Sound and Vibration, vol. 29, no. 10, pp. 20–24, 1995.

[27] J. Hu, "Life prediction and damage acceleration based on the power spectral density of random vibration," Journal of the IES, vol. 38, no. 1, pp. 34–40, 1995.

[28] S. F. Wong, P. Malatkar, C. Rick, V. Kulkarni, and I. Chin, "Vibration testing and analysis of ball grid array package solder joints," in Electronic Components and Technology Conference, 2007. ECTC'07. Proceedings. 57th, pp. 373–380, IEEE, 2007.

[29] D. Barker, J. Vodzak, A. Dasgupta, and M. Pecht, "Combined vibrational and thermal solder joint fatiguea generalized strain versus life approach," ASME J. Electron. Packag, vol. 112, no. 2, pp. 129–134, 1990.

[30] C. Basaran and R. Chandaroy, "Thermomechanical analysis of solder joints under thermal and vibrational loading," TRANSACTIONS-AMERICAN SOCIETY OF MECHANICAL ENGINEERS JOURNAL OF ELECTRONIC PACKAGING, vol. 124, no. 1, pp. 60–66, 2002.

[31] H. Qi, S. Ganesan, M. Osterman, and M. Pecht, "Accelerated testing and finite element analysis of pbga under multiple environmental loadings," in Business of Electronic Product Reliability and Liability, 2004 International Conference on, pp. 99–106, IEEE, 2004.

[32] V. Gektin, A. Bar-Cohen, and S. Witzman, "Coffin-manson based fatigue analysis of underfilled dcas," IEEE Transactions on Components, Packaging, and Manufacturing Technology: Part A, vol. 21, no. 4, pp. 577–584, 1998.

[33] I. Shohji, H. Mori, and Y. Orii, "Solder joint reliability evaluation of chip scale package using a modified coffin–manson equation," Microelectronics Reliability, vol. 44, no. 2, pp. 269–274, 2004.

[34] W. Ostergren, "A damage function and associated failure equations for predicting hold time and frequency effects in elevated temperature, low cycle fatigue," Journal of Testing and Evaluation, vol. 4, no. 5, pp. 327–339, 1976.

[35] P. Lall, G. Limaye, J. Suhling, M. Murtuza, B. Palmer, and W. Cooper, "Reliability of lead-free sac electronics under simultaneous exposure to high temperature and vibration," in Thermal and Thermomechanical Phenomena in Electronic Systems (ITherm), 2012 13th IEEE Intersociety Conference on, pp. 753–761, IEEE, 2012.

[36] A. Dasgupta, C. Oyan, D. Barker, and M. Pecht, "Solder creep-fatigue analysis by an energy-partitioning approach," ASME Journal of Electronic Packaging, vol. 114, no. 2, pp. 152–160, 1992.

[37] R. Darveaux, "Effect of simulation methodology on solder joint crack growth correlation and fatigue life prediction," TRANSACTIONS-AMERICAN SOCIETY OF MECHANICAL ENGINEERS JOURNAL OF ELECTRONIC PACKAGING, vol. 124, no. 3, pp. 147–154, 2002.

[38] R. Darveaux, C. Reichman, and N. Islam, "Interface failure in lead free solder joints," in Electronic Components and Technology Conference, 2006. Proceedings. 56th, pp. 12–pp, IEEE, 2006.

[39] P. Lall, S. Gupte, P. Choudhary, and J. Suhling, "Solder joint reliability in electronics under shock and vibration using explicit finite-element submodeling," IEEE transactions on electronics packaging manufacturing, vol. 30, no. 1, pp. 74–83, 2007.

[40] P. Lall, P. Choudhary, S. Gupte, and J. C. Suhling, "Health monitoring for damage initiation and progression during mechanical shock in electronic assemblies," IEEE Transactions on Components and Packaging Technologies, vol. 31, no. 1, pp. 173–183, 2008.

[41] L. Coffin and J. Tavernelli, "Experimental support for generalized equation predicting low cycle fatigue," Transactions of the American Society of Mechanical Engineers (ASME), Journal of Basic Engineering, vol. 84, pp. 533–537, 1962.

[42] J. H. Lau, Solder joint reliability: theory and applications. Springer Science & Business Media, 1991.

[43] K. Upadhyayula and A. Dasgupta, "An incremental damage superposition approach for reliability of electronic interconnects under combined accelerated stresses," in ASME International Mechanical Engineering Congress & Exposition, pp. 16–21, 1997.

[44] R. S. Li, "A methodology for fatigue prediction of electronic components under random vibration load," TRANSACTIONS-AMERICAN SOCIETY OF MECHANICAL ENGINEERS JOURNAL OF ELECTRONIC PACKAGING, vol. 123, no. 4, pp. 394–400, 2001.

[45] D. S. Steinberg and J. Wiley, "Preventing thermal cycling and vibration failures in electronic equipment," in 9th Annual IEEE Dayton Chapter Symposium, 1988.

[46] E. Wong, C. Lim, J. Field, V. Tan, V. Shim, K. Lim, and S. Seah, "Tackling the drop impact reliability of electronic packaging," in ASME 2003 International Electronic Packaging Technical Conference and Exhibition, pp. 757–763, American Society of Mechanical Engineers, 2003.

[47] J. Pitarresi, D. Celetka, R. Coldwel, and D. Smith, "The smeared properties approach to fe vibration modeling of printed circuit cards," ASME Journal of Electronics Packaging, vol. 113, pp. 250–257, 1991.

[48] J. M. Pitarresi and A. Akanda, "Random vibration response of a surface mount lead/solder joint," Advances in electronic packaging, vol. 4, pp. 207–215, 1993.

[49] G. Limaye, High Temperature Vibration Fatigue Life Prediction and High Strain Rate Material Characterization of Lead-Free Solders. PhD thesis, Auburn University, 2013.

[50] Y. Chen, C. Wang, and Y. Yang, "Combining vibration test with finite element analysis for the fatigue life estimation of pbga components," Microelectronics Reliability, vol. 48, no. 4, pp. 638–644, 2008.

[51] Y. Zhao, C. Basaran, A. Cartwright, and T. Dishongh, "An experimental observation of thermomechanical behavior of bga solder joints by moire interferometry," Journal of Mechanical Behavior of Materials, vol. 10, no. 3, pp. 135–146, 1999.

[52] J.-P. CIech, "Solder reliability solutions: a pc-based design-for-reliability tool," Soldering & Surface Mount Technology, vol. 9, no. 2, pp. 45–54, 1997.

[53] Y. Gu and D. Jin, "Drop test simulation and doe analysis for design optimization of microelectronics packages," in Electronic Components and Technology Conference, 2006. Proceedings. 56th, pp. 6–pp, IEEE, 2006.

[54] T. Miller, H. Schreier, and P. Reu, "High-speed dic data analysis from a shaking camera system," in SEM Conference and Exposition on Experimental and Applied Mechanics, Springfield, MA, June, pp. 4–6, 2007.

[55] S. Park, C. Shah, J. Kwak, C. Jang, J. Pitarresi, T. Park, and S. Jang, "Transient dynamic simulation and full-field test validation for a slim-pcb of mobile phone under drop/impact," in Electronic Components and Technology Conference, 2007. ECTC'07. Proceedings. 57th, pp. 914–923, IEEE, 2007.

[56] S. Park, A. Al-Yafawi, D. Yu, J. B. Kwak, J. Lee, and N. S. Goo, "Influence of fastening methods on the dynamic response and reliability assessment of pcbs in cellular phones under free drop," in Thermal and Thermomechanical Phenomena in Electronic Systems, 2008. ITHERM 2008. 11th Intersociety Conference on, pp. 876–882, IEEE, 2008.

[57] A. Al-Yafawi, S. Patil, D. Yu, S. Park, J. Pitarresi, and N. Goo, "Random vibration test for electronic assemblies fatigue life estimation," in Thermal and Thermomechanical Phenomena in Electronic Systems (ITherm), 2010 12th IEEE Intersociety Conference on, pp. 1–7, IEEE, 2010.